

# Transmission electron microscopic investigations of heteroepitaxial III/V semiconductor thin layer and quantum well structures



DISSERTATION  
zur Erlangung des Doktorgrades  
der Naturwissenschaften  
(Dr. rer. nat)

dem Fachbereich Physik  
der Philipps-Universität Marburg  
vorgelegt von

**Igor Németh**  
aus Wolfen

Marburg (Lahn) 2008

Vom Fachbereich Physik der Philipps-Universität Marburg  
als Dissertation angenommen am: 11.03.2008

Erstgutachter: PD. Dr. habil. Kerstin Volz  
Zweitgutachter: Prof. Dr. Ulrich Höfer

Tag der mündlichen Prüfung: 18.03.2008



*- London Underground -*



# Contents

<b>List of Tables</b>	<b>7</b>
<b>List of Figures</b>	<b>8</b>
<b>1. Introduction</b>	<b>1</b>
<b>2. Fundamentals</b>	<b>5</b>
2.1. Crystal structure . . . . .	5
2.2. Challenges of Heteroepitaxy . . . . .	5
2.2.1. Charge neutrality of the heterointerface . . . . .	6
2.2.2. Antiphase disorder . . . . .	7
2.2.3. Other planar defects: stacking faults, microtwins . . . . .	11
2.2.4. Lattice mismatch - Relaxation . . . . .	12
2.2.5. Difference in thermal expansion coefficients . . . . .	13
2.2.6. Interdiffusion . . . . .	14
2.3. Theory of electron diffraction . . . . .	14
2.4. Refined structure factor calculation . . . . .	27
2.4.1. Valence Force Field (VFF) . . . . .	28
2.4.2. Density Functional Theory (DFT) . . . . .	29
<b>3. Experimental Methods</b>	<b>32</b>
3.1. Crystal growth . . . . .	32
3.1.1. Growth methods . . . . .	32
3.1.2. Si Substrate and pretreatment . . . . .	33
3.1.3. Si buffer growth . . . . .	34
3.1.4. Si surface . . . . .	34
3.2. Structural analysis . . . . .	39
3.2.1. Atomic Force Microscopy . . . . .	39
3.2.2. High Resolution X-Ray diffraction (HRXRD) . . . . .	41
3.2.3. Techniques for APD detection . . . . .	44
3.3. Transmission electron microscopy . . . . .	45
3.3.1. Dark Field TEM . . . . .	46
3.3.2. Dark field TEM for composition analysis . . . . .	47
3.3.3. Dark field imaging of antiphase domains . . . . .	48

3.3.4.	Convergent beam electron diffraction (CBED)	57
3.3.5.	Polarity sensitive bend contours	64
3.3.6.	Detection of other planar defects	67
3.3.7.	High-resolution TEM	70
<b>4.</b>	<b>Quantitative compositional analysis of QWs by DFTEM</b>	<b>80</b>
4.1.	Refined structure factor calculation with VFF and DFT	80
4.2.	Ga(NAs)/GaAs	84
4.3.	Ga(NAs)/GaP	85
4.4.	Ga(PAs)/GaP	87
4.5.	(BGa)P/GaP	89
4.6.	Ga(NP)/GaP	91
4.7.	Ga(AsSb)/GaAs	92
<b>5.</b>	<b>Heteroepitaxy and defect characterization (GaP on Si)</b>	<b>94</b>
5.1.	Nucleation of GaP on Si	94
5.2.	The structure of APBs	101
5.2.1.	The stoichiometric {110} APB	101
5.2.2.	The non-stoichiometric {111} APB	103
5.3.	Correlation between APD structure and Si surface	104
5.4.	Annihilation of APDs	109
5.5.	Crystal polarity and Si surface reconstruction	115
5.5.1.	Discontinuous first monolayer - charge neutrality	116
5.5.2.	Growth conditions and polarity	119
5.6.	Detection and evolution of other planar defects	121
5.7.	Summary of optimized nucleation and growth conditions	130
<b>6.</b>	<b>Summary</b>	<b>132</b>
<b>7.</b>	<b>Zusammenfassung</b>	<b>135</b>
<b>A.</b>	<b>Appendix</b>	<b>138</b>
A.1.	Abbreviations	138
A.2.	TEM sample preparation	139
A.2.1.	Cross section sandwich samples	139
A.2.2.	Plan View samples	143

# List of Tables

2.1.	Thermal expansion coefficients of semiconductors . . . . .	13
2.2.	VFF parameters of binary compounds . . . . .	29
3.1.	Contrast rules for dynamical Bragg-lines in 002 CBED discs . . . . .	60
4.1.	Kinematic (002) electron form factors calculated by DFT . . . . .	81
4.2.	Strain of anion-cation bond lengths around isolated substitutional iso- electric impurities calculated using DFT and VFF . . . . .	81
5.1.	Polarity of the GaP layers and growth conditions . . . . .	120

# List of Figures

2.1. Unit cell of the diamond and zincblende structure . . . . .	5
2.2. Crystal polarity of GaP . . . . .	7
2.3. Origin of antiphase boundaries in zinc-blende structure . . . . .	8
2.4. Antiphase disorder on different planes of the zincblende structure . . . . .	8
2.5. False bond configuration of the self annihilating $\{111\}$ APBs . . . . .	9
2.6. Stacking faults, microtwins in zincblende crystal . . . . .	12
2.7. Scattering of a plane wave on a single atom . . . . .	16
2.8. Scattering on a unit cell . . . . .	17
2.9. Ewald construction . . . . .	19
2.10. N-content dependence of the structure factor of $Ga(N_xAs_{1-x})$ . . . . .	22
2.11. The components of the incident and scattered wave vector at the crystal surface . . . . .	23
2.12. Beam path in TEM . . . . .	25
3.1. Derivative AFM image of a KOH-etched Si (001) wafer . . . . .	35
3.2. Effect of the local misorientation and annealing on the Si surface step structure . . . . .	37
3.3. Surface dimer structure of the Si-surface and local coordinate system . . . . .	38
3.4. Assembly of the atomic force microscope (AFM) . . . . .	40
3.5. HRXRD diffractogram of a Ga(NAs)/GaP multi quantum well structure . . . . .	42
3.6. HRXRD diffractogram of a GaP thin layer grown on Si . . . . .	43
3.7. Crystal model of an APB for Bloch wave calculation of the 002 intensity . . . . .	49
3.8. Reflection intensities of GaP versus the sample thickness in zone axis excitation . . . . .	50
3.9. Intensities of the $\{002\}$ reflections of GaP versus the sample thickness . . . . .	51
3.10. APDs observed by $002/00\bar{2}$ DFTEM . . . . .	51
3.11. Image intensities of 111 dark field images of GaP antiphase domains . . . . .	53
3.12. Dark field image pair of APDs taken with (a) $\{\bar{1}\bar{1}1\}$ and (b) $\{11\bar{1}\}$ reflection . . . . .	54
3.13. Dark field images of antiphase domains using different reflections . . . . .	55
3.14. Unit cell of GaP viewed along the non-polar $[001]$ direction . . . . .	56
3.15. Plan view 020 dark field images of APDs in GaP. The tilt influence on the contrast . . . . .	57

3.16. Beam path in conventional diffraction and in CBED . . . . .	58
3.17. Excitation conditions and scattering paths for polarity determination in CBED . . . . .	61
3.18. Polarity determination in $[1\bar{1}0]$ GaP with CBED . . . . .	62
3.19. Polarity analysis with CBED in GaP antiphase domains . . . . .	63
3.20. Origin of bend contours . . . . .	65
3.21. Bend contour analysis on antiphase patterned $[001]$ GaP . . . . .	66
3.22. Dark field imaging of microtwins in cross section . . . . .	68
3.23. Contrast origin of stacking faults and microtwins . . . . .	69
3.24. HRTEM image simulation process . . . . .	73
3.25. Simulated high-resolution TEM images of $\{110\}$ APBs in GaP . . . . .	77
3.26. Simulated high-resolution TEM images of $\{111\}$ APBs in GaP with Ga - Ga false bonds . . . . .	78
3.27. Simulated high-resolution TEM images of $\{111\}$ APBs in GaP with P - P false bonds . . . . .	79
4.1. Static atomic displacement . . . . .	82
4.2. Calculated and measured dark field 002 intensities of Ga(NAs) normal- ized to GaAs . . . . .	85
4.3. 002 dark field micrographs of Ga(NAs)/GaP quantum wells . . . . .	86
4.4. Calculated and measured dark field 002 intensities of Ga(NAs) normal- ized to GaP . . . . .	87
4.5. 002 dark field micrographs of Ga(PAs)/GaP quantum wells . . . . .	88
4.6. Calculated and measured dark field intensity ratios of Ga(PAs)/GaP . . . . .	89
4.7. 002 dark field micrographs of (BGa)P/GaP quantum wells . . . . .	90
4.8. Calculated and measured intensity ratios of (BGa)P . . . . .	90
4.9. 002 dark field micrographs of Ga(NP) quantum wells . . . . .	91
4.10. Calculated and measured dark field 002 intensity ratios of Ga(NP) . . . . .	92
4.11. Calculated and measured dark field 002 intensity ratios of Ga(AsSb) . . . . .	93
5.1. Illustration of the growth sequence of the continuous growth mode . . . . .	94
5.2. AFM and HRTEM images of GaP nucleation layers on Si. Role of the first monolayer . . . . .	96
5.3. AFM and HRTEM images of the annealing effect of GaP nucleation layers on Si . . . . .	98
5.4. Illustration of the growth sequence of the different nucleation modes . . . . .	98
5.5. AFM and HRTEM images of GaP nucleation layers: Role of the GaP growth sequence . . . . .	100
5.6. HRTEM micrograph of a $\{110\}$ APB. . . . .	102
5.7. Dark field images of self annihilating APDs made with the 111 and $\bar{1}\bar{1}\bar{1}$ reflections and a geometrical model . . . . .	103

5.8. Correlation between Si surface step morphology and the lateral patterning of APDs in GaP . . . . .	105
5.9. Dark field 002 micrographs of the annealing effect on the surface of {110} APD patterned GaP . . . . .	106
5.10. AFM and plan view DFTEM micrograph of low-temperature grown GaP layer on the “optimized” Si surface . . . . .	109
5.11. Cross sectional 002 dark field micrograph of a GaP layer showing Type I and Type II APDs . . . . .	110
5.12. AFM and DFTEM images of high temperature grown GaP layers with kinking Type I APDs . . . . .	111
5.13. AFM and DFTEM images of self annihilation of APDs in GaP at high temperature growth and using “optimized” Si surface . . . . .	113
5.14. Shape of the self annihilating Type I APDs on plan view DFTEM images and on a geometrical model . . . . .	114
5.15. Local coordinate system and GaP polarity . . . . .	116
5.16. Polarity analysis of a single-domain GaP layer . . . . .	117
5.17. Origin of the small Type II APDs formed on the Si terraces . . . . .	119
5.18. GaP polarity by domination of one phase . . . . .	120
5.19. AFM, DFTEM and HRTEM images of high temperature nucleated and grown GaP . . . . .	122
5.20. AFM and dark field plan view and cross sectional study of a GaP layer nucleated with the combined scheme . . . . .	124
5.21. Correlation between stacking faults and polarity I. . . . .	125
5.22. Correlation between stacking faults and polarity II. . . . .	126
5.23. HRTEM image of an APB intersected by a stacking fault . . . . .	128
5.24. Time scheme of GaP heteroepitaxy . . . . .	131
5.25. TEM images of optimized GaP nucleation . . . . .	131
A.1. Cross sectional TEM sample preparation with Ti-holder . . . . .	140
A.2. Cross sectional TEM sample preparation with self-sustaining samples .	142
A.3. Plan view TEM sample preparation . . . . .	143

# 1. Introduction

The term “Silicon - based life” is used when describing the microelectronics industry. Due to its properties, Si is the ruling material of semiconductor chip industry and the basic material of the dominating CMOS (Complementary Metal Oxide Semiconductor) processing technology. The rapid trend of dimension reduction and increasing the density of metallization leads the Si-based semiconductor technology against a “red brick wall” of fundamental problems. A possible solution is looked for in optoelectronics, by usage of optical interconnects on the chip level [1]; it was predicted in the early 1990s that this would be realized at the beginning of the new millennium. Though basic components (waveguides, detectors, modulators) were demonstrated during the last years, the elemental light source, the *silicon laser*, is still lacking.

The basic problem is that phonon-mediated light emission due to the indirect band gap of Si is very inefficient. Different approaches were proposed to enhance the efficiency of the light emittance of Si, for example exploiting the quantum confinement in low dimensional silicon by introduction of Si-nanocrystals [2] or the internal atomic-like transitions of  $\text{Er}^{3+}$ -doped Si nanocrystals [3] were used for light amplification. The limitation of the indirect band gap was proposed to be evaded by using the intravalence-band transitions. Si/Ge quantum cascade lasers exploiting this effect were reported to show electroluminescence [4]. The first continuous wave (cw) all-Silicon optically pumped Raman-laser was demonstrated in 2005 [5].

The approach of exploiting the advantageous direct band gap of the compound III/V materials by heteroepitaxy was already proposed in the 1980s [6]. The lattice mismatch between the compound semiconductors (GaAs, InP) and Si resulted however in a large density of misfit dislocations ( $10^{12} \text{ cm}^{-2}$ ). Efforts to avoid dislocations (Si/Ge graded or relaxed layers, thermal annealing cycles of directly deposited heteroepitaxial III/V layers) suppressed the dislocation densities to  $10^6 \text{ cm}^{-2}$ , but this value was still too high to hinder the rapid degradation of laser diodes [7].

An alternative approach, which is being followed at the Central Technology Laboratory at the Philipps University Marburg recently, is the integration of a nearly lattice matched direct band gap material onto Si. The Ga(NAsP) multi quantum well heterostructure system was introduced, which can be grown pseudomorphically on GaP substrates [8]. The direct band gap characteristic was verified [9]. Furthermore, the first electrical injection laser structures of this novel material system were realized, which exhibit laser characteristics both at low temperature [10] and at room temperature [11]. In order to transfer the material system to Si substrates, a thin defect-free

single crystalline GaP layer has to be grown heteroepitaxially on the Si substrate. Since the GaP/Si material system is almost lattice matched (the lattice mismatch is 0.36% at room temperature), lattice relaxation is not a primary concern; the main challenge is to cope with the formation of planar defects.

Misfit relaxation and planar defect-free GaP thin films grown on 4° off-oriented Si (001) substrates by low temperature MBE growth were presented by Yonezu et al. [12]. Since CMOS technology uses exact Si (001) substrates (for the possible prospective integration) the experiments were carried out also on nominally exact Si (001) substrates in order to be compatible. The growth took place in a commercial MOVPE machine using the less toxic, liquid precursors tertiarybutyl arsine (TBP) and triethyl gallium (TEGa), exhibiting sufficient decomposition characteristics even at low temperature.

This thesis presents the characterization, evolution and the methods to suppress the predominant crystal defects of the GaP/Si heteroepitaxial system. As threading and misfit dislocations were absent in thin layers of GaP on Si, the main problem was the formation of planar defects: antiphase boundaries (APB) and stacking faults (SF) or microtwins (MT). The first one (APB) forms on the monosteps of the Si surface and is a fundamental problem of heteroepitaxy, while the others (SFs and MTs) occur as a result of inadequate nucleation conditions which lead to 3D growth of the first monolayers.

The characterization and optimization was carried out using standard structural investigation methods, such as Atomic Force Microscopy (AFM) for the investigation of layer surface morphology and High Resolution X-Ray Diffraction (HRXRD) for measuring crystalline quality. High Resolution Transmission Electron Microscopy (HRTEM) was used to investigate the nucleation of GaP on specially treated Si surfaces. For the detection of antiphase domains (APD), a special dark field imaging method [13] with the 002 and  $00\bar{2}$  reflections was used. A novel imaging method using the {111} reflections is also presented, which enables the detection of APDs in much thinner TEM foils than the 002/ $00\bar{2}$  technique would allow.

With the combination of the investigation methods, the APD structure of the GaP thin films was correlated to the monostep morphology of the Si surface. The influence of the growth parameters (growth sequence, growth temperature) on the development of the APD evolution was investigated. In layers where a single phase was dominant, the crystal polarity (identified by Convergent Beam Electron Diffraction (CBED)) was found to be determined by the growth conditions of the nucleation step. Small self annihilating APDs were found, which did not originate from the Si monosteps, but from the terraces of the Si. Their appearance was correlated to another fundamental problem of heteroepitaxy, the charge neutrality of the heterointerface, occurring by growing polar material (e.g. GaP) on nonpolar Si-substrate.

---

The other main topic of this thesis is the quantitative compositional evaluation of ternary III/V zincblende compound quantum well structures, like the ternary subsystems of the Ga(NAsP) material system. Dark field Transmission Electron Microscopy using the chemical sensitive 002 reflection is generally used for assessing material (in)homogeneity of mixed compound quantum well structures. Moreover, the method is suitable for estimating the absolute composition of the ternary material by measuring the change in 002 image intensities. The change in image intensity, and therefore the composition, can be estimated by calculating the structure factors of the ternary and binary compounds by the virtual crystal approximation. It was found that when the isovalent impurities have different covalent radii than the host crystal, the impurities introduce a significant lattice distortion (static atomic displacement (SAD)) [14]. This displacement modifies the structure factor values, which can be calculated by the Valence Force Field method of Keating [15]. As was reported for the Ga(NAs)/GaAs material system, the neglect of the static atomic displacements results in inadequate structure factor values and an underestimation of the N-content in the Ga(NAs) quantum wells [16]. The atomic scattering factors of the elements for structure factor calculations are generally taken from the isolated atom calculations of Doyle and Turner [17]. Rosenauer et al. suggested ab initio recalculation of the atomic scattering factors for the elements bond in crystalline structure and presented the calculation for the (GaIn)As material system [18]. This thesis presents the intensity calculations of the 002 reflection of several ternary materials, which are the material basis of many quantum well heterostructures, grown either on GaAs or GaP. Materials such as dilute N-content Ga(NAs) and Ga(AsSb) are important because of their advantageous optical properties, while the incorporation of B or N into GaP can lower the lattice mismatch and increase the critical thickness when growing thicker layers on Si. The thesis is structured as follows:

The basis of *quantitative compositional evaluation of ternary III/V zincblende compound quantum well structures*, the theoretical description of electron scattering and the tools of refined structure factor calculation are presented in **Chapter 2**. The experimental methods of composition evaluation is described in **Section 3.2.2** and **Section 3.3.2**. The results of refined structure factor calculations for the GaAs- and GaP-based materials with the experimental results of HRXRD and the evaluation of chemical sensitive 002 dark field TEM imaging are presented in **Chapter 4**.

The other main topic, the *heteroepitaxial growth of GaP on Si (001) and its structural characterization*, is introduced in **Chapter 2** by summarizing the challenges of heteroepitaxial growth. The crucial defect types of the low-lattice mismatched GaP/Si material system are emphasised and theoretical description of electron scattering describing image formation of TEM is provided. **Chapter 3** presents the methods of conventional structural characterization (AFM, HRXRD), and the methods of dark

field imaging techniques of TEM and the CBED method. Image intensity simulations are presented in order to support the standard 002 dark field imaging and the novel 111 dark field technique used for APD detection. MOVPE growth and the Si-buffer surface morphology is presented in **Section 3.1** followed by the results of the correlation between growth conditions of GaP and the defect structure of the nucleation and thicker layers in **Chapter 5**.

## 2. Fundamentals

*This chapter summarizes the main challenges of heteroepitaxy: the crystal defect types of heteroepitaxial zincblende systems. A theoretical description of electron scattering serves as a basis to understand the image formation of TEM. At the end, an introduction to the methods (VFF, DFT) of refined structure factor calculation is given.*

### 2.1. Crystal structure

Elemental semiconductors such as Si and Ge crystallize in diamond structure. The  $sp^3$ -hybridization of the valence electrons results in a local configuration, where each atom is bond covalently to its four neighbors in tetrahedral form. The diamond structure (Figure 2.1 (a)) can be described by two face centered cubic (fcc) lattice, where the second fcc lattice is translated with the  $T = a/4[111]$  vector. The investigated III/V compound semiconductors crystallize in the zincblende (sphalerite) structure (Figure 2.1 (b)), which is similar to the diamond structure, but one of the fcc sublattices is occupied by the group III-atoms, and the other one is occupied by the group V-atoms.

### 2.2. Challenges of Heteroepitaxy

The main objective of this thesis is the investigation of the nucleation process and thin layer growth of GaP on Si substrates. The epitaxy of III/V materials on elemental substrates introduces problems that are not present in the homoepitaxial growth of III/V compounds. The following points give an overview of the most important challenges that must be considered when growing III/V material on elemental sub-

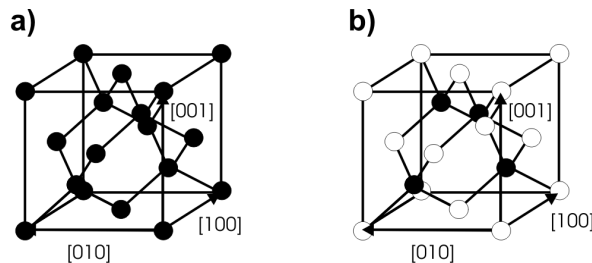


Figure 2.1.: Unit cell of the diamond (a) and the zincblende structure (b).

strate. The order of the issues represents also their hierarchy, starting with problems that have to be solved necessarily in order to achieve acceptable crystal qualities before optimizing any III/V device on the elemental substrate. The description deals with heteroepitaxy in general: these problems emerge in all systems, e.g. GaAs/Si, GaAs/Ge, InP/Si, GaP/Si... As the main focus of the thesis is on the GaP/Si material system, the peculiarities of this system will be emphasized.

### 2.2.1. Charge neutrality of the heterointerface

The first question concerning the growth of III/V material on elemental substrates is what determines and influences the interface structure? In the simplest picture, the first layer of the III/V material adjacent to the Si topmost layer is one of the bulk sublattices of the III/V structure. The factor that determines which III/V atoms are bonded to the IV surface was earlier assumed to be the strength of the IV/V and III/IV bonds. In Si-based epitaxy, as the Si - As and Si - P bonds are stronger than the Ga - Si bonds, the first sublattice was predicted to be anionic. This model has to be treated critically because of the electrical neutrality of the interface between the III/V material and the elemental substrate. Since the zincblende III/V material is polar and the elemental substrate is non-polar, the electric charge conditions of the interface have to be considered. The assumption that the first layer of the III/V crystal on the elemental substrate is an unbroken bulk sublattice of the III/V crystal introduces a vast charge on the interface. The Ga - Si and the P - Si bonds carry a charge of  $\pm e/4$ . If the first atomic plane on the Si surface was a continuous Ga plane, the two bonds with the Si lattice would introduce a donor-like charge defect with the charge density of  $e/a^2$  which is equal to  $3 \times 10^{14}$  donors/cm<sup>2</sup>. This enormous charge would build up an electrical field of  $4 \times 10^7$  V/cm in the epitaxial layer. This charge could be neutralized by mobile electrons in the conduction band. However, the atoms at the interface would still be affected by the field, since the neutralizing charge would extend over a large distance in the material. Early investigations [19] showed that the unbroken first sublattice of the III/V crystal in (001) polar on non-polar heteroepitaxy is energetically highly unfavorable. Since then, different interface configuration models were presented introducing atomic rearrangements on the interface. According to these models, not only the III/V crystal might be affected by the rearrangements, but the topmost Si atomic layer also. Si atoms are supposed to leave the last Si-plane and either incorporate in the first III/V layer, or leave the crystal. Kroemer pointed out [20] that, if the interface rearrangement goes towards completion, there is no more energetic preference of the first atomic layer to be a group V plane. The sublattice allocation of the III/V is then assumed to be determined by the nucleation kinetics.

This work primarily investigates the evolution and annihilation of planar defects introduced in the next part, but their possible interrelation with the charge neutrality of the heterointerface will also be discussed.

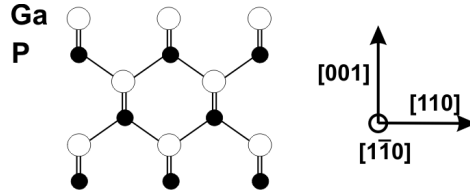


Figure 2.2.: Crystal polarity of GaP. The atoms on the top end of the bonds that are in the plane perpendicular to the image are Ga: the crystal is Ga-polar. Note, if the viewing direction is another  $\langle 110 \rangle$  direction perpendicular to the actual, the polarity reverses!

### 2.2.2. Antiphase disorder

The face-centered (fcc) compound semiconductors (GaP, GaAs, InP, GaSb) are non-centrosymmetric. The ordering of the cationic and anionic fcc sublattices can be described by the *crystal polarity*. This polarity should not be mixed with the polarity of the bonds. Crystal polarity describes the sublattice allocations of the III/V material. For easier understanding of the electron diffraction results, the following definition will be used: if the zincblende lattice is viewed from one of the  $\langle 110 \rangle$  directions (Figure 2.2), the atoms at the ends of the bonds which point out of the image plane (shown by parallel lines) determine the crystal polarity. In the crystal model in Figure 2.2, the atom at the top of these bonds is Ga, at the bottom is P. The atom at the top end of these bonds will be the reference, when describing the crystal orientation: the crystal model in this case is Ga-polar.

Growing a compound semiconductor on an elemental one, crystal domains can form, which have relatively reversed polarity. Such a crystal domain is called an **inversion domain** or **antiphase domain** (APD). The latter name will be used in this work. As two domains with different polarity adjoin, or when dealing with growth processes, coalesce, a planar defect: an **antiphase boundary** (APB) can be formed. The first description of this type of crystal defect can be found on the pages of the *Zeitschrift für Kristallographie* from 1931 [21]. This type of defect in heteroepitaxial compound semiconductor was first discussed by Holt in 1969 [22] in GaAs grown on Ge by Bobb et al. in 1966 [23]. During the growth process, there are two possibilities for the formation of the antiphase disorder: the compound material nucleates on an atomically smooth Si surface, but not with the same initiating fcc-sublattice. It can happen, if two crystal domains nucleated on the Si-surface are rotated by  $90^\circ$  around the  $[001]$  direction. As shown in Figure 2.3 (a), the crystal domains on the left and on the right side have their local orientation perpendicular to the orientation of the middle crystal domain. This formation is assumed to occur when the nucleated first monolayer of the compound material is not a continuous monolayer. In the other case, when the nucleation is assumed to be continuous, but the Si-surface has monolayer high steps, there is also a possibility to form such an antiphase defect. The closest equal lattice planes of the diamond-structured silicon in  $[001]$  have a distance of  $a/4$ . This distance in the

## 2. Fundamentals

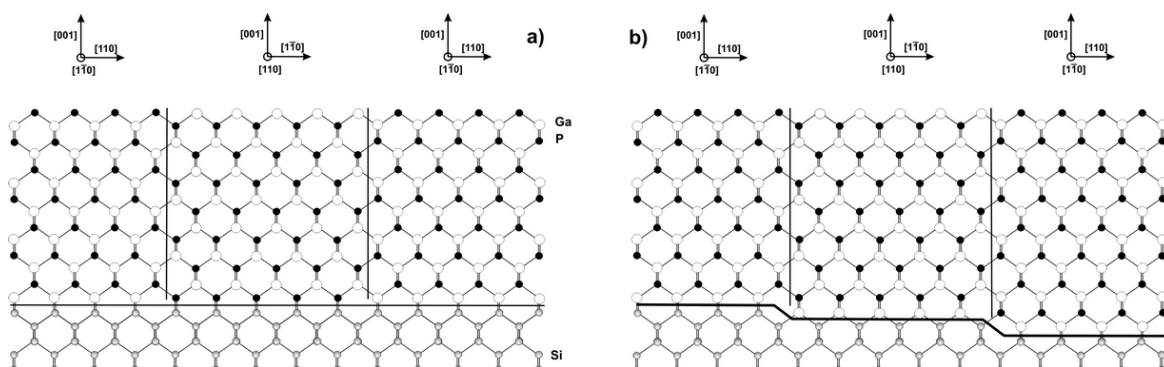


Figure 2.3.: Antiphase boundaries in zinc-blende structure. (a) APB lying on a  $\{110\}$  plane originating from discontinuous first GaP sublattice (b) APB lying on a  $\{110\}$  plane, originating from a monolayer high step of the Si-surface.

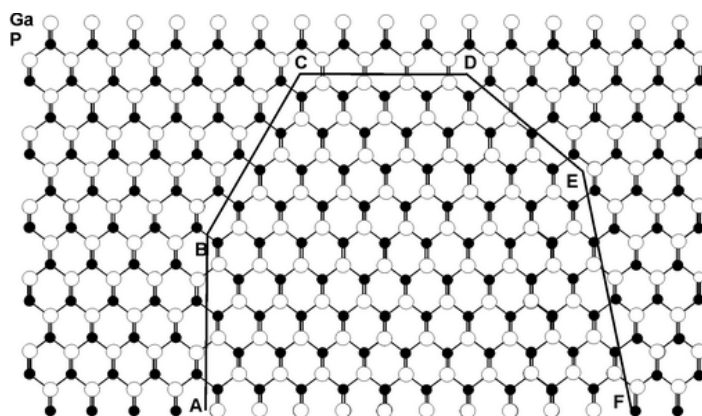


Figure 2.4.: Antiphase boundaries in zinc-blende structure. APBs on different crystallographic planes: AB parallel to  $\{110\}$ , BC: parallel to  $\{111\}$ , CD: parallel to  $\{100\}$ , DE: parallel to  $\{211\}$ , EF: parallel to  $\{311\}$

compound material is  $a/2$ . This means that, if a compound material is nucleated on a Si surface, consisting of  $a/4$  - monolayer steps, the grown compound material will have a change in the  $[001]$  lattice plane sequence - an antiphase boundary above the Si monostep (as illustrated on 2.3 (b)).

Two antiphase related crystal domains (APDs) can have their interface on various crystallographic planes. The possibilities are outlined in Figure 2.4. The APB lying on the  $(110)$  plane (between points A and B in Figure 2.4) is stoichiometric, i.e. it consists of an equal number of cation-cation and anion-anion antisite bonds. The total number of anions and cations is the same, as in the perfect crystal. As the strength of the antisite bonds Ga - Ga and P - P is not the same as the covalent Ga - P bonds, so that the local bonds are distorted. There are APBs that consist of unequal number of false bonds. Such non-stoichiometric APBs are on the  $\{211\}$  (DE) and  $\{311\}$  (EF) crystallographic planes. In these cases there are a net surplus of one of the alternating

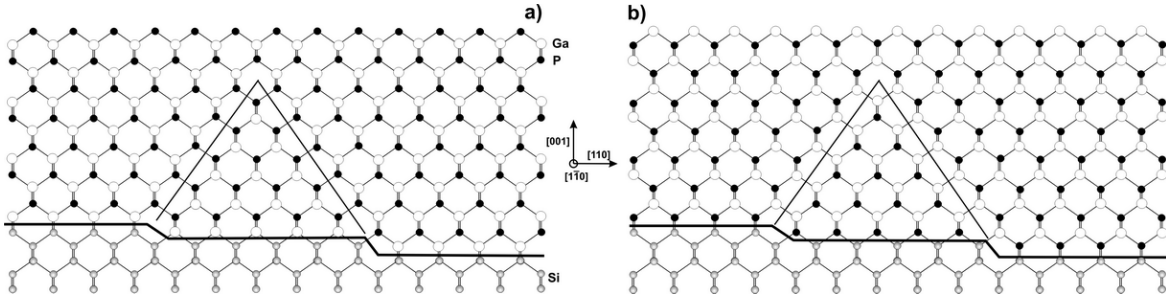


Figure 2.5.: False bond configuration of the self annihilating  $\{111\}$  APBs (a) APB lying on the  $\{111\}$  planes with false P - P bonds, (b) APB lying on the  $\{111\}$  planes with false Ga - Ga bonds

false bonds. The APBs on the  $\{111\}$  planes (BC) or on the  $\{100\}$  planes (CD) are built up of a pair of false planes of Ga - Ga or P - P. From which atomic species are they built up depends on the local bond configurations as shown in Figure 2.5 illustrating two possible  $\{111\}$  APBs (a) showing the case when the APB consists of false P - P bonds and (b) showing the case of false Ga - Ga bonds. This image illustrates a very important phenomenon: the *self annihilation of APBs*. If two neighboring APBs are inclined towards each other, they can meet and self annihilate. The region above the intersection of the APBs is single phase.

The APBs are highly energetic defects and have to be avoided before the III/V device integration. In order to elucidate the energetic preference of the different types of APBs, *ab initio* Density Functional Theory (DFT) calculations can be used as presented by Vanderbilt [24] for GaAs. With the DFT method, which will be described in section 2.4.2, the total energy of the crystal supercell can be calculated. The energy surplus attributable to the presence of the APB in the supercell of the simulation can be calculated by extracting the total energy of the supercell of the ideal crystal from the total energy of the supercell containing the APB defect. Preliminary DFT results show that the non-stoichiometric  $\{110\}$  APB has lower areal formation energy than the non-stoichiometric  $\{111\}$  APB. However, these results have to be treated critically, since significant differences exist between the real APB structure and the computable APB structures. When comparing the structure of the real APBs and the computable APB configurations the following has to be considered: calculations can be carried out on supercells with different sizes, they contain always a pair of APBs to satisfy the periodic boundary conditions, the size of the supercell represents the lateral separation width of the APBs, and the relative formation energy shows an increase with the increase of the supercell size (separation) and is saturated above a certain value. Since the real APBs in the GaP material are separated by larger distances than any supercell size of the DFT calculation, the preliminary values correspond to those separation values in the calculations, for which the formation energies show no more supercell-size dependence. The non-stoichiometric APBs, like the  $\{111\}$  type one is either Ga or P rich, consisting of only Ga - Ga or only P - P bonds. In both cases, the interface has

an excess charge, which makes them acting as donor or acceptor layers. The supercell has to contain an equal number of Ga and P atoms, therefore it has to include both the Ga - Ga and P - P interfaces separated by a specific distance. They act like two sheets of a capacitor and therefore contribute to the total energy with their electrostatic energy. The electrostatic energy diverges linearly with the separation distance. This is valid as long as the donors and acceptors remain ionized. At a specific separation length, where the electrostatic energy becomes comparable with the band gap energy of the semiconductor, the ionized states are no longer favorable, and a charge transfer occurs from one Ga - Ga APB to the P - P APB. Above this critical separation distance the material is no longer an insulator, but becomes neutral and metallic. In the calculation, the Ga - Ga and P - P type of  $\{111\}$  APB cannot be separated, since the supercell has to contain equal number of Ga and P atoms. Therefore, if there was an energetic preference between the Ga - Ga or P - P terminated  $\{111\}$  APBs, it could not be revealed. The other critical point is, that the energy surplus of the  $\{111\}$  APBs in the supercell originates from the electrostatic energy of the parallel Ga - Ga and P - P  $\{111\}$  planes. Despite that the parallel configuration does not describe exactly the experimentally observed  $\{111\}$  APB configurations, the formation energies of the non-stoichiometric  $\{111\}$  Ga - Ga or P - P APBs are expected to be higher, than of the stoichiometric  $\{110\}$  APB. The reason is, that the  $\{111\}$  APBs are extended charged defects, while the  $\{110\}$  APBs are locally compensated.

There were various attempts to grow APD free, single phased III/V material on elemental substrates. The main approaches of the suppression of APDs were the following:

**Different orientation of the substrate.** The method of Kroemer used higher-indexed Si-substrate for GaAs growth. It exploited the two sublattices of the III/V crystal having a different number of back bonds to the Si substrate. The sites with the double back bonds were expected to be occupied by the stronger bonding As, while the sites with the single back bonds were occupied by the weaker bonding Ga. Antiphase disorder free growth was proved by etching methods. The most commonly used Si-surfaces were the (211), but (311), (411), (511) were also investigated.

**Use of off-oriented Si (001) with misorientation towards the [110] direction.**

The principle of this method is the suppression of monolayer high steps on the Si surface and generation of even number layer high steps, which can be adjoined to the III/V sublattices without the evolution of antiphase disorder. It was found that a step-doubling of the misoriented Si (001) surface occurs during annealing [25]. As the detailed studies of Kaplan [26] showed, most of the surface steps of the Si are double steps, if the Si surface is misoriented by a few degrees towards the [110] direction. Using such surfaces, the growth of antiphase disorder-free GaAs layers [27] and GaP layers [28] were reported.

**High temperature annealing of the Si (001) surface.** The perfect step doubling mechanism of the nominally exact Si (001) surface during a long high temperature annealing process (20 min at 1000°C) was shown [29]. The developed surface terraces

were found to belong to the same Si-sublattice.

This thesis describes an approach of the suppression of antiphase domains through double step generation according to the latter method, and the choice of growth conditions for which the antiphase boundaries are restricted to the  $\{111\}$  planes and tend to self annihilate.

### 2.2.3. Other planar defects: stacking faults, microtwins

In fcc crystals, the  $\{111\}$  planes are close-packed planes. To understand the planar defects arising from the change of the stacking sequence, the easiest way is to have the observation direction in one of the  $\langle 110 \rangle$  directions. Doing so, the crystal is a stack of three different planes, named A, B, C as they follow each other. If the crystal is perfect, the stacking sequence is: ...ABCABCABC.... If this stacking sequence is interrupted or some planes are permuted, a **stacking fault** arises. To see the specific structure of such a stacking fault, describe the shift of the planes as a shearing operation: plane A sits in its original position, but the following planes, beginning with B are translated by a vector of  $\frac{1}{6}\langle 11\bar{2} \rangle$ . In this case, plane B has moved to the original position of plane C; plane C is becoming the original B. The changed stacking sequence is:

ABCABCABCABC $\Rightarrow$ ABCA|CABCABC.

This is illustrated in Figure 2.6 (a); one plane of type B is missing from the crystal as a vacancy plane and therefore its name is: **intrinsic stacking fault**.

It is also possible (Figure 2.6 (b)), that there is one plane too much, an interstitial plane, in the crystal. This has a stacking sequence change of:

ABCABCABCABC $\Rightarrow$ ABCABAABC

This is an **extrinsic stacking fault**. If the above mentioned  $\frac{1}{6}[11\bar{2}]$  translation occurs not for just one plane, but several times, a **multiple stacking fault** is formed.

If the stacking sequence is changed so that it is mirror symmetric onto a plane, having a sequence of

ABCABCABCABC $\Rightarrow$ ABCABCCBACBA,

the crystal on one side of this plane adjoins its **twin** from the other side (Figure 2.6). This is called a **microtwin**. The microtwin can be also understood as a rotation of the twin crystal by  $60^\circ$  or  $180^\circ$  around a  $\langle 111 \rangle$  direction.

Depending on how the stacking faults are formed, they can be described by their *Burgers vector* of the partial dislocation by which they terminate. If the Burgers vector of the dislocation at the origin of the stacking fault is not equal to the lattice translation vector, it is a partial *Frank dislocation* with a Burgers vector of  $b = \pm\frac{a}{3}\langle 111 \rangle$ . In the case where the lattice translation is equal to the lattice translation vector, the dislocation is a partial *Shockley dislocation* with the Burgers vector  $b = \frac{1}{6}\langle 11\bar{2} \rangle$ .

According to reports, stacking faults and microtwins are generated at the initial growth

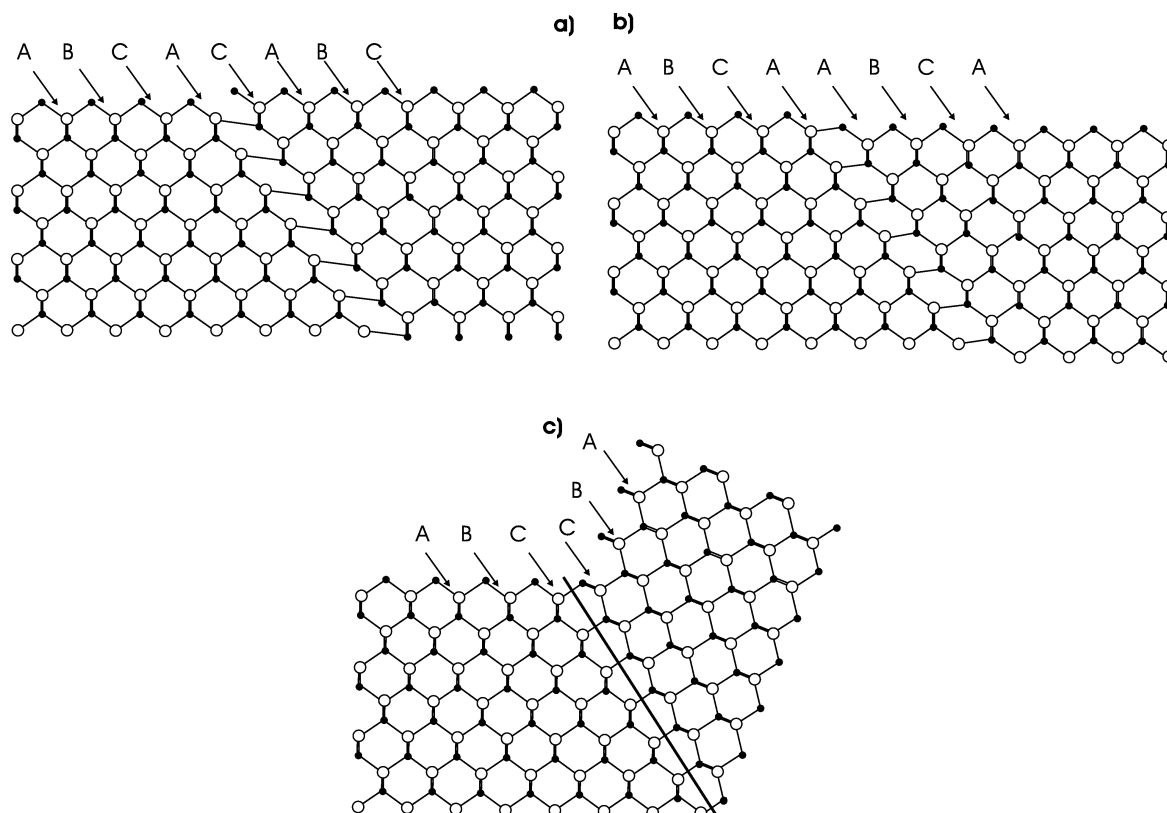


Figure 2.6.: Planar defects of the zincblende crystal: (a) intrinsic stacking fault, (b) extrinsic stacking fault, (c) microtwin.

stage [28]. Three dimensional growth was attributed to be the reason for their formation. Understanding the influence of growth conditions on their evolution is essential in order to suppress them.

#### 2.2.4. Lattice mismatch - Relaxation

The difference between the lattice constant of the III/V material and that of the elemental substrate introduces strain in the material. Due to epitaxial crystal structure, the epilayer adopts the lateral lattice constant of the elemental substrate and the lattice constant is distorted in the growth direction. This tetragonal distortion of the unit cell is determined by the elastic properties of the III/V material. The epitaxial layer remains strained until it reaches a value of the *critical thickness*. Exceeding this thickness dislocations lower the total energy of the crystal. Existing models [30], [31] predict the critical thickness in epitaxial systems to decrease with increasing the macroscopic strain of the system. For highly strained material systems such as GaAs/Si (with  $\Delta a/a=4\%$  lattice mismatch, where the critical thickness is approximately 4 monolayers) enormous efforts were made to decrease the dislocation density in the epilayer,

since any amount of dislocation density degrades the performance and the lifetime of the III/V-devices. However, different approaches only reduced the dislocation densities to  $10^6 - 10^7 \text{ cm}^{-2}$ , which were unacceptably high for high-performance devices.

The GaP/Si material system investigated in this work has a lattice mismatch value of  $\Delta a/a=0.36\%$  at room temperature. This value enables the growth of 70 nm thick GaP layers without relaxation-associated dislocation generation [28]. Thicker layers can be grown by strain compensation of the GaP/Si system by addition of N or B to the GaP.

### 2.2.5. Difference in thermal expansion coefficients

The epilayer and the substrate material differ in terms of thermal expansion. This causes a problem in the growth of heteroepitaxial layers, if the layer is deposited on high temperature, where the actual lattice mismatch is different from the value at room temperature. The lattice mismatch of the GaP and Si in the range of the growth temperature (at  $637^\circ\text{C}$ ) is  $\Delta a/a=0.52\%$ , while at room temperature  $\Delta a/a=0.36\%$  [32] [33]. The material system is more compressively strained at the growth temperature, than at room temperature. When the material is cooled down after the growth, a strain relief of  $0.2\%$  appears. In strained thin layers, which are not relaxed, this effect lowers the resulting strain. Assuming a thick heteroepitaxial layer, which is completely relaxed at the growth temperature, this effect does not act as strain relief, but as additional tensile strain. Due to the difference between the thermal expansion coefficients, the thick wafer material will shrink slower than the epilayer. The total amount of tensile strain accumulated upon cooling down from the growth temperature to room temperature is:

$$\epsilon_t = \int_{T_{room}}^{T_{growth}} [\alpha_{substrate}(T) - \alpha_{epi}(T)] dT \quad (2.1)$$

The expression of Equation 2.1 can be simplified by neglecting the temperature dependence of the thermal expansion coefficients. If the thermal expansion coefficients are treated as a constant (as listed in Table 2.1), the accumulated tensile strain has

Semiconductor	Thermal expansion coefficient at 300K ( $K^{-1}$ )
Si	$2.6 \times 10^{-6}$
Ge	$5.9 \times 10^{-6}$
GaP	$4.65 \times 10^{-6}$
GaAs	$5.7 \times 10^{-6}$

Table 2.1.: Thermal expansion coefficients of semiconductors

the simple linear form of:

$$\epsilon_t = (\alpha_{substrate} - \alpha_{epi})\Delta T \quad (2.2)$$

Since this tensile strain develops by the cooling process of the material system, the dislocation relaxation mechanisms are less efficient at relieving this strain, since the dislocation gliding processes are slower at low temperature. Reaching room temperature, only a small part of the accumulated thermal tensile strain is relieved by relaxation. The residual tensile strain can result in the appearance of microcracks in the epitaxial layer. This phenomenon is not only important in thick relaxed layers, but it has to be taken into account in strain compensated material systems as well. The critical cracking thickness of the GaAs/Si material system is between 3-5  $\mu m$  with lateral separation of the microcracks below 200  $\mu m$  [34]. This phenomenon also gives a thickness limitation for large wafer production also in the GaP/Si material system. In the framework of this thesis, thin epitaxial layers were investigated far below this thickness value. The thermal expansion difference has to be taken in further steps of III/V device growth, when growing thick layer structures on complete wafers.

### 2.2.6. Interdiffusion

The atomic interchange across the interface of the III/V material and the elemental substrate can cause detrimental autodoping of the III/V device: it can unpredictably change the doping characteristics of the interfaces, resulting in parasitic p/n junctions. Ga atoms act in the Si substrate as p-type electron acceptors, while the P atoms can act as n-type electron donors. The Si atoms interdiffusing into the GaP layer can be amphoteric dopants: if they are incorporated into the group III sublattice, they act as donors, if they occupy a group V position, they are acceptors. This cross-doping is an important issue when optimizing device structures grown on Si. This work, however, concentrates on the structural evolution of the GaP material system; the investigation of doping and interdiffusion will be a part of the future optimization process.

## 2.3. Theory of electron diffraction

The main structural investigation method of this thesis is Transmission Electron Microscopy (TEM). This section describes electron diffraction and contrast formation in TEM by the interaction of the high energy electrons with the crystalline specimen.

### Kinematical approximation

The description of diffraction theory starts with the scattering of an electron by a single atom that is tightly bound in a crystal. Only the case of elastic scattering is considered,

in which momentum and energy are conserved. Owing to the large difference between the respective masses of the electron and the crystal ions, the energy transfer from the electron to the crystal is negligible and the electron wavelength does not change in the scattering process.

**Scattering on a single atom** Electron scattering on a single atom can be described by the stationary Schrödinger equation

$$\nabla^2\Psi(\mathbf{r}) + \frac{8\pi^2me}{h^2}(E + \Phi(\mathbf{r}))\Psi(\mathbf{r}) = 0, \quad (2.3)$$

where  $E$  and  $m$  are the relativistically corrected values of the accelerating potential and of the mass of the incident electron, respectively,  $\Phi(\mathbf{r})$  is the Coulomb potential of the scattering atom,  $e$  is the elementary charge, and  $h$  is Planck's constant. The relativistic correction should be considered when using the usual accelerating voltages of 100kV-3MV, since the electrons in the TEM are travelling with 50-99% of the light velocity. The relativistic corrections, already included in Equation 2.3 are:

$$E = U \left( 1 + \frac{eU}{2m_0c^2} \right) \quad (2.4)$$

$$m = m_0 \sqrt{1 + \frac{h^2}{m_0^2c^2\lambda^2}} \quad (2.5)$$

$$\lambda = \frac{h}{\sqrt{2m_0eU(1 + eU/2m_0c^2)}} \quad (2.6)$$

where  $U$  is the accelerating voltage of the microscope,  $m_0$  the electron rest mass,  $\lambda$  the de Broglie wavelength of the electron and  $c$  is the speed of light in vacuum. Equation 2.3 can be interpreted as an inhomogeneous differential equation. It can be transformed to the integral equation

$$\Psi(\mathbf{r}) = \Psi_0(\mathbf{r}) + \frac{2\pi me}{h^2} \int_{\Omega} \frac{\exp(-2\pi ik'|\mathbf{r} - \mathbf{r}'|)}{|\mathbf{r} - \mathbf{r}'|} \Phi(\mathbf{r}')\Psi(\mathbf{r}')d^3\mathbf{r}', \quad (2.7)$$

where  $k'^2 = \frac{2me}{h^2}E$  [35] and  $\Psi_0(\mathbf{r})$  is a solution of the homogeneous part of the differential Equation 2.3. The integral term of the right side of the equation is a special solution of the inhomogeneous differential equation,  $\mathbf{r}'$  specifies the position vector in the scattering volume ( $\Omega$ ), while  $\mathbf{r}$  is the position vector of the observation point. Figure 2.7 shows the scattering of a plane wave on a scattering volume  $\Omega$  (an atom).

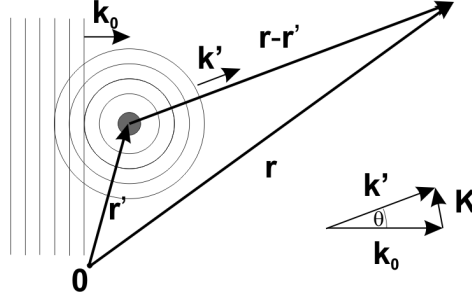


Figure 2.7.: Scattering of a plane wave on a single atom

The solution of the homogeneous differential equation of 2.3 can be obtained when  $\Phi(\mathbf{r}) = 0$ . This condition describes the incident electron wave <sup>1</sup>

$$\Psi_0(\mathbf{r}) = \exp(-2\pi i \mathbf{k}_0 \mathbf{r}), \quad (2.8)$$

where  $\mathbf{k}_0$  is the wave vector of the incident plane wave (Figure 2.7). According to the first Born approximation, the wave function  $\Psi$  can be substituted by incident plane wave in the integral of Equation 2.7. If the scattering is observed from a large distance,  $|\mathbf{r}'| \ll |\mathbf{r}|$ , with the

$$|\mathbf{r} - \mathbf{r}'| \approx r - \frac{\mathbf{r} \mathbf{r}'}{|\mathbf{r}'|} \quad (2.9)$$

approximation Equation 2.7 can be written as

$$\Psi(\mathbf{r}) = \Psi_0(\mathbf{r}) + \frac{1}{r} \exp(-2\pi i k' r) \frac{2\pi m e}{h^2} \int_{\Omega} \frac{\exp(-2\pi i (\mathbf{k}_0 - \mathbf{k}') \mathbf{r}')}{|\mathbf{r} - \mathbf{r}'|} \Phi(\mathbf{r}') d^3(\mathbf{r}'). \quad (2.10)$$

The scattering vector  $\mathbf{K}$  (as illustrated in Figure 2.7) is defined by

$$\mathbf{K} = -(\mathbf{k}_0 - \mathbf{k}' \frac{\mathbf{r}}{|\mathbf{r}|}) = -(\mathbf{k}_0 - \mathbf{k}'). \quad (2.11)$$

It is related to the scattering angle  $\Theta$  by:  $K = (\frac{2}{\lambda}) \sin \frac{\Theta}{2}$ . Substituting  $\mathbf{r} - \mathbf{r}'$  by  $r$ , Equation 2.10 becomes:

$$\Psi(\mathbf{r}) = \Psi_0(\mathbf{r}) + \frac{1}{r} \exp(-2\pi i k' r) f(\mathbf{K}), \quad (2.12)$$

---

<sup>1</sup>The so-called *crystallographical* sign convention is used. The phase factor of the electron wave contains the minus sign. In the *quantum mechanical* sign convention the plane wave travelling in the direction of  $\mathbf{k}$  is described without the minus sign by:  $\exp(2\pi i \mathbf{k}_0 \mathbf{r})$ . More on the sign conventions can be found in [36] and [37]

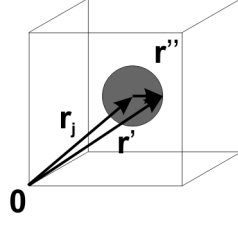


Figure 2.8.: Scattering on a unit cell

where  $f(\mathbf{K})$  is the *atomic scattering factor*. It is also called *scattering length*, due to its length dimension or *atomic form factor*. This quantity characterizes the strength of the electron scattering.

$$f(\mathbf{K}) = \frac{2\pi m e}{h^2} \int_{\Omega} \exp(2\pi i \mathbf{K} \mathbf{r}') \Phi(\mathbf{r}') d^3(\mathbf{r}'). \quad (2.13)$$

**Scattering on a unit cell** The scattering of the electron wave on a unit cell can be described as the electron plane wave scattering from each atom of the unit cell. Therefore, the potential distribution of an atom ( $\Phi(\mathbf{r}')$ ) has to be substituted in Equation 2.12 by the potential distribution of the unit cell. This potential can be described as a sum over all atoms in a unit cell. The position vector ( $\mathbf{r}'$ ) has to be substituted by the vector (Figure 2.8)

$$\mathbf{r}' = \mathbf{r}_j + \mathbf{r}'', \quad (2.14)$$

where  $\mathbf{r}_j$  denote the positions of the atoms in the unit cell. The integration has to be done over the  $\mathbf{r}''$  vector on the potential distribution  $\Phi_j(\mathbf{r})$ . The wave function scattered on the unit cell can be written as

$$\Psi_s(\mathbf{r}, \mathbf{K}) = \frac{1}{r} \exp(-2\pi i k' r) \cdot \frac{2\pi m e}{h^2} \cdot \sum_j \int_{\Omega} \exp(2\pi i \mathbf{K} (\mathbf{r}'' + \mathbf{r}_j)) \Phi(\mathbf{r}'') d^3(\mathbf{r}''), \quad (2.15)$$

The summation of all atomic form factors weighted with the atomic positions in the unit cell yields the *structure amplitude* of the unit cell, which is also referred to as the *structure factor*.

$$F_s(\mathbf{K}) = \sum_j f_j(\mathbf{K}) \exp(2\pi i \mathbf{K} \mathbf{r}_j) \quad (2.16)$$

**Scattering on a crystal** The electron diffraction of the crystal can be described as the interaction of the scattered waves emanating from the periodic assembly of unit cells. Therefore, the structure factors of the unit cells have to be summed up with their origins at positions  $R = n_1 \mathbf{r}_1 + n_2 \mathbf{r}_2 + n_3 \mathbf{r}_3$ , where  $n_{1,2,3}$  are integers and  $\mathbf{r}_{1,2,3}$

are the lattice translation vectors.

$$G(\mathbf{K}) = F_S(\mathbf{K}) \sum_{n_1, n_2, n_3} \exp\{2\pi i \mathbf{K} (n_1 \mathbf{r}_1 + n_2 \mathbf{r}_2 + n_3 \mathbf{r}_3)\} \quad n_{1,2,3} \in \mathbf{N} \quad (2.17)$$

Until now the physical expansion of the crystal was not taken into consideration. As the scattering of the electron beam on the TEM sample has to be described, the finite extension is considered by the sample thickness ( $t$ ). All the points of the sample surface are elemental sources of waves of Equation 2.18. These waves have different phases at the observation point due to the different path lengths. Summing the contributions of all points, the interference of the waves can be described using for example Fresnel's zone construction method [38]. If the wave is scattered on a sample with thickness  $t$ , its wave function is [35]:

$$\Psi_s(\mathbf{K}) = i\lambda t \frac{F_s(\mathbf{K})}{V_E} \exp(-2\pi i \mathbf{k}_0 \mathbf{R}), \quad (2.18)$$

where  $V_E$  is the volume of the unit cell. In the kinematical approximation, the amplitude decreases linearly with the sample thickness  $t$ . The  $1/r$  dependence of the amplitude in Equation 2.12 disappears in Equation 2.18. It has to be noted that, if this approximation were valid, the amplitude of the diffracted wave would become equal to that of the incident wave at a specific thickness value. Exceeding this thickness value the energy conservation would be violated. The dark field micrographs for the composition analysis are obtained under the so-called *two-beam excitation conditions* [38], where only one set of planes are in Bragg position. Under such circumstances the kinematical theory breaks down reaching sample thickness of  $\xi(\mathbf{g})/\pi$ , where  $\xi$  is the *extinction length* [39] corresponding to reflection  $\mathbf{g}$ . For the  $\mathbf{g}(002)$  reflection and the used 300 kV acceleration voltage, this critical thickness is 390 nm and 140 nm for GaAs and GaP, respectively. Since the usual sample thickness is between 30 and 50 nm for the composition evaluation, the kinematical theory can be trusted in 4.

The electron diffraction pattern is the constructive interference of the scattered waves emanating from a periodic arrangement of unit cells. The lattice amplitude  $G(\mathbf{K})$  (Equation 2.17) gives the conditions of this constructive interference. Summing the structure amplitudes of the unit cells,  $G(\mathbf{K})$  results in a peaked function, which has its maxima for scattering vectors  $\mathbf{K}$ , that obey

$$\mathbf{K}\mathbf{R} = n, \quad n \in \mathbf{N}. \quad (2.19)$$

This equation describes the Laue conditions for electron diffraction. It is fulfilled, if the scattering vector  $\mathbf{K}$  is equal to a *reciprocal lattice vector*  $\mathbf{g}_{hkl}$  with the Miller-indices  $h, k, l$  such as

$$\mathbf{K} = \mathbf{g}_{hkl}. \quad (2.20)$$

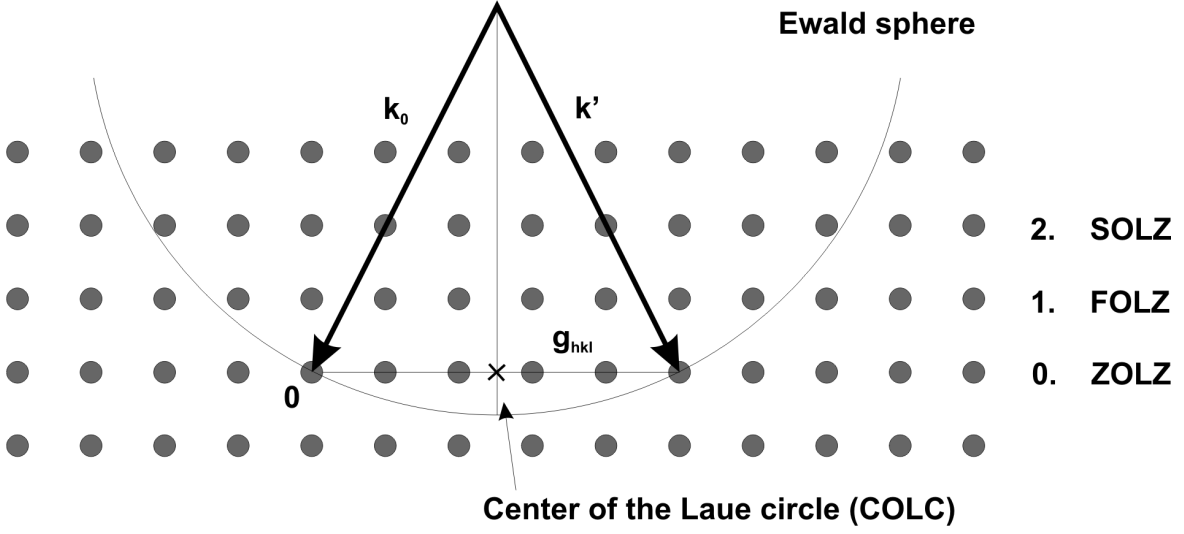


Figure 2.9.: Ewald construction. The center of Laue circle (COLC) is at the intersection of the bisector between  $\mathbf{k}_0$  and  $\mathbf{k}'$  and of the Zeroth Order Laue Zone (ZOLZ). The electrons are scattered maximally, where the Ewald sphere intersects a reciprocal lattice point.

The Laue equation in expanded form is:

$$\mathbf{KR} = \mathbf{g}_{hkl}\mathbf{R} = \begin{pmatrix} h \\ k \\ l \end{pmatrix} \begin{pmatrix} n_1 \\ n_2 \\ n_3 \end{pmatrix} = hn_1 + kn_2 + ln_3 = n. \quad (2.21)$$

The Laue conditions are illustrated in Figure 2.9. For elastic scattering the lengths of the incident wave vector  $\mathbf{k}_0$  and the scattered wave vector  $\mathbf{k}$  are equal, otherwise their difference has to be an integer multiple of the reciprocal lattice vector ( $\mathbf{k}-\mathbf{k}_0=m\mathbf{g}_{hkl}$ ). This means that an incident electron wave is scattered only if a reciprocal lattice point is intersected by the sphere, which has the radius of  $|\mathbf{k}_0|=1/\lambda$  and its center is at the origin of the incident wave vector  $\mathbf{k}_0$ ; this is called the Ewald construction. One plane slice of reciprocal space is observed in the TEM. The spherical section of the Ewald sphere is called the Laue Circle. Its center (COLC) is at the perpendicular projection of the center of the Ewald sphere on the reciprocal lattice plane containing the origin of the reciprocal lattice. This plane is the Zeroth Order Laue Zone (ZOLZ). The next plane in the direction of  $-\mathbf{k}_0$  is the First Order Laue Zone (FOLZ), and so on. The scattering angle is the higher order Laue zones is larger, than in the ZOLZ. Reflections of these zones occur only at large tilt of the crystal, or by incidence of electron waves which have wave vectors with non-parallel components with the optic axis (for example in Convergent Beam Electron Diffraction).

The structure factor  $\mathbf{F}_s(\mathbf{k})$  for the case of the zinc-blende structure (after substituting the atomic positions in the unit cell) is:

$$\mathbf{F}_s(\mathbf{g}_{hkl}) = 4 \{f_A(\mathbf{g}_{hkl}) + f_B(\mathbf{g}_{hkl})\exp(2\pi i(h+k+l)/4)\}, \quad (2.22)$$

## 2. Fundamentals

---

where  $f_A(\mathbf{g}_{hkl})$  is the atomic scattering factor of the group III element and  $f_B(\mathbf{g}_{hkl})$  is the atomic scattering factor of the group V element. The  $h, k, l$  values, for which the structure factor is zero are called the *kinematical extinction*. The non-zero values of the structure factor in the zincblende structure are:

$$\begin{aligned}
 F_s(\mathbf{g}_{hkl}) &= 4(f_A + f_B) & \text{if } h, k, l & \text{ even} & h + k + l &= 4m \\
 F_s(\mathbf{g}_{hkl}) &= 4(f_A + if_B) & \text{if } h, k, l & \text{ uneven} & h + k + l &= 4m + 1 \\
 F_s(\mathbf{g}_{hkl}) &= 4(f_A - f_B) & \text{if } h, k, l & \text{ even} & h + k + l &= 4m + 2 \\
 F_s(\mathbf{g}_{hkl}) &= 4(f_A - if_B) & \text{if } h, k, l & \text{ uneven} & h + k + l &= 4m + 3. \quad (2.23)
 \end{aligned}$$

The intensity of a scattered beam is:

$$I(\mathbf{g}_{hkl}) = |\Psi_s(\mathbf{g}_{hkl})|^2 \propto |F_s(\mathbf{g}_{hkl})|^2. \quad (2.24)$$

Using one reflection for the imaging process, this expression gives the intensity of the specific image as well. The image made with  $\mathbf{g}_{hkl} = 0$  is the *bright field image*. If one selects one diffracted beam for the imaging, a *dark field image* is obtained. The image intensities of the different dark field images, hence are:

$$\begin{aligned}
 |F_s|^2 &= 16(f_A + f_B)^2 & \text{if } h, k, l & \text{ even} & h + k + l &= 4m \\
 |F_s|^2 &= 16(f_A^2 - f_B^2) & \text{if } h, k, l & \text{ uneven} & h + k + l &= 4m + 1 \\
 |F_s|^2 &= 16(f_A - f_B)^2 & \text{if } h, k, l & \text{ even} & h + k + l &= 4m + 2 \\
 |F_s|^2 &= 0 & \text{otherwise} & & & \\
 \end{aligned} \quad (2.25)$$

Up to now, the scattering centers were considered to be on their equilibrium position on the lattice sites. The thermal motion of the atoms ( $\tilde{\mathbf{r}}$ ) can be taken into account by calculating the temporal mean value of the structure factor:

$$\tilde{F}_s(\mathbf{K}) = \sum_j f_j(\mathbf{K}) \exp(-2\pi i \mathbf{K}(\mathbf{r}_j - \tilde{\mathbf{r}})) = F_s(\mathbf{K}) \exp(-2\pi i \mathbf{K} \tilde{\mathbf{r}}). \quad (2.26)$$

Using the assumption, that the thermal motion results a Gaussian probability density around the equilibrium point, the mean value of the amplitude can be written as:

$$\tilde{F}_s(\mathbf{K}) = F_s(\mathbf{K}) \exp(-\pi^2 \mathbf{K}^2 \mathbf{b}^2), \quad (2.27)$$

where  $\mathbf{b}$  is the average amplitude of the motion of the atom. The effect of the thermal motion of the atoms on the squared value of the structure factor is

$$\left| \tilde{F}_s(\mathbf{K}) \right|^2 = |F_s(\mathbf{K})|^2 \exp(-2\pi^2 \mathbf{K}^2 \mathbf{b}^2). \quad (2.28)$$

The exponential term describes the decrease of the reflection intensities due to diffuse scattering. The diffuse scattering, and hence the background, increases with increasing temperature and so the reflections become weaker. The modifying term in Equation 2.28 is called the *Debye-Waller factor*. The values of the Debye-Waller factors for the materials investigated in this work were taken from [40].

**Chemical sensitivity** The structure factor of the zincblende structure was presented for the binary case, where only one kind of atom occupies the group III and the group V sublattice, respectively. For the case of ternary materials, if a sublattice is occupied by two atomic species, the atomic form factor of the mixed lattice sites is taken into consideration as the linear interpolation of the scattering factors of the elements. In the  $Ga(N_xAs_{1-x})$  material system the atomic scattering factor of the group V sublattice is calculated as:

$$f_{(N_xAs_{1-x})}(\mathbf{g}_{hkl}) = xf_N(\mathbf{g}_{hkl}) + (1-x)f_{As}(\mathbf{g}_{hkl}) \quad (2.29)$$

This value is used as  $f^B$  in 2.22 to get the structure factor for the specific reflection. The structure factor of the  $\mathbf{g}(002)$  reflection in this virtual crystal approximation is:

$$F(002) = 4(xf_C + (1-x)f_B - f_A) \quad (2.30)$$

It is obvious that changing the ratio ( $x$ ) of the atomic species on the sublattice changes the scattering factor, and therefore the structure factor and the reflection intensity also changes. Depending on which reflection is used, the composition dependence can be different. The dependence of the structure factor on the mixing of the sublattices is defined by the *chemical sensitivity of a reflection*  $S(\mathbf{g}_{hkl})$  [35]:

$$S(\mathbf{g}_{hkl}) := \frac{\partial}{\partial x} \left( \frac{F_s(\mathbf{g}_{hkl}, x)}{F_s(\mathbf{g}_{hkl}, 0)} \right) = \frac{\partial}{\partial x} F_s^N(\mathbf{g}_{hkl}, x), \quad (2.31)$$

where the quantity  $F_s^N$  is the structure factor normalized to structure factor of the binary material. The chemical sensitivity of the 002 and 004 reflections in Ga(NAs) is illustrated in Figure 2.10 The structure factor of the 002 reflection changes more rapidly with the composition than the structure factor of the 004 reflection. For this reason the 002 and any reflection where  $h+k+l=4m+2$  are referred to as *chemical sensitive reflections*.

Up to now, the scattering was described as the interference of single scattering events. As mentioned previously, this is valid only for very thin samples. To be able to calculate the intensity of the scattered reflections in thicker thickness regions, the dynamical approximation should be used.

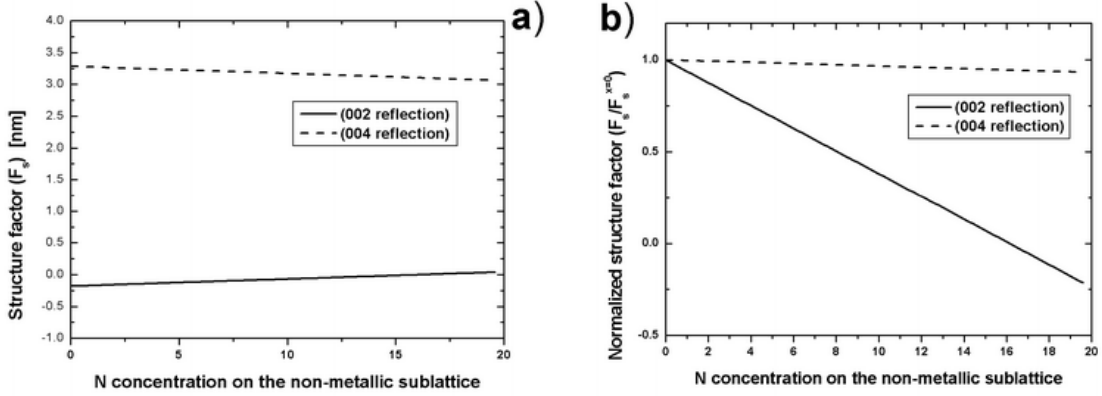


Figure 2.10.: The structure factor dependence from the sublattice mixing in  $Ga(N_xAs_{1-x})$ . (a) the structure factor value versus the N concentration, (b) the structure factor values normalized to the GaAs value.

### Dynamical approximation

Beyond the kinematical theory, the dynamical approach takes into consideration that the scattering process is built up from *multiple scattering* events: the electron wave is scattered not only once in the sample, but is rescattered on the lattice points. From the different approaches (for an overview see [41]), the Bloch wave theory of Bethe [42] is used most widely. This section gives an outline of this approach.

The starting point again is the Schrödinger equation (Equation 2.3). Unlike the kinematical approach,  $\Phi(\mathbf{r})$  describes the crystal potential and  $\Psi(\mathbf{r})$  is expanded as a Fourier series, based on the reciprocal lattice:

$$\Phi(\mathbf{r}) = \sum_{\mathbf{g}} V_{\mathbf{g}} \exp(-2\pi i \mathbf{g} \cdot \mathbf{r}). \quad (2.32)$$

The solutions of the Schrödinger equation (Equation 2.3) on this basis are the *Bloch waves*:

$$\Psi_{\mathbf{k}}(\mathbf{r}) = u_{\mathbf{k}}(\mathbf{r}) \exp(-2\pi i \mathbf{g} \mathbf{r}) = \sum_{\mathbf{g}} C_{\mathbf{g}}^{\mathbf{k}} \exp(-2\pi i (\mathbf{k} + \mathbf{g}) \mathbf{r}), \quad (2.33)$$

where  $u_{\mathbf{k}}(\mathbf{r})$  are lattice periodic functions and  $C_{\mathbf{g}}^{\mathbf{k}}$  are called the *Bloch wave coefficients*. Inserting equations 2.32 and 2.33 into the Schrödinger equation (Equation 2.3) and using the abbreviations for the mean electron wavenumber in the crystal  $\kappa^2 = \frac{2me}{\hbar^2}(E + V_0)$ , where  $V_0$  is the mean inner potential, and  $U_{\mathbf{g}} = \frac{2me}{\hbar^2}V_{\mathbf{g}}$  one obtains:

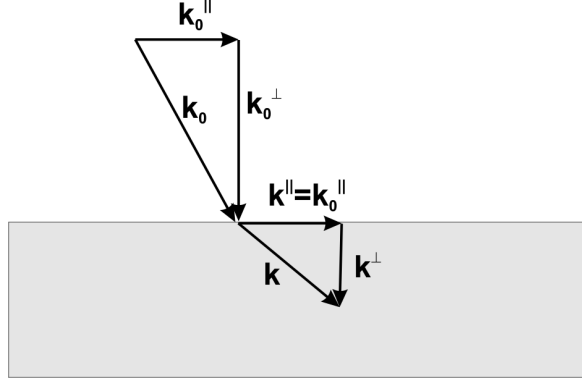


Figure 2.11.: The incident ( $\mathbf{k}_0$ ), the scattered wave vector ( $\mathbf{k}$ ) and their components parallel and perpendicular to the crystal surface.

$$\begin{aligned} & \sum_{\mathbf{g}} [\kappa^2 - (\mathbf{g} + \mathbf{k})^2] C_{\mathbf{g}}^{\mathbf{k}} \exp(-2\pi i(\mathbf{g} + \mathbf{k})\mathbf{r}) + \\ & + \sum_{\mathbf{h}} \sum_{\mathbf{g} \neq \mathbf{h}} U_{\mathbf{g}'} C_{\mathbf{h}}^{\mathbf{k}} \exp(-2\pi i(\mathbf{k} + \mathbf{h} + \mathbf{g}')\mathbf{r}) = 0. \end{aligned} \quad (2.34)$$

This equation is fulfilled for all  $\mathbf{r}$ , if the following part disappears:

$$[\kappa^2 - (\mathbf{g} + \mathbf{k}^2)] C_{\mathbf{g}}^{\mathbf{k}} + \sum_{\mathbf{g} \neq \mathbf{h}} U_{\mathbf{g}-\mathbf{h}} C_{\mathbf{h}}^{\mathbf{k}} = 0. \quad (2.35)$$

Equation 2.35 is called the *secular equation*. This, under the high-energy approximation (where the  $\mathbf{g}$  vectors are restricted to the Zero Order Laue Zone) can be written as an eigenvalue equation. Therefore, the wave vectors ( $\mathbf{k}_0$ ,  $\mathbf{k}$ ) are split into components parallel ( $\mathbf{k}_0^{\parallel}$ ,  $\mathbf{k}^{\parallel}$ ) and perpendicular ( $\mathbf{k}_0^{\perp}$ ,  $\mathbf{k}^{\perp}$ ) to the crystal surface, as shown schematically in Figure 2.11. The continuity conditions of the electron wave function are fulfilled if the parallel components are equal ( $\mathbf{k}_0^{\parallel} = \mathbf{k}^{\parallel}$ ). For the expression in the square brackets in the secular Equation 2.35, one obtains:

$$\kappa^2 - (\mathbf{g} + \mathbf{k})^2 = (\kappa^2 - \mathbf{k}^{\perp 2}) - (\mathbf{k}^{\parallel} + \mathbf{g})^2 = 0, \quad (2.36)$$

since  $\mathbf{k}^{\parallel} \cdot \mathbf{k}^{\perp} = \mathbf{k}^{\perp} \cdot \mathbf{g} = 0$ . For typical TEM electron energies between 200 and 400kV, one can use the high energy approximation:  $\kappa \approx |\mathbf{k}^{\perp}|$ . If  $\kappa^2 - \mathbf{k}^{\perp 2}$  is understood as a function of  $k^{\perp}$ , a first order Taylor expansion yields:

$$\kappa^2 - \mathbf{k}^{\perp 2} \approx 2\kappa(\kappa - k^{\perp}). \quad (2.37)$$

Hence, the secular equation turns into the following eigenvalue equation:

$$-(\mathbf{k}^{\parallel} + \mathbf{g})^2 C_{\mathbf{g}}^{\mathbf{k}} + \sum_{\mathbf{g} \neq \mathbf{h}} U_{\mathbf{g}-\mathbf{h}} C_{\mathbf{h}}^{\mathbf{k}} = -2\kappa(\kappa - k^{\perp}) C_{\mathbf{g}}^{\mathbf{k}}. \quad (2.38)$$

Using the notation of the reciprocal lattice vector of the ZOLZ  $\mathbf{g}_n$   $n = 1, \dots, N$ , the exact solution of the Schrödinger equation is obtained, if all the excited reflections are taken into account ( $N \rightarrow \infty$ ). In practice,  $N=300-500$  is used for Bloch wave calculations close to the zone axis orientation, and  $N \approx 15$  if the specimen is oriented a few degrees tilted from the zone axis. If one defines the matrix  $\mathbf{D}$  and the column vector  $\mathbf{C}$  as

$$[\mathbf{D}]_{m,n} := \begin{cases} -\left(\mathbf{k}^{\parallel} + \mathbf{g}_m\right)^2 & m = n \\ V_{\mathbf{g}_m - \mathbf{g}_n} & m \neq n \end{cases} \quad (2.39)$$

$$[\mathbf{C}]_n := C_{\mathbf{g}_n}, \quad (2.40)$$

the eigenvalue equation

$$\mathbf{D}\mathbf{C} = 2\kappa(\kappa^{\perp} - \kappa)\mathbf{C} \quad (2.41)$$

is obtained, with its  $N$  eigenvalues  $2\kappa(\kappa^{\perp j} - \kappa)$ ,  $j = 1, \dots, N$ , and  $N$  normalized eigenvectors  $\mathbf{C}^j$ .

The total exit wave function is given by

$$\Psi(\mathbf{r}) = \sum_{j=1}^N \alpha^{(j)} \Psi^{(j)}(\mathbf{r}). \quad (2.42)$$

$$\Psi^{(j)}(\mathbf{r}) = \sum_{n=1}^N C_{\mathbf{g}_n}^{(j)} \exp \left[ -2\pi i \left( \mathbf{k}^{\perp j} + \mathbf{k}^{\parallel} + \mathbf{g}_n \right) \cdot \mathbf{r} \right]. \quad (2.43)$$

The  $\alpha^{(j)}$  are called the *excitation amplitudes* of the  $j$ th Bloch wave  $\Psi^{(j)}(\mathbf{r})$ . They are obtained from the continuity of  $\Psi$  at  $z=0$ . The wave function at the lower surface of the sample can be calculated by splitting  $\mathbf{r}$  into parallel and perpendicular components to the sample surface and summing the reflections:

$$\Psi(\mathbf{r}) = \sum_{j=1}^N F(\mathbf{g}_n) \exp \left[ -2\pi i (\mathbf{g}_n + \mathbf{k}^{\parallel}) \mathbf{r}^{\parallel} \right], \quad (2.44)$$

where

$$F(\mathbf{g}_n) = \sum_j^N C_0^{*(j)} C_{\mathbf{g}_n}^{(j)} \exp(-2\pi i \mathbf{k}^{\perp(j)} t). \quad (2.45)$$

$F(\mathbf{g}_n)$  is the *amplitude of the beam*  $\mathbf{g}_n$  and it is a function of the sample thickness  $t$ .

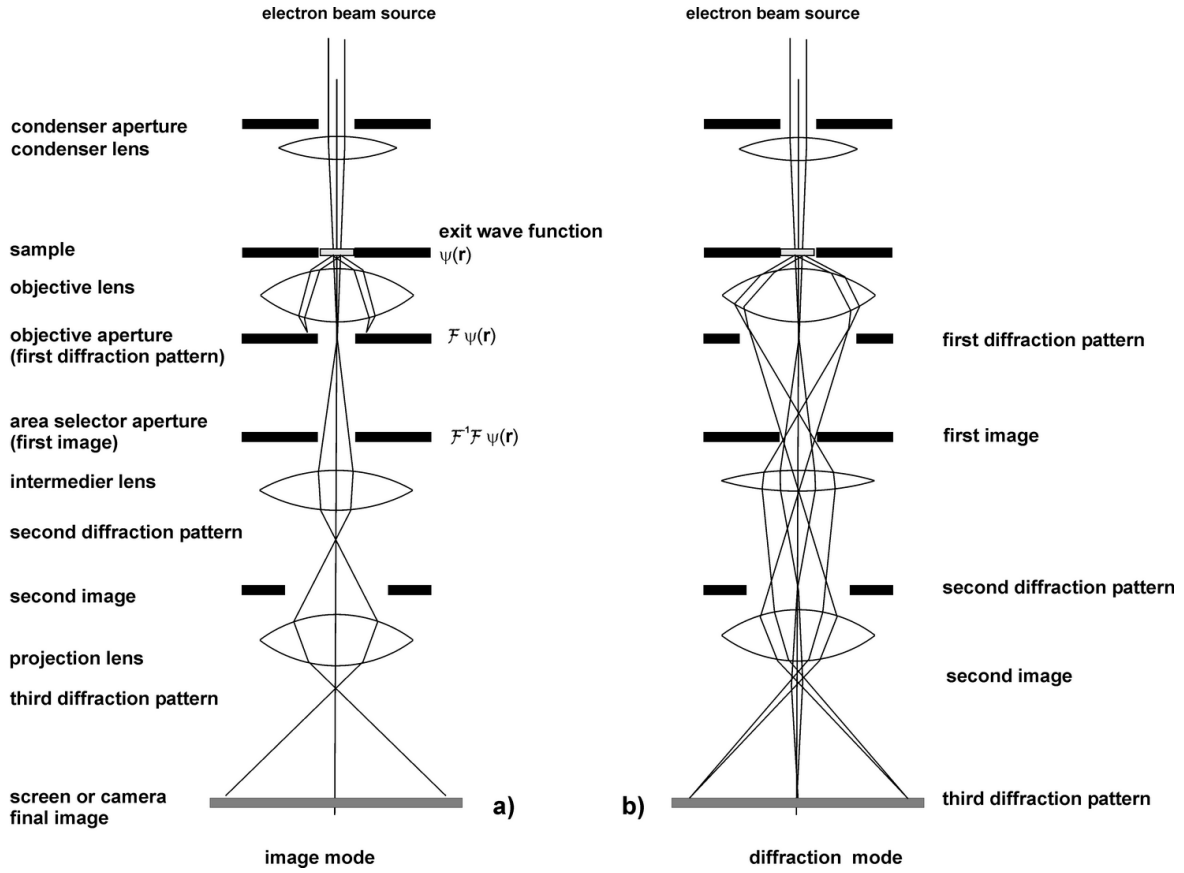


Figure 2.12.: Beam path in TEM. (a) in image mode, (b) in diffraction mode.

**Image formation** The former section described what happens to an electron beam as it penetrates a thin TEM sample: the electron wave is scattered on the crystal and it can be described by the exit wave function, as it leaves the lower surface of the sample. In this part the image formation process will be described as the interaction of the electromagnetic field of the TEM column with the exit wave.

The electron beam is magnified and modified by the *objective lens* and the *projection lenses*. Assuming an ideal microscope, what happens with the electron beam after leaving the sample is shown schematically in Figure 2.12: The electron beam after leaving the sample propagates through the *objective lens*, which has a magnification between 20 and 100 times. The objective lens generates the diffraction pattern in its back focal plane. This pattern can be described as the Fourier transform of the sample exit wave function:  $\tilde{\Psi}(\mathbf{g}) = \mathcal{F}\Psi(\mathbf{r})$ , where  $\mathbf{g}$  is a vector in the reciprocal lattice plane and  $\mathbf{r}$  is in the plane perpendicular to the beam direction. The first magnified image appears in the back image plane of the objective lens (on the first image plane). This is the result of an inverse Fourier transform of the diffraction pattern:  $\tilde{\Psi}(\mathbf{r}) = \mathcal{F}^{-1}\tilde{\Psi}(\mathbf{g}) = \mathcal{F}^{-1}\mathcal{F}\Psi(\mathbf{r})$ . The image on the screen is obtained by two

more Fourier and inverse Fourier transforms performed by the intermediate and the projection lenses as it is illustrated in Figure 2.12 (a). The diffraction pattern of the sample can be obtained when the back focal plane of the objective lens is projected onto the screen as shown in Figure 2.12 (b). Up to now an *ideal microscope* was described. In reality, due to lens aberrations and defocus, the situation is more complex. Though different lenses magnify the electron wave, it is enough to take only the aberration of the objective lens into consideration. Lens aberrations generally decrease with decreasing angle of incidence, therefore their effect for the projecting lenses can be neglected. The *spherical aberration* describes the phase shifting effect of the objective lens on the electron wave in the back focal plane. The value of the phase shift due to spherical aberration is given by:

$$\chi_s = \frac{1}{2}\pi C_s \lambda^3 (\mathbf{k} \cdot \mathbf{k})^2, \quad (2.46)$$

where  $\mathbf{k}$  is the wave vector,  $\lambda$  is the wavelength and  $C_s$  is the spherical aberration coefficient (typical value between 0.6-1.2 mm). The phase shift induced by the defocus is:

$$\chi_{\Delta f} = \pi \Delta f \lambda (\mathbf{k} \cdot \mathbf{k}), \quad (2.47)$$

where the defocus is  $\Delta f$ . Their combined effect can be described as an additional phase plate in the reciprocal space.

$$T_{CTF}(\mathbf{k}) = \exp(i\chi) = \exp(i(\chi_s + \chi_{\Delta f})) \quad (2.48)$$

is referred to as the *contrast transfer function* of the illumination system. The interference of the scattered electrons in the back image plane of the objective lens can now be considered with their additional phase:

$$\tilde{\Psi}(\mathbf{r}) = F^{-1} \{ F(\mathbf{r}) \cdot \exp [i(\chi_s + \chi_{\Delta f})] \}. \quad (2.49)$$

The intensity in the image plane is

$$I(\mathbf{r}) = \tilde{\Psi}^*(\mathbf{r}) \tilde{\Psi}(\mathbf{r}). \quad (2.50)$$

By doing the scalar product, only those Bloch waves are considered, which were not filtered out by the objective aperture. The contrast formation when imaging with electron or light waves arises from two mechanisms: the amplitude and the phase contrast. The amplitude contrast has an atomic number dependence, hence differently scattering materials can be distinguished spatially. The same is valid for the phase contrast. In general, both mechanisms contribute to the contrast formation, but different imaging methods exploit different contrast mechanisms: the high resolution imaging is based predominantly on the phase contrast and the dark and bright field imaging on the amplitude contrast.

Up to now coherent nonlinear imaging was considered. The thermal energy distribution of the electrons emitted from the cathode introduces temporal incoherence, the finite size of the filament spatial incoherence, resulting as focus spread in the image formation. Detailed descriptions can be found e.g. in [35] and [43]. Their effect will be considered later on (when simulating HRTEM images in Section 3.3.7) as a combined *focal spread* value, characterizing the microscope's image formation.

Acquiring only one HRTEM image gives only the amplitude information of the scattered electron wave and the phase information is lost. Recently developed methods are dedicated to retrieve this information. Performing the *object wave reconstruction*, several images are acquired (the so-called *defocus series*) with different phase information. The phase and defocus information from the images are the basis for recalculating the exit plane wave. The specifications of the method are detailed in the works of Urban and Thust in [44] and [45].

## 2.4. Refined structure factor calculation

This section presents suitable methods of structure factor calculation for ternary III/V materials: The Valence Force Field (VFF) method and the Density Functional Theory (DFT). The methods presented here can be also applied to quaternary and more element mixtures.

Section 2.3 presented, that the 002 structure factor of ternary solid solutions can be calculated by linear interpolation of the atomic scattering factors of the mixed elements. This is the so-called *virtual crystal approximation*. It assumes that the sites of the mixed sublattice are occupied by an element, which has an averaged atomic scattering factor. Glas et. al. [14], [46] showed that this assumption is valid only if the constituents do not introduce significant distortions of the lattice. If appreciably larger or smaller atoms are incorporated in the crystal, they can distort the lattice locally. This effect then should be taken into consideration when calculating the structure factor by introducing a *static atomic displacement* ( $\mathbf{u}_j$ ). The structure factor (Equation 2.51) of a  $\mathbf{g}_{hkl}$  reflection can then be written in the modified form of:

$$F_s(\mathbf{g}) = N^{-1} \left\{ \sum_j f_j(\mathbf{g}) \exp [2\pi i \mathbf{g} \cdot (\mathbf{r}_j + \mathbf{u}_j)] \right\}, \quad (2.51)$$

where  $N$  is the number of unit cells over which the summation is made, values for  $\mathbf{u}_j$  were calculated using the Valence Force Field method.  $f_j$  are the formerly defined atomic scattering factors. For the values of the atomic scattering factors generally the values of the isolated atoms calculated by Doyle and Turner [17] are used. The real electron density distribution of the solid can differ from the isolated atom one, therefore a recalculation of the atomic form factor of the atom in the solid would improve the accuracy of the structure factor value. Rosenauer et al. [18] proposed

the usage of the modified atomic scattering factor calculated *ab initio* for the actual compound. These data are absent for most III/V compounds.

### 2.4.1. Valence Force Field (VFF)

The modified positions of the atoms in the supercell can be calculated by the method of Keating [15] utilized for the zinc blende crystal structure [47].

This approach describes the strain energy  $E_{strain}(\mathbf{r}_s)$  of the crystal in terms of the bond stretching and of the bond bending:

$$E_{strain}(\mathbf{r}_s) = \frac{1}{4} \sum_{i=1}^4 \frac{3}{4r_{0si}^2} \alpha_{si} (\mathbf{r}_{si} \cdot \mathbf{r}_{si} - r_{0si}^2)^2 + \frac{1}{4} \sum_{i=1}^4 \sum_{\substack{j=1 \\ j \neq i}}^4 \frac{3}{4r_{0si}r_{0sj}} \beta_{isj} (\mathbf{r}_{si} \cdot \mathbf{r}_{sj} - r_{0si}r_{0sj} \cos \theta_{0isj})^2, \quad (2.52)$$

where the first part describes the bond stretching and the second part the bond bending and  $s$ ,  $i$ , and  $j$  are the atomic labels,  $r_0$  is the equilibrium interatomic distance,  $\theta_0$  is the equilibrium bond angle,  $\mathbf{r}_{si} = \mathbf{r}_s - \mathbf{r}_i$  is the relative position vector of atomic species. The summation is made over the first  $i$ ,  $j$  nearest neighbors of the atom  $s$ . The coefficients of the bond stretching and bond bending terms are related to the elastic coefficients of the binary zinc blende materials [15]:

$$\alpha = \frac{r_0}{\sqrt{3}}(C_{11} + 3C_{12}) \quad (2.53)$$

and

$$\beta = \frac{r_0}{\sqrt{3}}(C_{11} - C_{12}). \quad (2.54)$$

In the case of asymmetrical bonds (when atom  $i$  and  $j$  is not identical, the  $\beta_{isj}$  is assumed as an average of  $\beta_{isj} = (\beta_{isi} + \beta_{jsj})/2$  [48].

The force field parameters used for the different binary compounds are summarized in Table 2.2.

The values of GaAs, GaSb, and GaP were determined from experimental values of elastic parameters [49]. The parameters of the zincblende GaN was taken from [48]. Because of the large uncertainty in elastic properties reported in the literature for BAs and BP, their lattice constants and elastic parameters were calculated using DFT and the force field constants were determined with equations 2.53 and 2.54. The calculated elastic properties of BAs are:  $C_{11} = 284$  GPa,  $C_{12} = 82$  GPa, and  $a_0 = 0.47373$  nm. The values for BP are:  $C_{11} = 358$  GPa,  $C_{12} = 86$  GPa, and  $a_0 = 0.4497$  nm. The theoretical lattice constant values of BAs and BP are 1% less than the reported experimental values [50], which is typical when using DFT with the

Table 2.2.: Force-field parameters ( $\alpha$ ,  $\beta$ ) and equilibrium bond length ( $r_0$ ) for the zincblende binary solids.

Compound	$\alpha$ [N/m]	$\beta$ [N/m]	$r_0$ [nm]
GaAs	35.46	9.3	0.24479
GaP	44.49	10.70	0.23601
GaN	81.4	17.1	0.19572
GaSb	31.84	7.33	0.26396
BAs	62.88	23.84	0.20513
BP	69.27	30.59	0.19477

local density approximation. The supercell used for the simulations contained 27000 atoms, built up from  $15 \times 15 \times 15$  III/V unit cells having a volume of  $8.176^3 \text{ nm}^3$ . The epitaxial strain of the material was included in the calculation as described in [18]. The lateral lattice constants were fixed to the value of the substrate material GaAs or GaP and the lattice parameter was altered in the growth direction with the change of the chemical composition to model the tetragonal distortion of the crystal due to the epitaxial conditions. The mixed compounds are generated as random alloys by placing a substitutional impurity on the host sublattice with concentration  $x$ . The initial positions of the atoms were the ideal sublattice sites. By minimizing the strain energy

$$\frac{\partial (\sum_s E(\mathbf{r}_s))}{\partial \mathbf{r}_s} = 0 \quad (2.55)$$

with keeping the macroscopic strain at the original value, the atoms can be displaced compared to the initial ideal positions. The structure factor of the supercell with the atomic repositions can be calculated as:

$$F(\mathbf{g}) = \sum_j f_j \exp(i2\pi \mathbf{g} \cdot \boldsymbol{\rho}_j), \quad (2.56)$$

where  $\boldsymbol{\rho}_j$  is the vector of the fractional coordinates of the atom  $j$ . The atomic form factors  $f_j$  are calculated with the method described in the following part.

### 2.4.2. Density Functional Theory (DFT)

The ground state chemical and physical properties of the crystalline material can be calculated without the need of any *a priori* empirical information. The straightforward way would be to solve the corresponding many-electron Schrödinger equation. It is not only impossible to determine, but also to manipulate the ground state wave function. A feasible way to consider simpler functions, which still contain as much useful information, as possible. One possibility to calculate the electronic structure of the matter, *ab initio* methods, like the *Hartree-Fock* [51] approach. The Hartree-Fock

method describes the stationary electronic state by a many-body wave function which is the solution of the Schrödinger equation. The nuclei of the atoms are treated as fixed objects generating a static potential in which the electrons are moving. The complicated many-body wave function results in huge computational effort and makes the method unsuitable for large and complex systems. The main point of the density functional theory (DFT) [52] is to replace the many-body wavefunction of the electrons with a simple treatable electron density. In the *Kohn-Sham* approach the non-interacting electrons are moving in an effective potential of the nuclear charges. The ground state energy is found by minimizing the energy expression having the terms of the interaction with the external potential, the self interaction of the charge density and internuclear repulsion, which all depend only on the arbitrary electron density function  $\rho(\mathbf{r})$ . The only term which contains also a functional of the whole charge distribution - the kinetic, exchange and correlation energy density - is made to be dependent only on the value of the density at  $\mathbf{r}$  by the *local density approximation* (LDA) [53].

The method is implemented in the Wien2k software package [54], which was used in this work to calculate the atomic scattering factors of the zincblende ternary compounds. The calculations were restricted to a cubic supercell of 64 atoms with periodic boundary conditions. The ternary compound was simulated by substituting one atom in the GaAs or GaP host lattice with an isoelectronic impurity B, N, P, As, or Sb. The lattice constant was kept at the equilibrium DFT value of GaAs or of GaP. The atomic positions were optimized and the converged distribution of the charge density was obtained. After the structure optimization and obtaining the charge density, the x-ray structure factor was calculated. The x-ray structure factor of the 64-atom unit cell can be split to the contribution of the individual atomic spheres ( $f_{x_j}^{inner}$ ) and the interstitial parts of the unit cell ( $f_x^{out}$ ). The x-ray atomic form factor of one atom is a sum of the individual scattering factor and a part of the equally distributed interstitial part [18]:

$$f_x = f_{x_j}^{inner} + f_x^{out}/n, \quad (2.57)$$

where  $n$  denotes the number of the atoms in the unit cell.

The electron atomic form factors can be retrieved from the x-ray form factors by the *Mott-Bethe relationship* [55]:

$$f_e = \frac{m e^2}{2\pi \hbar^2 \epsilon_0 (4\pi s)^2} (Z - f_x), \quad (2.58)$$

where  $m$  is the electron mass,  $e$  is the elementary charge,  $h$  is the Planck's constant,  $\epsilon_0$  is the permittivity of free space,  $s = 1/2d$  with  $d$  being the spacing between the  $\mathbf{g}$  diffracting planes and  $Z$  is the atomic number.

The values of  $f_{x_j}^{inner}$  calculated by Wien2k include the relaxed atomic positions due

to the phase factor  $\exp(i2\pi\mathbf{g}\cdot\boldsymbol{\rho}_j)$ , which is implicitly present in  $f_{xj}^{inner}$  and should be subtracted before applying Equation 2.58.

### Structure factor calculation with DFT

The density functional method is suitable for calculating not only the atomic form factors, but also for the direct calculation of the structure factors. After minimizing the total energy iteratively, the ground state charge distribution and the relaxed positions of the nuclei are obtained. The Mott-Bethe formula gives again the relation between the calculated x-ray structure factor and the electron structure factor.

$$F_e = \frac{me^2}{8\pi\epsilon_0 h^2 s^2} (\mathcal{Z} - F_x), \quad (2.59)$$

where  $F_x$  is the x-ray structure factor calculated as the Fourier transformation of the charge density and  $\mathcal{Z}$  is the nucleus charge modified by the phase factor:

$$\mathcal{Z} = \sum_j Z_j \exp(i2\pi\mathbf{g}\cdot\boldsymbol{\rho}_j). \quad (2.60)$$

This approach will be referred to in the following as the “full DFT”. This kind of calculation provides the most accurate data for the structure factor values, therefore it is used as a reference value for the other approaches. However, this calculation can be done only on the small sized supercell, which is inappropriate for the investigation of random alloys of desired composition. The structure factor for the various compositions can be calculated with the combination of the two available methods: the atomic scattering factor values calculated by DFT serving as input constants for the VFF calculations, from which the lattice distortion and the structure factor values can be obtained.

## 3. Experimental Methods

*The first part of this chapter introduces the growth method (MOVPE), the pretreatment of the substrates and the Si surface morphology. The second part describes all the structure analytical methods, that were used for the characterization of the Si and GaP based materials. An overview of the conventional techniques (AFM, HRXRD) and a deeper insight into the techniques, which were improved during this work, such as the contrast of APBs and APDs in dark field TEM imaging and multislice simulation of APDs in HRTEM simulation is given.*

### 3.1. Crystal growth

A short description of the used MOVPE growth process is given in this section. The pretreatment of the Si wafers and homoepitaxial deposition of Si on nominally exact Si (001) wafers is described. The most important aspect, the surface structure development of Si is presented as function of slight wafer misorientation and thermal annealing conditions.

#### 3.1.1. Growth methods

The suitable methods for heteroepitaxial deposition of GaP layers on Si and growing the dilute nitride GaP-based material systems are Molecular Beam Epitaxy (MBE) and Metalorganic Vapour Phase Epitaxy (MOVPE). The advantages of MBE over MOVPE are the use of elemental sources and the accessible lower temperature regime, which is necessary for the nucleation of the GaP layers on Si. This drawback of the MOVPE is now overcome by the usage of the later described novel group V precursors, which still feature satisfactory decomposition at temperatures around 400-450°C.

The epitaxial growth of the GaP-based ternary and quaternary quantum-well structures and the heteroepitaxial growth of GaP on the Si substrates were both carried out in a horizontal MOVPE reactor system (AIX 200). The growth temperatures were varied in the temperature regime between 400°C and 700°C. The actual substrate temperature was calibrated to the Al/Si eutectic formation at 577°C. Both, the GaP and the Si surfaces were pretreated before the growth to improve the surface quality: the GaP substrates were wet chemically etched with a mixture of nitric acid, hydrochloric acid and water. The Si substrates underwent a more sophisticated pretreatment as

it is detailed in the next paragraph. The precursors for As, P, Sb, N and B were the following: tertiarybutyl arsine (TBAs), tertiarybutyl phosphine (TBP), triethyl antimonide (TESb), unsymmetric dimethyl hydrazine (UDMHy) and triethylborane (TEB), respectively. As Ga-sources triethyl gallium (TEGa) and trimethyl gallium (TMGa) were used. All these liquid precursors have sufficient decomposition characteristics even in the used low-temperature regime, and the liquid group V precursors are less toxic than the V-hydrides. The carrier gas was Pd purified  $H_2$ . The used reactor pressure was 50 mbar for the growth of the GaP- and GaAs-based materials, and was varied between 50 mbar and 950 mbar in the case of the Si homoepitaxy. The main aspects of the growth are discussed in the following paragraphs, and in Section 5.1.

### 3.1.2. Si Substrate and pretreatment

The used Si substrates were provided by G-materials and Crystec. Before mounting into the MOVPE reactor, the Si substrates underwent a wet-chemical etching process, similar to the standard RCA cleaning process, used in the CMOS technology. As it is described in [56] [57]:

1. 5 min rinse in concentrated  $H_2SO_4$  in ultrasonic bath
2. 3 min rinse under high purity water (18M $\Omega$ ) flow
3. 10 min heating in a solution of  $NH_4OH : H_2O_2 : H_2O$  (1:1:3) at 90°C to form a thin oxide-layer
4. 3 min rinse under high purity water (18M $\Omega$ ) flow
5. 10 sec rinse in 3% HF solution to remove the oxide-layer
6. 3 min rinse under high purity water (18M $\Omega$ ) flow
7. 10 min heating in  $HCl : H_2O_2 : H_2O$  (3:1:1) at 90°C to develop a thin oxide-layer
8. 3 min rinse under high purity water (18M $\Omega$ ) flow
9. Drying of the substrates with Nitrogen
10. Immediate mounting into the MOVPE reactor

#### 3.1.3. Si buffer growth

During the pretreatment of the Si-wafer the native Si-oxide layer was “replaced” by the less stable chemically established one. This allows the usage of lower temperature in the deoxidation step: The reactor temperature was raised to 975°C for 15 min in order to desorb the Si-oxide layer. This value was found as optimum for the morphology of the Si-buffer after overgrowth. After the deoxidation the reactor temperature was decreased to the temperature value, where the Si buffer growth took place. The Si-buffer was grown homoepitaxially with Vapour Phase Epitaxy (VPE) using Silane ( $SiH_4$ ) as Si-source and Pd-purified  $H_2$  as carrier gas. The reactor pressure was 200 mbar and the growth temperature 850°C, where the Silane decomposes sufficiently. The used growth rate was 1 $\mu$ m/hour. The thickness of the Si-buffer was 500 nm in order to bury defects of the original Si substrate surface and reach an atomically smooth surface, where the nucleation of the GaP can take place. The optimal conditions for the Si-buffer growth were verified by TEM investigations. No diffraction contrast of the Si-buffer and substrate interface could be seen on the micrographs in any bright or dark field image.

#### 3.1.4. Si surface

The surface of the Si-buffer, grown as described above, is atomically smooth. The AFM results (Figure 3.2 (a)) indicate surface undulation in the range of the detection limit of the AFM, being in the order of one Si monolayer thickness ( $a/4=0.1358$  nm). The shape and the lateral morphology of the steps are not ordered. As the main aim is to grow the heteroepitaxial GaP layer without anti-phase disorder, one goal is to suppress the one monolayer high steps of the Si-surface and favour the evolution of two monolayer ( $a/2=0.2716$  nm) high steps.

There are two main issues that determine the evolution of the mono/doublestep structure of the Si-surface: the **misorientation of the Si-substrate** and the **high temperature annealing conditions** subsequent to Si-buffer growth (temperature,  $H_2$  pressure, annealing time). In the following, the effects of these parameters will be discussed.

#### Role of Si-substrate misorientation

All the growth experiments were carried out on nominally exact Si (001) surfaces. The choice of this surface is interesting from the point of view of future application aspects: the heteroepitaxial GaP layers grown on Si could serve as virtual GaP surface for Ga(NAsP)-based optoelectronic devices. As the CMOS-technology uses nominally exact oriented Si (001) wafers, for future integration, the growth of GaP should be optimized on such Si-wafers. Double-step formation of highly miscut Si-surfaces at high temperature annealing conditions is well-known [28].

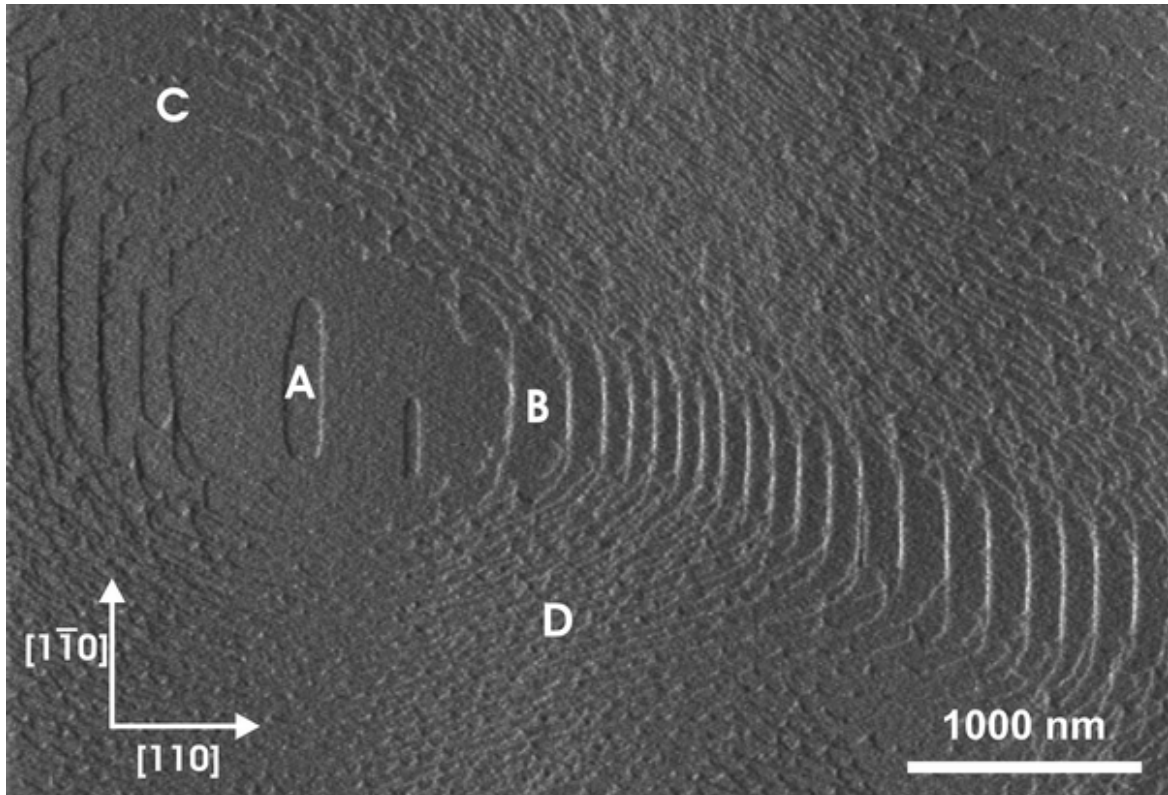


Figure 3.1.: Derivative AFM image of a KOH-etched Si (001) wafer: The effect of the changing local misorientation on the surface step morphology and double step evolution.

Although the wafers are specified as “exact” substrates, they always have a slight off-orientation. This effect comes from the sawing process of the melt pulled Si ingots. The offcut of the nominally exact substrates were specified by  $\pm 0.5^\circ$  and the actual misorientation of the substrates was between  $0.1\text{-}0.2^\circ$ . The offcut of the substrates, which were oriented towards the  $[110]$  direction was also  $0.1\text{-}0.2^\circ$ . The influence of the direction of this slight misorientation will be described first on a specially prepared Si-wafer: anisotropic KOH-etching of a formerly smooth Si (001) wafer results in an undulated surface structure, having changing local off-orientations. This wafer was annealed for 10 minutes at  $975^\circ\text{C}$  and 950 mbar  $H_2$  reactor pressure. The derivative AFM image (Figure 3.1) enhances the atomic step structure of the Si-surface and shows the following phenomenon: the part of the wafer signed with **A** is atomically smooth. It is a two monolayer deep indentation on the Si-surface. In this position, the local orientation of the wafer is exactly (001). This “dip” is surrounded by a plateau, which is also atomically flat. As moving away from this position, the degree and the direction of the local misorientation changes. Tilting the miscut towards one of the  $\langle 110 \rangle$  directions, the character and the edge morphology of the terraces alter. The monosteps (e.g. seen on position **D**) evolve into double steps: the steps seen

at position **B** or **C** are already double steps, decorated only with small monostep edges. This experiment confirms that the direction of the local surface misorientation is essential in order to reach a double-stepped Si-surface morphology under the applied annealing conditions.

#### High temperature post-growth annealing

The double stepping of the Si (001) surface can hence be initiated when the wafers undergo a post-growth annealing step right after the buffer growth [29]. The applied annealing parameters were varied to find the optimal conditions. The annealing was carried out in  $H_2$  atmosphere at the pressure of 50, 200 or 950 mbar. The annealing time was varied between 1 min and 40 min and the annealing temperature between the 975°C and 1025°C.

#### The optimal Si (001) surface

The combined influence of the misorientation and the annealing conditions of the Si (001) surface will be described in this part. The results of the study are summarized in Figure 3.2.

A very important step of the optimization process of the Si-surface morphology is seen in Figure 3.2 (b). This surface has the misorientation inclined not exactly towards a  $\langle 110 \rangle$  direction. The annealing conditions (200 mbar  $H_2$  pressure, 10 min at 975°C) did not enhance the double-step formation. The surface is decorated with monolayer high terraces: one terrace is almost straight, while the other one has a “sawtooth”-shaped profile. The terrace edges can be seen in Figure 3.2 (b) running from the top left corner towards the bottom right one. Although these conditions result in mono-stepped Si-surface, it was very important to deduce the characteristics of the evolution of the antiphase structure of the overgrown GaP layers. For easier terminology, these annealing conditions and surface misorientation of the Si will be referred to later on in the TEM studies as the “not-optimized” Si-surface. Figure 3.2 (c) shows a further step towards double step formation. The misorientation of this surface was not towards one of the preferred  $\langle 110 \rangle$  directions. The annealing of the surface took place at 975°C for 10 minutes with increased  $H_2$  pressure (950 mbar). The observed trend was the following: although the surface was still mono-stepped, the terrace edges were closer to each other, than on the Si surfaces that were annealed at lower reactor pressures. The edges of the “sawtooth” shaped terraces were parallel  $[110]$  and  $[1\bar{1}0]$  directions. This confirms that the H present during the annealing plays an large role in stabilizing the double steps.

The superimposition of the right misorientation and the right annealing conditions is seen on the Si surface in Figure 3.2 (d). The surface normal of this Si surface was

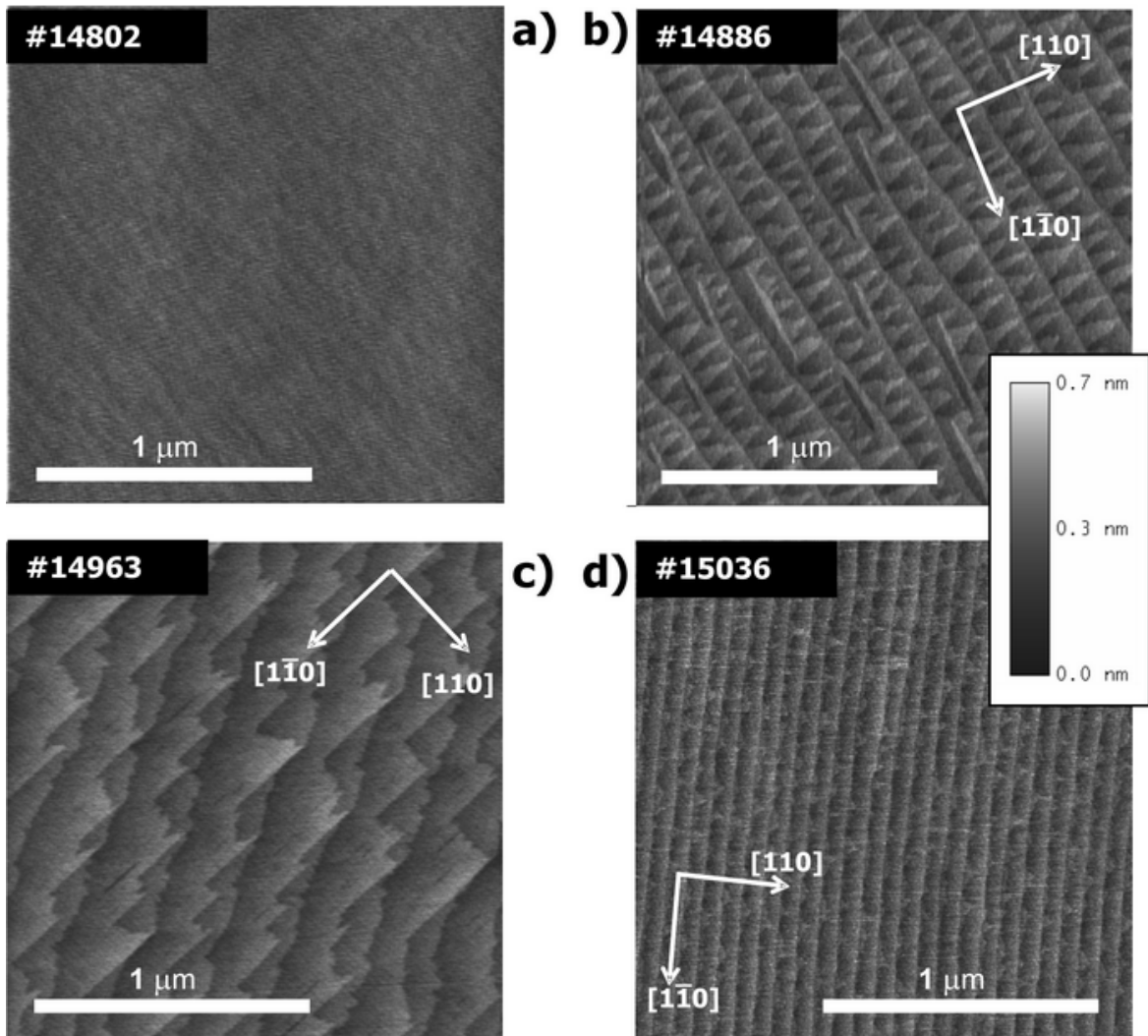


Figure 3.2.: AFM images of a (a) Si-surface grown using  $SiH_4$  at  $850^\circ C$  at 950 mbar reactor pressure without further annealing step, and with different annealing conditions and different surface normal misorientations: (b) wrong annealing conditions (200 mbar  $H_2$  pressure, 10 min at  $975^\circ C$ ), wrong misorientation (surface normal inclined, but not towards a  $\langle 110 \rangle$ ). This Si surface is referred to as “not-optimized”. (c) correct annealing conditions (950 mbar  $H_2$  pressure, 10 min at  $975^\circ C$ ), wrong misorientation, (d) correct annealing, correct misorientation (surface normal  $[001]$  inclined towards a  $\langle 110 \rangle$  direction). This is referred to as the “optimized” Si surface.

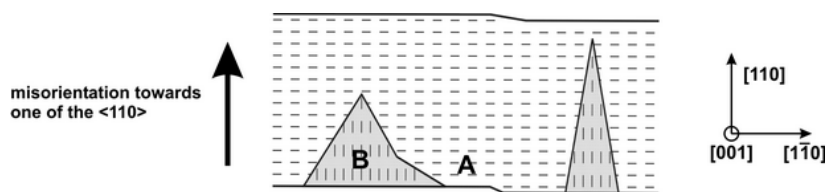


Figure 3.3.: Surface dimer structure of the Si-surface: the dimers of the terraces are oriented parallel to the down-step edge of the terrace, while the dimers of the monostep high “sawtooth-like” platforms are perpendicular to the down-step terrace edges. The  $[1\bar{1}0]$  direction of the local coordinate system is parallel with the terrace dimers, while the  $[110]$  is perpendicular to them.

slightly inclined towards a  $\langle 110 \rangle$  direction and the annealing was carried out at  $975^\circ\text{C}$  for 10 minutes with increased  $H_2$  pressure (950 mbar). The surface was decorated with terraces, which had a height separation of two monolayers of Si ( $a/2=0.2716$  nm). These terrace edges only exhibited a slight undulation; a small fraction of the terrace edges was still decorated with the “sawtooth”-patterned monolayer high stepped features. Although the monolayer high steps still existed on the surface, they were much closer to each other than in the formerly described surfaces. This will be referred to later on as the “optimized Si-surface” and its importance will be described in Section 5.4.

The structure of the Si (001) surfaces can be understood in the terms of the surface reconstruction. Aspnes and Ihm showed [58] that the double step formation of the misoriented Si by  $\pi$ -bond step reconstruction is energetically favorable. The  $\pi$ -bond step reconstruction is possible only if the surface reconstruction of the double stepped terraces is  $(2\times 1)$ . This means that, on the surface of the double stepped terrace, the Si dimers are parallel with the down-step terrace edge. If there is a monolayer high platform on this terrace, it is from the other Si-sublattice. This means that the dimers of the monolayer high sawtooth-like platforms are perpendicular to the down-step edges of the terraces. Figure 3.3 shows the orientation of the surface Si-dimers on a slightly misoriented Si surface schematically: the surface Si-dimers on the terrace (**A**) are oriented parallel with the down-step terrace edge, while on the monostep high platforms (**B**) they are perpendicular to the down-step terrace edge, irrespective whether the surface normal is inclined towards  $[110]$  or the  $[1\bar{1}0]$  direction, as these directions are equal in the diamond structure. Since these directions are not equal in the zincblende structure, but the Si surface determines the orientation of the zincblende crystal grown on it, a *local coordinate system* will be used in the following. The direction of the Si surface dimers on the double stepped terraces is defined arbitrarily as the  $[1\bar{1}0]$  direction. The direction which exhibits dimers perpendicular to the terrace is  $[110]$ , as it is shown in Figure 3.3.

The optimal preparation of the nominal Si (001) can be summarized in the following way: the enhancement of the double step evolution of the nominal Si (001) surface is the highest when the slight misorientation of the surface is inclined towards a  $\langle 110 \rangle$

direction and the thermal annealing of the Si surface is carried out at 975°C for 10 minutes in  $H_2$  atmosphere at 950 mbar reactor pressure.

The next step of the optimization of the GaP growth is the execution of proper nucleation. This is a crucial step in order to suppress all types of planar defects: APBs, stacking faults and microtwins. Their evolution, the way of their suppression and the conditions of the GaP nucleation are discussed in Section 5.1.

## 3.2. Structural analysis

In this section the different structural characterization methods are introduced that were used during this work. The first part describes the conventional methods (AFM, HRXRD). The TEM part describes conventional techniques and improved methods like the 002/00 $\bar{2}$  and the 111 dark field imaging techniques for APD detection, the Convergent Beam Electron Diffraction (CBED) method for polarity analysis, HRTEM image simulation and contrast mechanisms of other planar defects. The presented methods are presented in “chronological order”: they are introduced in that order, a given sample would be investigated in. The description focusses their physical principle, the information they provide and specifics concerning the application of the investigated material system.

### 3.2.1. Atomic Force Microscopy

Atomic Force Microscopy (AFM) is a subnanometer sensitive surface investigation method. It provides topographical information from micrometer large semiconductor surfaces with monolayer height resolution.

The AFM is a scanning probe method, exploiting the interaction between a scanning tip and the semiconductor surface. The tip detects the interactions (mechanical force, van der Waals forces, electrostatic forces) between the sample and the measurement system. The tip is scanned over the sample surface and the changing magnitude of interaction results the location-dependent height information: the topography. The operation principle of the digital instruments Nanoscope IIIa digital instruments [59] is demonstrated in Figure 3.4 and in the following:

The scanning probe is a pyramidal shape, several 100 nm long Si tip with a radius of 10 nm. It is located on the end of the *cantilever*, a 100  $\mu\text{m}$  long and 4  $\mu\text{m}$  wide plate spring. The cantilever is attached to a few mm large holder. In the used working mode of the AFM the Van der Waals and the Coulomb interactions are exploited. In both cases, the forces act to bend the cantilever. This bending is used for measuring the z-directional deviation using a laser beam projected on the back of the cantilever. The reflected ray is detected by a photodiode. The photodiode is divided into an array of four parts and detects only relative deviation. This relative signal is transferred

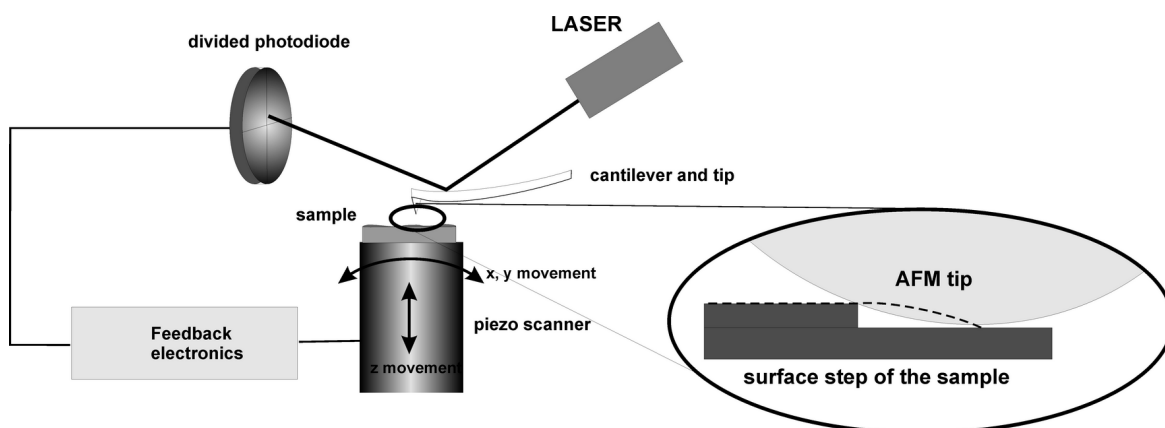


Figure 3.4.: Assembly of the atomic force microscope (AFM)

along to the electronic feedback system. This feedback system directs the cylindrical piezo-scanner, upon which the sample is mounted. The piezo-scanner generates the horizontal movement of the sample, thus executes the scanning. The controlling voltage applied in the z-direction of the piezo crystal provides the precise movement of the sample in the z-direction in order to maintain constant height by correction of the bending of the cantilever. Movement in z-direction (i.e. the local height) in combination with the x - y position results in a three dimensional topographical image of the sample surface. The scanning is done in *tapping mode*. This method permits the usage of the AFM in an ambient atmosphere. In tapping mode the cantilever is vibrated by a piezo resonator, oscillating at a frequency close to the resonant frequency of the cantilever. If the tip approaches the surface, the attractive van der Waals forces modify the resonance frequency of the cantilever; other forces damp the oscillation. The tip-surface distance is set by the tuning of the oscillation amplitude. The lateral scan area of the AFM depends on the x-y movement of the piezo crystal which is a result of bending from its z-axis. The maximal scan area of the used scan unit is  $125 \mu m^2$ . The lateral resolution is determined by the tip curvature, since the obtained image is always a convolution of the sample surface and the tip geometry (as illustrated in the zoomed part in Figure 3.4). This limits the lateral resolution to approximately 10 nm. The height resolution is in the order of one atomic layer of the investigated semiconductor materials such that monoatomic steps of Si can be resolved routinely by the used experimental setup. However, due to the limited lateral resolution, if there was a 10-20 nm wide monolayer deep dip on the surface, the AFM tip could not follow this height undulation, and hence cannot image it.

Although vertical resolution is the main power of the AFM, very small height steps can be smeared out due to the noise of the imaging. The steps structure can be made visible on the differential image, which is simply the derivative of the original one.

### 3.2.2. High Resolution X-Ray diffraction (HRXRD)

High Resolution X-Ray diffraction is a powerful structural investigation method for epitaxial thin layers and heterostructures. In the framework of this thesis it was used for two purposes: (1.) to evaluate the crystal quality of the heteroepitaxial GaP thin layers grown on Si substrates and measure the film thickness, and (2.) to evaluate compositional information via determining the macroscopic strain of GaP-based ternary quantum well structures. In this part, the fundamentals of HRXRD will be discussed. The X-rays are elastically scattered from the zinc-blende crystal structure, and when they are under Bragg conditions, the scattered waves interfere, and result a characteristic diffraction peak. For the investigation of strained III/V thin films or multilayers usually the (004) reflection is used. According to kinematical theory, this reflection is “strong” and also sensitive to the strain of the crystal. If an epitaxial, tetragonally strained layer is deposited on a substrate, the (004) reflection of the layer appears at a different angle than the above mentioned substrate reflection. What is measured experimentally (a diffractogram), is a narrow angle interval around the (004) substrate reflection  $\vartheta_{Sub}$ . The measurement is a  $\omega/2\vartheta$  scan or (004) rocking curve, carried out by altering  $2\vartheta$  and  $\omega$  angles simultaneously. In the case of a compressively strained epitaxial layer, where the [001] lattice constant  $a^\perp$  of the epilayer is larger than that of the substrate ( $a_0$ ), the additional reflection appears at a lower angle than the substrate reflection ( $\vartheta_{Bulk} < \vartheta_{Sub}$ ). If the deposited layer is tensile strained, such that the [001] lattice constant  $a^\perp$  of the epilayer is smaller than of the substrate, the 004 reflection appears at higher angle ( $\vartheta_{Bulk} > \vartheta_{Sub}$ ). According to the kinematic theory of scattering, and taking only single scattered beams into consideration, the relation between the strained lattice mismatch  $\varepsilon^\perp$  and the separation of the substrate and layer peak ( $\Delta\vartheta$ ) can be approximated by:

$$\varepsilon^\perp = \frac{\Delta a^\perp}{a_0} = \frac{a^\perp - a_0}{a_0} = -\Delta\vartheta \cdot \cot \vartheta_{Sub} \quad (3.1)$$

The value of the relaxed lattice mismatch relation to the lattice constant of the substrate ( $a_0$ ) can be obtained by using the theory of elastic deformation of crystals:

$$\varepsilon = \frac{\Delta a}{a} = \frac{a - a_0}{a_0} = \frac{C_{11}}{C_{11} + 2C_{12}} \cdot \varepsilon^\perp, \quad (3.2)$$

where  $C_{11}$ ,  $C_{11}$  and  $C_{12}$  are the elastic constants of the different crystal directions. The elastic constants can be derived from elasticity theory.

If the deposited material contains more elements than the simple binary compound, the lattice constants are calculated by the linear combination of the components using Vegard’s law [60]:

$$a(A_x B_{1-x} C) = x a(AC) + (1 - x) a(BC) \quad (3.3)$$

### 3. Experimental Methods

This will be important for the later quantitative analysis of ternary quantum wells in Chapter 4. The suitability of this linear assumption was proven to be valid for Ga(NAs)/GaAs by comparative SIMS (secondary ion mass spectrometry) and HRXRD measurements.

The ternary GaP-based quantum wells are deposited several times on the substrate, each separated by GaP barriers, building up a multi quantum well (MQW) heterostructure, in order to form a periodic superlattice in the crystal, which results in an additional periodic peak pattern in the diffractogram (Figure 3.5). Evaluating the distance of the satellite reflections ( $\Delta\vartheta_{Sat}$ ) using kinematical theory, the thickness of one superlattice period (the sum of the barrier,  $d_{Barr}$ , and the quantum well,  $d_{QW}$ , thickness) can be obtained:

$$D_{MQW} = d_{QW} + d_{Barr} = \frac{\lambda}{2 \cos \vartheta_{Sub} \cdot \Delta\vartheta_{Sat}} \quad (3.4)$$

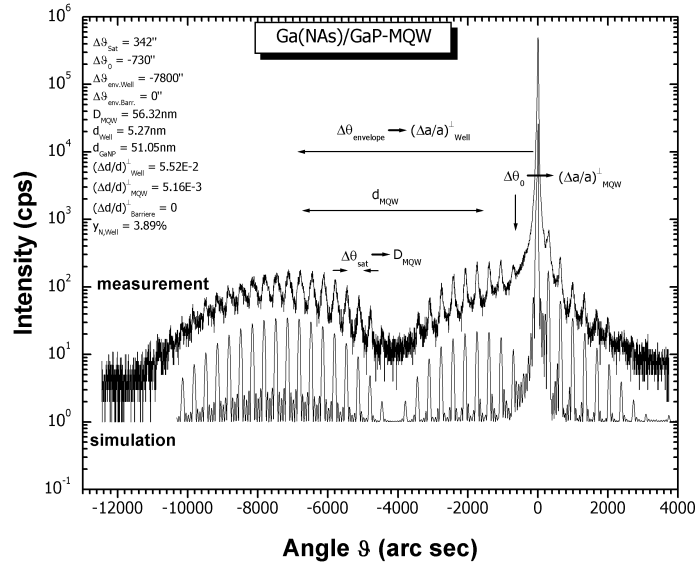


Figure 3.5.: HRXRD diffractogram of a Ga(NAs)/GaP multi quantum well structure

Figure 3.5 depicts an experimental (004) diffractogram of a Ga(NAs) multi quantum well structure grown on GaP substrate. The most intense peak is the 004 peak of the GaP substrate. The modulated satellite reflections on the lower angle side of the substrate peak are from the quantum well structure. The distance between the substrate peak and the maximum of the envelope of the modulated satellite peaks gives the strained lattice mismatch  $\varepsilon^\perp$  of the quantum wells through Equation 3.1.

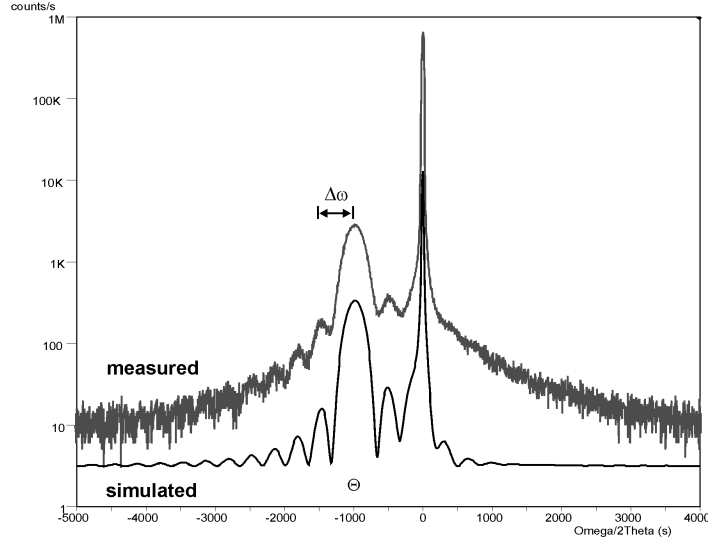


Figure 3.6.: HRXRD diffractogram of a GaP thin layer on grown on Si

The strained lattice mismatch of the whole layer package  $\varepsilon_{MQW}^{\perp}$  is given by the relative angular separation of the 0th order peak  $\Delta\vartheta_0$  and the substrate peak. The thickness of the quantum well,  $d_{QW}$ , and the barrier,  $d_{Barr}$ , can be determined with the help of an additional equation:

$$\varepsilon_{MQW}^{\perp} \cdot D_{MQW} = \varepsilon^{\perp} \cdot d_{QW} + \varepsilon_{Barr}^{\perp} \cdot d_{Barr}. \quad (3.5)$$

In the case where both the quantum well and the barrier are strained, an additional envelope function appears. From the position of this maximum, the strained lattice mismatch of the barrier ( $\varepsilon_{Barr}^{\perp}$ ) can be calculated.

Until now, the kinematic theory of X-ray diffraction was used to describe the diffractograms. It is actually valid only in a small angular interval around the substrate Bragg peak. At higher or lower angles the kinematic scattering cannot describe the real situation. Therefore dynamical theory of X-ray scattering, taking into account multiple scattering and beam extinction, is used to simulate real layer structures. In practice the quantities obtained by kinematical theory serve as initial parameters for the simulation using dynamical theory. Iterative fitting of the experimental diffractogram then results in an X-ray profile, describing the real structure.

By now we have seen that the thickness parameters and the strained lattice mismatch value can be obtained from diffractograms. The sampling size is several  $\text{mm}^2$  and is therefore representative of the film as whole.

The integral composition of the crystal is deduced from the measured strained lattice mismatch, assuming Vegard's law [60] (Equation 3.2).

This evaluation of HRXRD measurements also gives valuable information in the case of epitaxially grown thin layers. A typical diffractogram of an epitaxial thin GaP

layer grown on Si is shown in Figure 3.6. The right-hand peak is the substrate and the broader and less intense one is from the compressively strained bulk GaP layer. The extent to which the thickness fringes are present is a measure of how smooth and perfect the GaP/Si interface and the GaP layer surface is. If the layer surface is undulated, the fringe structure of the layer peak vanishes.

The thickness,  $d$  of the GaP layer can be estimated by the integrated layer peak intensity. Due to extinction of the X-ray beam, this is valid only up to a certain thickness limit. If thickness fringes are present, the layer thickness can be approximated by

$$d = \frac{\lambda \sin(\epsilon)}{\Delta\omega \sin(2\theta)}, \quad (3.6)$$

where  $\Delta\omega$  is the angular separation of the thickness fringes,  $\theta$  is the average Bragg angle of the fringes and  $\epsilon$  is the angle between the diffracted beam and the sample surface. The broadening of the layer peak can be due to several reasons: macroscopic curvature of the substrate, mosaic spread or the dislocation density. The angular separation between the layer and substrate peak is related to the lattice mismatch of the system. If the layer peak is closer to the substrate peak than expected for perfect strain, the layer is closer to its normal lattice constant and has therefore relaxed.

The XRD measurements were carried out with an X'Pert Pro diffractometer, using the  $K_{\alpha 1}$  line ( $\lambda = 0.15406$  nm) of a Cu X-ray source. A parabolic mirror was used for intensity enhancement and an asymmetric 4xGe(220)-Monochromator was applied to monochromize the beam. The scattered beam was detected by a proportional X-ray counter (type PW 3011/20). For the dynamical simulation of the obtained diffractograms, the software of L. Tapfer (PASTIS-CNRSM, Brindisi, Italy) and the commercial X'Pert Epitaxy program from PANalytical were used.

#### 3.2.3. Techniques for APD detection

There are several methods that can be used for the detection of antiphase boundaries and domains and assessing their distribution in a film. In the following, the most common techniques of them will be discussed. A more detailed description can be found in [6].

**Anisotropic etching.** Similar to dislocation-density determination, it is possible to show the existence and gain a lower limit of the density of antiphase domains bordered with  $\{111\}$  APBs. An etching solution is used that attacks the (111)B planes, occupied by the group V atoms, but not the (111)A planes, terminated by the group III atoms. As the orientation of the (111)B planes differ in  $[110]$  and  $[1-10]$ , the shape of the etch pit is related to crystal polarity. Despite the simplicity of this method, it is not sensitive to APDs that are smaller than 200 nm or bordered by stoichiometric APBs (like  $\{110\}$ ) or (111)A planes.

**X-ray scattering.** The properties of the *fundamental reflections* [(004, 008)] are exploited in X-ray scattering to gain information such as strain, derived composition and quality of sample. The *superlattice reflections* [(002), (006)] are sensitive to antiphase domains, since these planes are affected by group III - group V disorder. The study of Neumann et al. [61] describes the method used for detecting APDs in GaAs. The intensity of a fundamental reflection is proportional to  $(f_A + f_B)^2$  and is present even if all lattice sites are randomly occupied with group III and group V atoms. On the other hand, the intensity of a superlattice reflection is proportional to  $(f_A - f_B)^2$ , and vanishes in the case of complete site disorder. An antiphase domain rearranges the ordering in the (002) planes and causes a Lorentzian broadening of the superlattice peak, proportional to the probability of the formation of an APB. Having acquired this information, the average separation length between two APBs can be estimated. Considering all factors that can affect peak broadening (instrumental resolution, the inherent width of the Bragg-reflection, sample mosaicity), this method gives an upper limit for APB separation. No geometrical information can be retrieved with this method.

In summary, these methods are not sufficient for the detection of the antiphase domain structure in the thin layer GaP/Si system, which is the subject of this work.

### 3.3. Transmission electron microscopy

This section presents the main techniques of TEM which were used throughout this work. The methods are discussed from the point of view of what information can be gained, with special emphasis on the material systems that are the focus of this thesis. Though some methods are technically similar, they will be presented in a thematically split way. One part deals with a special method that is used in the quantitative composition evaluation of ternary quantum well structures. The other group of methods are used for thin layer and defect characterization and are discussed from the point of view of the GaP/Si heteroepitaxial layers.

The former section described methods for APB detection. Though they are convenient and straightforward to perform, the information that can be gained on the APBs is limited. If one wants to image the APDs the most efficient tool is the Transmission Electron Microscope. One can determine which crystallographic planes are affected by the antiphasing so that individual antiphase domains can be detected. The antiphase boundaries can be resolved by high resolution imaging. The polarity of the crystal in the different domains can be determined by Convergent Beam Electron Diffraction (CBED).

This section gives a detailed introduction to these methods, starting with dark field imaging methods, then CBED and finally high resolution imaging and simulation. The fundamentals of the electron-matter interaction, scattering and image formation in the

transmission electron microscope was discussed in Section 2.3. The dark field imaging, HRTEM and some of the CBED experiments were performed using a JEOL 3010 microscope, at Philipps University, Marburg. This microscope operates at 300kV and is equipped with an Ultra High Resolution (UHR) polepiece and a thermal emission LaB<sub>6</sub> cathode. The nominal point-resolution is 0.17 nm. The other part of the CBED experiments were done at Christian Albrechts University of Kiel using a Philips CM30 operating at 300 kV, equipped with LaB<sub>6</sub> cathode and having point resolution of 0.23 nm.

A crucial part of the TEM investigations is sample preparation, as inhomogeneities and imperfections have a direct influence on the image. Since the electron beam has to penetrate through the material, the investigated sample has to be thinned down. The final thickness of the sample should be between 4-150 nm, depending on the analysis to be performed. TEM samples were prepared in cross-section, along the [110], [1 $\bar{1}$ 0] and [010] zone axes, or in plan view (top view) in the [001] zone axis. For cross-sections, the wafers were cut, mounted into a Ti-holder and ground down mechanically, then thinned to electron transparency by Ar-ion milling. There is an other method that was also used for high resolution samples: the sample holder is substituted by “dummy” wafer parts in order to have better electrical contact with the sample holder of the microscope. In the case of plan view samples, a piece of the wafer was cut with a circle-profiled ultrasonic saw and ground down from the back side mechanically, and subsequently milled with the Ar-ion beam. The technical details are provided in Appendix A. The optimization of the sample preparation for the material combinations investigated here, can be found in [62].

#### 3.3.1. Dark Field TEM

The dark field imaging technique is widely used in the structural analysis of single crystalline semiconductors. The term “dark field” comes from the image nature: the different crystallographic planes of the single crystalline specimen scatter the electron beam differently. Using objective apertures, one can select different scattered beams in the microscope, and perform imaging with one single beam. If the direct beam is selected, a **bright field image** is obtained. An image obtained using one of the scattered beams is called a **dark field image**. The terminology relates to the contrast: it is inverted compared to the bright field image. The sample should be illuminated by tilting the incident beam in order to keep the diffracted beam on the optical axis; this is axial dark field imaging. If one places only the objective aperture around the selected reflection and makes a so-called “dirty” dark field image, the diffracted beams remain inclined from the optical axis and the resolution decreases due to the lens aberrations. Dark field imaging using various diffracted beams is a widely used tool to examine defects in crystalline semiconductors. Besides the development of imaging techniques for the material systems under investigation here, one aim of this work

was the optimization of the heteroepitaxy of the GaP/Si material system. For this purpose, the imaging methods developed in this project were used to investigate the link between deposition conditions and antiphase disorder for example.

### 3.3.2. Dark field TEM for composition analysis

Dark field imaging with the 002 reflection is a technique to investigate the composition of mixed III/V semiconductors. Due to the chemical sensitivity of the 002 beam (introduced in Section 2.3), it is generally used to determine the chemical homogeneity of quantum well compositions on the nanometer scale. As the intensity of the 002 reflection is dependent on chemical composition, it can be a direct way to deduce quantitative chemical compositional information of the quantum wells. This section presents the technical aspects of the experimental 002 dark field images, which will be presented in Chapter 4. The main points are summarized after the work of Torunski [62], who optimized the 002 dark field imaging for the GaAs-based quantum well heterostructures:

- The TEM samples have to be prepared in the [010] zone axis, and not in one of the more commonly used  $\langle 110 \rangle$  zone axes, in order to avoid unwanted additional intensity of the double diffraction of the  $\{111\}$  reflections to the 002 reflection.
- In order to suppress the contribution of the sample thickness gradient to the image intensity, the TEM foil has to be possibly planparallel. Therefore, the sample should be ion-milled using a low incident angle ( $3.5\text{-}4.5^\circ$ ) of the Ar-beam. This is a crucial requirement when preparing a N-containing quantum well samples, since N hardens the quantum well material. The barrier material between the hardened quantum wells is sputtered away preferentially at higher incident angle of the ion-beam ( $>6^\circ$ ).
- The sample structure of the quantum well heterostructures is usually a multiple stack: the 5-10 nm thick quantum wells are separated by 80-100 nm barriers. The quantum wells should not be closer to each other than this value because of an additional contrast effect: the 002 crystal planes of the quantum well material can bend due to TEM foil relaxation of the lattice mismatched quantum well material at the sample surfaces (see [62], page 89). The bent crystal planes scatter out some intensity from the quantum well, which appears as a bright/dark contrast in the barrier material of the 002 images. This has to be taken into account when normalizing the quantum well dark field intensities to the GaP barrier intensities.
- The sample tilt has to be chosen to excite the 002 reflection such that the reflection has sufficient intensity for the usual thickness range of dark field imaging.

This can be achieved by tilting the sample approximately  $3^\circ$  in the plane of the quantum well and barrier interface and tilt slightly ( $0.1^\circ$ ) in perpendicular direction. The center of the Laue circle at (20, 0, 1.5) was found to be the optimal position for these requirements [62].

TEM images were recorded using a 2048x2048 pixel Peltier-cooled digital CCD camera. In order to extract chemical information from the images of quantum well materials, the image intensity was measured using Digital Micrograph software. The intensity value of the barrier material served as a reference value of the binary GaAs or GaP. The 002 dark field images obtained with the above described conditions will be presented in Chapter 4, supported by the results of the refined structure factor calculation of the various ternary III/V compounds.

#### 3.3.3. Dark field imaging of antiphase domains

In this section the contrast of antiphase disorder related defects in  $\{002\}$  and  $\{111\}$  dark field images using both cross-section and plan view geometries will be discussed. The method introduced is suitable for any non-centrosymmetric zincblende crystal grown heteroepitaxially on elemental substrate. Studies using this method helped a lot to understand heteroepitaxy [63].

The imaging first will be discussed for the cross sectional view, where it is more straightforward and then a method will be shown, which enables to see the antiphase domains (APDs) also from plan view. The APBs can be observed only in a proper way, if they are “edge-on” in the electron beam direction. This means, that the TEM samples should be prepared in one of the  $\langle 110 \rangle$  directions. In this case the crystallographic plane, on which the APBs lie on, is parallel to the viewing direction as seen in Figure 3.7 (a). Figure 3.7 (b) depicts the diffraction pattern of the GaP material in the  $[1\bar{1}0]$  zone axis. The (002) and  $(00\bar{2})$  crystal planes are affected most by the antiphase disorder. Due to the  $180^\circ$  rotation around the  $[110]$  direction, the (002) plane on one side of an APB is equal to the  $(00\bar{2})$  on the other side of the APB. The amplitudes of the electron beam scattered from these lattice planes are not equal. This was first calculated for zone axis orientation by Kuan [13]. The effect was later explained by Pond et al. [64]. The kinematical theory of the scattering is however not able to explain the contrast. The additional intensity is the result of multiple scattering. Dynamical theory should be used to understand the full contrast (described in 2.3).

#### Contrast of 002/ $00\bar{2}$ dark field images

In this paragraph, the contrast of the antiphase domains in the 002/ $00\bar{2}$  dark field images is explained using image intensity simulation. This contrast in the image pair technique will be used as a standard tool for the detection of antiphase domains. It is important that the observation direction should be in one of the polar directions

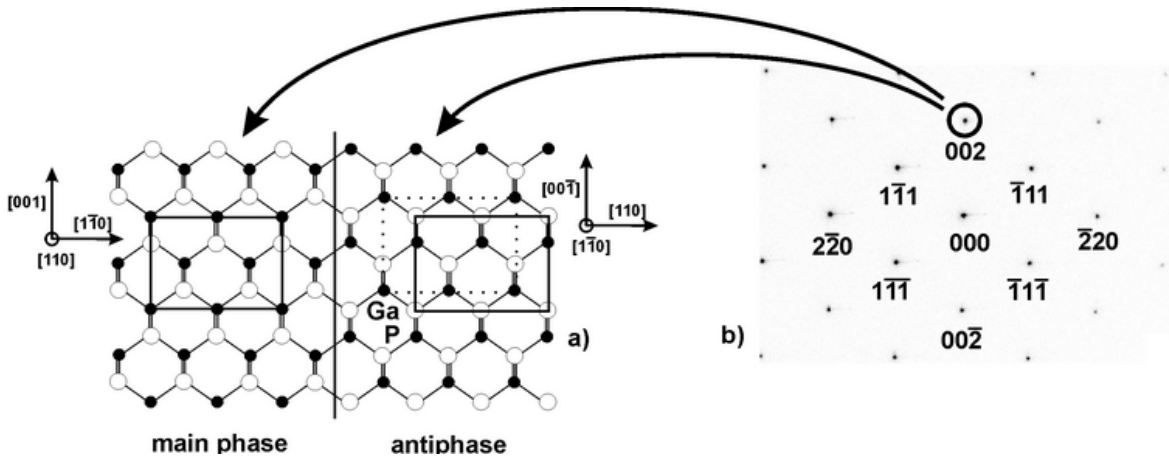


Figure 3.7.: Crystal model of two neighboring crystal domains: “main” phase and antiphase. The unit cells used for Bloch wave intensity calculation of the 002 reflection are depicted (a) and imaging with the 002 reflection by selecting the beam with the objective aperture (circle) (b).

$\langle 110 \rangle$  of the GaP crystal.

The contrast change originates from dynamical scattering effects. The dynamical effects can be already observed in the zone axis excitation. Figure 3.8 shows different beam intensities versus the GaP sample thickness. The intensities of the 000, 002, 002̄, etc. reflections were calculated using the Bloch wave method (as described in 2.3) via the EMS simulation program [65]. To phenomenologically treat electron losses due inelastic scattering, the absorption was set to 0.001 1/nm. The difference between the 002 and 002̄ beam intensities was distinguishable, though their intensities were quite low. Hence the method of Kuan, who only exploited (002) beams in the zone axis, was developed further in the present thesis. To increase the intensity of a specific reflection, the sample was tilted out by a few degrees to enhance the excitation. The reflection is in Bragg position, and therefore strongly excited, if the Laue-circle passes through it. A reflection  $(k,k,l)$  of the Zeroth Order Laue Zone (ZOLZ) is on the Laue circle with its center of  $(K,K,L)$  if  $(k - K)^2 + (l - L)^2 = K^2 + L^2$ . Such an excitation of the 002 beam can be done if the sample is tilted in the plane of the GaP-Si interface (001) and tilted only a few tenth of a degree in the plane perpendicular to the surface. The main question of the imaging is, how the intensity develops with the tilt and how the antiphase disorder affects the contrast.

For deeper understanding, a crystal region, which contains two antiphase domains as in Figure 3.7, can be considered.

Assume one phase is the main phase, and the other one as the antiphase. When imaging, the objective aperture is put around the 002 beam of the main phase crystal. The intensity of the antiphase on the image is given by that reflection, which is scattered to the position of the 002 of the main phase. The intensity of this reflection is equal to the intensity of the 002̄ reflection of the main phase. Tilt conditions can

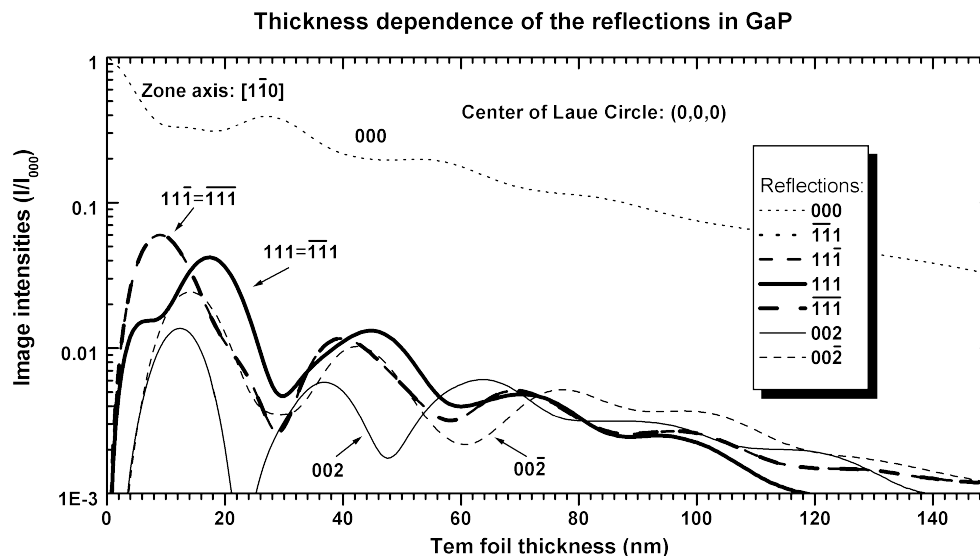


Figure 3.8.: Intensities of the  $\{002\}$  and  $\{111\}$  reflections in GaP in  $[1\bar{1}0]$  zone axis orientation. The intensity is plotted on logarithmic scale versus the sample thickness. The dotted line is the direct 000 beam.

be chosen so that the 002 reflection of the main phase is strongly excited and the  $00\bar{2}$  reflection of the main phase remains weak. Such conditions can be set by moving the COLC to the  $(\bar{9},9,1)$  position (in the  $[110]$  zone axis). The intensity profiles of the respective reflections can be seen in Figure 3.9 (a). Since, in the chosen tilt position, the 002 reflection exhibits significantly higher intensity than the  $00\bar{2}$  reflection, the anti-phase related crystal domains can be distinguished on the micrographs by their dark contrast. The TEM foil thickness where the intensity difference is the largest, and therefore the antiphase contrast is the strongest, is between 60 and 90 nm. If one tilts the sample to the symmetrical  $(\bar{9},9,\bar{1})$  COLC position, the  $00\bar{2}$  reflection of the main phase, and hence the 002 reflection of the anti phase, will be excited. The crystal domains of the antiphase should appear brighter on the micrographs.

Experimental images taken with these conditions are shown in Figure 3.10. The left-hand image, obtained using the 002 reflection, exhibits crystal domains that appear with different intensity. The intensity change crossing an observable crystal defect is shown by the white and gray arrows. The main phase is marked by a gray arrow and the antiphase by a white arrow. The dark contrasts between two crystal domains are the antiphase boundaries. Their wide, dark contrast results from the following: the boundaries of the domains are lying on the crystallographic  $\{110\}$  and  $\{111\}$  planes, i.e. parallel to the zone axis. To enhance the intensities of the  $\{002\}$  reflections, the sample was tilted out from the zone axis in the plane of the interface by  $3-4^\circ$ . Hence, the projection of the 60-90 nm thick sample results in 3-5 nm wide interface region in the image.

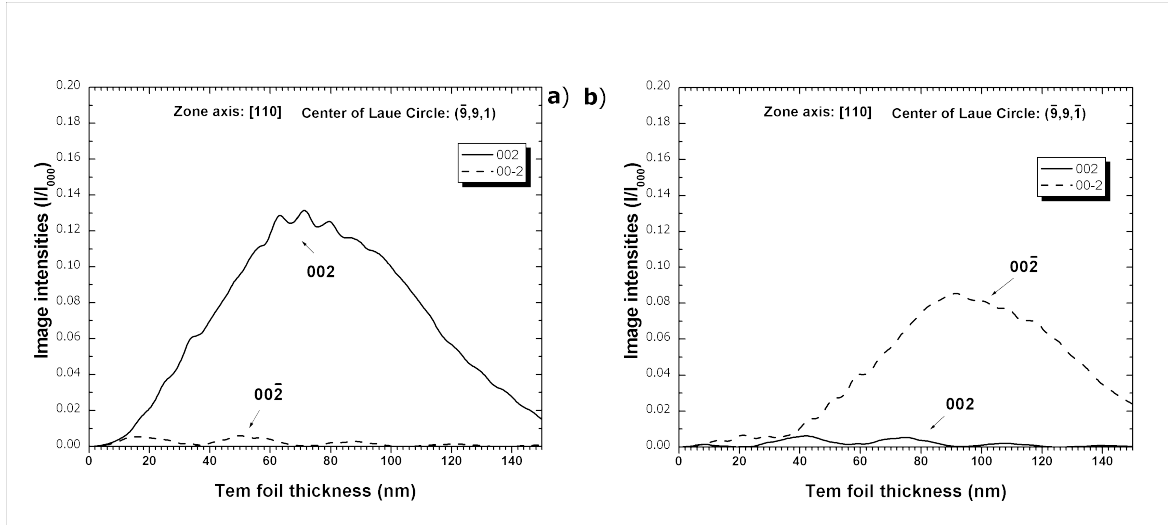


Figure 3.9.: Reflection intensities of the  $\{002\}$  reflections in GaP in  $[110]$  zone axis. The intensity of the excited  $002$  and the weak  $00\bar{2}$  reflections at COLC  $(\bar{9},9,1)$  is plotted in (a) versus the sample thickness. The intensity profile of the excited  $00\bar{2}$  and the weak  $002$  reflections (COLC  $(9,9,\bar{1})$ ) of the main phase is shown on (b).

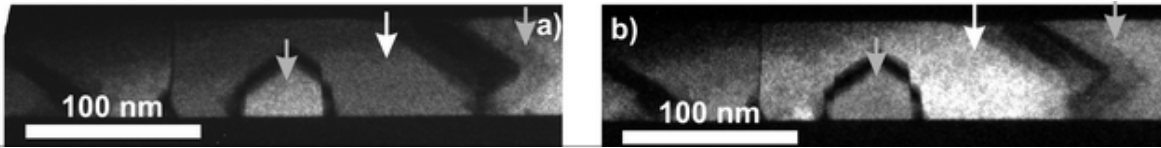


Figure 3.10.: Antiphase domains observed by (a)  $002$  dark field image and (b)  $00\bar{2}$  dark field image. The arrows note the contrast change.

The optimum sample thickness for this imaging technique poses a further challenge: as it will be shown later (in Section 5.2), smaller antiphase domains are important in this material system. The detection of antiphase domains of the size of 5-30 nm in a 60-90 nm thick TEM foils is difficult. If they are buried somewhere in the foil, the material from the main phase surrounding the APD suppresses the contrast resulting from the intensity difference. Using the  $002$  and  $00\bar{2}$  reflections it is more difficult to image the material at lower sample thickness of 20-50 nm. The image intensities are much lower than at the thicker regions, for this reason it is not easy to find the contrast inversion in the sample.

In conclusion, the image contrast of the antiphase related crystal domains in GaP arises from the different intensity profile of the  $002$  and  $00\bar{2}$  reflections. The intensity difference can be enhanced by tilting the sample to strongly excite the reflections. Simultaneously, the tilt restricts the accessible sample thickness regions and broadens the image of the boundaries of the domains due to projection. Taking images with the  $002$  and  $00\bar{2}$  enables the detection of antiphase domains by their contrast change

in the foil thickness range of 60-90 nm. Despite the loss of contrast, the antiphase boundaries remain visible (without the pronounced dark-bright contrast change on their sides) at thinner sample regions.

In the following, a novel way of imaging the APDs in thinner sample regions and minimization of the projection of APBs will be described. The antiphase domains can also be imaged using the  $\{111\}$  reflections. The origin of the contrast and the experimental evidences will be discussed in the next section.

#### Contrast of 111 dark field images

The starting point of the discussion is again Figure 3.8. It can be seen that in zone axis orientation two pairs of the four  $\{111\}$  reflections have equal intensity. The ones which have components in the growth direction are equal ( $111=\bar{1}\bar{1}1$ ) and those which have components opposite to the growth direction ( $11\bar{1}=\bar{1}\bar{1}\bar{1}$ ) are also equal. The difference in intensity of the respective pairs originates in the case of these reflections also from dynamical effects i.e. multiple scattering. As before, when imaging with these beams, the zone axis excitation is not sufficient for good contrast. Therefore, the sample should be tilted a few degrees out from the zone axis. To understand the origin of the intensity, if a sample contains regions with different orientations, a similar process will be followed, like in the case of the  $\{002\}$  imaging. If an image is made with a specific reflection of the main phase crystal, this specific reflection is indexed differently in the anti-phased crystal domain.

If a TEM sample region contains crystal domains with different orientations (main phase and antiphase), the crystal structure can be modeled like the topmost image in Figure 3.11. The images and plots on the right side concern the main phase material, while the left column describes the antiphase material. The unit cells, which were used for calculating the reflection intensities, are the same as in the  $002/00\bar{2}$  case. Here the  $[1\bar{1}0]$  zone axis is used for describing the main phase, while the  $[110]$  describes the antiphase. To get the same unit cell, besides the rotation, it has to be shifted also by  $[1/4, 1/4, 1/4]$  lattice constant in the diagonal  $[111]$  direction. As the unit cell is constructed, the relations of the reflections have to be determined. This can be understood by observing the second row of images in Figure 3.11. The image shows the diffraction pattern of the main phase on the right. Assume that the sample is tilted to the  $(1,1,3)$  COLC position. In this case, the  $\bar{1}\bar{1}1$  reflection is near to the Laue-circle and is excited strongly. When imaging with this beam, the information originating from the antiphase crystal is different. The  $\bar{1}\bar{1}1$  reflection is the  $1\bar{1}1$  in the antiphase material. Hence, the intensity of these reflections must be compared. At this point, it is enough that one excited reflection, the  $\bar{1}\bar{1}1$  is chosen for imaging. Its intensity has to be compared on the lower plot pair with the intensity of the  $1\bar{1}1$  reflection from the antiphase material (on the left side). The main points to be noticed: (1.) the intensities with this low tilt are already comparable with the  $\{002\}$  intensities (7

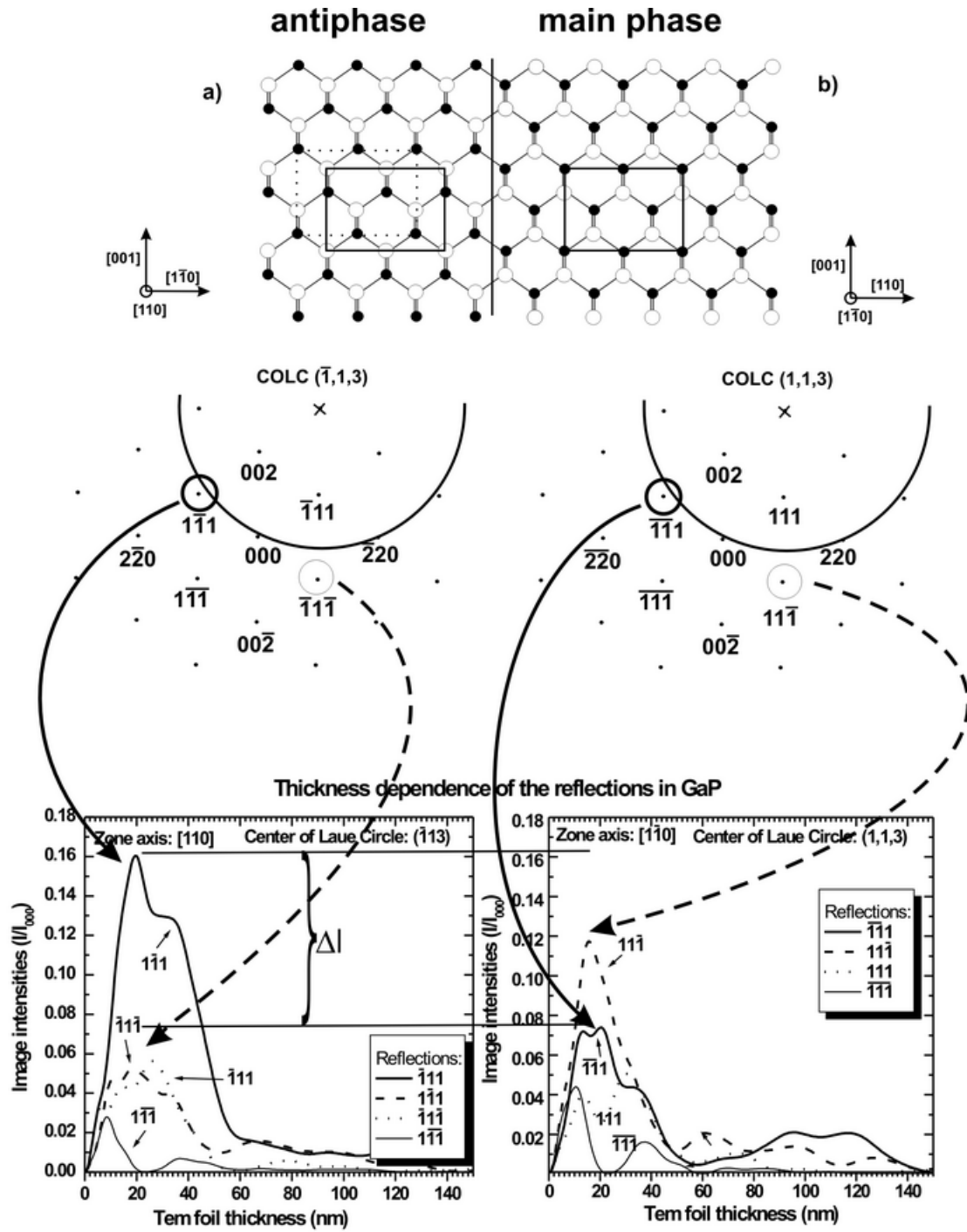


Figure 3.11.: Image intensities of 111 dark field images of GaP antiphase domains: the right column (starting from the top) shows the crystal model with the unit cell used of for the intensity calculation; the diffraction pattern with selecting the  $1\bar{1}1$  (thick circle) and  $11\bar{1}$  (thin circle) reflections for imaging and the simulated intensities. The left column shows the same for the antiphase crystal. The image intensity differences can be seen comparing the lower plots.

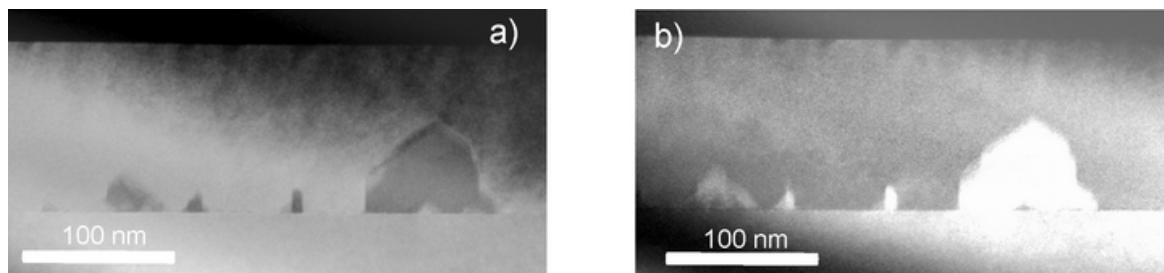


Figure 3.12.: Dark field image pair of APDs taken with (a)  $\{\bar{1}\bar{1}1\}$  and (b)  $\{11\bar{1}\}$  reflection

and 16 % of the direct beam intensity); (2.) the intensities of both reflections have maxima at the same sample thickness, and this thickness is quite low (20 nm); (3.) The intensity ratio is large enough to be easily detectable ( $I_{main}/I_{anti}=0.5$ ). These facts already fulfil the requirements to be able to observe the antiphase relation as contrast change. However, the  $\bar{1}\bar{1}1$  reflection of the main phase is not the most intense. Though the  $11\bar{1}$  is not on the Laue circle, it is brighter than the formerly discussed  $\bar{1}\bar{1}1$ . This is reasoned by dynamical effects, or even inelastic scattering such as the Kikuchi effect, as the  $11\bar{1}$  reflection spot is located on one strong Kikuchi band. Hence, this COLC position is perfect for imaging also with the other reflection pair. The  $11\bar{1}$  reflection of the main phase material can also be used (thinner circles on the diffraction patterns). This would then select the  $\bar{1}\bar{1}1$  reflection for the antiphase material. Comparing the intensities (guided by the dashed curved lines) leads to the conclusion that this tilt is actually a perfect excitation condition for these beams too. First of all these beams also have different intensities, but moreover the intensity ratio is inverted compared to the  $\bar{1}\bar{1}1/11\bar{1}$  image pair. The main phase intensity is now stronger and the antiphase is weaker. The intensity ratio is  $I_{main}/I_{anti}=2.4$ . Furthermore, the maxima of the intensities are at the same sample thickness (20 nm), which is also the sample thickness where the  $\bar{1}\bar{1}1/11\bar{1}$  reflection pair have their maxima.

All these considerations suggest that the  $\{111\}$  reflections are also suitable for imaging the antiphase domains, especially in thin sample regions. An experimental image pair is shown in Figure 3.12. The observed contrast change in the image is unambiguous. The GaP layer is generally single phased, and the areas showing the contrast change are the antiphase domains. The estimated sample thickness is 20 nm. The observation of the small sized 10-20 nm wide domains also supports this, since their dimension in the perpendicular direction is also similar. The intensity ratios estimated from the calculation also match with the measured values.

The question of sample tilt needs to be commented: as it was shown, one tilting position fulfills the requirements for both images of the image pair. The tilting is not that critical as it is during  $\{002\}$  imaging. Suitable intensity differences can be obtained by low tilt angles. Doing the experiments, the images can be obtained by other symmetrical tilts at COLC positions such as  $(\bar{1}\bar{1}3)$ ,  $(\bar{1}1\bar{3})$  and  $(11\bar{3})$ . Doing the

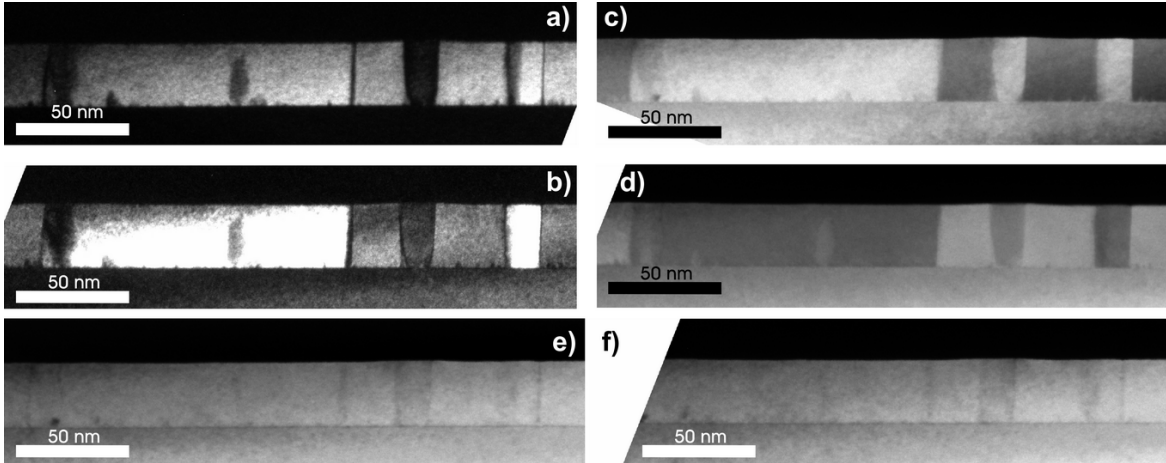


Figure 3.13.: Dark field images of antiphase domains using different reflections: (a) 002, (b)  $00\bar{2}$ , (c)  $1\bar{1}1$ , (d)  $11\bar{1}$ , (e) 220 and (f)  $\bar{2}20$ .

proper transformations, similar results are obtained, differing only in the sign of the contrast change. As a consequence of the low tilts, the interfaces of the APDs are not smeared out to the extent as observed for the  $\{002\}$  case.

To compare the two imaging methods directly, the same area of a GaP thin layer was imaged with the methods described above (Figure 3.13). The sample thickness was approximately 20 nm. The images of Figure 3.13 (a) and (b) are the image pair made with the 002 and  $00\bar{2}$  reflections. It is observable, that although the boundaries are resolved, the domains do not show any contrast change. The boundaries have a 1-2 nm wide shadow arising from projection due to the tilt. Figure 3.13 (c) and (d) are the  $\{111\}$  images. The contrast change is unambiguous. The domain boundaries show no dark contrast due to the low tilt. Figure 3.13 (e) and (f) are images taken with the excited 220 and  $\bar{2}20$  reflections. Since these reflections are not sensitive to the crystal polarity, the GaP crystal exhibits homogeneous contrast, interrupted only by the slight contrast of the boundaries.

### Polarity sensitive contrast in plan view

Plan view investigations are generally suitable for crystal defect characterization of thin films. The lateral dimension of defects is directly observable, their propagation in the layer can be followed by tilting techniques, and larger areas can be imaged than in cross section. In this paragraph, it will be discussed, how this method can be used for imaging antiphase domains.

The starting point is the unit cell of the zincblende structure, viewed along the  $[001]$  zone axis. In plan view samples, the electron beam propagates along the growth direction of the layer. The  $[001]$  view of the unit cell is shown in Figure 3.14 (a). In this projection the polarity cannot be determined as the figure suggests: the atom

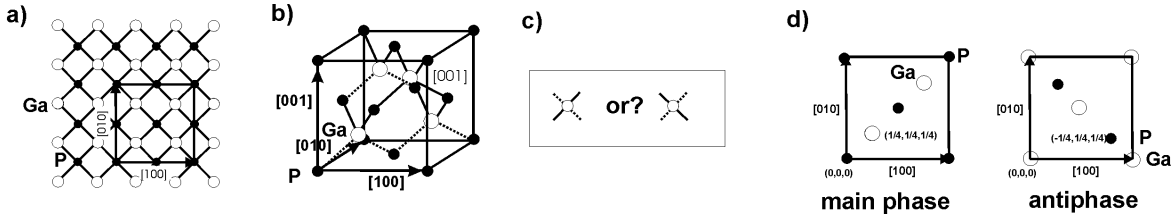


Figure 3.14.: Unit cell of GaP (a) viewed along the non-polar [001] direction, (b) perspective view (c) the bonds of Ga from the topview

locations are indistinguishable, whether they are above each other or below. The conventional unit cell is defined such that the atom with the smaller atomic number (smaller scattering amplitude) is located at  $(0,0,0)$  in the unit cell (in our case the P). The larger atom (Ga), with the larger scattering amplitude, is located at  $(1/4,1/4,1/4)$  as shown in Figure 3.14 (b). What distinguishes the main phase from the antiphase in this projection is the direction in which the bonds between Ga and P run. Figure 3.14 (c) shows the possibilities schematically: the dashed lines show Ga - P bonds that point toward the observation direction (on the image - downwards), the continuous lines are the bonds that point opposite to the observation direction (on the image - upwards). This is the information that distinguishes the crystal orientation in top view. Spiecker developed a method for zincblende-structured compound semiconductors to determine the polarity from the [001] observation direction [66]. This method is based on evaluating convergent beam electron diffraction discs, but the concept also enables polarity sensitive imaging in the GaP crystal.

The relationship between the unit cells of the main phase and the antiphase are indicated in Figure 3.14 (d) by showing respectively their first two atomic layers.

For imaging the  $\{020\}$  reflections are used, because they are less disturbed by the thickness fringes than the  $\{004\}$  or  $\{220\}$  reflections. In order to excite, for example, the 020 reflection strongly, the sample should be tilted out from the zone axis towards the  $(h,1,0)$  direction. By doing this, the Laue circle intersects the 020 reflection. Increasing the tilt, the intensity of the 020 reflection increases. Figure 3.15 shows 020 dark field images with different sample tilt. Figure 3.15 (a) is made with a  $\sim 2^\circ$  tilt, having the COLC approximately at  $(8,1,0)$ , (b) is made with a  $\sim 5^\circ$  tilt, having the COLC  $(20,1,0)$  and, in the case of (c), the sample was tilted out to such an extent that the reflections from the First Order Laue Zone were excited. This is at  $11^\circ$  tilt and COLC  $(41,1,0)$  position. The rise of the contrast change can be explained in this case also by dynamical scattering. If the sample is tilted out, reflections from the First Order Laue Zone are also in a Bragg position. These reflections can scatter into the 020 reflection by double diffraction, which is also in a Bragg position. Which reflections interfere exactly, will be discussed in the next section. The fact that the intensity of the main phase increases is enough to distinguish it from the other phase. As the antiphase is basically the rotated main phase crystal, it is excited differently: its relative

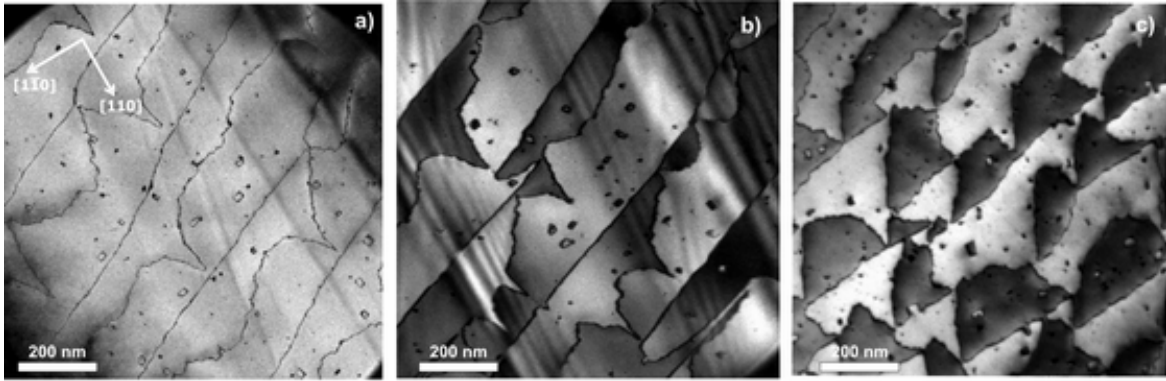


Figure 3.15.: Plan view 020 dark field images of GaP antiphase domains. The sample tilt enhances the contrast: the 020 reflection was excited: (a) close to zone axis in ZOLZ (b) further from the zone axis in the ZOLZ (c) excited in the FOLZ.

COLC position is not the same. The relative COLC of the antiphase crystal is also rotated with  $90^\circ$  around the  $[001]$ . When imaging with the 020 reflection of the main phase, that reflection is not indexed as the 020 of the  $90^\circ$  rotated antiphase, but as the 200 or the  $\bar{2}00$ . These reflections are not excited, they are not in Bragg position, and therefore their intensity is low.

### 3.3.4. Convergent beam electron diffraction (CBED)

The convergent beam electron diffraction in the TEM is a universal method for crystalline materials: it is suitable for measuring sample thickness, measuring lattice constants, characterizing defects and determining even three dimensional properties such as unit cell, point group and space group.

Here, a basic introduction to CBED pattern formation will be given, without specifying all its possibilities. The CBED patterns then will be described as a tool for the polarity determination in the zincblende compound semiconductors, focusing on the GaP material.

The power of the CBED lies in the three dimensional information content of the CBED patterns. Its origin can be understood from Figure 3.16. In conventional electron diffraction the incident electron beam is considered to be a plane wave travelling in one direction, usually parallel to the optic axis (Figure 3.16 (a)) and the diffracted beams are also parallel. The incident wave can be described with one single wave vector  $\mathbf{k}_0$  and the Ewald sphere with its radius  $1/\lambda$ . In CBED, however, the sample is not illuminated by a parallel beam. By changing the current of the condenser lens, the incident beam is focused onto the specimen (Figure 3.16 (b)), such that the incident rays reach the specimen at different angles, resulting in a cone-shaped beam. To some degree all electrons in the cone can be diffracted, and the diffracted beams leave the sample in a set of cones with typically less than 1 degree opening angle. The cones are

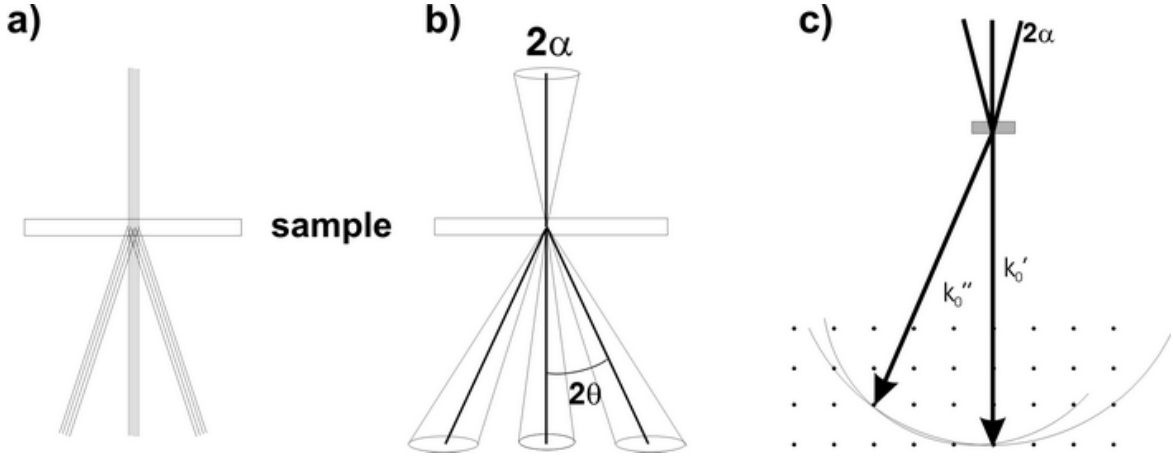


Figure 3.16.: Beam path in (a) conventional diffraction and (b) in convergent beam electron diffraction. (c) the various  $\mathbf{k}$  vectors in CBED define various Ewald spheres

magnified in the TEM column and intersected by the viewing screen or the camera, resulting in the characteristic CBED disc patterns. The three dimensional information originates from the following: the incident electrons in the cone have any  $\mathbf{k}_0$  vector within a range of the  $\alpha$  semi-angle. In reciprocal space there is a continuum of Ewald spheres, which rock in the range of  $\alpha$ . The effect of sending electrons into the sample over a range of incident angles is that they have also different z-components. This brings reflections from higher order Laue zones (HOLZ) into Bragg position, and to appear in the diffraction pattern. At this point the CBED becomes a three dimensional phenomenon. More general information on CBED can be found in [38], [43] and [67]. Here, the focus is on CBED as a tool for polarity analysis.

The first approach to describe crystal polarity of zincblende semiconductors is from Taftø and Spence [68]. In their work they compared the dynamic electron diffraction of the centrosymmetric Ge with the slightly polar GaAs. The slight polarity means that the GaAs lattice consists of two different atoms with similar atomic number  $Z$  (Ga=31, As=33) and scattering amplitude. The atomic number of Ge ( $Z=32$ ) is between Ga and As. They observed polarity dependent behavior of CBED disks and explained it as the interference of singly and double diffracted beams.

If the electron plane-waves travelling along  $\mathbf{k}$  are described (using the crystallographical sign convention) by  $exp(-2\pi i\mathbf{k}\mathbf{r})$ , the structure factor for the reflection  $\mathbf{g}$  is:

$$F_{\mathbf{g}} = \sum_j f_j(\vartheta) \cdot exp(2\pi i\mathbf{g}\mathbf{r}_j), \quad (3.7)$$

where  $f_j(\vartheta)$  denotes the atomic scattering amplitude of the atom  $\mathbf{k}$  for the scattering angle  $\vartheta$  that corresponds to the twice of the Bragg-angle of the reflection  $\mathbf{g}$ ,  $\mathbf{r}_j$  is the position of the atom  $\mathbf{k}$ , and the sum is taken over all atoms in the unit cell. The structure factors of the zincblende structure are as described in Equation 2.25.

The  $\varphi_{hkl}=2\pi\mathbf{g}\mathbf{r}_j$  phase factor contains the information about the crystal polarity. If the structure is centro-symmetric, the imaginary part of the structure factors can be eliminated by placing the origin of the coordinate system in a center of symmetry. In this case every atom at  $\mathbf{r}_j$  is identical to the one at  $-\mathbf{r}_j$  so that the contribution of the two atoms together is  $f_j(\vartheta) \cdot 2\cos(2\pi\mathbf{g}\mathbf{r}_j)$ , a real number within the Born-approximation. But in the case of a polar crystal, the structure factors may remain complex if their phases are  $\neq 0$ . If the diffraction is considered *kinematically* (see 2.3), the phase information of the structure factors is lost because only the modulus contributes to the beam intensities (as described by Equation 2.24).

To assess the crystal polarity information, multiple scattering has to be considered (see *dynamical diffraction* in Section 2.3). In the so called *thin crystal approximation* the  $\omega$  phase change, which is sustained during the n-times elastic scattering under Bragg-condition along the  $\theta \rightarrow \vec{g}_1 \rightarrow \vec{g}_2 \rightarrow \dots \rightarrow \vec{g}_n$ , can be written as [68]:

$$\omega = -\frac{n\pi}{2} + \sum_{i=1}^n \varphi_{\Delta g_i} \quad (3.8)$$

where  $\varphi_{\Delta g_i}$  denotes the phase of the structure factor of the reflection  $\Delta\mathbf{g}_i = \mathbf{g}_i - \mathbf{g}_{i-1}$ .

In the case where  $f_A$  is smaller than  $f_B$  due to  $Z(A) < Z(B)$  (compounds which have strong polarity like AlP, GaP, InP, InSb), the phases of the structure factors can be written as:

$$\varphi_{hkl} = 0 \quad \text{if } h + k + l = 4m \quad (3.9)$$

$$\varphi_{hkl} \approx \pi/4 \quad \text{if } h + k + l = 4m + 1 \quad (3.10)$$

$$\varphi_{hkl} = \pi \quad \text{if } h + k + l = 4m + 2 \quad (3.11)$$

$$\varphi_{hkl} \approx -\pi/4 \quad \text{if } h + k + l = 4m + 3 \quad (3.12)$$

Taftø and Spence used, that a singly diffracted beam  $(000) \rightarrow (002)$  and a doubly diffracted one  $(000) \rightarrow (hkl) \rightarrow (002)$  interfere constructively (or destructively) in the crystal, if the reflection  $(hkl)$  is of type  $h+k+l=4m+3$  ( $h+k+l=4m+1$ ). The phase shift upon single diffraction is:

$$\omega_s = -\frac{\pi}{2} + \varphi_{002} = \frac{\pi}{2} \quad (3.13)$$

and upon double diffraction can be written as:

$$\omega_d = -\pi + \varphi_{hkl} + \varphi_{-h,-k,2-l} \approx \pm \frac{\pi}{2} \quad (3.14)$$

In the latter expression “+” refers to the case of  $h+k+l=4m+3$  and the “-” sign refers to case of  $h+k+l=4m+1$ . In the thin film approximation the amplitude of the singly diffracted beam grows linearly with the crystal thickness ( $t$ ) and the amplitude of a doubly diffracted beam grows with ( $t^2$ ). Therefore, in thin sample regions, the

intensity of the direct (000) beam is dominated by single diffraction, and beyond a certain thickness, the double diffraction overcomes the single one, and even inhibits it. The constructive/destructive interference is a useful tool to track the polarity information, as it appears as a detectable contrast effect. This effect is easily observable in the diffraction discs of convergent electron beam diffraction (CBED) patterns when the two reflections (002) and (hkl) are set simultaneously into Bragg-condition (Figure 3.17 (a)). By symmetry, the reflection (h,k,2-l) fulfills the Bragg condition, too. The latter two reflections are so far from each other that the scattering between them can be neglected. The CBED method has an advantage over the selected area diffraction (SAD): a whole range of excitation conditions is realized within the diffraction disc. The constructive/destructive interference can be unambiguously identified from the diffraction discs as an additional positive/negative contrast on the background which is determined by the single-scattered (000)→(002) reflection. Measurement of the absolute intensities is not needed. The double scattering of the (hkl) and (h,k,2-l) reflections appears as a characteristic cross of bright (dark) *dynamical Bragg-lines* in the (002) disc when  $h+k+l=4m+3$  ( $h+k+l=4m+1$ ).

This method can be used for GaAs with the double diffraction (000)→(hkl)→(002) via an odd-indexed reflection (hkl) of type  $\{1,1,11\}$  and (h,k,2-l) of type  $\{1,1,\bar{9}\}$ . Constructive interference can be observed in the 002 Bragg case of the  $\bar{1},1,11$  and the  $\bar{1},1,\bar{9}$  and the destructive interference in the 00 $\bar{2}$  case of the  $\bar{1},1,\bar{1}\bar{1}$  and the  $\bar{1},1,9$  reflections. The direct transfer of the method to other compound semiconductors is possible, but also not straightforward [69].

$Z_A < Z_B$	$h+k+l=4m+1 \Rightarrow \text{dark}$
(GaAs, GaSb, InSb, ZnSe,...)	$h+k+l=4m+3 \Rightarrow \text{bright or faded}$
$Z_A > Z_B$	$h+k+l=4m+1 \Rightarrow \text{bright or faded}$
(GaP, InP, InAs, ZnS, ...)	$h+k+l=4m+3 \Rightarrow \text{dark}$

Table 3.1.: Contrast rules for dynamical Bragg-lines in 002 CBED discs (and dynamical bend contours in 002 dark-field images). The bright contrast refers to weak polarity, while the faded contrast to strong polarity of the compound.

The effects of stronger polarity:

- The 002 structure factor  $F_{002} = 4(f_A - f_B)$  increases
- The phases of the structure factors of reflections  $F_{hkl} = 4(f_A \pm i f_B)$  of the odd-index reflections deviate from  $\pm\pi/2$  to a larger extent (for values see [70])

The latter fact leads to a weaker interference of the singly diffracted (000)→(002) beam with the doubly diffracted (000)→(hkl)→(002) compared to GaAs. This weaker interference results in weaker contrast effects in the CBED patterns. Marthinsen et al. [71] and Spiecker [69] proposed the  $\{115\}$  and  $\{117\}$  reflections for material with

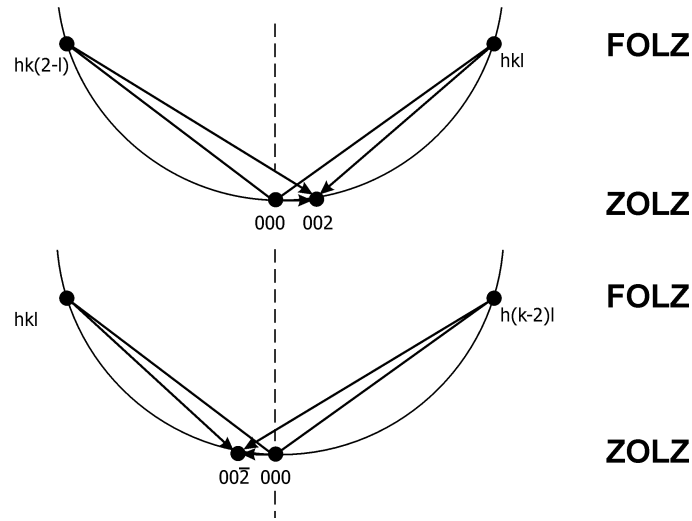


Figure 3.17.: Excitation conditions and scattering paths for polarity determination in CBED in  $\langle 110 \rangle$ . The doubly scattered reflections from the FOLZ interfere with (a) the 002 (b) with the  $00\bar{2}$  reflection.

stronger polarity.

Simulation of the CBED patterns are generally done with the Bloch wave method. The simulation software MBFIT developed by K. Tsuda [72] was used in this work. The process of the polarity determination in the GaP material system is summarized in the next section.

### Polarity determination of GaP

Figure 3.18 illustrates, how the polarity can be determined for GaP thin layers. The cross sectional sample in this case was prepared in the  $[1\bar{1}0]$  direction. Figure 3.18 (c) is a 002 dark field image of the investigated region of the GaP thin layer. The electron beam was focused on the sample to obtain the CBED discs as it is shown on the zoom Figure 3.18 (d). The sample was tilted out from the zone axis to COLC(9,9,1) to excite the 002 reflection and the 117 and  $11\bar{5}$  reflections from the First Order Laue Zone (FOLZ). The constructive interference between the 002 and the 117/ $11\bar{5}$  beams appears as faded cross in the 002 disc (Figure 3.18 (b)). This was not in itself a decisive result, since the faded cross can be easily mixed up with the constructive interference of beams scattered from the Si crystal. The deciding factor is the appearance of the destructive interference of the  $11\bar{5}$  and  $11\bar{7}$  beams in the  $00\bar{2}$  disc. To search for this, the sample was tilted to COLC(9,9, $\bar{1}$ ), bringing the  $00\bar{2}$ ,  $11\bar{5}$  and  $11\bar{7}$  reflections into Bragg position. At this position, a dark cross appears in the  $00\bar{2}$  disc, as seen in Figure 3.18 (a). Both CBED patterns match with the simulation made of the Ga-polar GaP

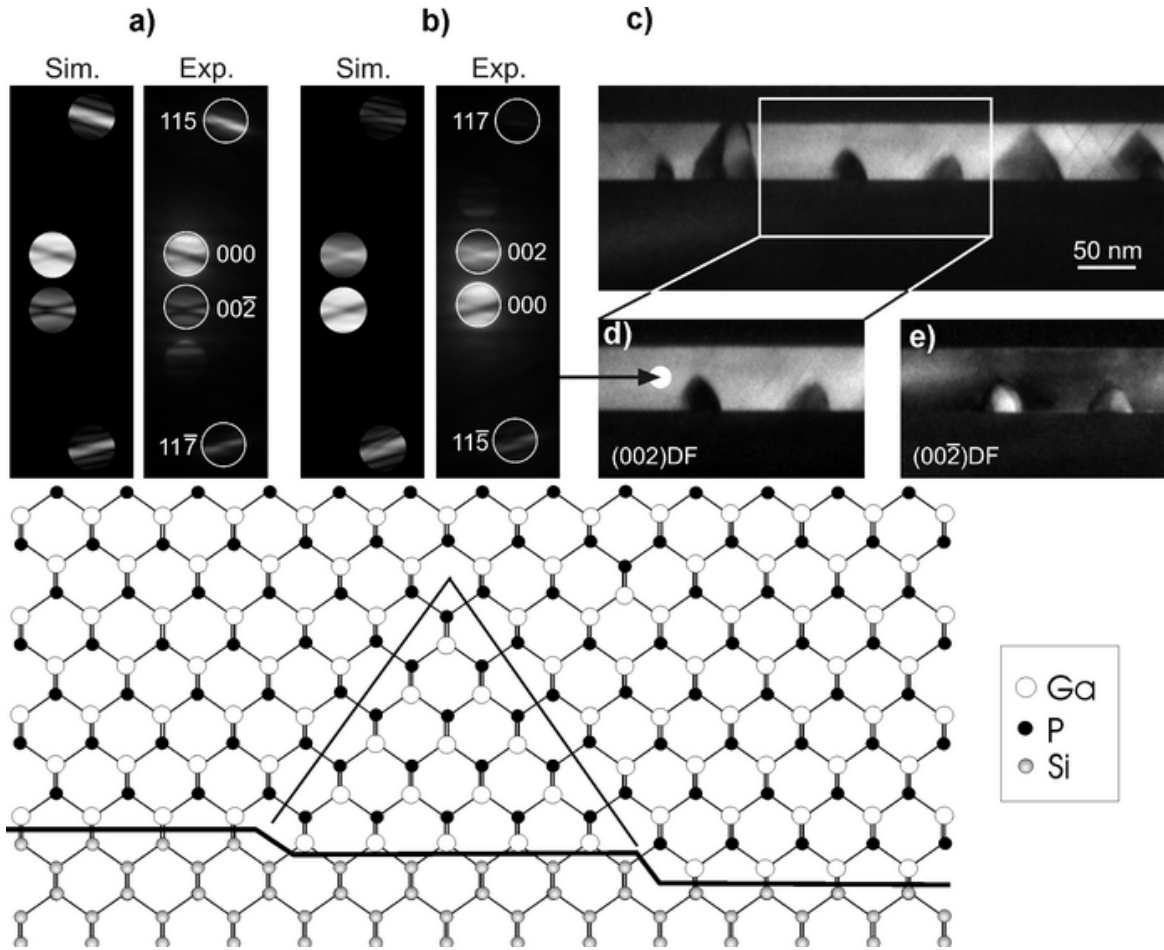


Figure 3.18.: Polarity determination in  $[1\bar{1}0]$  GaP with CBED. (a) shows the destructive interference as dark cross in the  $00\bar{2}$  disc, (b) the constructive interference (faded cross) in the 002 disc, (c) is a dark field image from the 46 nm thick GaP layer containing antiphase domains. (d) and (e) are dark field 002 and  $00\bar{2}$  images from the investigated area. The arrow depicts the position of the focused electron beam. The crystal model shows the derived polarity information.

unit cell, which is constructed as the crystal model illustrates. Since 002/ $00\bar{2}$  dark field microscopy only proves antiphase disorder to reveal the polarity information of the main phase and antiphase domains, the same CBED experiments should be done by focusing the electron beam onto the antiphase domains. Though the beam can be focused in a few nm diameter spot on the sample, the size of the domains (30-60 nm) in this particular sample was too small for the analysis. The constructive/destructive interference could not be clearly observed when performing CBED on the antiphase.

If APDs are large enough, polarity information can be obtained directly from them. Figure 3.19 shows CBED results for a thick GaP layer, where for strain compensation a small amount of N was added to the material during the bulk growth after the GaP nucleation layer growth. The 002 (a) and  $00\bar{2}$  (b) dark field images reveal the existence

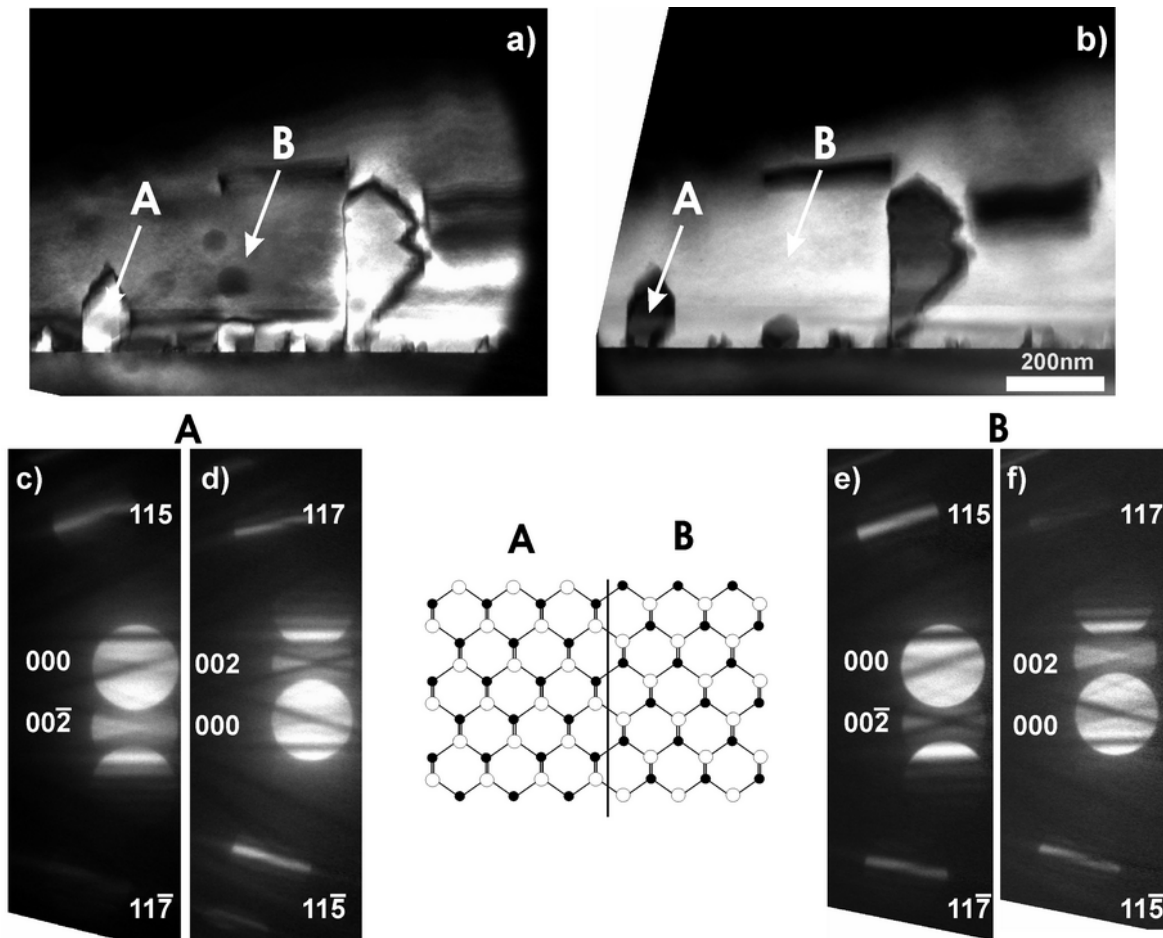


Figure 3.19.: Polarity analysis of a Ga(NP)/GaP/Si layer: (a) dark field  $00\bar{2}$  and (b)  $002$  micrograph showing the same sample area. The polarity change between the main phase (B) and the antiphase (A) is supported by the inverted interference phenomena of the  $\{11\bar{5}\}/\{117\}$  reflections in the CBED discs: The main phase (B) shows (f) faded contrast in the  $002$  disc and (e) dark cross in the  $00\bar{2}$  disc. The antiphase (A) is inverted: the cross on (d)  $002$  is dark and on (c)  $00\bar{2}$  is faded. Note the traces of the focused electron beam, which results in local accumulation of amorphous carbon on the sample surface.

of APDs in the layer by their contrast reversal (as described in former paragraphs). The APDs are larger than in the previous example. The CBED experiments were done both by focusing the incident beam on the main phase of the layer and on the antiphase domain. Damage caused by the focused beam is even observable in Figure 3.19 (a) as local accumulation of amorphous carbon on the sample surface. The main phase (spot **B**) shows constructive interference in the 002 disc and destructive interference in the  $00\bar{2}$  disc, while the antiphase (spot **A**) shows it reversed: the cross in the 002 disc is dark (destructive interference) and it is faded in the  $00\bar{2}$  disc (constructive interference). The reversal of the interference is a proof for the dark field imaging of the polarity change crossing the domain boundary. Beyond proving the existence of the antiphase, the absolute polarity of the domains can be determined, as shown on the crystal model in Figure 3.19.

### 3.3.5. Polarity sensitive bend contours

There is an other effect which can bring specific lattice planes to Bragg-position and results in contrast changes in bright field and dark field images in the form of dark and bright lines. This effect, when imaging defects, is mainly an inconvenience, that arises from the macroscopic bending of the TEM foil. By considering its origin, this drawback can be turned into a method, suitable deducing crystallographic information from the zincblende crystal structure in strongly bent TEM samples.

The *bend contours* occur when a specific set of lattice planes is not parallel everywhere to sample bending and they rock in and out of the Bragg condition, as shown in Figure 3.20. The sample is tilted such, that the  $\{hkl\}$  planes are parallel with the incident beam. These planes always remain normal to the sample surface, even if the sample bends. Assume, that the TEM foil bends evenly. In this case, the  $\{hkl\}$  planes satisfy Bragg condition in A, and the  $\{\bar{h}\bar{k}\bar{l}\}$  planes satisfy the Bragg condition in B. The systematic row of reflections is drawn below the specimen. If the sample is bent downwards (as illustrated),  $\mathbf{g}$  is on the opposite side of  $\mathbf{0}$ . If it would be bent upwards, they were on the same side. Now, by making a bright field image with the  $\mathbf{0}$  reflection, one observes two dark lines, because the bent planes scatters out from  $\mathbf{0}$ . But if a dark field image is made with the reflection  $\mathbf{g}$ , one observes a bright line on the left, since that is where  $\mathbf{g}$  is excited. If the  $\bar{\mathbf{g}}$  reflection is used for dark field imaging, the bright line appears on the right. These lines are referred to as bend contours in the diffraction contrast images. It is important to emphasize that these contours on the images are pure amplitude contrast and not phase contrast. A practical hint for distinguishing them from real sample features is that they move with the sample tilt. Another practical advantage of this effect is that the tilt can be followed easily in image mode, when searching for the zone axis for example.

The bend contours can be readily observed in plan view [001], where the samples show preference for bending due to the sample preparation anyway. For the point of

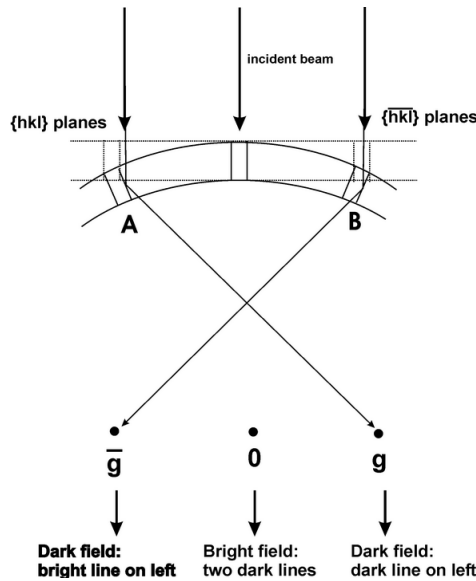


Figure 3.20.: Origin of bend contours

view of the antiphased GaP material, the bend contours of the  $\mathbf{g}\{002\}$  reflections are interesting [70]. The novelty of the method is that it is performed in the image mode of the TEM. It is based on the effects of the dynamical scattering on the crossings of the bend contours. The sample is tilted out from the  $[001]$  zone axis by several degrees perpendicular to  $[100]$  or  $[010]$  in order to excite odd  $hkl$  reflections from the higher order Laue zones. The interference of the excited HOLZ reflections and the  $\{020\}$  reflections cause the appearance of narrow lines crossing each other on the broad band of the  $\{020\}$  bend contours. These lines are equivalent to the HOLZ crosses in the CBED experiments (discussed in Section 3.3.4). The dynamical HOLZ lines are always dark in bright field mode and are either dark or bright in dark field mode, depending on the character of the interference, i.e. it is constructive or destructive. After the proper indexing of the lines, their contrast sequence can then be used to retrieve the polarity information.

Since one of the main aspects of this work is the detection of antiphase domains in the heteroepitaxial GaP thin layers, this method will be demonstrated in the antiphase patterned GaP material. Since the method requires extended single phased material and the usual antiphase domain size is too small in this material system, it was not suitable to determine the polarity of the domains, but was sufficient to detect the antiphase relation of two neighbouring domain separated by boundaries laying on the  $\{110\}$  planes.

The method is demonstrated in Figure 3.21. The sample was tilted towards a  $\langle 010 \rangle$  direction, by about  $8^\circ$  in order to excite reflections from the HOLZ. The diffraction pattern in 3.21 (e) shows the reflections from the First Order Laue Zone. Figure 3.21

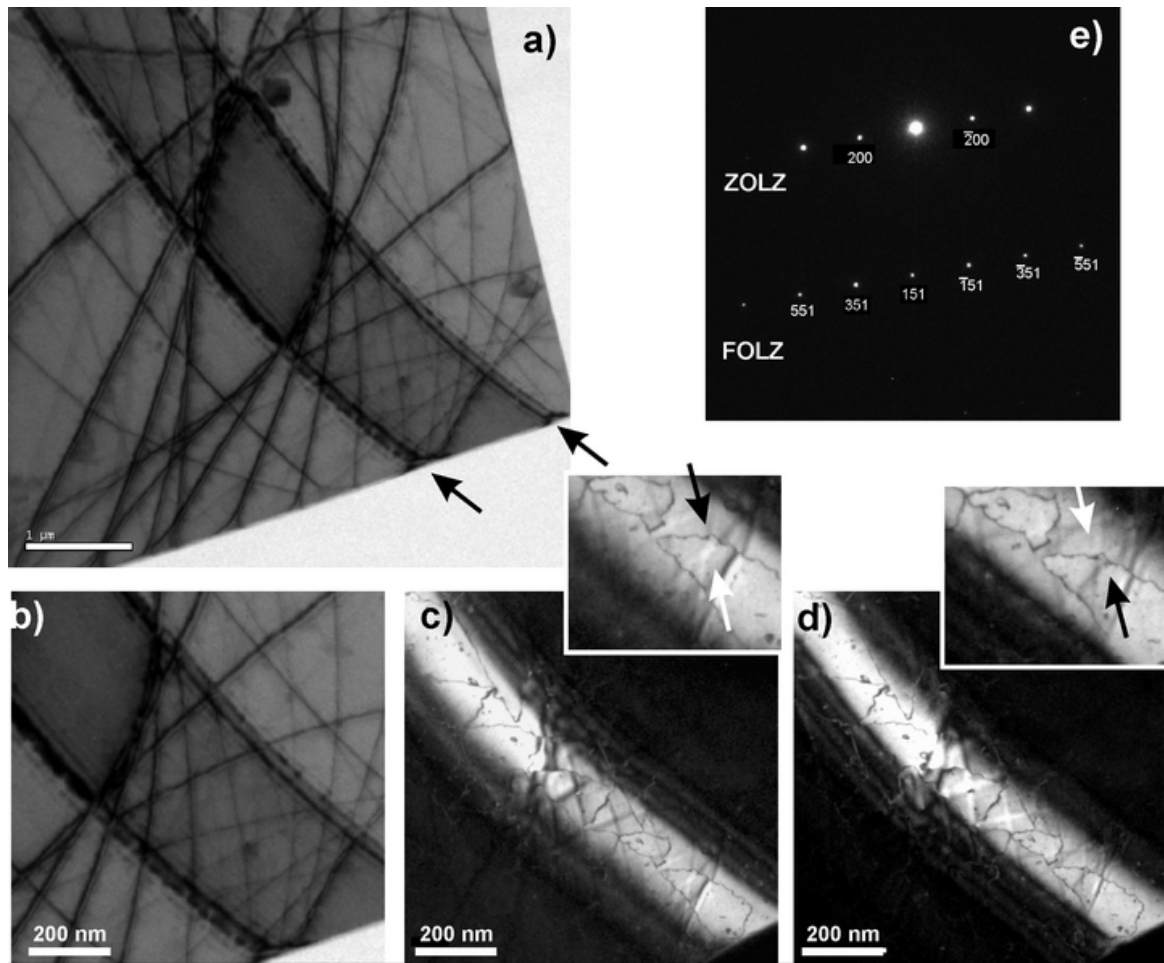


Figure 3.21.: Bend contour analysis on antiphase patterned [001] GaP: (a) is a bright field image of the edge of the plan view sample. The dark borders of the broad diagonal band are the 200 and  $\bar{2}00$  bend contours (marked with arrows). The narrow curved lines are the HOLZ bend contours. (b) is a magnified part of (a), where the dark field images are made: (c) with the 200 reflection, (d) with the  $\bar{2}00$  reflection. The broad bright bands are the 200 and  $\bar{2}00$  bend contours, the narrow HOLZ contours appear alternating in bright and dark. The contrast change along one line indicates the polarity change when crossing a boundary (magnified images).

(a) is a bright field image showing an edge of the plan view sample. The dark rims of the broad band running diagonal from the top left to the bottom right corner are the  $\{200\}$  bend contours (marked with arrows). Their origin was described in the beginning of the paragraph. The narrow intersecting curved lines are the contours of the reflections of the first order Laue zone. Each line corresponds to a reflection from the FOLZ. The crossing of such lines is equivalent to the dark or bright/faded crosses of the CBED patterns, though here they appear all in dark, due to the above described reasons. Figure 3.21 (b) is a magnified part of Figure 3.21 (a), at the position, where the dark field images of Figure 3.21 (c) and (d) were made. The dark field image shows the  $\{200\}$  bend contour bright, as expected. The additional narrow contours of the FOLZ lines appear partly bright on the images. Their exact sequence could determine the exact orientation of the sample, but it can be seen, that it is quite difficult to index them properly in this case. What is not seen on the bright field images is the domain structure of the GaP material. They appear on the dark field images. One can observe that the HOLZ lines change their contrast: crossing a boundary of two domains of the GaP material, they change from dark to bright or vice versa. An example of the contrast change is marked with arrows. In single phase material, the HOLZ contours have complementary contrast on the 200 and  $\bar{2}00$  images: a single contour line is bright on the 200 and dark on the  $\bar{2}00$  image. In this case their contrast alters, when intersecting an APB, since the polarity on one side of the boundary is the inverse of the other side.

### 3.3.6. Detection of other planar defects

Besides APBs, the other prominent planar defect types of the zincblende semiconductors are stacking faults and microtwins. Their structure was described in Section 2.2.3. The contrast they give in TEM imaging will be presented in this section.

Both defects occur on the  $\{111\}$  crystallographic planes. The thickness of a stacking fault can be between one and several ( $\sim 5$ ) atomic planes, the thickness of a microtwin can be between several atomic planes and several 10 nm. A microtwin can spread laterally over several hundred nanometers and vertically throughout the whole layer thickness from the bottom to the top. They can be observed “edge-on” in cross sections in dark field or at high resolution by observing their terminating  $\mathbf{b}=\mathbf{a}/3\langle 111 \rangle$  Shockley partial dislocation or  $\mathbf{b}=\mathbf{a}/6\langle 11\bar{2} \rangle$  Frank partial dislocation, or in plan view through their dynamical contrast fringes. As shown, stacking faults occur when the stacking sequence is disturbed on the  $\{111\}$  planes. This disturbance is described by the lattice translation vector of the stacking fault, which is  $\delta\mathbf{r}=\mathbf{a}/6\langle 11\bar{2} \rangle$ .

Figure 3.22 shows the example of the microtwin and stacking fault observation in cross sectional dark field imaging. Figure 3.22 (a) is a *selected area diffraction* pattern in zone axis excitation of a GaP layer, which contains a microtwin and a stacking fault. The selected area diffraction is obtained by putting the area selector aperture in the

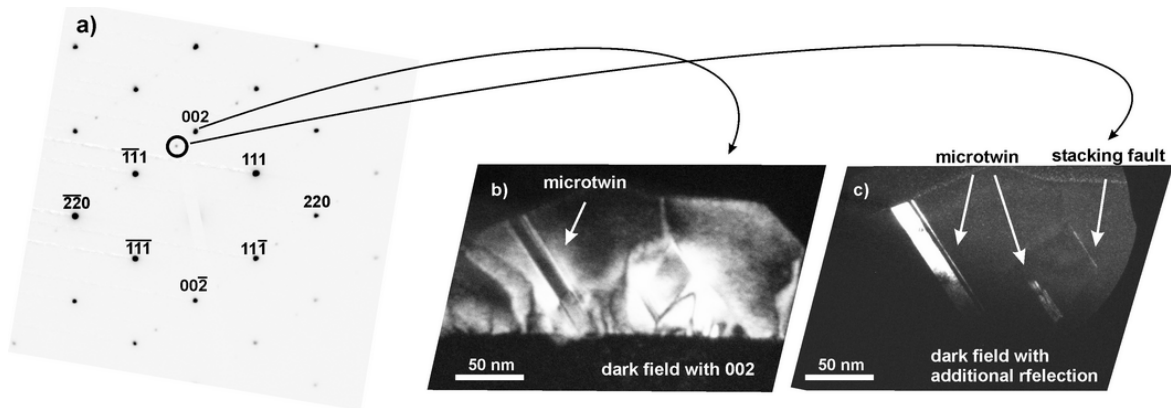


Figure 3.22.: Dark field imaging of microtwins in cross section: (a) is the selected area diffraction (SAD) pattern of a GaP thin layer with microtwins and stacking faults. Note the additional reflections at  $1/3$   $111$  positions (one is marked with black circle): the Bragg reflection from the microtwins. (b) is a dark field image taken with  $002$ . (c) is a dark field image taken with the additional reflection, where fulfilling the Bragg conditions makes the microtwin visible.

beam path in the first image plane to let only the diffracted beams from the selected sample area contribute in the further image and diffraction pattern formation. The direct beam was blocked to protect the CCD camera. Besides the expected reflections or GaP, additional reflections were observable at  $1/3$   $hkl$  positions. After tilting the sample to two-beam condition, in order to excite the  $002$  reflection, a conventional  $002$  dark field image was acquired (Figure 3.22 (a)). The Si substrate appears dark and the GaP layer brighter. The example crystal area is far from perfect: the surface is modulated and threading defects are observed throughout the layer. The white arrow depicts a broad band parallel to the  $(\bar{1}\bar{1}1)$  plane. Figure 3.22 (c) show the equivalent dark field image, made by positioning the objective aperture around the additional reflection near to  $002$ . The sample was not tilted, since the additional reflection was strong enough to use it for imaging. The image is generally dark, showing no intensity in the Si and in the GaP observed and the layer surface can hardly be seen. The only area that “shines out” from the GaP layer is at the position of the broad dark band on the  $002$  image. This area is a microtwin, where the lattice is mirrored about the  $(\bar{1}\bar{1}1)$  lattice plane. The additional reflections originate from microtwin lamellae. They are also in Bragg position, therefore the intensity of those areas is high on image (c). There is one more microtwin band and also a thin stacking fault in the image, which are invisible in Figure 3.22 (b) due to other defects.

If the microtwins or stacking faults are on those  $\{111\}$  planes, which are not “edge-on”, but have their normal in the plane perpendicular to the image plane, they are normally invisible. The only contrast they show is when the TEM sample is prepared by chance so that they intersect the TEM foil. This phenomenon can be seen in Figure 3.19 and in Figure 5.7.

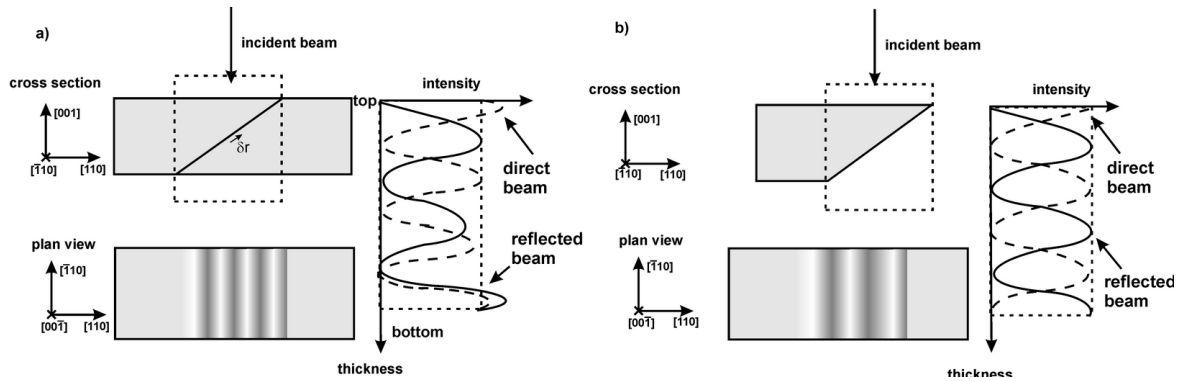


Figure 3.23.: The origin of the contrast of stacking faults and microtwins in dark and bright field imaging. (a) the planar defect on a  $\{111\}$  plane cuts the sample into two wedges. (b) The contrast formation of a wedge shaped sample: in two-beam condition the intensity oscillates between the direct and the diffracted beam with the “wavelength” of the extinction length. The result in plan view: oscillating thickness fringes (lower image). The fringe contrast of the stacking faults in plan view (lower image on (a)) is a superposition of two wedge shaped samples displaced from each other with the lattice translation vector of the planar defect.

Though microtwins and stacking faults are not “edge-on” in the  $[001]$  direction of the plan view, dynamic effects let them become visible. Figure 3.23 presents schematically the origin of the contrast of a stacking fault in plan view. The stacking fault on a  $\{111\}$  plane slices the plan view TEM foil into two wedge shaped sample pieces that are translated from each other by the lattice translation vector  $\delta\mathbf{r}$  of the stacking fault, as shown in Figure 3.23 (a). It is easier to understand the contrast formation taking one wedge first: the upper drawing in Figure 3.23 (b) is basically a wedge shaped TEM sample. Consider dynamical two beam conditions: only one diffracted beam and the direct beam are excited. The intensity of these beams changes with the local sample thickness due to the beam extinction. They both go through maxima and minima, but with different phase: the intensity oscillates between the diffracted and the direct beam as it is illustrated on the intensity-thickness diagram on the right. The “wavelength” of this oscillation is the extinction length. This phenomenon results in the well-known *thickness fringes*. Both the bright and dark field images show them. The image is patterned with alternating dark and bright lines perpendicular to the thickness gradient. The dark and bright field images are complementary: the lines are in opposite phase. Now, introducing the stacking fault as two wedge shaped crystals displaced with  $\delta\mathbf{r}$  along the wedge results in a new intensity profile, which is no longer complementary: the *stacking fault fringes*. The intensity profiles of the diffracted and direct beams are shown on the right side of Figure 3.23 (a); intensity simulations can be found e.g. in [73]. From the asymmetry of the fringe systems, the direction of the stacking fault (the top and the bottom) and its character can be determined. The contrast of the fringes can be described by the following [43]:

- The bright field fringe system is symmetrical. The outer fringes are either both dark or both bright, depending on the sign of the phase factor. The fringe contrast is suppressed in the center of the foil due to absorption.
- The dark field fringe system is asymmetrical: the outer fringes are not the same. If the image is an axial dark field, where  $\mathbf{g}$  has opposite sign to the excited reflection in the bright field image, the dark and bright field fringes are reversed at the top of the foil. The reverse is true if the same  $\mathbf{g}$  is used in the dark and bright field images.

Determination of the intrinsic or extrinsic nature of stacking faults can be done by comparing the obtained fringe contrasts with the following rules [43]: if the origin of the  $\mathbf{g}$  vector is placed at the center of the fault in a dark field image (formed by tilting the weak  $\mathbf{g}$  onto the optic axis so that is opposite to the  $\mathbf{g}$  used in the bright field image),  $\mathbf{g}$  points away from the bright outer fringe if the fault is intrinsic, and toward the bright fringe if the fault is extrinsic for all  $\{111\}$ ,  $\{400\}$  and  $\{220\}$  type reflections, irrespective the inclination of the fault. If the  $\{200\}$ ,  $\{222\}$  or  $\{440\}$  reflection is used the reverse is valid.

#### 3.3.7. High-resolution TEM

High resolution imaging is one approach to use the phase information of the scattered electron beam, which is lost at the use of the conventional diffraction or dark field methods. The main aspects of HRTEM can be understood by the phase of the electron wavefront and its alteration caused by the specimen and after leaving the specimen, caused by the electromagnetic lens system. What one “sees” is the interference pattern of the forward scattered and diffracted electrons. This requires very thin and perfect electron transparent regions of the TEM foil. The specimen itself is approximated by an object, which causes this phase shift of the electron wavefront. As it will be seen, the observed image is not simply the projected potential of the sample structure, but the result of the interaction with the lens system. To be able to evaluate the obtained images, simulation is needed. This is also, how HRTEM investigations were carried out to characterize the atomic structure of the defects.

There are several methods to simulate the effect of sample and lens system interaction with the electron beam. Many material and machine parameters, as well as experimental conditions, contribute to the observed image and have to be considered in the simulation. The image is sensitive to the following parameters:

1. The alignment of the beam with respect to the specimen and the optical axis.
2. The coherence of the beam.
3. Chromatic aberration of the objective lens.

4. Spherical aberration of the objective lens.
5. Intrinsic vibration of the material (Debye-Waller factor).
6. The specimen thickness.
7. The defocus of the objective lens.

The first and the last two parameters can be influenced directly by the microscopist during the imaging. Proper alignment of the electron beam in the TEM column and exact setting of the sample in the used zone axis is crucial. The exact zone axis is also therefore used in the image simulation. The second and the third parameters are determined by the microscope itself and values for the JEOL 3010 (chromatic aberration  $C_c=1.3\text{mm}$ , spherical aberration  $C_s=0.6\text{mm}$ , defocus spread 10 nm, beam spread 0.5 mrad) were taken into account in the simulation. Higher order lens aberrations become generally more important if it is necessary to increase resolution and therefore the transmitted range of spatial frequencies of the electron beam. The intrinsic parameters of the investigated semiconductor materials were taken into account from tables [40]. The last two parameters: the specimen thickness and the defocus of the objective lens are kept as two “tunable” parameters during imaging and also in the image simulation. Experimentally the exact sample thickness is generally not known and changes in the TEM sample laterally. Therefore the images are simulated for different thicknesses. When imaging a defect, it is also important, that the TEM sample has a specific thickness to be “visible”. The perturbation of the electron beam has to be large enough when penetrating through a defect, in order to have an observable phase change compared to the perfect crystal. Also, the detection of a defect can depend on the defocus conditions.

It was shown for the perfect crystal [74], (soon after the first acquired HRTEM images), that the experimental images can be understood in terms of images of Bloch waves. Although the number of diffracted beams is large, only a few Bloch waves determine the appearance of the lattice image. This method is very fast and accurate for imaging the crystal, but applicable only to perfect crystals and small unit cells. Since the objective of the investigations were to image crystal defects, a software was needed to simulate larger unit cells that contained defects. The **multislice method** was first pioneered by Cowley and Moodie [75]. The software used to simulate the experimental images was the CERIOUS modelling software package and its HRTEM module. It was developed in collaboration with Dr. Owen Saxton, University of Cambridge. The model of the crystal and the defect were built with its crystal modelling module and the simulation was done with the HRTEM module.

The general idea of multislice methods is that the sample model is sectioned into few atomic layer thick slices, which have their normal in the beam direction. The perturbation of the electron beam (the output beam) caused by a crystal slice is

calculated and treated as the incident beam of the next slice. The simulation uses the prerequisite, that there is no crystal inhomogeneity in the viewing direction.

Figure 3.24 illustrates the image formation process of the TEM and also the main steps of the image simulation.

**Model building.** The first step of any image simulation is the specification of the specimen parameters. If a perfect crystal is to be imaged, the unit cell must be fixed. This can be done by giving lattice parameters, space group and the basis. If a defect structure is to be imaged, a larger unit cell or a “supercell” is needed. In this case, every atom is put directly into the unit cell, not by the symmetry operations.

The planar defects of GaP can be imaged if the observation direction is parallel with their plane, i.e. the electron beam is “edge on”. Since Fourier transformations are used throughout the calculations, it is faster if the large unit cell is periodical. The unit cell is hence treated with periodic boundary conditions in the lateral ( $x$  and  $y$ ) directions. The slicing is done in the  $z$  direction. The unit cell parameter in  $z$  direction can be chosen as the slice thickness  $\Delta z$ .

Having constructed the “supercell”, the next step is to calculate the structure factor:

$$F(\mathbf{k}) = \frac{2\pi\hbar^2}{m_e e V} \sum_i f_i(\mathbf{k}) e^{i2\pi\mathbf{k}r_i}, \quad (3.15)$$

where  $V$  is the volume of the unit cell,  $i$  is the index of the atom in the unit cell,  $\mathbf{k}$  is the diffraction vector, which takes only values from the reciprocal lattice vector ( $\mathbf{g}$ ). In the following,  $\mathbf{k}$  is restricted to two dimensions and the structure factor is evaluated in the zone normal to the direction of the electron beam ( $z$ ). The structure factors are calculated only for the Zeroth Order Laue Zone, i.e., where  $w=0$  in the vector  $\mathbf{k}=[uvw]$ . The projected potential of the unit cell  $\phi_p(x, y)$  is the Fourier transform of  $F(\mathbf{k})$  (3.15), integrated over the  $z$ -dimension of the slice.

**Propagating through the sample.** The transmission function of a slice of a unit cell, neglecting absorption and treating it as a phase object, is:

$$q(x, y) = e^{i\sigma\phi_p(x, y)\Delta z}, \quad (3.16)$$

where  $\sigma \equiv 2\pi m_e \lambda \hbar^{-2}$  is the “electron interaction parameter” and measures the interaction strength between the electron beam and the specimen. The quantity  $\phi_p(x, y)$  is usually referred to as the “phase grating”. In the case of high energy electrons penetrating thin specimen slices, the slices cause small changes in the phase of the wave function. These phase changes have the same  $x$ - $y$  pattern of  $\phi_p(x, y)$  and are proportional to the projected potential. The transmission function is calculated for each different slice in the unit cell along  $z$ . Considering a plane wave with the amplitude of a unit, the output after the first slice is  $q_1(x, y)$ . At this point, this output function is convoluted with the free space propagator,  $p(x, y)$ , to reach the next slice. The free

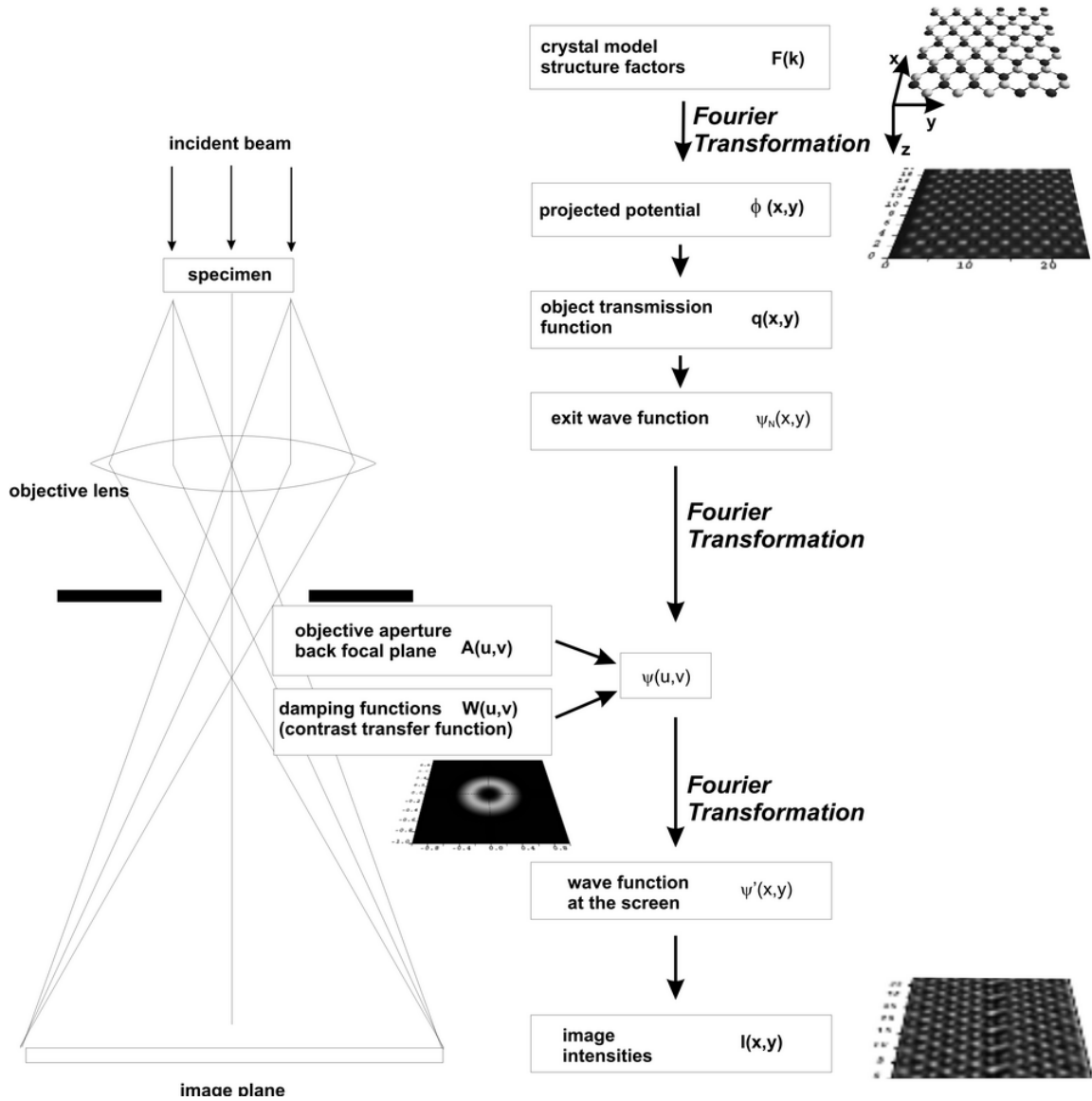


Figure 3.24.: High Resolution Image simulation process: the ray diagram shows the basic image formation. The right side illustrates the main steps of the simulation process

space propagator of a spherical wave is a Green's function "kernel":

$$p(R) \equiv \frac{-i}{R\lambda} e^{ikR} \quad (3.17)$$

The propagator (Fresnel-propagator) used in this case is a simplified one, assuming that the propagation happens along  $z$  direction under small scattering angles, and therefore the  $z$ -dependence can be ignored:

$$p_R(x, y) = \frac{-i}{R\lambda} e^{ik(x^2+y^2)/R}. \quad (3.18)$$

Repeating the process, the exit wave function of the  $N^{\text{th}}$  slice is:

$$\Psi_N(x, y) = q_N(x, y) [\Psi_{N-1}(x, y) * p(x, y)]. \quad (3.19)$$

The full form of  $\Psi_N(x, y)$  can be written by expanding the recursion. The diffraction vector is in this notation  $k \equiv 2\sin\Theta/\lambda = (u^2 + v^2)^{1/2}$ , where  $u \equiv \Delta k_x$  and  $v \equiv \Delta k_y$ , and the index  $N$  is dropped from  $p_N(x, y)$  assuming equal spacing between the slices. In reciprocal space the wave function is:

$$\Psi_N(u, v) = q_N(u, v) [\Psi_{N-1}(u, v) * p(u, v)], \quad (3.20)$$

where the propagator has the form of:

$$p(u, v) = e^{i\pi\varsigma(u,v)\Delta z}. \quad (3.21)$$

$\varsigma(u, v) = \lambda k^2$  is the  $z$ -component of the deviation parameter for the diffraction  $\mathbf{k} = [uv]$  and  $[uv]$  is the distance to the Ewald sphere along the beam direction. Some more considerations: the "phase grating" approximation treats the waves as parallel plane waves satisfying the Laue conditions perfectly, and the curvature of the Ewald sphere is taken into account through the propagator. One more role of the propagator is to include the effects of the crystal or beam tilt through asymmetries. The beam tilt is more detrimental than the crystal tilt alone, since it is a combined effect of being tilted from the optical axis of the microscope and the specimen zone axis. This has to be considered in the experimental procedure to avoid any misalignment in the experimental setup.

**Propagation through the microscope.** All the effects of the microscope, the defocus, spherical aberration and instrument deficiencies are applied to the wave function  $\Psi(u, v)$  in the back focal plane of the lens system before doing the next Fourier transformation to get the final wave function at the object plane  $\Psi(x, y)$ . The phase change caused by the spherical aberration ( $C_s$ ) and the defocus ( $\Delta f$ ):

$$W(u, v) = \pi\lambda k^2 \left( \frac{1}{2}\lambda^2 C_s k^2 - \Delta f \right). \quad (3.22)$$

The defocus can be taken into consideration also by adding this defocus ( $\Delta f$ ) path to the final propagator. The objective aperture is modeled with an aperture function  $A(u, v)$ , which is zero outside the aperture radius and unity inside. The modified wave function after the objective aperture is:

$$\Psi'(u, v) = \Psi(u, v)A(u, v)e^{-iW(u,v)}. \quad (3.23)$$

In the next step, the deviations of the incident illuminations from the ideal plane wave have to be included. The effects resulting in a spread in the focus can be treated together. Starting with the direct reason of the change of the focal length: fluctuations of the objective lens current,  $I$ , chromatic aberration,  $C_c$ , in combination with the energy spread of the incident beam. The energy spread is the result of the instability of the accelerating voltage,  $V$ , and the thermal energy,  $E$ , of the electrons coming from the filament. All the spread effects are treated as Gaussian damping functions. The total focal spread  $\Delta$  is gained by their convolution, resulting in a value of a few nm for  $\Delta$ .

The convergence of the beam also has an effect similar to focal spread (blurring the image and reducing the resolution) and can also be treated as a damping function multiplier for the exit wave at the back focal plane. The approximations for the damping functions can be done only for thin samples, where the transmitted beam is dominant and serves as a reference phase for the optical axis. For thicker samples with strong diffracted beams the situation is not so simple. The wave function in the back focal plane with all modifying factors (objective aperture, beam instabilities, beam convergence and the phase shift (described by the contrast transfer function in Section 2.3)) included, is:

$$\Psi'(u, v) = \Psi(u, v)A(u, v)A_{C_c}(u, v)A_\alpha(u, v)e^{-iW(u,v)}. \quad (3.24)$$

By Fourier transformation of  $\Psi'(u, v)$  the wave function in the image plane on the viewing screen  $\Psi'(x, y)$  is calculated. The intensity of the simulated image is then:

$$I(x, y) = \Psi'^*(x, y)\Psi'(x, y). \quad (3.25)$$

### High Resolution TEM imaging of GaP antiphase boundaries

In this section the results of the above mentioned image simulation method for the case of the GaP antiphase boundaries will be described. The supercell is constructed in such a way that the plane of the antiphase boundary is perpendicular to the slice, dividing the slice laterally in the  $(x, y)$  plane (the schematical models shown in Figures 3.25, 3.26 and 3.27). The left part of the slice is Ga-polar and the right is P-polar. During the model building, new atoms can be put in the supercell, they can be exchanged or interfaces can be built. The atoms were distributed on the perfect zinc blende lattice

sites, having the bond length of the ideal lattice. In order to get closer to the real situation, where the false Ga - Ga and P - P deviate from the Ga-P bond length, the crystal model is relaxed. This relaxation is carried out by the Open Force Field method embedded in the Cerius software. This force field method is similar to the Valence Force Field method used for recalculating electron scattering factors in Chapter 4. It relaxes the crystal by means of fine repositioning of the atoms on the lattice sites by minimizing the strain energies of the bonds. Due to this relaxation, the edge of the supercell can also be slightly deformed. Using the periodic boundary conditions, anomalous contrast can occur at the rim of the slice. Therefore, the lateral size of the slice was chosen so that the anomalous contrast cannot interfere at the middle part of the slice, where the interesting region, i.e. the APB, is located. The following types of antiphase boundaries were investigated: the stoichiometric  $\{110\}$  APBs and the APBs laying the  $\{111\}$  planes. As the latter one is non-stoichiometric, it can be built up either with Ga - Ga or P - P false bonds on the  $\{111\}$  planes. The lateral slice size was 2 nm x 2.5 nm in the case of the  $\{110\}$  APBs, and 4 nm x 4.5 nm for the  $\{111\}$  APBs. The slice thickness was 0.4 nm in all cases. The incident electron beam was propagated in the  $[1\bar{1}0]$  direction. The maximum simulated thickness was 20 nm. Image series of different defocus and thickness were simulated. The full series was made between 2 nm and 20 nm sample thickness with the step of 2 nm and between -100 nm and +90 nm defocus with the step of 10 nm. Only a selection of the full series is presented here.

Figure 3.25 shows a simulated HRTEM image series of a GaP crystal having an  $\{110\}$  type antiphase boundary (APB) in the middle. The images are presented as the function of the sample thickness (vertical) and objective lens defocus (horizontal). It can be seen on the simulated images, that the GaP dumbbells along the  $\langle 110 \rangle$  directions are not resolved (their distance is  $a/4 = 0.1363$  nm). Simulated images exhibit bright spots, which are the merged projections of the Ga and P atomic columns (as seen on the image with 6 nm thickness at -30 nm defocus in Figure 3.25). Changing the defocus or the sample thickness this so called “bright atom contrast” can change. At specific conditions the atomic columns show up with dark contrast, while the space between the atomic columns appears to be bright. This can be seen on the image with 10 nm thickness and -30 nm defocus values in Figure 3.25. Increasing the sample thickness for a constant defocus value, the intensity of the bright spots decreases, and positions that were dark became brighter. This is due to the extinction of the direct beam: if the sample thickness reaches the extinction length, the atom columns appear dark. The contrast changing phenomenon of the atomic columns can be also observed in Figure 3.27. At a fixed defocus value, for example at -30 nm, increasing the sample thickness, does not only decrease the spot intensities, but also double the spatial frequencies. This frequency doubling can be explained in the terms of extinction of the direct beam: in samples having a thickness between  $1/4$  and  $1/2\xi_{000}$  (extinction length of the direct beam) the intensity of the diffracted beams increases and the intensity of

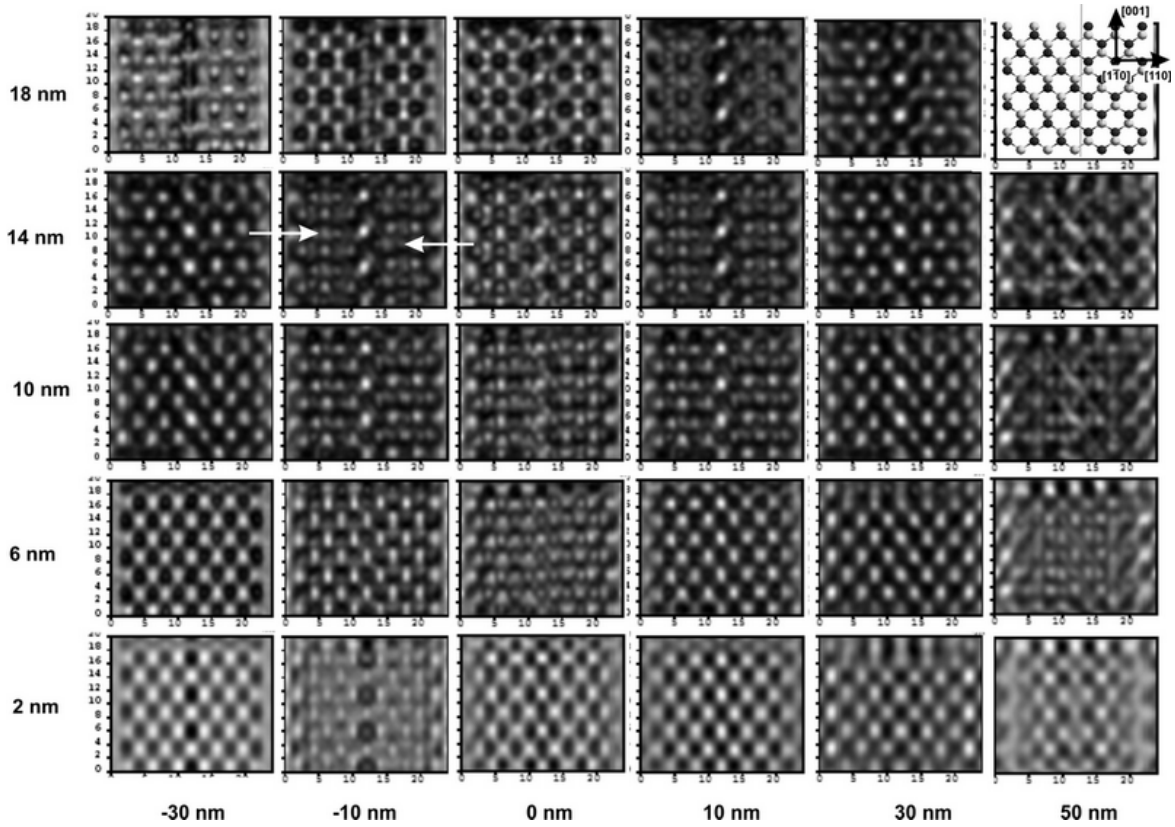


Figure 3.25.: Simulated high-resolution TEM images of  $\{110\}$  APBs in GaP

the 000 direct beam decreases. With these higher intensities the opposite diffracted beams can interfere with each other and can result in periodic intensity increase at half of the spacing of the interference between the same Bragg beams and the direct 000 beam. This can be observed in this case for the 6 nm thick GaP first. Reaching  $1/2\xi_{000}$  the atom column positions become bright again. The atom column positions remain bright until the sample thickness reaches  $\xi_{000}$ , exactly one extinction length. At this thickness they become dark again, and the full cycle starts to repeat. This has also a practical benefit: it is worth performing the image simulation thickness series, for example, in the steps of  $1/8$  increment of the extinction length in order to scan through the whole range of image contrast. The extinction length can be determined by plotting the intensity versus the sample thickness for the 000 direct beam. It has to be emphasized that it is not possible to correlate the experimental High Resolution pattern only with one of the simulated images using this technique. There are identical simulated patterns, which are the result of different defocus and thickness combinations. A more developed technique, the exit plane wave reconstruction, is a possible candidate to retrieve more information from the HRTEM micrographs by recording experimental defocus series with spherical aberration corrected microscopes [76].

### 3. Experimental Methods

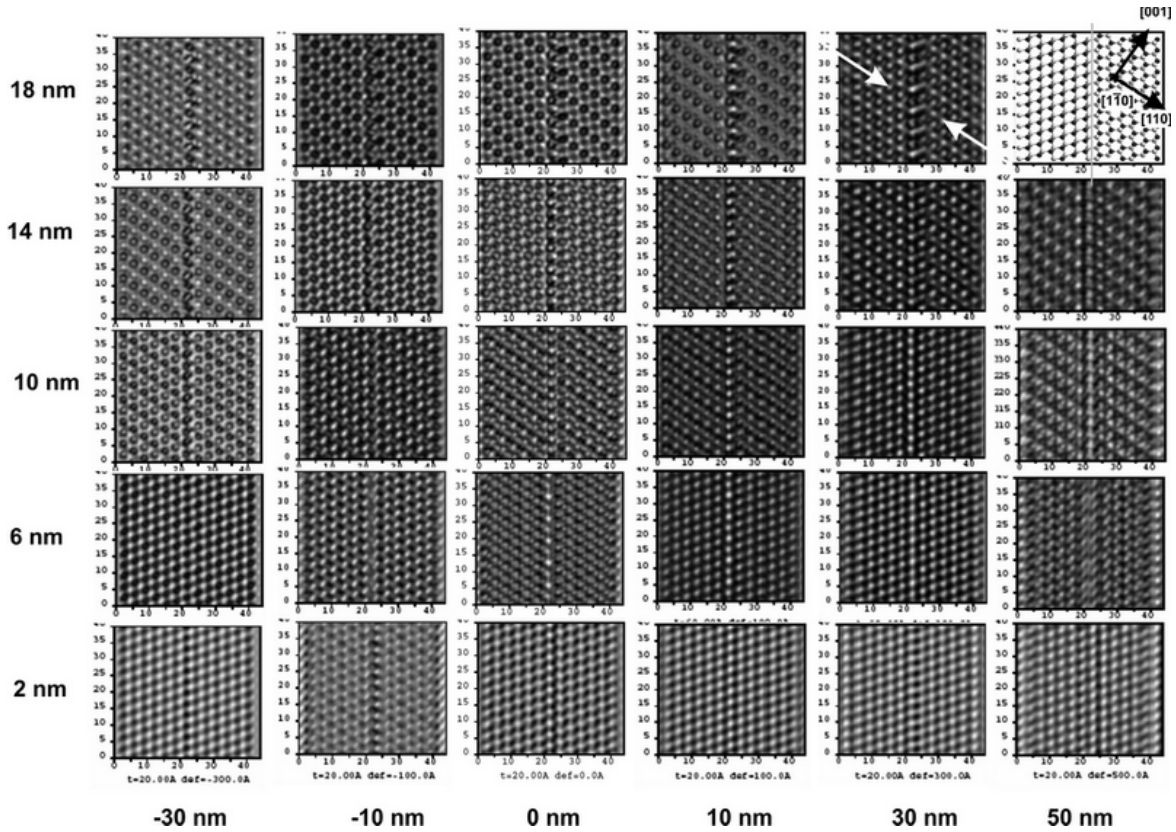


Figure 3.26.: Simulated high-resolution TEM images of  $\{111\}$  APBs in GaP with Ga - Ga false bonds

In this study (Section 5.2), individual high resolution lattice images were acquired with the microscope and compared with simulated images. The information content of the high resolution images of the different types of antiphase boundaries is the following: the “edge-on” antiphase boundary in the GaP crystal can be observed with the Jeol JEM 3010. The APBs can be mapped at different sample thicknesses and defocus values. Although, according to instrument resolution, the Ga-P dumbbells can not be resolved, at specific imaging conditions a shift of the merged Ga-P column was observed. This is depicted by a pair of white arrows on single images of the defocus-thickness series in Figures 3.25, 3.26 and 3.27.

The horizontal row of bright spots on one side of an APB is shifted in  $[001]$  as compared to the other side of the APB with the value of around one quarter of the lattice constant. It is difficult to state an exact value of the shift distance because different thickness-defocus conditions suggest different shift values up to the level of one quarter of the lattice constant. The reason for the vertical shift of the intensity maxima is presumably the following: by increasing the specimen thickness additional intensity rises at double spatial frequency, located at half distance between the bright spots mapping the atomic columns. The origin of this additional intensity is the

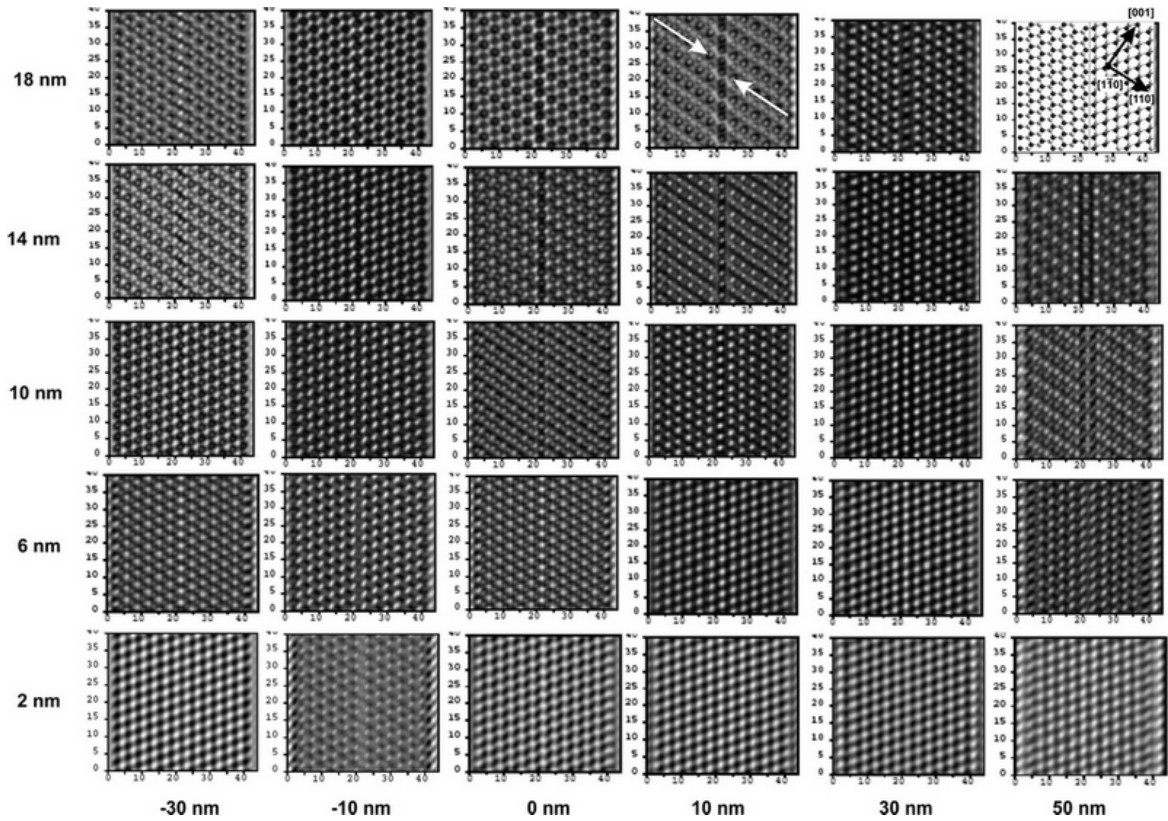


Figure 3.27.: Simulated high-resolution TEM images of  $\{111\}$  APBs in GaP with P - P false bonds

interference of opposite Bragg beams [43]. If one considers that the amplitudes of the opposite  $002$  and  $00\bar{2}$  and also the  $111/\bar{1}\bar{1}1$  and  $11\bar{1}/\bar{1}\bar{1}\bar{1}$  are not equal even in zone axis excitation, their interference can result in non mirror-symmetrical intensity distribution concerning the  $(001)$  plane. Hence, if one observes the shift of the intensity maxima, on the two sides of a  $(110)$  or a  $(111)$  plane in  $[001]$  direction, the defect is possibly an antiphase boundary. This observable shift is enough for qualitative interpretation of the experimental images.

# 4. Quantitative compositional Analysis of Ternary III/V quantum well Structures by dark field TEM

*The main topic of this chapter is the quantitative composition determination of ternary GaAs- and GaP-based quantum wells by chemically sensitive 002 dark field imaging. The dark field image intensities are compared with the results of refined structure factor calculations introducing static atomic displacements of the zincblende structure due to the isoelectronic impurities by Valence Force Field methods and the recalculation of the atomic scattering factors using DFT.*

## 4.1. Refined structure factor calculation with VFF and DFT

The basics of structure factor calculation that have to be taken into consideration in order to describe the ternary III/V zincblende material has been introduced in Section 2.4. These are:

1. There is a redistribution of the electron density forming chemical bonds in the zincblende structure compared to the electron density in isolated atom approximation (Doyle and Turner [17]).
2. There may be a significant displacement of the atoms from their equilibrium position caused by the lattice distorting effect of substitutional impurities.

The effect of the redistributed electron density resulting in modified atomic scattering factors was calculated using the density functional theory. The results are summarized in Table 4.1. The table compares the values of the isolated atom approximation of Doyle and Turner [17] with the values obtained by DFT.

The lattice distorting effect of the substitutional impurities was calculated as *static atomic displacement* by the Valence Force Field method. As shown, density functional theory is suitable for calculating both lattice distortion and electron redistribution, but due to its huge computational effort and small applicable supercell size, it was used only as a reference method for the calculation of static atomic displacements.

Compound	Ga	As	P	N	Sb	B
Calculated for bulk:						
GaAs:X	3.97	4.34	3.00	1.52	6.37	1.58
GaP:X	3.81	4.17	2.86	1.45	6.15	1.45
Calculated for isolated atoms:						
GaAs:X	4.00	4.45	3.14	1.58	6.59	1.56
GaP:X	3.89	4.33	3.04	1.54	6.42	1.50

Table 4.1.: Kinematic (002) electron form factors [Å] for various substitutional isoelectric impurities in GaAs and GaP calculated by DFT and the corresponding values for isolated atoms calculated following [17]. In order to include the relativistic correction for electrons travelling with velocity  $v$ , the values have to be multiplied by  $(1 - v^2/c^2)$ , where  $c$  is the velocity of light in vacuum.

To verify the accuracy of the combined method, DFT for the calculation of the atomic form factors and VFF for the atomic displacements, the bond length of the single substitutional impurities was calculated both by full DFT and by the combination of DFT calculation for the atomic scattering factors and the VFF method for calculation of the atomic displacements. The strain value of the bonds were compared:

$$\epsilon = (r - r_0)/r_0, \quad (4.1)$$

where  $r$  is the relaxed anion-cation bond length of the impurity and  $r_0$  is the equilibrium anion-cation bond length of the zincblende crystal.

Table 4.2 summarizes the bond distortions calculated by DFT, VFF and analytically from Equation 4.6 (described later). The consistency of the DFT and VFF values proves that the VFF method is satisfactory for the bond relaxation calculation.

Compound	DFT	VFF	From Equation 4.6.
GaAs:N	-0.155 <sup>1</sup>	-0.159	-0.142
GaAs:B	-0.113 <sup>2</sup>	-0.118 <sup>3</sup>	-0.116
GaAs:Sb	+0.053	+0.050	+0.060
GaAs:P	-0.025	-0.025 <sup>4</sup>	-0.027
GaP:Sb	+0.082	+0.072	+0.086
GaP:As	+0.025	+0.023 <sup>5</sup>	+0.027
GaP:N	-0.127 <sup>6</sup>	-0.132	-0.122
GaP:B	-0.122	-0.124	-0.122

Table 4.2.: Strain of anion-cation bond lengths around isolated substitutional isoelectric impurities in GaAs and GaP 64-atom cubic supercells calculated using DFT and VFF. The values are normalized to the bond length of the host crystal. From previous studies: <sup>1</sup>-0.151 (DFT [77]), <sup>2</sup>-0.114 (DFT [78]), <sup>3</sup>-0.127 (VFF [78]), <sup>4</sup>-0.029 VFF [79]), <sup>5</sup>+0.025 (VFF [79]), <sup>6</sup>-0.137 (DFT [77]).

**Analytical calculation of the structure factor** In order to avoid the huge computational effort of the VFF methods, analytical description can be done with some simplifying assumptions. If a ternary  $A(B_{1-x}C_x)$  compound is investigated with  $x \rightarrow 0$ , the substitutional isoelectric impurities are so rare that their interaction can be neglected, and they can be treated as isolated impurities. Furthermore, it can be assumed for simplicity, that the bond relaxations displace only the atoms around the impurity, which are first neighbors as illustrated in Figure 4.1. The amount of atoms

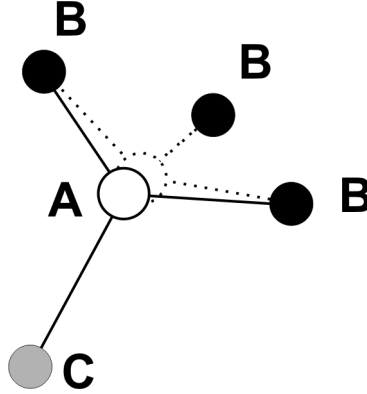


Figure 4.1.: Static atomic displacement. The local bond configuration of the isolated substitutional impurity atom  $C$  in the zincblende  $AB$  host crystal. The dotted lines show the equilibrium unrelaxed bond configuration of  $AB$ .

affected by the displacement is  $4x$  since the atoms of the zincblende structure are four-fold coordinated. The other atoms (next nearest neighbors) are assumed to remain on the unperturbed positions  $\rho_0$ . Using these assumptions, the structure factor of the ternary material is reduced to the two atom basis, and can be written as:

$$F(\mathbf{g}) = xf_C + (1-x)f_B + (1-4x)f_A \cos(2\pi\mathbf{g} \cdot \rho_0) \quad (4.2)$$

$$+ 4xf_A \cos[2\pi(1+\epsilon)\mathbf{g} \cdot \rho_0], \quad (4.3)$$

where  $\epsilon$  is the bond distortion introduced by the impurity atom, defined by Equation 4.1. Owing to the inequality  $\epsilon \ll 1$ , Equation 4.4 can be simplified using a series expansion [14]:

$$F(\mathbf{g}) \approx xf_C + (1-x)f_B + [1 - 8x(\pi\epsilon\mathbf{g} \cdot \rho_0)^2]f_A \cos(2\pi\mathbf{g} \cdot \rho_0). \quad (4.4)$$

For the 002 reflection, the structure factor can then be written as:

$$F(002) \approx xf_C + (1-x)f_B - [1 - 2x(\pi\epsilon)^2]f_A. \quad (4.5)$$

This equation is similar to the original Equation 2.30 presented for the virtual crystal approximation. The only difference is the additional factor  $2x(\pi\epsilon)^2$ , which describes

the static atomic displacement caused by the impurity atom C and vanishes if  $\epsilon = 0$ . Equation 4.5 allows the structure factor for dilute alloys to be calculated without the huge computational effort of the VFF method. The necessary bond stretching parameters can be taken from Table 4.2 and calculated once with VFF or DFT. An approximate analytical expression was found to give a rough estimate for the bond strains. The first attempt to predict the bond strains analytically was done by Martins and Zunger [47] as they calculated the bond length around substitutional impurities in zincblende material. The expression they proposed, which relied only on the VFF parameters of materials, estimated the bond strain with high deviation from the DFT values. Instead, the approach used in this work derived an analytical expression for the lattice distortion around the isolated impurity. The optimal bond strain is derived by minimizing the Valence Force Field strain energy functional (Equation 2.52). Assuming atom C as the isolated impurity substituting an atom B in the AB host zinc blende crystal, the optimal bond strain is [80]

$$\epsilon \approx \frac{3 \alpha_{AC}(r_{0AC}^2 - r_{0AB}^2)}{(2 \alpha_{AB} - 3 \alpha_{AC}) r_{0AC}^2 + 9 \alpha_{AC} r_{0AB}^2}, \quad (4.6)$$

where the  $\alpha$  values are conventional VFF parameters. The results for the bond strain, that are predicted by Equation 4.6, are also presented in Table 4.2. These bond strain values give a comparable estimate as the VFF and the DFT values. These results were also applied to estimate the structure factor values of the different investigated compounds. Thus, a completely analytical estimation can also be given for the structure factors aside from DFT and VFF calculations.

The chemical sensitivity of a particular reflection was defined by Equation 2.31. In order to predict how the bond stretching affects the chemical sensitivity of the 002 reflection, equation 4.5 is substituted into Equation 2.31 and, after the derivation, in the  $x \rightarrow 0$  limit one obtains:

$$S_{002} \approx \frac{f_C - f_B + 2(\pi\epsilon)^2 f_A}{f_B - f_A} \quad (4.7)$$

The effect of bond strain due to atomic displacement on chemical sensitivity is presented when discussing the specific ternary alloy and compared with the experimental data.

The comparison of the predicted intensity ratio values and the experimental data will be organized according to the material systems. The measured and calculated intensity values will be compared to the concentration of the isoelectric impurity determined by HRXRD. The error bar of the composition determination by HRXRD measurements rises from the error of the strained lattice mismatch measurement of the quantum wells, which was determined by the maximum position of the multi quantum well envelope function. This value can be measured to within  $\pm 120''$  accuracy. Since materials introduce different strain in the host crystal, the resulting error bar of the

composition determination can differ. Its value for example for the Ga(NAs) material system is  $\pm 0.2\%$  N.

At each investigated ternary material system the 002 dark field image series is presented and the retrieved compositional information is compared with the above described estimation methods. The role of the bond strain is discussed at each material system.

## 4.2. Ga(NAs)/GaAs

The Ga(NAs) ternary material system grown on GaAs substrates with up to 10% of N content was investigated in the terms of its structure factor evolution and lattice distortion caused by the N. It was found [62] [16], that the virtual crystal approximation does not describe the crystal structure properly. When the neighbors of the nitrogen atoms were assumed to occupy the ideal positions on the cation sublattice, the N composition of the quantum well was underestimated by a factor of two, compared to (004) HRXRD results with (002) dark field measurements. When the static atomic displacement of the Ga atoms due to the N were taken into account when calculating the structure factor, the structure factor calculation provides matching results with the HRXRD measurements. The static atomic displacement caused by the nitrogen atoms was calculated by the Valence Force Field method by minimizing the strain energy of the supercell as described in Section 2.4.1. The atomic form factors for those studies were taken as the isolated atom approximation of Doyle and Turner (see Table 4.1). This work presents the recalculated values of the structure factors of the Ga(NAs) material system for up to 10% of N content by using the modified atomic form factors obtained by DFT. Figure 4.2 presents the predicted intensity ratios using the modified atomic form factors. The open symbols show the values of the structure factor calculation with the virtual crystal approximations; the full symbols show the values obtained by taking the static atomic displacement into account. The result of the reference method (shown by the cross), the “full DFT” calculation for the 64 atom unit cell with a single impurity of nitrogen (representing 3.125% N on the anion sublattice), shows perfect match with the prediction of the structure factor calculation with SAD. The -16% strain of the Ga - N bond calculated by VFF was supported by the DFT calculations. The effect of using the DFT calculated atomic form factors can be seen when comparing the values taken from [16]. The intensity ratio values calculated with the Doyle and Turner atomic form factors are shown by the triangles in Figure 4.2. The DFT calculated atomic form factors lower the predicted intensity ratios in a small extent. This means that the introduction of the recalculated atomic form factors acts against the effect of the static atomic displacement by the means of their intensity prediction of the Ga(NAs) material.

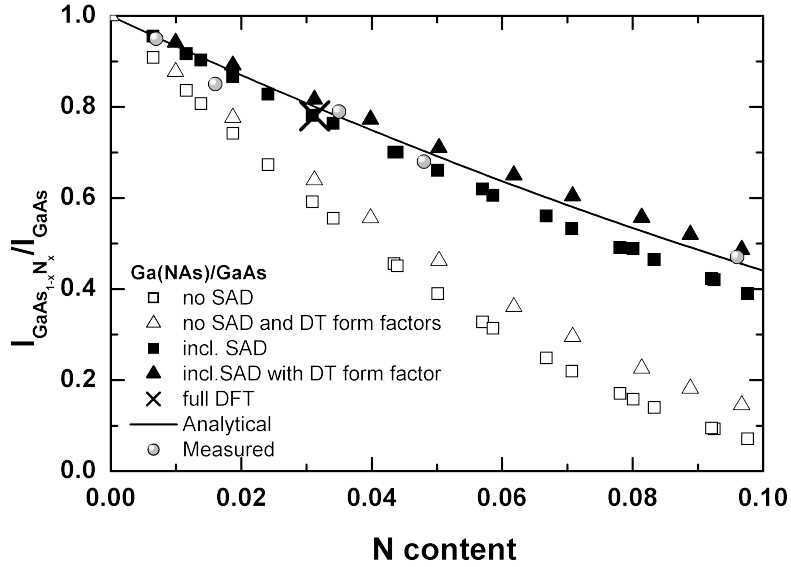


Figure 4.2.: Calculated and measured dark field 002 intensities of Ga(NAs) normalized to GaAs

### 4.3. Ga(NAs)/GaP

The Ga(NAs) ternary material system grown on GaAs is tensile strained. If it is deposited on GaP, the macroscopic strain is compressive for N content below 17.6 %. The amount of strain decreases by increasing the quantity of incorporated N. The lattice matched composition is at 17.6% of N. However, the growth of compositions having such high N content is not possible at the present time. Specific TEM samples having Ga(NAs) quantum wells with different N content up to 13% were prepared. The 002 dark field micrographs are presented in Figure 4.3. The arrow pointing downwards represents increasing N-content, while the arrow pointing upwards indicates increasing lattice mismatch of the quantum well with respect to the GaP substrate and barrier material. The structural evolution of the quantum wells with increasing N-content was investigated and a study on its effect on the optoelectronic properties was published in [81]. Figure 4.4 presents the obtained experimental intensities normalized to the GaP barrier intensity level. For the intensity ratio calculations in this case the Doyle and Turner atomic form factor values were used and the structure factor was calculated taking the static atomic displacement into account (full squares) as well as using the virtual crystal approximation (open squares). The local lattice distortion caused by the N atoms lowers the chemical sensitivity of the 002 reflection. The nitrogen content predicted by the intensity ratios of Ga(NAs) and GaP underestimated the N content approximately by a factor of two, similar to the Ga(NAs)/GaAs material system, when static atomic displacements were not taken into account.

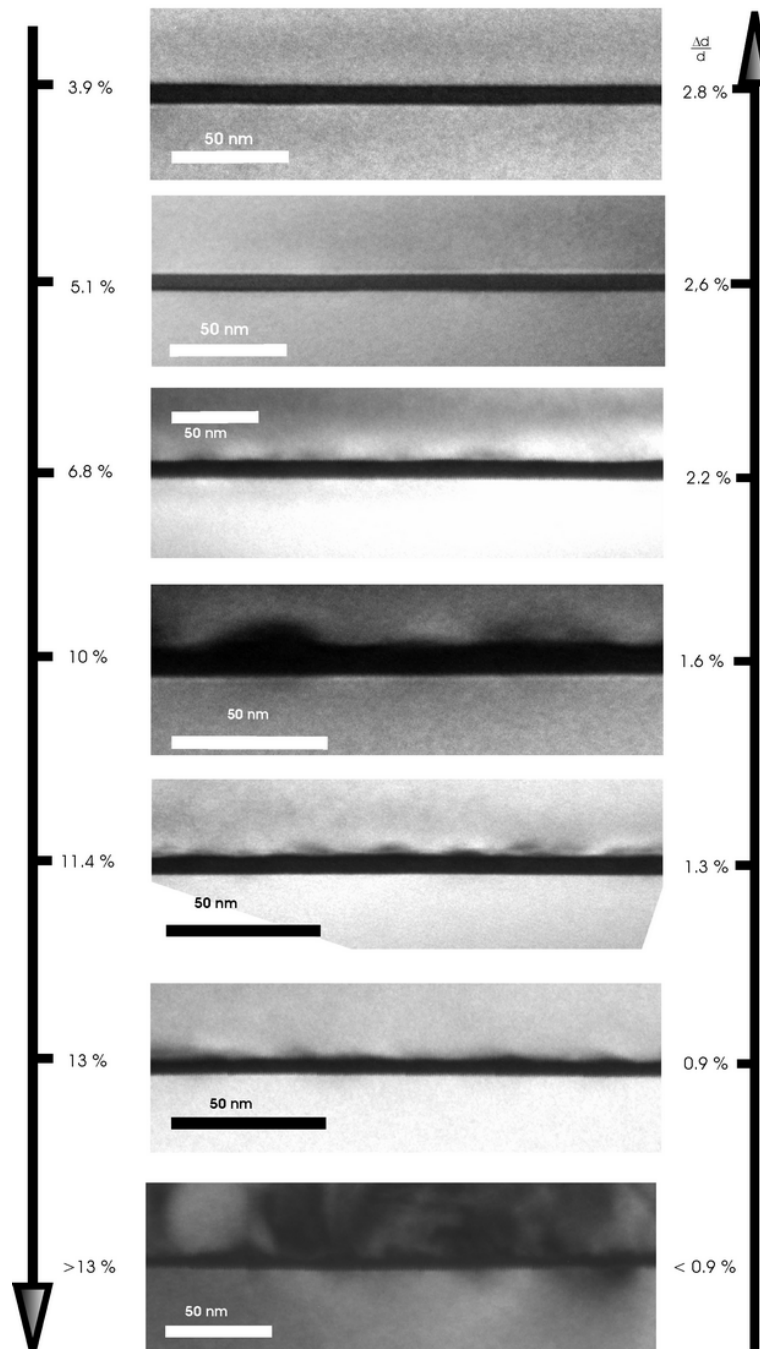


Figure 4.3.: 002 dark field micrographs of Ga(NAs) quantum wells with different N concentrations grown on GaP. The N-concentrations obtained from X-ray diffraction and the lattice mismatch is indicated on the arrows.

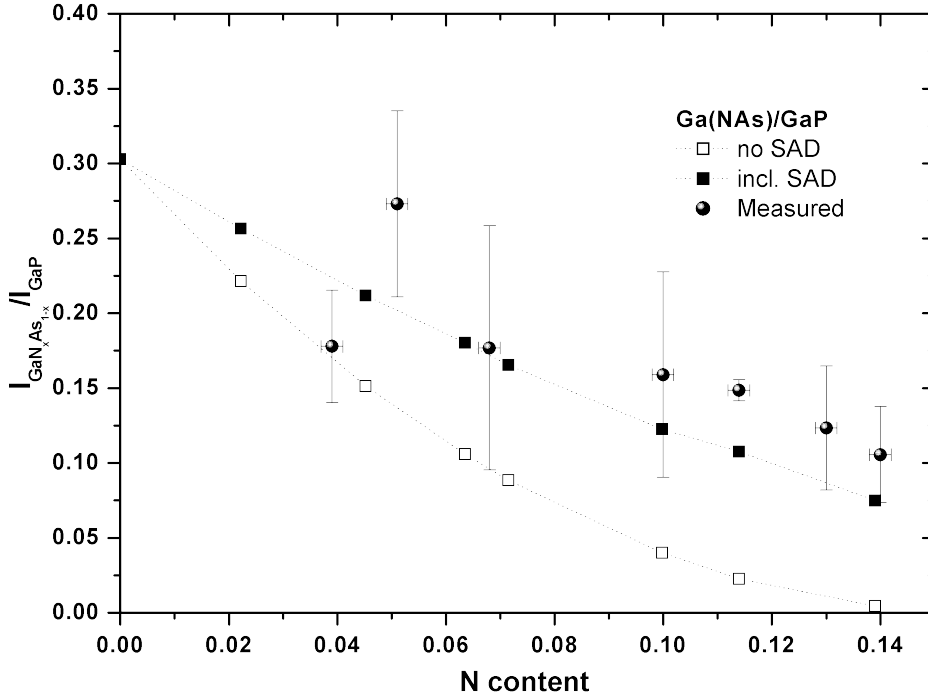


Figure 4.4.: Calculated and measured dark field 002 intensities of Ga(NAs) normalized to GaP. The atomic form factors were used from Doyle & Turner [17]. The dotted lines are guides for the eye.

#### 4.4. Ga(PAs)/GaP

The incorporation of As in the GaP host crystal is possible beyond the dilute limit. Compressively strained Ga(PAs) quantum wells were deposited on GaP with As contents up to 60.7%. The 002 dark field images of the different As-containing quantum wells are presented in Figure 4.5. As-content and compressive strain increases from top to bottom. The appearance of the dark contrast band above the quantum wells is due to foil relaxation of the cross sectional TEM sample, as described in Section 3.3.2. The intensity ratios were also derived in this case from sample regions, where the barrier was not affected by the additional intensity. The intensity ratios are plotted as a function of the X-ray composition values of P in Figure 4.6.

Figure 4.6 (a) shows the measured and calculated values of intensity ratios for the dilute limit. According to the calculations, the As impurities stretch the Ga - As bonds by a small amount. The introduced bond strain is only +2.5%, as calculated by DFT (VFF resulted +2.3%, the analytical equation +2.7%). Due to this small value of lattice distortion, the refined structure factor calculations resulted in similar

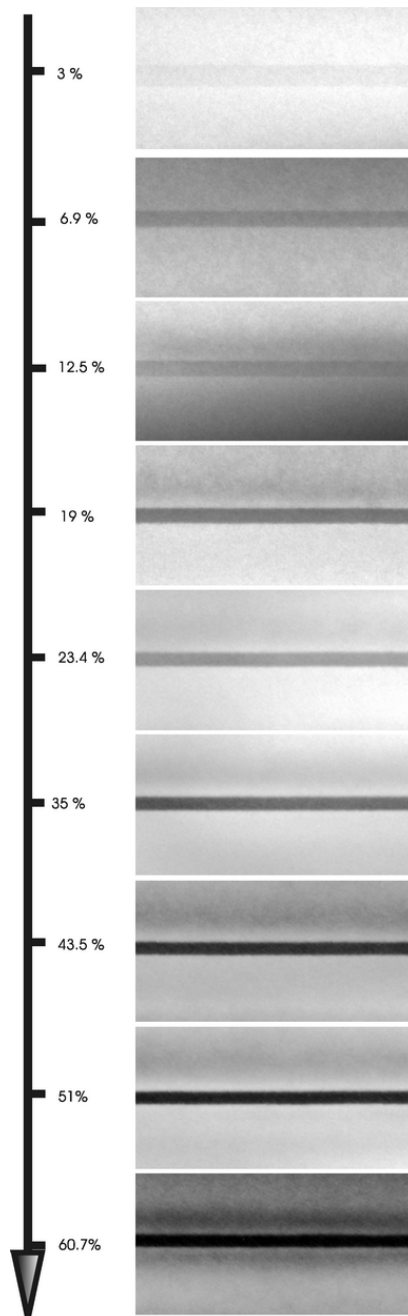


Figure 4.5.: 002 dark field micrographs of Ga(PAs)/GaP quantum wells with different As concentrations. The As-concentrations obtained from X-ray diffraction is indicated.

values to the virtual crystal approximation (open squares) and by taking the static atomic displacement into account (black squares). The VFF method predicts slightly lower values of the intensity ratios. The increase of the steepness of the intensity vs. As-composition curve was not significant. However, at dilute concentrations, the mea-

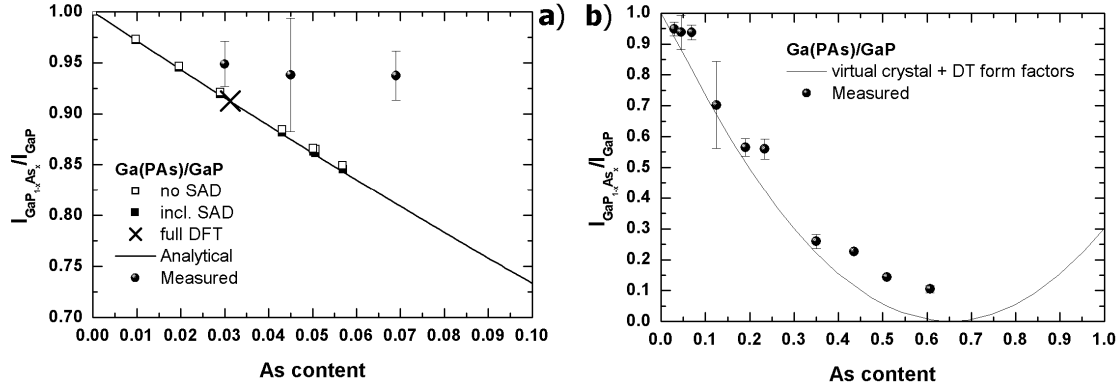


Figure 4.6.: Calculated and measured dark field intensity ratios of Ga(PAs)/GaP (a) in the dilute limit (<10% As) (b) for higher As concentration (>10% As), calculated with the virtual crystal approximation using Doyle & Turner atomic form factors.

sured values show higher intensity ratios.

The incorporation of As in GaP is possible far above dilute concentrations. The measured intensity ratios for higher As-containing quantum wells can be seen in Figure 4.6 (b). The static atomic displacement, caused by the impurity element of the mixed sublattice, cannot be interpreted as in the dilute limit. The bonds are presumably not distorted to the same extent as in the dilute limit, since the first neighbors of the impurities are affected also by the bond distortion effect of other impurities of the local environment. The effect of the bond distortion probably decreases with increasing impurity concentration. Therefore, the intensity ratios for higher concentrations can be estimated better by the virtual crystal approximation. Figure 4.6 (b) shows the intensity ratios of the virtual crystal approximation. For the calculation of the structure factors (intensity ratios) for high impurity concentration, the form factor values of the isolated atom were used, since they give also acceptable estimation.

## 4.5. (BGa)P/GaP

The incorporation of B atoms on the cation sublattice introduces tensile macroscopic strain in the material system. It is, therefore, a candidate for strain compensation in strained multi quantum well heterostructures. The 002 dark field images of the (BGa)P/GaP quantum wells are presented in Figure 4.7, with the B-content obtained from HRXRD measurements. The slightly darker contrast band in the barrier below the quantum well arises from the thin foil relaxation and associated bending of the 002 crystal planes, as described in Section 3.3.2.

The experimentally obtained intensity ratios of the (BGa)P/GaP quantum wells are shown in Figure 4.8. According to the VFF and DFT results, the B atoms distort the lattice to almost the same extent, as the nitrogen atoms. The strain they introduce

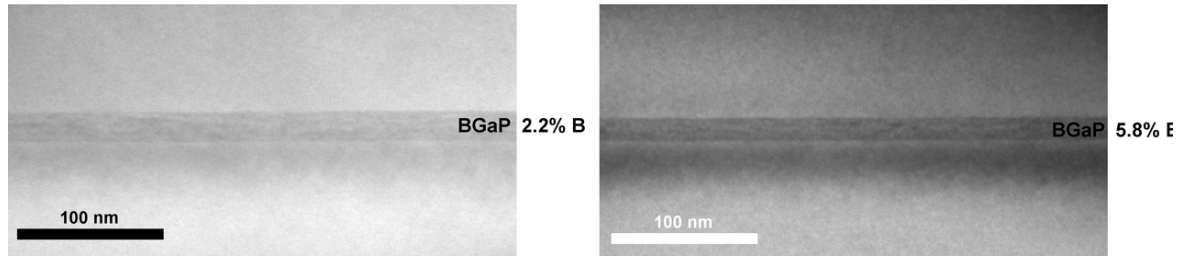


Figure 4.7.: 002 dark field micrographs of (BGa)P/GaP quantum wells with different B concentrations. The B-concentrations obtained from X-ray diffraction are indicated.

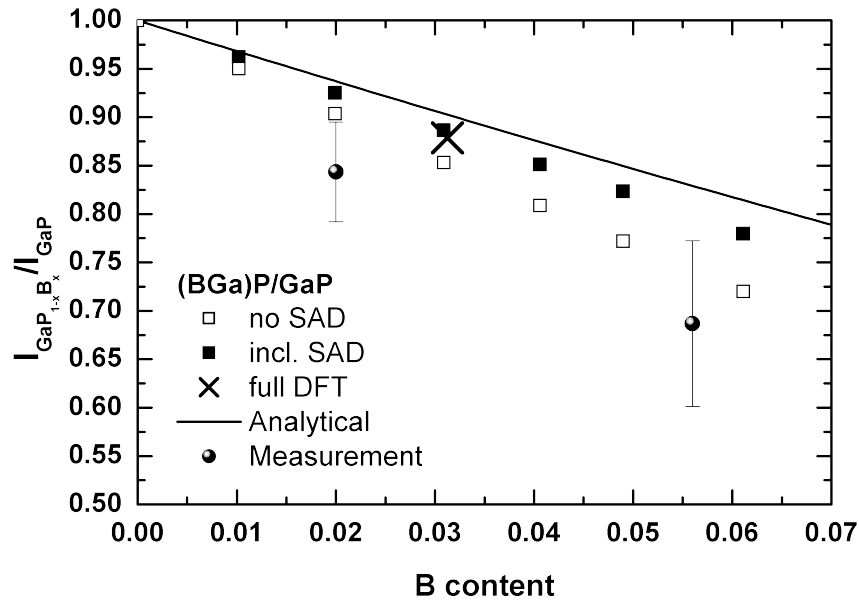


Figure 4.8.: Calculated and measured intensity ratios of (BGa)P/GaP quantum wells.

to the B-P bonds is -12.2%, determined by DFT, and -12.4% by VFF. The value of -12.2%, predicted by the simplified analytical Equation 4.6 matches the values of the previous methods. The intensity ratios obtained by the simulation methods are also included in Figure 4.8. The value of the full DFT (black cross) calculation fits the prediction of the VFF calculation with the static atomic displacement (full squares). The analytical prediction (solid line) slightly overestimates the latter intensity ratios. However, the experimental data (full circles) are closer to the intensity ratios predicted by the virtual crystal approximation (open squares). This deviation might be due to the phase separation of the (BGa)P material.

## 4.6. Ga(NP)/GaP

It was seen in the case of GaAs, that (incorporating N into the zincblende lattice,) N impurities introduce a large strain to the Ga-N bonds. The bond strain is a slightly less (-12.7% calculated by DFT, -13.2% calculated by VFF and -12.2% predicted by the analytical formula) when the host crystal is GaP. The N atoms distort the GaP lattice to a lesser extent than the GaAs due to the smaller lattice constant of the GaP. The experimental images of quantum wells with different N-composition are presented in Figure 4.9. The derived intensity ratios are included in Figure 4.10.

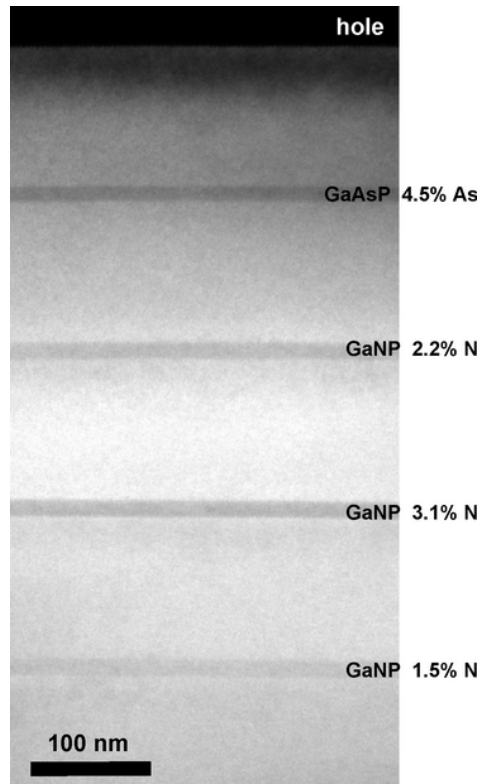


Figure 4.9.: 002 dark field micrographs of Ga(NP) quantum wells with different N concentrations. The N-concentrations obtained from X-ray diffraction is indicated. The topmost quantum well is Ga(AsP) with 4.5% As

The experimental values show an obvious decrease with increasing N-content. The intensity drops by 17 % for 4.1% N-content. In order to exclude the influence of nonproper imaging conditions, a Ga(AsP) quantum well was also grown in one of the investigated samples. The Ga(AsP) intensity was also measured and its ratio to the GaP barrier material was compared to the other measured Ga(AsP) values and structure factor predictions. The intensity ratios of the Ga(AsP) quantum well compared to values of Ga(AsP) quantum wells of other samples proved proper imaging conditions. The calculated intensity ratios show an increase with increasing N-content.

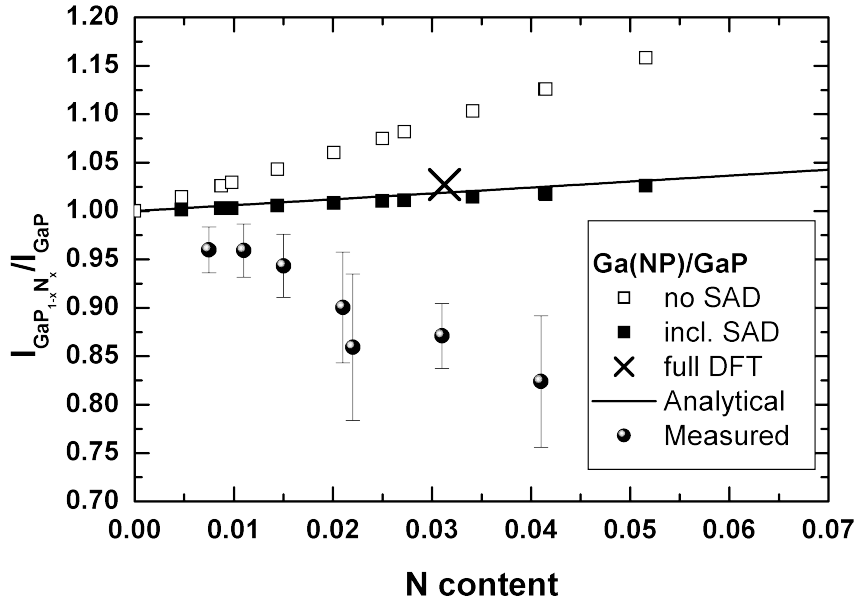


Figure 4.10.: Calculated and measured dark field 002 intensity ratios of Ga(NP) normalized to GaP

The virtual crystal approximation (open squares) predicts a steep rise of the intensity ratio vs. N-content curve. Introducing the static atomic displacement of the Ga atoms caused by the N impurities reduces the gradient. The intensity for 4.1% N is only 2% larger than the GaP intensity in comparison to 16% predicted by the virtual crystal approximation. Taking the static atomic displacement into account, the chemical sensitivity of the 002 reflection decreases strongly. To clarify the deviation of the experimental and theoretically predicted composition values, further investigations are needed for this particular material system.

#### 4.7. Ga(AsSb)/GaAs

When incorporating a smaller atom into the host crystal (Ga(NAs), (BGa)P, Ga(NP)) in dilute concentration, the lattice distortion effect of the substitutional impurities reduces the gradient of the intensity ratio vs. impurity content curve. When a larger atom is incorporated into the crystal, the bond strain is positive, and the steepness of the intensity ratio vs. impurity content increases with introducing the static atomic displacements.

Due to the ratio of the atomic form factors in Ga(AsSb), the intensity ratio curve was predicted to increase with increasing Sb-content; this increase was proven experimentally by incorporating Sb into GaAs [82].

Within the dilute limit, at low Sb-concentrations, the predicted values deviate from each other only to a small extent. The slight effect of the static atomic displacement is due to the low bond strain (5.3% calculated by DFT, 5.0% by VFF and 6.0% analytically), that the Sb introduces. The increase of the gradient of the intensity ratio vs. Sb-content curve was insignificant.

Above dilute concentrations (shown in Fig 4.11 (b)), where the analytical prediction

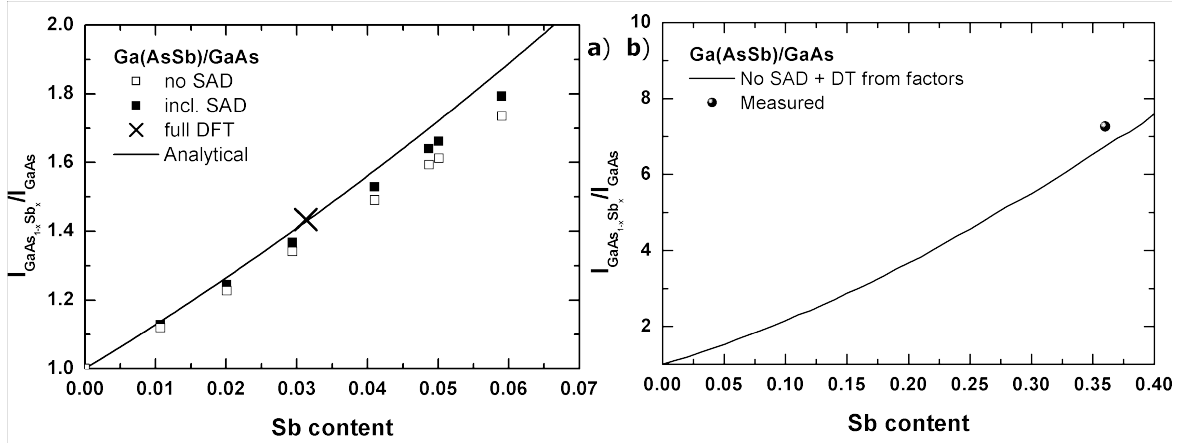


Figure 4.11.: Calculated and measured dark field 002 intensity ratios of Ga(AsSb) normalized to GaAs (a) in the dilute limit. (<7%Sb) (b) for higher Sb-concentration (>7%), calculated by virtual crystal approximation and Doyle & Turner form factors (DT).

was no longer valid and the effect of bond distortion was also negligible, the intensity ratios were estimated with the virtual crystal approximation and the form factor values of the isolated atom approximation were used. The indicated measured data point in the graph is a Ga(AsSb) quantum well with approximately 36% Sb content, far above the dilute limit.

This chapter presented experimental results of dark field image intensities of different ternary zinc blende III/V materials which form an important basis for composition quantification in mixed III/V alloys. The impurity concentration dependence of the intensity ratios made it possible to estimate the impurity content of the quantum wells. The intensity ratios of the quantum wells were calculated with different approaches. The virtual crystal approximation was found to be ineffective in the case of impurities, which introduce local lattice distortions, since the assumption of ideal lattice positions for dilute alloys underestimates the impurity concentration by a factor of two. The structure factors (the intensity ratios) were recalculated using the values of atomic form factors obtained from DFT calculations. The introduction of modified atomic form factors did not change the structure factor values significantly. For compositions above the dilute limit, the lattice distortion was weaker. The structure factor values can be estimated by the virtual crystal approximation in this case.

## 5. Heteroepitaxy and defect characterization (GaP on Si)

*This chapter presents the optimization process of GaP heteroepitaxy on the specially prepared Si (001) surfaces by the suppression of stacking faults and microtwins and the annihilation of APBs. The results are illustrated by the help of the improved TEM techniques presented in Chapter 3.*

### 5.1. Nucleation of GaP on Si

The growth of the thin GaP layers was optimized in two steps: the nucleation layer followed by the overgrowth layer. As will become apparent in the following sections, the first step is crucial with respect to the charge neutrality and the suppression of stacking faults and microtwins, the latter one is important for the annihilation of the antiphase domains. The growth of the nucleation layer was carried out after the Si-buffer growth and pretreatment (discussed in Section 3.1.2). To characterize the nucleation layers, dedicated samples were grown for this purpose. The layer thicknesses were between 1.5 - 5 nm. After removal from the reactor, surface morphology was investigated by AFM, and [1-10] cross-sectional TEM samples were prepared for High-Resolution TEM imaging. The nucleation studies were carried out on the “not-optimized” Si-surface (Figure 3.2 (b)). This, however, has no influence on the structure of the first few monolayers of GaP grown on this substrate.

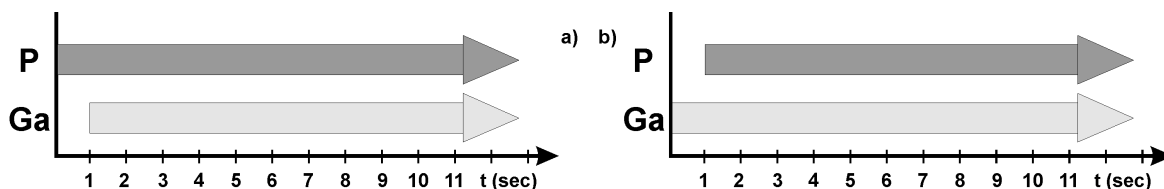


Figure 5.1.: Growth sequence of GaP nucleation layers. Role of the first monolayer: (a) the growth is started by opening the P source for 1 second and then Ga source was opened, (b) the growth is started by opening the Ga-source, and the P source was opened after 1 second.

### Role of the first monolayer

For growing a polar material on non-polar substrate, the first deposited monolayer may determine the local charge neutrality of the interface, as described in Chapter 2. To study the dependence of morphology, which is influenced by charge neutrality, on growth conditions, the following experiments were carried out: thin GaP nucleation layers were grown for 13 second growth time, but different metalorganic sources were opened first at the beginning of the growth. Figure 5.1 shows the temporal course of the growth: the growth was started by opening the P-source and the Ga-source was opened only after a second. Further growth took place by continuous operation of the sources (Figure 5.1 (a)). The other possibility is shown in Figure 5.1 (b), where the growth was started by opening the Ga-source, and the P-source was opened after one second of growth.

The effect of the different first monolayers on morphology are summarized in Figure 5.2. The surface morphology characterized by AFM, and the crystal structure characterized by cross sectional HRTEM, was compared: Figures 5.2 (a) and 5.2 (b) show the nucleation layers started with the P source (TBP), while (c) and (d) show layers started with the Ga precursor (TEGa). The results for different growth temperatures are also included in Figure 5.2. The images of the left column show the layers deposited at 450°C, while the growth temperature of the layers in the right column was 400°C.

The AFM images show island-like morphology in all cases: the characteristic underlying Si surface is not observable any more; 10-20 nm wide GaP islands with the height up to 3 nm are nucleated on the Si surface. AFM results suggest that layers started with the P source opened first have a smoother surface morphology. The layer deposited at lower temperature also seemed smoother than the equivalent Ga-first film.

The latter phenomenon may be due to the fact that the precursors have a lower cracking efficiency at such a low temperature (400°C), therefore the growth rate also decreases with decreasing temperature. Due to the lower growth rate, less material was deposited. This was confirmed by the cross sectional HRTEM measurements. The main result of the crystal structural investigations was that, irrespective of the first species lead into the reactor and irrespective of the growth temperature, the GaP was nucleated in 3D islands. The nucleation layer was not continuous, the island structure of the GaP is clearly observable on the cross sectional high resolution micrographs in Figure 5.2 (a)-(d). The upper HRTEM image of the nucleation layers show the GaP islands at very thin TEM foil regions. The real lateral size of the islands is 5 to 10 nm. These island sizes are smaller than the ones measured by AFM. This is due to the limited lateral resolution and the result of the AFM tip - surface geometry described in Section 3.2.1. At the thin cross section regions (upper HRTEM images), it can be seen that the islands are not coalesced.

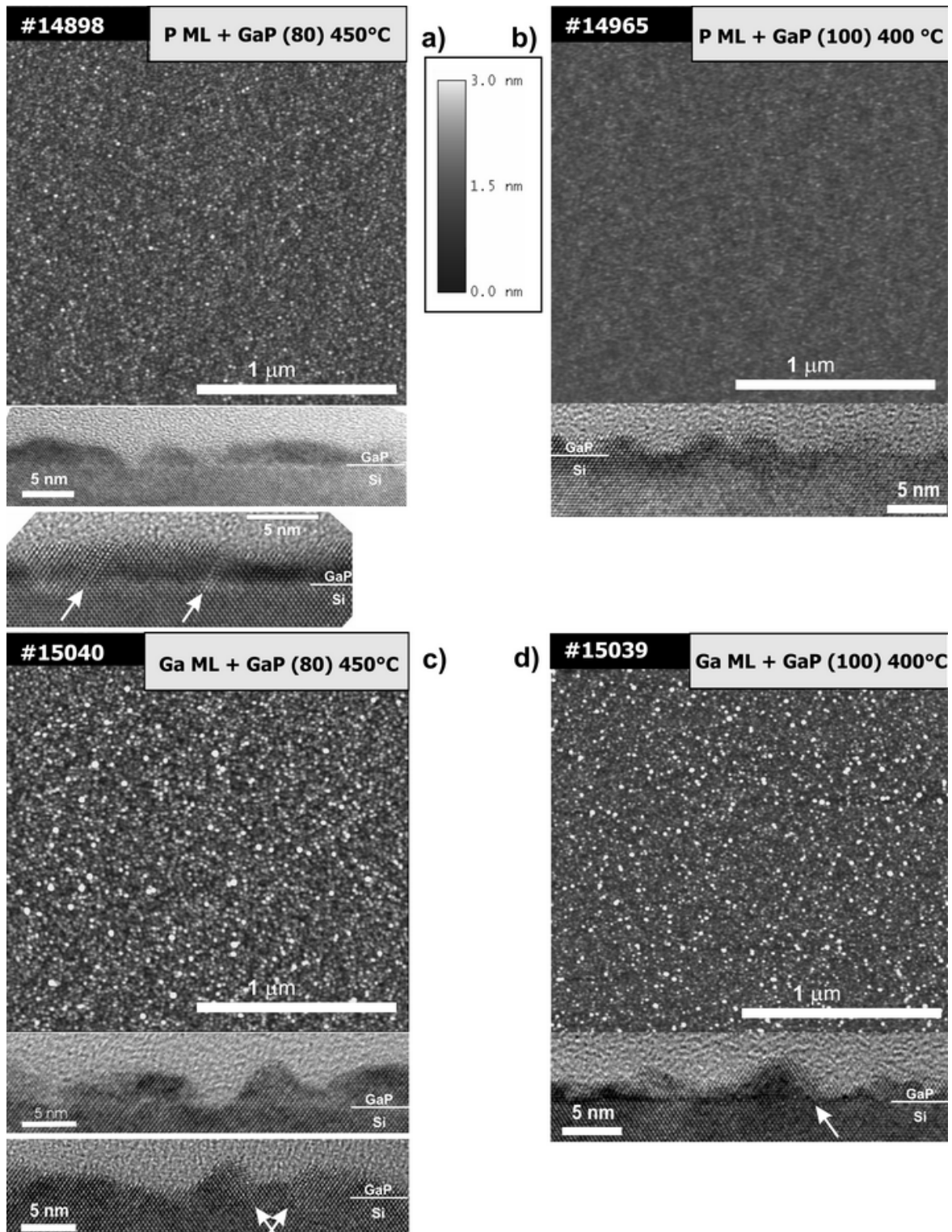


Figure 5.2.: GaP nucleation layers: Role of the first monolayer. AFM (upper) and HRTEM (lower) images of GaP layers deposited with different first monolayer at different temperatures: Layers grown by starting with the P source (a) at  $T_{growth} = 450^{\circ}\text{C}$  (#14898). (b)  $T_{growth} = 400^{\circ}\text{C}$  (#14965). GaP nucleation layers grown by opening the Ga source first: (c) at  $T_{growth} = 450^{\circ}\text{C}$  (#15040), (d) at  $T_{growth} = 400^{\circ}\text{C}$  (#15039). The GaP/Si interfaces are marked in the HRTEM micrographs.

Another important result of the crystal structure analysis is the observation of the formation of two kinds of planar defects already at this initial stage of GaP growth: stacking faults and microtwins. They are shown with white arrows on the lower HRTEM images of Fig 5.2 (a) and (c). More analysis on stacking fault and microtwin formation and their evolution can be found in Section 5.6.

The existence of stacking faults and microtwins in the as-grown layer clarifies that these types of planar defects do not originate from the overgrowth process, but are already incorporated during the very first monolayers of growth.

The comparative study of the morphology by AFM and the crystal structure by HRTEM showed that the first monolayer (the precursor that was led into reactor first) had a minor effect on the surface morphology: the layers started with the P source resulted in slightly smoother nucleation layers. Comparing the crystal structure of the layers by HRTEM, they were similar: irrespective of the first monolayer, the GaP was nucleated in 3D islands, which can be a sign of charge neutrality not being fulfilled under these nucleation conditions. Stacking faults and microtwins were observed in the growing islands.

### **Annealing of the nucleation layer**

Since the overgrowth of the nucleation layers is carried out at a significantly higher temperature (up to 675°C in comparison to 400-450°C), effect of the high temperature step on the nucleation layers was investigated. A combined AFM - HRTEM study was carried out, with the results shown in Figure 5.3. The first column in Figure 5.3 (a) depicts micrographs of the nucleation layer. It was deposited at 450°C with first monolayer of P. This layer was in-situ annealed in the reactor for 1 sec at 675°C under TBP stabilization. It can be seen that the layer underwent some distortion: smoother platforms and development of trenches were observed. (Figure 5.3 b)). Though the morphology does not exactly reflect the underlying Si-surface, a triangular patterning can be observed. As one compares the HRTEM images, the same can be seen on 5.3 (d), lower image: the island tops became smoother compared to the as-grown layers, but the separation between the islands is increased (shown by the black arrows).

The influence of the nucleation conditions on stacking fault and microtwin formation and the way of their suppression is discussed in the following section.

### **Role of the growth sequence**

It was shown previously, that the GaP was nucleated in the form of islands in the investigated growth parameter space, and the density of stacking faults was very high. Given an average separation distance of 20 nm between stacking faults, and assuming the maximal TEM foil thickness to be 20 nm, the estimated planar defect density is larger than  $10^{11}/cm^2$ . The following study shows how the stacking faults and mi-

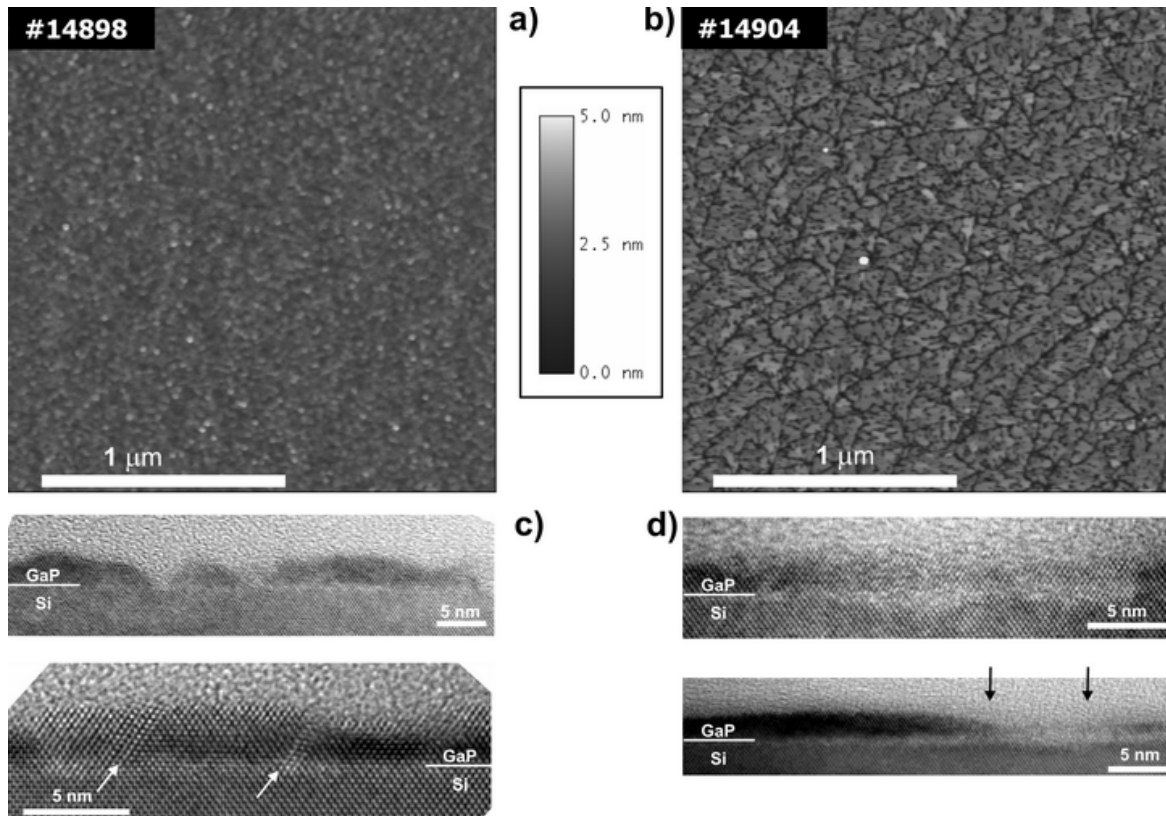


Figure 5.3.: Annealing effect: AFM and HRTEM images of GaP nucleation layers.  $P/Ga=80$ ;  $T_{nucleation}=450$  °C; the used Si surface is the not optimized one. The left column (a), (c) shows the as-grown layer, while the right column (b), (d) shows the layer after 1 sec annealing at 675 °C

cro twins were suppressed and a stacking fault and microtwin free 2D nucleation layer was realized.

The study compares different growth modes. The difference in the growth sequence is illustrated in Figure 5.4.

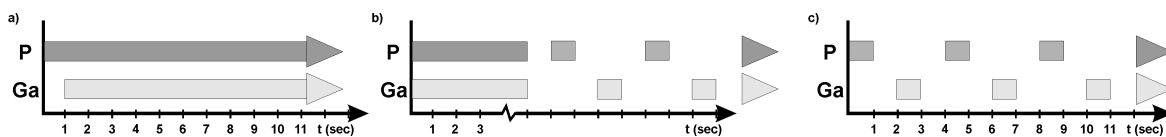


Figure 5.4.: Growth sequence of GaP nucleation layers. (a) continuous growth, (b) combined growth, (c) Flow Rate Modulated Epitaxy (FME).

The investigated growth modes were the following:

*Continuous growth*: the growth was carried out by opening one of the sources first and, after one second, opening the other one. According to the slightly smoother morphology, when growing with a P-first monolayer, in this study the P-source was opened first, followed by the Ga (Figure 5.4 (a)). This growth mode was used in the

experiments of the former paragraphs already.

*Combined growth:* the first monolayers were deposited by continuous growth as described previously, then the following monolayers were deposited with pulsed TBP and TEGa flow: the P-source was opened for one second, then all sources were closed for one second (growth interruption, (GI)), the Ga-source was opened for one second and followed by one second growth interruption. This sequence was repeated throughout the rest of the growth (Figure 5.4 (b)).

*Flow-Rate Modulated Epitaxy (FME):* the pulsed TBP and TEGa flow was carried out during the whole growth time (Figure 5.4 (c)). For specific experiments the first monolayer was Ga. In this case the role of the first monolayer (Ga or P) was also studied.

The results of the different growth sequences on the GaP surface morphology and the crystal structure are summarized in Figure 5.5.

Comparing the surface morphology of a continuously grown layer with one deposited using the combined sequence, (Figure 5.5 (a) vs. Figure 5.5 (b)), the latter exhibited smoother morphology. This was a combined effect of lower growth rate due lower growth temperature, smooth nucleation layer as is apparent from the HRTEM micrographs. Referring to the HRTEM images of the different nucleation layers (Figure 5.5 (c) vs. Figure 5.5 (d)), the layer with the combined-sequence appeared to be thinner, but almost continuous; the lateral size of the islands was larger than for the continuous growth, greater than 10 nm. As the HRTEM images show, it can be characterized as a two dimensional continuous layer with greater surface undulation.

Observing the layer grown by completely alternating growth sequence (FME) by AFM (Figure 5.5 (e)), the surface morphology was rougher than both the combined-grown and the continuously-grown film. The grain-like features on the surface are higher (their height exceeds 5 nm) and have larger lateral dimensions (up to 70 nm) as well. This is a crucial point at the optimization of the overgrown layers: despite the higher surface undulation, the layer is perfect single crystalline and continuous, without stacking faults or microtwins. HRTEM images prove this: Figure 5.5 (f) was taken from the layer between the grains. Monolithic crystalline material was deposited, and continuously covered the Si substrate in 3 nm thickness. Figure 5.5 (g) is a HRTEM image taken from an island: the GaP island on the top of the continuous layer was also perfectly single crystalline.

It was shown in this section, that the prominent planar defects of the heteroepitaxial GaP layers grown on Si (the stacking faults and microtwins) originate from the inappropriate nucleation of the first monolayers of the epitaxial layer. As shown by the HRTEM analysis, the stacking faults and microtwins were suppressed by depositing the nucleation layer using Flow Rate Modulated Epitaxy, resulting in a continuous, two dimensional single crystalline layer. Generation of the other type of planar defects, the antiphase domain, depends on the step structure of the Si surface. The APB structure, its correlation with the Si surface morphology, and the mechanisms of

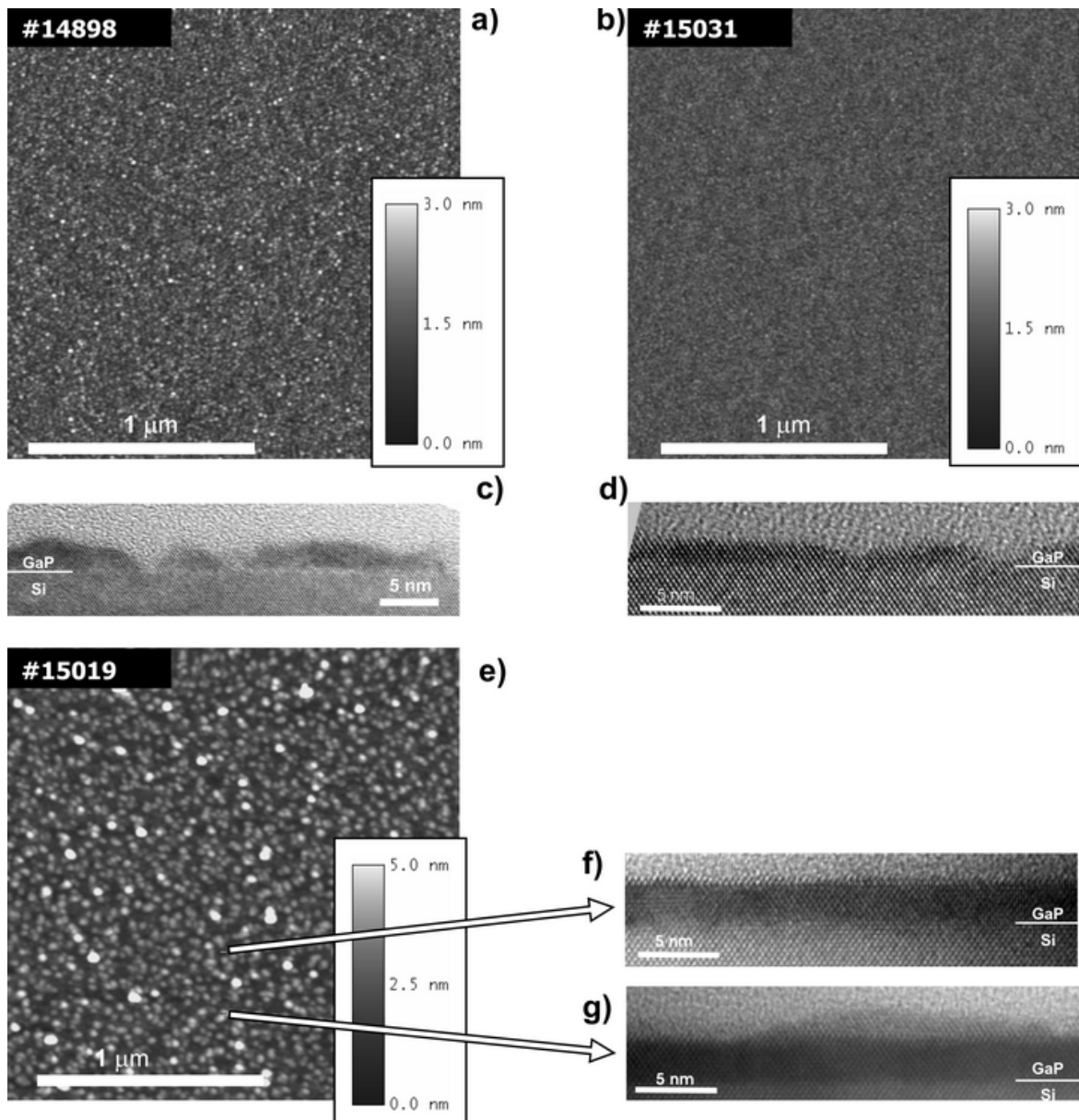


Figure 5.5.: Role of the GaP growth sequence: AFM images of nucleation layers with different growth sequences: (a) continuous growth: (#14898).  $P/Ga=80$ ;  $T_{nucleation}=450$  °C, (b) “combined” nucleation:  $T_{nucleation}=400$  °C,  $P/Ga=100/80$  (#15031) (e) Flow Rate Modulated Epitaxy (FME) at  $T_{nucleation}=450$  °C (#15019) HRTEM images: (c), (d) show the nucleated GaP island in continuous and combined nucleation mode. The HRTEM images of the FME nucleated GaP layer (f) shows the continuous single crystalline layer, between the surface islands and (g) single crystalline islands on the top of the continuous layer.

APB-annihilation are discussed in the following sections.

## 5.2. The structure of APBs

This section presents the results of the structural analysis of the types of APBs present in the heteroepitaxial GaP/Si material system.

Antiphase domains form at the deposition of the first monolayers during the heteroepitaxial process. Section 2.2.2 presented the possible formation mechanisms of antiphase boundaries and domains.

The APBs can develop on different crystallographic planes as shown in Figure 2.4. In the following, the antiphase boundary structures, detected in the GaP layers grown on Si in this study, will be presented, irrespective of their origin, but concentrating on which crystallographic plane they develop. The conventional and improved TEM techniques used for the characterization were described in Section 3.2. Though different planes of the zincblende structure can be affected by antiphase disorder (Figure 2.4), the most prominent types are the stoichiometric  $\{110\}$  APB and the non-stoichiometric  $\{111\}$ .

### 5.2.1. The stoichiometric $\{110\}$ APB

As the crystal model of the stoichiometric  $\{110\}$  APB (Figure 2.3 (a) or (b)) shows, the APB lays on one of the  $\{110\}$  planes. The APB can be observed in cross sectional TEM only if it is “edge-on”. Figure 5.6 (a) is a cross sectional HRTEM image of a stoichiometric  $\{110\}$  APB penetrating through the whole layer starting from the Si surface and reaching the GaP surface. As it is described in Section 3.2, the contrast of the atomic columns does not give information of the orientation of the crystal. The upward or downward orientation of the GaP dumbbells cannot be resolved in the used experimental setup. Figure 5.6 (b) is a magnified section of the APB region in (a). The left and right part of the image is separated by the APB. The fact that this crystal defect is an APB was also confirmed by the multislice simulation of the HRTEM images. The method was described in Section 3.2. In Figure 5.6 (c), a selected image from the complete defocus-thickness image series is shown. A shift between the atomic layers in  $[001]$  on the two sides of the defect can be seen and is marked with white arrows. The extent of the shift was  $a/4$ , a value corresponding to one monolayer. There was an observable shift in the bright contrast points in the experimental images as well. The bright contrast points can be associated either with the projection of the atomic columns, or with the space in between. In either case, the lattice was shifted in the  $[001]$  direction. The agreement between the simulated structure of an  $\{110\}$  antiphase boundary and the experimental image proves that this planar defect is an antiphase

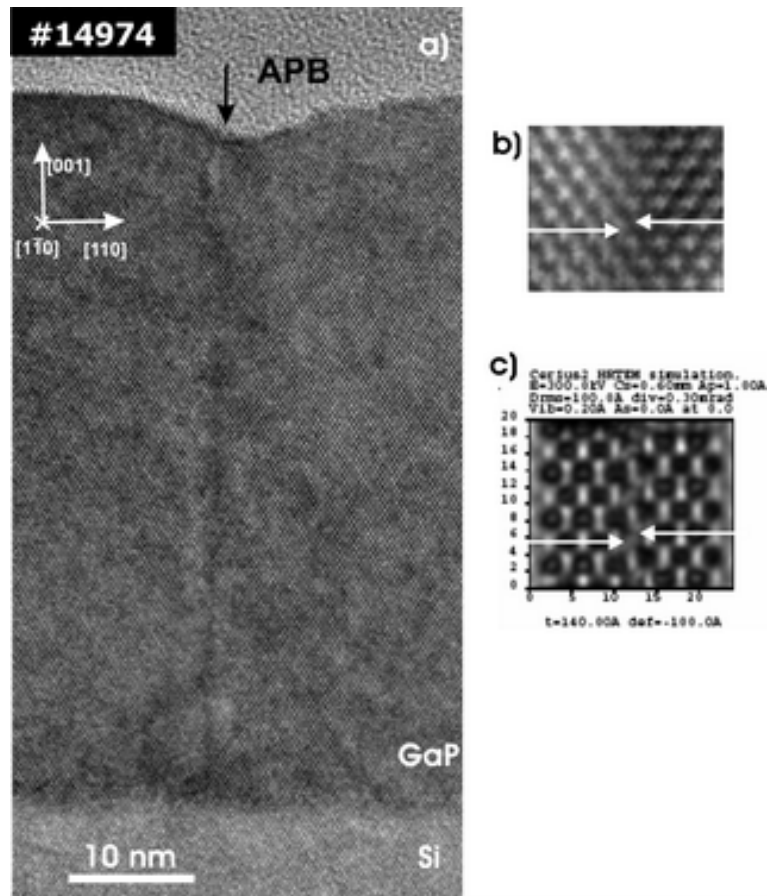


Figure 5.6.: (a) High resolution TEM image of a type  $\{110\}$  antiphase boundary indicated by the black arrow. The APB penetrates through the whole layer. (b) a zoomed image of (a), (c) simulated HRTEM image of an APB with 14 nm sample thickness and -10 nm defocus. The white arrows on both the experimental image and on the simulated one indicate the shifted monolayers of the binary material on the two sides of the APB. (#14974)

boundary. The crystal regions on the two sides of the boundary are antiphase domains. The limited resolution of HRTEM was insufficient to directly measure the relaxation of the Ga - Ga and P - P false bonds. The experimental results of Cohen and Carter [83] concerning rigid-body lattice translation show that the length of the Ga - Ga bonds was extended by 8%, and the length of the P - P bonds was contracted by 4% compared to bond length of the GaP crystal.

The same type of crystal defect was investigated using the dark field image pair technique using either the  $111/\bar{1}\bar{1}\bar{1}$  or the  $002/00\bar{2}$  reflections. The techniques were introduced on this specific type of antiphase boundary, as described in Section 3.2 and illustrated in Figure 3.13.

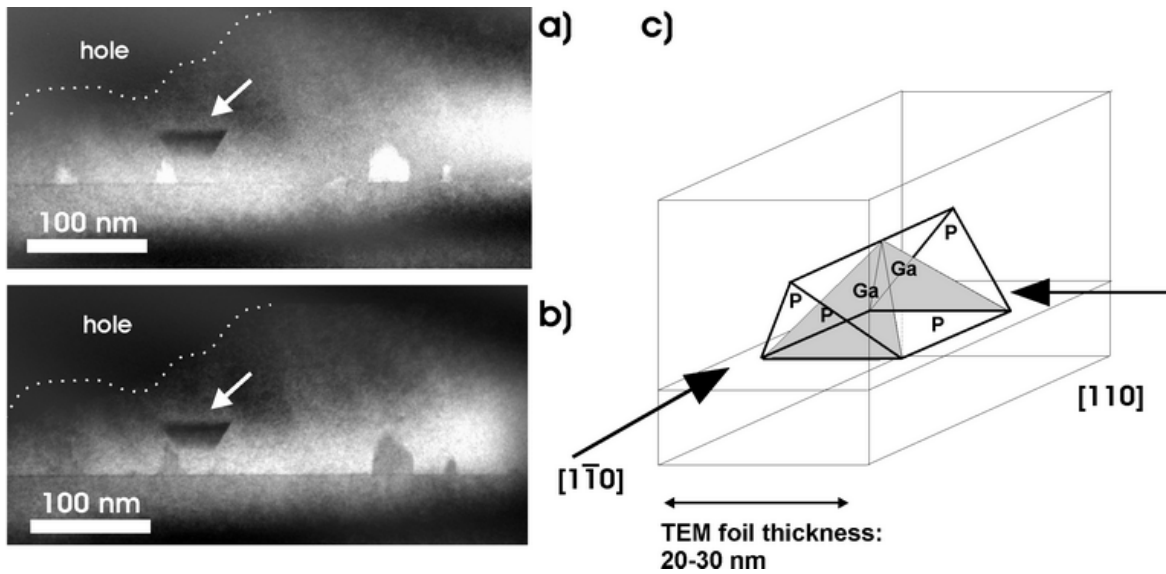


Figure 5.7.: Self annihilating antiphase domains in GaP. (a) 111 and (b)  $\bar{1}\bar{1}\bar{1}$  dark field images taken along the  $[1\bar{1}0]$  zone axis. The APDs can be identified by their altering contrast on the two images. The white arrows depict a stacking fault. (c) is a geometrical model of a self annihilating APD buried in the TEM foil. The differently terminated  $\{111\}$  planes are marked with name of the element.

### 5.2.2. The non-stoichiometric $\{111\}$ APB

The crystal model of a non-stoichiometric  $\{111\}$  antiphase boundary was presented in Figure 2.5 (a) and (b). The experimental proof for its existence in the material system was supported by the proper dark field imaging techniques.

Dark field imaging using the 111/ $\bar{1}\bar{1}\bar{1}$  diffracted beams revealed antiphase boundaries laying on the  $\{111\}$  planes (Figure 5.7). The image pair on the left was taken from the thinnest, still suitable, part of the TEM foil. The dotted white line marks the edge of the TEM foil. The triangular shaped annihilating antiphase domains change their contrast on the two dark field images. The largest self-annihilating APD on the right starts to develop on the  $\{110\}$  planes, perpendicular to the GaP-Si interface but, after 10 nm of growth, the boundaries incline towards each other onto the  $\{111\}$  planes and at  $\sim 40$  nm of height they meet and self annihilate. This kinking phenomenon and the growth conditions leading to self-annihilation will be discussed in Section 5.4.

Staying at the structure of the self-annihilating APDs, more can be learned about the schematic spatial geometrical model of a self-annihilating APD bordered by  $\{111\}$  type of APBs. The model is shown in Figure 5.7 (c). The model presents an antiphase domain with of a small lateral size. From one sideview (the observation direction shown as  $[1\bar{1}0]$  on the image) the APD is bordered by two APBs laying on two  $\{111\}$  planes inclined towards each other and also intersecting each other and self-annihilating. That was observed by HRTEM and dark field imaging. Looking at the APD from a perpendicular direction (shown as  $[110]$  on the image), the APD is bordered by APBs

laying on such  $\{111\}$  planes that are inclined away from each other if one assumes, that the antiphase boundaries always consist of the same atomic species of Ga or P as depicted in Figure 5.7 (c). The APD appears from this direction to be trapezoid-like with the shorter base at the bottom. This side view of a self-annihilating APD was not observed in the case of small 15-20 nm wide APDs. The reason is the following:

To see the contrast change from the other sideview (from the  $[110]$  on the image), the foil should be prepared so, that the surfaces of the wedge shaped TEM foil cut out a part of the APD. TEM foils are typically thicker than 15-20 nm, i.e. the width of the APD seen from the  $[1\bar{1}0]$  direction, the TEM foil prepared in the  $[110]$  direction, therefore, never contains solely anti-phased material. As seen on the diagram, if a TEM foil is prepared from the other side view of the APD, it contains material from both phases. Although the scattered electron beam carries the information from both phases, it integrates through the sample, and the information cannot be unambiguously separated.

If the APBs are built up from different species, the APD looks like a pyramid, as shown also in Figure 5.7 (c). These APBs consist of one species of Ga - Ga bonds on one pair of  $\{111\}$  planes and they consist of P - P bonds on the other pair of  $\{111\}$  planes.

The feature marked with white arrows in Figure 5.7 (a) and (b) was not an APD. Its contrast was not reversed between inside and outside like the APD's. The feature originated from a single point at the interface. The contrast in this part of image arises from a stacking fault, that was intersected by the TEM foil. More on the detection of such stacking faults and their behavior will be discussed in Section 5.6.

### 5.3. Correlation between APD structure and Si surface

In the former section, the structure of the antiphase domains was discussed, irrespective of whether they originated from Si monosteps, or from non-uniformity of the first deposited GaP layer. Experimental images were presented, showing the antiphase domains and boundaries from the "sideview". The lateral structure of the APDs, how they pattern the deposited GaP material and how they correlate with the underlying Si-surface monostep morphology will be discussed in this section.

In order to build up a full understanding of the APD structure of the deposited GaP layers, the following was considered:

- The morphology and step structure of the Si surface. This was determined by AFM of the homoepitaxial Si layers.
- The proof of the existence of APDs by dark field image pairs (using either the  $\{002\}$  or  $\{111\}$  technique).

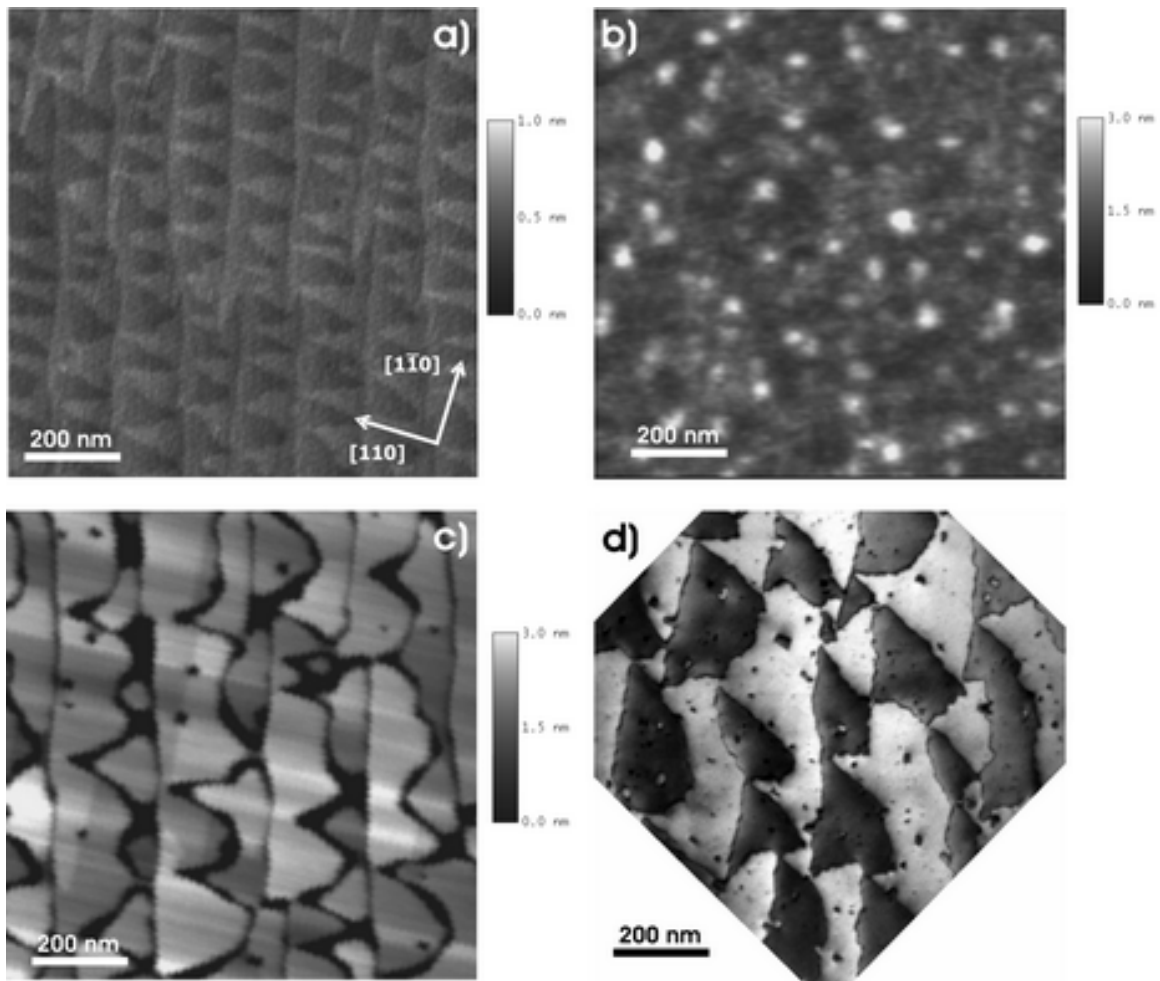


Figure 5.8.: A comparative study of the Si surface, the GaP surface and the lateral patterning of the APDs in the GaP. AFM images are: (a) the “not optimized” Si surface, where the parallel and “sawtooth-like” lines are the monolayer high steps of the surface; (b) the surface of the as-grown 57 nm thick GaP layer; (c) the surface of the same GaP layer after post-growth annealing: the plateaus smoothed, but became separated by 3-4 nm deep trenches. A plan view TEM micrograph of the same GaP sample is shown in (d). The contrast corresponds to the polarity of the crystal. The image compared with (a) proves, that the lateral patterning of the APBs follows the monostep morphology of the Si-surface.

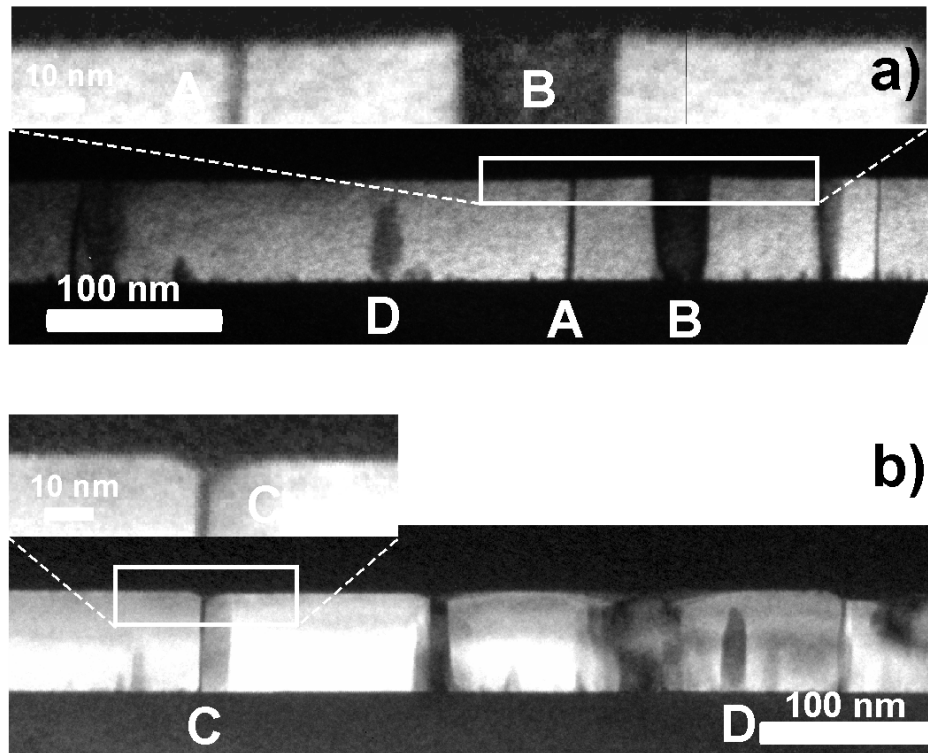


Figure 5.9.: Comparison of an as-grown and an annealed GaP layer containing APBs which penetrate through the whole layer and reach the surface. Dark field 002 images of (a) the as-grown and (b) the annealed sample. The trenches are observable on the second one, where the APBs reach the surface.

- The APB structure and the crystallographic planes, they lie on. This information was obtained from HRTEM and from the dark field image pairs.
- The morphology of the deposited and thermally annealed GaP surface determined by AFM. This is routinely the first information to be obtained from a newly grown layer, and can provide indications concerning the development of antiphase domains, as will be discussed later.
- Plan view TEM measurements reveal the information, how the antiphase structure looks like from the top. The information content of such images was described in Section 3.3.3.

The investigated GaP layers were deposited on both “not-optimized” and “optimized” Si surfaces. The “not-optimized” surfaces had a slight miscut in arbitrary directions and consisted of monolayer high steps (as seen in Figure 3.2 (b)), while the normal the “optimized” surfaces were misoriented slightly towards a  $\langle 110 \rangle$  direction and were decorated mainly with double stepped terraces (as seen in Figure 3.2 (d)).

Correlation between the underlying Si surface and the lateral patterning of the GaP antiphase domains can be determined when the APBs run in the growth direction: the

stoichiometric  $\{110\}$  APBs are of this type (described in more detail in the previous section). It can be shown that these APBs mainly arise at low growth temperature of the GaP layer. Hence, to correlate the APD structure with the Si surface terrace structure, the growth temperature was kept at 450°C.

Figure 5.8 shows the results of a combined AFM-plan view TEM study of the underlying Si surface morphology and the lateral structure of the APDs in the GaP. Figure 5.8 (a) is an AFM image of a “not-optimized” Si surface. The almost parallel lines running vertically in the image, and the “sawtooth” shaped features pointing to the left with their tips, are the monolayer high down-step edges of the Si surface. The second AFM image shows the surface of a 57 nm thick GaP layer, with undulation of the surface in the range of 2-3 nm, and containing grain-like features of 20 to 30 nm diameter. No monolayer or double layer high steps were recognized. From this image it is not possible to draw any conclusion concerning the APD morphology.

Post-growth annealing has a smoothening effect on the surface of the GaP. To exploit this effect, the 57 nm thick GaP layer was also thermally annealed. The result of annealing at 675°C for 10 minutes is seen in Figure 5.8 (c). Smoothened terraces were separated by deep trenches. The trench depth was 3-5 nm and the width was between 5-20 nm. If one compares this AFM image with Figure 5.8 (a), the similarity of the morphology is obvious. It can be inferred from this comparison that the trench morphology of the annealed GaP layer reflects the original monostep structure of the Si surface. If the trenches were located above the monostep edges of the Si surface, and the main type of APBs in the material is type  $\{110\}$ , running in the growth direction, the trenches should indicate the locations of antiphase domains.

To verify that the GaP crystal areas separated by the trenches were really in antiphase relation to each other, plan view TEM investigation was carried out. Figure 5.8 (d) is a dark field TEM micrograph, taken with the (020) reflection, with the special excitation conditions described in Section 3.3.1 to make the antiphase domains visible. The contour shape was similar to the trench structure of the annealed GaP surface and to the monosteped Si surface. The bright-dark contrast change on the sides of the terrace contour indicated that the domains on the different sides of the boundary were of different polarity. The contrast change of the dark field plan view image proves that the lateral structure of the antiphase domains follow the morphology of the monosteped Si surface.

Comparing these AFM images with cross sectional TEM images of the same GaP layer, the existence of  $\{110\}$  APBs was proven. The corresponding dark field images are shown in Figure 5.9. The vertical lines on the micrographs are  $\{110\}$  APBs penetrating through the whole layer and reaching the surface. The two images compare the as-grown layer with the annealed layer. In the as-grown layer (Figure 5.9 (a)) can be seen, that the surface is not undulated above the APB (marked with **A** and zoomed image) which was separated laterally from other  $\{110\}$  APBs more than 30 nm. Above a  $\{110\}$  APB in the annealed layer (marked with **C** in Figure 5.9 (b) and

showed on a zoomed image) a 4 nm deep trench is observable. This is a further proof that trenches develop, where the  $\{110\}$  APBs reach the surface, during annealing.

The fact that the material upon annealing simply “leaves” the locations where an APB intersects the surface is possibly due to the lower bonding energy of the P - P and Ga - Ga false bonds. These bonds can break up easier than bonds in the perfect crystal, and hence atoms with false bonds are easier to evaporate.

It was shown in the last part that APBs originate from the monosteps of the Si surface, and the lateral patterning of the developing APD structure reflects the morphology of the step edges of the monolayer high Si terraces. There were some more phenomena left to clarify: in Figure 5.8 (c) black spots of 20-30 nm diameter were observed, corresponding to 3-4 nm deep “dips” on the annealed GaP surface. The plan view (Figure 5.8 (d)) image also shows contrast change in narrow domains within the bigger domains, following the Si terrace structure. Those small APDs are 20-30 nm wide and column-shaped. It is possible that the grain-like undulation on the as-grown GaP layer (the white spots in Fig (5.8 (b)) correspond to the buried 20-30 nm broad, column-like APDs. The cross sectional image of the as-grown layer (Figure 5.9 (a)) shows a narrow APD (marked with **B**). The surface was undulated above this narrow APD by a 1-3 nm.

Hence, the  $\{110\}$  APBs do not exclusively develop on the down-step edges of the monolayer high stepped Si surface, but also on the Si terraces. There are two possibilities for the generation of APBs on the Si surface terraces:

The APBs form on 10-30 nm wide one monolayer high islands or one monolayer deep dips on the Si terraces. The reason why these islands or dips were not detected on the AFM images of the Si surface is the finite lateral resolution of the AFM tip.

The other possibility is that the surface of the Si terrace was atomically smooth, as the AFM measurements indicate. The APBs originate from non-continuous Ga or P coverage in the very first atomic layer, as shown on the model in Figure 2.3 (a). The evolution of this type of APD is discussed in the next section.

In the study described above, the lateral structure of the antiphase domains of GaP was correlated with the monostep structure of the underlying Si surface. Beyond this correlation, a simple and fast analysis method was found to detect whether the overgrown GaP layer is single phased immediately below its surface. Instead of the direct but experimentally problematic method of plan view TEM investigations, a combination of post growth annealing and a routine AFM measurement can yield the same information. If the surface of the annealed GaP sample was smoothed, but did not become decorated with trenches, the GaP crystal is single phased in the upper part of the thin layer.

The “not-optimized” Si surface was used for the experiments described up to now. Overgrowth experiments of GaP and analysis of antiphase patterning on the “optimized” double-stepped Si surface were also carried out. Figure 5.10 (a) is the AFM image and (b) is a plan view dark field 020 micrograph of a GaP layer grown at 450°C

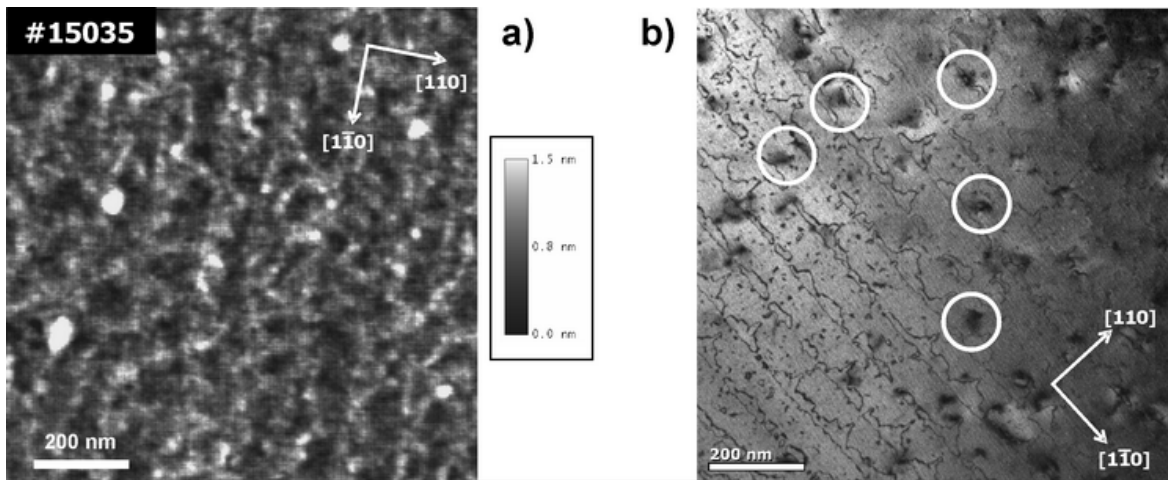


Figure 5.10.: AFM image (a) and Plan view 020 dark field micrograph (b) of a GaP layer grown at low-temperature (450°C) on the “optimized” Si surface. The  $\{110\}$  APBs, which are seen as dark lines under these imaging conditions are penetrating through the whole layer, reflecting the Si terrace morphology.

on the “optimized” Si surface. The morphology of the Si surface was recognizable, and the APBs penetrate through the whole layer on the  $\{110\}$  planes. These experiments prove that low growth temperature resulted in the formation of APBs on the  $\{110\}$  planes, which originate from the Si terrace edges and penetrate through the layer. This issue will be important in the next section. The origin of the additional shadows on Figure 5.10 (b) marked with white circles will be discussed in Section 5.6.

## 5.4. Annihilation of APDs

The main focus of this section is to determine the Si surface morphology and the GaP growth conditions necessary for self-annihilation of APDs. The kinking of the  $\{110\}$  APBs into  $\{111\}$  APBs are presented. The influence of the lateral size of the APDs and the growth temperature on the kinking and the self annihilation is discussed.

In order to grow antiphase-free GaP on Si(001), the following two issues are important:

- The suppression of monosteps on the Si surface and formation of doublesteps.
- If any APDs are generated in the layer, they must self annihilate during the growth.

Up to now, the antiphase domains were classified by the crystallographic planes that confine them. They can also be classified by their origin. APDs may originate from the monolayer high **down-step edges of the Si** surface terrace structure. They pattern

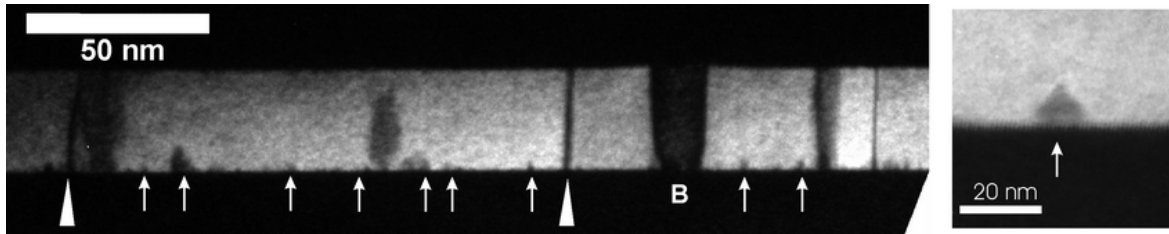


Figure 5.11.: Cross sectional 002 dark field micrograph of a GaP layer. APDs originating from the down-steps of the Si terraces (Type I) are depicted with triangles. The self-annihilating APDs originating on the Si terraces (Type II) are shown with the small arrows. The column-shaped Type II APD marked with **B** originates from monolayer high island or monolayer deep dip of the Si surface

the GaP material following the monostepped terrace structure of the Si substrate. This kind of APD will be referred to as **Type I** APD.

**Type II** APDs originate on the terraces of the Si surface. These small “triangle”-like APDs are 3-15 nm wide and they are bordered by  $\{111\}$  APBs. Self annihilation was observed after 5-15 nm film growth, such that the GaP material above these APDs was single phase.

Figure 5.11 illustrates examples of both types of APBs. The APDs originating from the Si terraces (Type II) are marked with the small arrows and a zoomed image. The possible origin and behavior of Type II APDs will be discussed in Section 5.5.1. The focus in this section is on the Type I APDs. They can be seen also on Figure 5.11, marked with white triangles. As a reminder, this was the sample where the APD pattern of the GaP was correlated with the Si monolayer stepped terrace structure (described previous section). This sample served as a starting point for the following study.

### Kinking of the APBs

Using low temperature (450°C) growth of GaP, the antiphase boundaries of Type I, which were formed on the Si monosteps, penetrate through the whole layer on the  $\{110\}$  planes. (Figures 5.8, 5.10 and 5.11.)

The following study shows the behavior of the APBs when the temperature of the GaP growth was increased to higher values (575-675°C). The nucleation was carried out at lower temperature (450°C), as discussed previously. The effects of higher temperature overgrowth are summarized in Figure 5.12. Figure 5.12 (a) and (b) are the AFM images showing the surface morphology of the 57 nm thick GaP layer. The surface modulation appeared to be island-like. Trenches were observed, but their contour did not reproduce the underlying Si-surface. After the post growth annealing (in this case the annealing temperature was equal with the growth temperature, 675°C), the trenches on the surface of the annealed sample became deeper and the plateaus

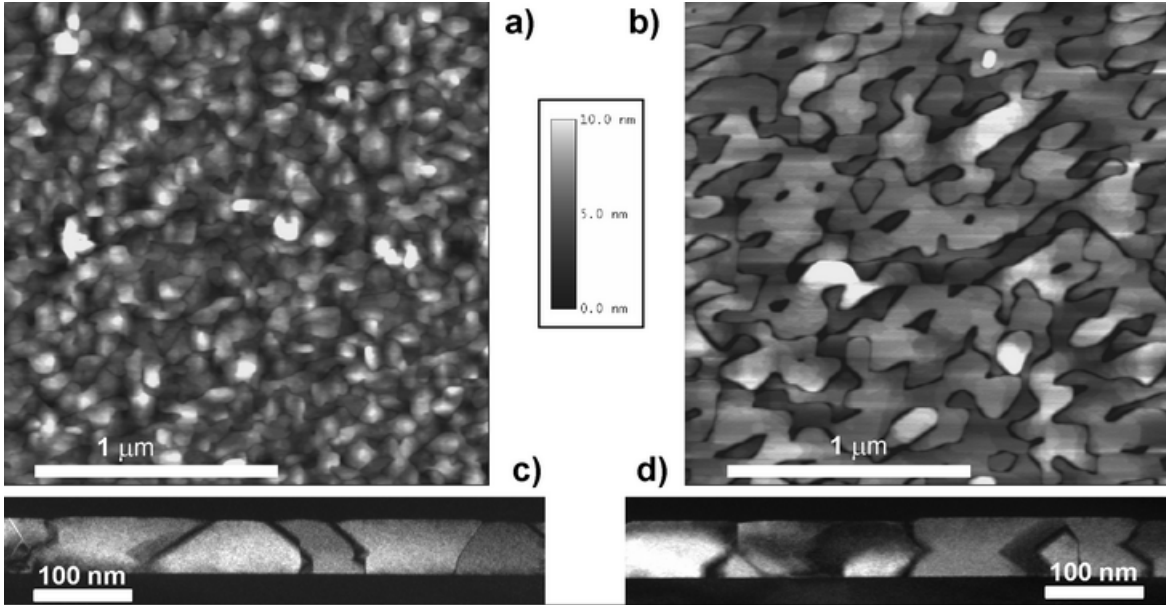


Figure 5.12.: AFM and DFTEM images of 57 nm thick GaP layers (#14903).  $P/Ga=80$ ;  $T_{nucleation}=450^{\circ}\text{C}$ ;  $T_{growth}=675^{\circ}\text{C}$ . AFM images of (a) the as-grown and (b) the annealed layer (annealing took place ex-situ at  $675^{\circ}\text{C}$  for 10 minutes under TBP stabilization). 002 dark field images of (c) the as-grown and (d) the annealed sample

smoothened. The islands had curved borders, resembling interlocking “jigsaw-puzzle” pieces, each several hundred nm in lateral dimensions. In this case, the trench structure did not reflect the triangle-patterned Si surface. From previous studies, one expects those trenches to be located at the intersection between the antiphase boundaries and the GaP surface. To prove this, cross sectional TEM samples were prepared. The 002 dark field micrographs are depicted in Figure 5.12 (c) (as-grown) and (d) (annealed). The bright areas on the micrographs are the domains of the GaP, separated by the zigzag black lines. These lines are the antiphase boundaries. The expected contrast change was not as apparent in these images, as compared to previous samples, since the foil was not at the optimal thickness for 002/00 $\bar{2}$  dark field analysis.

In general, this sample contains primarily APBs, that lie on the  $\{111\}$  planes. Also, they do not run along one specific  $\{111\}$  plane, but kink to another plane after growth of 20-30 nm of GaP. There was a minority of APBs, that began on the  $\{110\}$  planes (seen as vertical line on the micrographs) and then kinked to one of the  $\{111\}$  planes. Despite the kinking of the  $\{111\}$  type of APBs, annihilation was not observed. The reason is that they form far away from one another on the monostep edges of the wide terraces of the “not-optimized” Si surface, so the APBs do not have the chance to meet each other and annihilate.

The Type II APDs, that originate on the terraces of the Si surface and not from the step edges of the terraces, were found to self annihilate also at lower growth tempera-

ture (450°C), whereas antiphase boundaries separated more than 30 nm reached the GaP surface. The APBs separated by 15-20 nm were inclined towards one another, as shown in Figure 5.11. This phenomenon is independent from the growth temperature, and other growth parameters (V/III ratio, growth sequence) do also not affect the phenomenon. A possible explanation could be that the APBs introduce strain fields around them in the crystal, which have an extension in this characteristic length range. As the strain field interacts with the strain field from an other APB, they kink towards each other and annihilate. By annihilation, the crystal can minimize its total energy. This explains the non-self annihilating phenomenon of Type II APBs, that originate on the Si terraces, but were separated more than 20-30 nm from each other. These APBs remain on the {110} planes and penetrate through the layer at low growth temperature. However, they kink towards {111} at higher growth temperature, but do not annihilate due to the large inter-APB distance.

This being the case, obtaining an APD-free GaP film could be achieved by decreasing the spatial separation of the monosteps on the Si-surface; a perfectly double stepped Si surface would not necessarily be required.

### **Decrease the spatial separation of the step edges on the Si surface**

The studies described above used the “not-optimized” Si surface (Figure 3.2 (b)), where the lateral distance between the monostep edges of the Si terraces was between 50-200 nm. The results suggested that the use of “optimized” Si surfaces (Figure 3.2 (b)) could be the way to decrease the spatial separation of the step down edges of the terraces and hence initiate self-annihilation of APDs.

The following part describes the evolution of the APBs using the optimized Si surface, in which the monosteps are closer to one another. The APBs, as expected, were kinked from the {110} planes towards {111} or developed on the {111} from the beginning of the deposition. Figure 5.13 illustrates the effect of increasing growth temperature. The sample shown on the left side was grown at 575°C, while the growth of the sample on the right was grown at 675°C. The AFM images revealed a smooth GaP surface. The surface undulation was almost an order of magnitude lower than of the samples in Figure 5.12. The thinner sample deposited at 575°C, had some trenches on the surface, but the density is lower than in the sample shown in Figure 5.12. The surface of the thicker sample grown at 675°C was even smoother; trenches were absent the surface topography consisted only of GaP monolayer terrace steps. The 002 dark field micrographs below the respective AFM images show the APB evolution of the samples: in Figure 5.13 (c) the majority of the APBs were kinked to the {111} planes, met with one another and annihilated before the growth was terminated. Those APBs, that did not annihilate, reached the GaP surface, resulting in trenches that were 40 to 50 nm wide and 2 to 5 nm deep. Had the growth continued beyond 46 nm of layer thickness, all the APBs would have eventually annihilated. The sample in

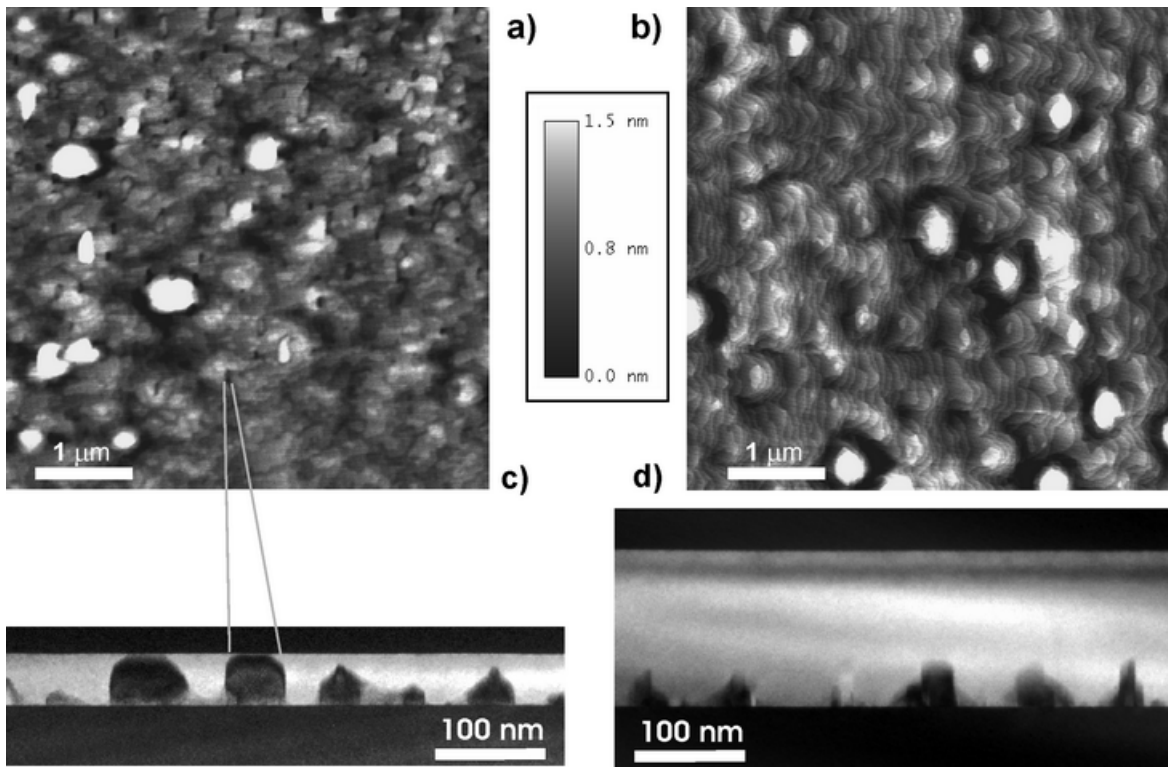


Figure 5.13.: APB evolution in GaP grown on “optimized” Si surfaces at high growth temperature. AFM images of (a) a 46 nm thick GaP layer deposited at 575°C (#15045), (b) 140 nm of GaP deposited at 675°C (#15093). The small trenches on (a) are the few APBs that reach the GaP surface. The cross sectional 002 dark field TEM images of the layers show: (c) the majority of the APBs kinking and annihilating in the thinner layer, (d) the APBs are all annihilated in the thicker layer after 50 nm thickness of GaP and the material above is single phased.

Figure 5.13 (d) shows the total annihilation of all APBs after  $\sim 50$  nm of deposited layer; above this distance from the GaP-Si interface, the GaP was single phase. The achievement of single phase material at lower GaP thicknesses was attributable to the higher growth temperature used for this sample.

More on the kinking of the APBs and the three dimensional shape of the APDs can be learned from Figure 5.14: (a) is a plan view dark field 020 image from the layer shown in Figures 5.13 (a) and (c). The dark-bright contour seen on the image follows the monostepped terrace edges of the underlying Si surface. Figure 5.14 (b) is a topview of the kinking phenomenon: it shows the triangle-based straight column shaped APD. The vertical surfaces of the APD kink to the  $\{111\}$  planes. The arrows indicate the direction in which they kink. The kinking phenomenon of the APBs was proven by the appearance of fringes in the 020 weak beam dark field image (Figure 5.14 (c)). This fringe formation has the same origin as that of stacking faults, described in Figure 3.23. In this case, the APBs on the  $\{111\}$  planes “cut” the TEM foil into two wedge shaped pieces. Figure 5.14 (d) is a geometrical model showing the kinking

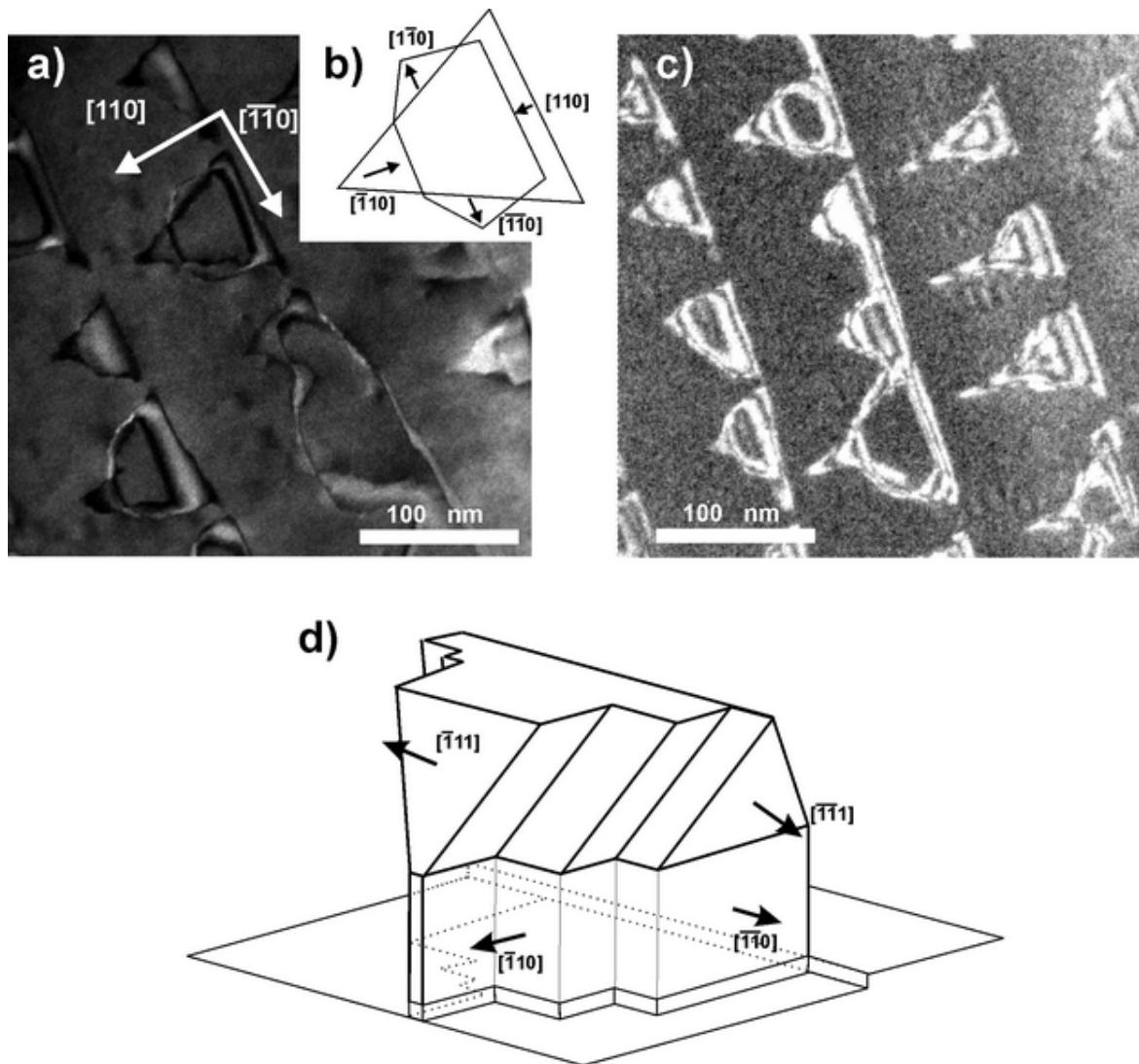


Figure 5.14.: (a) Plan view dark field 020 TEM image of the antiphase domains starting to develop in the growth direction then kink onto the  $\{111\}$  planes. The image (b) shows the APBs in topview: the boundaries parallel to the surface terrace edges kink towards each other, the ones perpendicular to the terrace edges incline away from each other. The appearance of the fringe contrast on the weak beam dark field image (c) proves the kinking of the APB. The geometric model on (d) illustrates the kinking of the boundaries from the growth direction.

phenomena in 3D. This model also reveals that the faces of the column-shaped APD are faceted; this was not apparent in Figure 5.14 (b). The vertical APBs lie on the  $\{110\}$  planes; the APDs is faceted on the  $\{110\}$  planes. Facetting was also observed in APBs that penetrated through the whole layer.

The results of this section can be summarized in the following way: the APBs, that originate on the Si surface terraces, but not from the down-step edges of the monolayer high terraces and are closer to each other than 20 nm, self-annihilate irrespective of growth temperature. Since  $\{111\}$  APBs are energetically unfavorable, their evolution was explained by interaction between neighboring APBs, possibly due to the strain fields they introduce. The behavior of the APBs originating from the down-step edges of the monolayer high terraces was influenced by growth temperature: APBs propagated vertically on the  $\{110\}$  planes at low growth temperature (450°C) and kinked to  $\{111\}$  planes at higher growth temperature (575°C - 675°C). If the Si surface terrace monostep edges were too far from each other, the kinked  $\{111\}$  APBs did not annihilate. If the lateral distance between the Si terrace steps was reduced (this was achieved by the optimization of the Si surface), the kinked  $\{111\}$  APBs were more likely to find each other and annihilate. The annihilation phenomenon was observed at 575°C growth temperature after only 40 nm layer thickness. The layers grown at 675°C showed complete annihilation of APDs after the growth of 50 nm of GaP, resulting in the growth of single phased GaP material above this thickness.

## 5.5. Crystal polarity and Si surface reconstruction

In this part the crystal polarity information obtained by CBED will be correlated to the Si surface dimer structure and the possible structure of the GaP first layer will be discussed and correlated to growth conditions.

The crystal polarity was measured with CBED on cross sectional TEM samples. The detailed description of the technique can be found in Section 3.3.4. This method gives a direct indication of whether the heavier atoms (Ga-polar) or the lighter atoms (P-polar) are situated at the top of the bonds that run in the plane of the observation direction. The Si surface structure was presented in Section 3.1.4. The polarity in this definition reverses by changing the viewing direction of the cross sectional samples by 90°. To avoid problems due to switching between the 90° rotated coordinate systems, a local coordinate system was used, as defined in Section 3.1.4. This coordinate system was fixed to the 2x1 dimer orientation of the Si surface. The Si dimers of the double stepped terraces and the terrace edges are parallel with the  $[1\bar{1}0]$  direction; the tilt direction of the Si surface is set to be towards the  $[110]$  direction (Figure 5.15 (a)). Figure 5.15 shows the cross sectional models of the two possible crystal orientations on the Si terraces viewed in the local  $[1\bar{1}0]$  direction. The Si surface dimers point out from the plane of the image. If one assumes a continuous first layer of the GaP

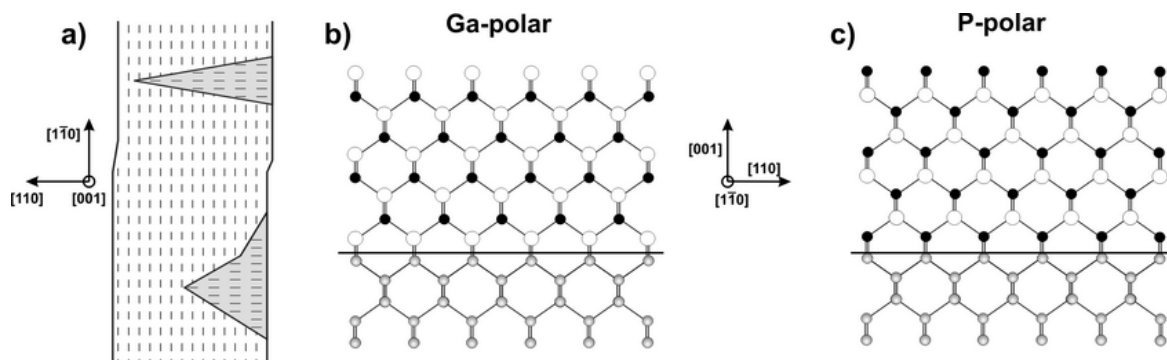


Figure 5.15.: Definition of the local coordinate system (a): the Si surface dimers on the doublestep terraces are parallel with the  $[1\bar{1}0]$  direction. The surface is tilted towards the  $[110]$  direction. Possible configurations of GaP crystal polarity in observation direction  $[1\bar{1}0]$ : (b) The crystal is Ga-polar and the first layer is Ga (c) the crystal is P-polar, the first layer is P.

crystal, and the first layer is Ga as seen in Figure 5.15 (b), the GaP layer is Ga polar. If the first layer is P, the crystal is P polar as (c) shows. The polarity determination of a single phase GaP layer in the  $[1\bar{1}0]$  direction is presented in Figure 5.16. The samples chosen for polarity study had a dominating main phase and the domains of the other phase were buried in the layer. The outlined Si surface illustrates the Si terrace direction in this sample.

Hence, if a continuous first layer of GaP is assumed, the element of the first layer can be deduced from the polarity information retrieved by CBED. If the crystal is Ga-polar, the first monolayer is Ga. If the CBED shows P polarity, the first monolayer consists of P atoms. The prerequisite is that the terrace direction is known from prior AFM analysis or TEM plan view investigation.

### 5.5.1. Discontinuous first monolayer - charge neutrality

Until now, the first monolayer of the GaP crystal was assumed to be continuous. It was pointed out in early investigations that the assumption of continuous III/V lattice planes on heterointerfaces of polar and nonpolar materials are energetically highly unfavorable. This is because the Ga - Si and P - Si bonds are charged defects with  $\pm q/4$  charge per bond. If the first layer on the Si were a continuous Ga or P plane, a charge density of  $q/a^2$  would build up an electric field in the order of  $10^7$  V/cm. In a macroscopic material this field could be neutralized, but in the growth process it would lead definitely to the breaking of the continuous planes and three dimensional growth. Different models were established for the nucleation of III/V material on elemental surfaces assuming the neutrality to be the key property in the interface atomic structure [19] [20]. These models introduce atomic rearrangements on the polar-nonpolar interface. They assume the breaking of the first Ga or P plane and even the breaking of the last Si plane to achieve the local charge neutrality. A different mechanism will

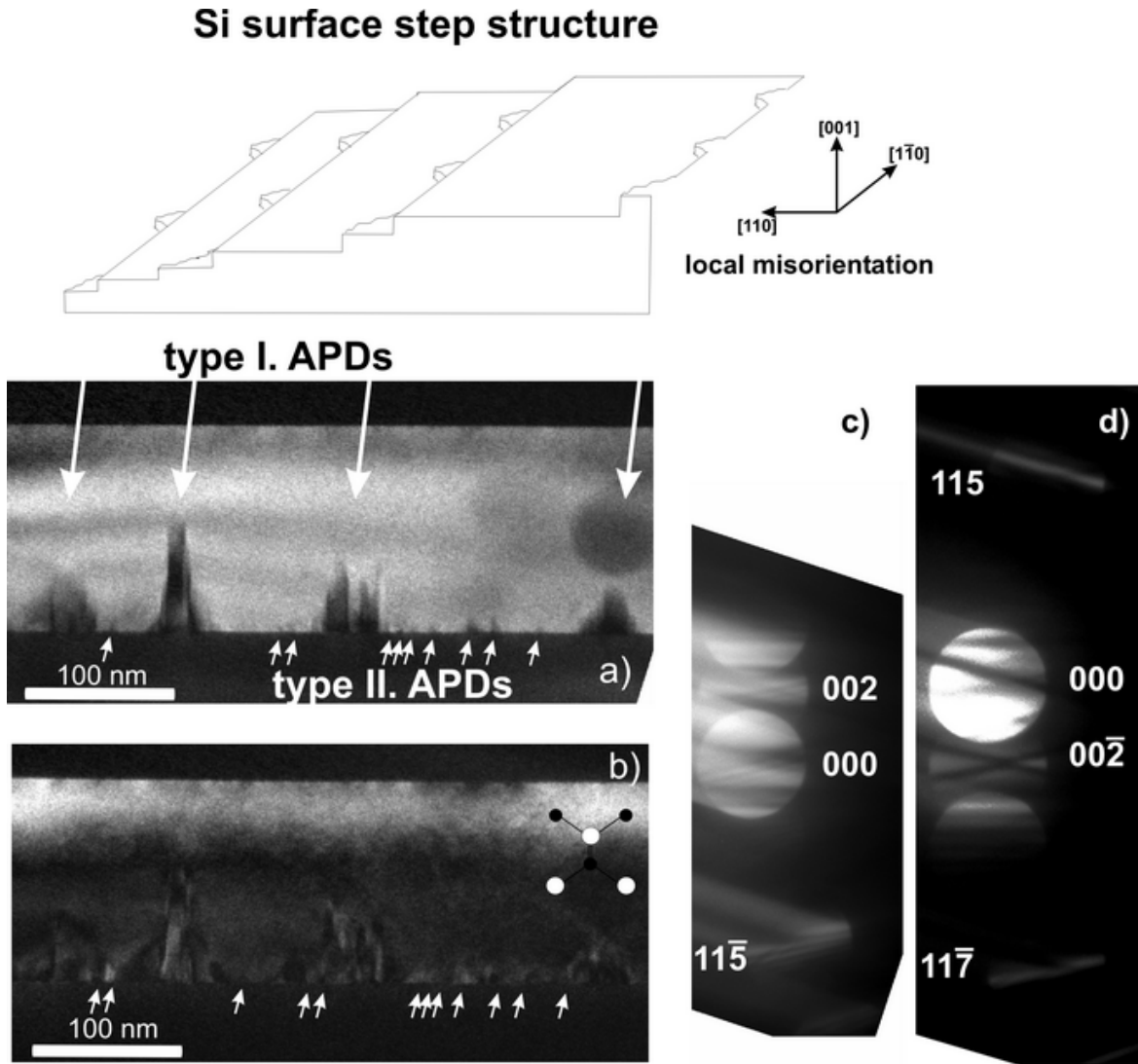


Figure 5.16.: Polarity analysis of a single-domain GaP layer (a)  $002$  dark field (b)  $00\bar{2}$  dark field micrographs taken with the excitation conditions used for obtaining CBED patterns. (c) CBED pattern with the  $002$  reflection excited. The white cross in the  $002$  disc shows the constructive interference of the  $11\bar{7}$  and  $11\bar{5}$  beams. (d) CBED pattern with the  $00\bar{2}$  excited: the dark cross reflects to the destructive interference of the  $115$  and  $11\bar{7}$  beams. Comparison with simulations proves that the layer in this observation direction is Ga-polar.

be suggested, based on the role of small APDs on the Si terraces. Self annihilating antiphase domains were observed in the dark field micrographs in Figure 5.16 (a) and (b). The two types of antiphase domains, introduced in Section 5.4, can be distinguished here as well: Type I APDs, which are marked with the thicker white arrows in Figure 5.16 originated from the monostep edges of the Si surface terraces. These APBs penetrated up to 50-70 nm into the GaP layer and self annihilated. This phenomenon was described in Section 5.3. APDs of type II are marked with the smaller white arrows. They formed on the Si surface terraces. Two possible generation mechanisms were introduced to explain the origin of the APDs which formed on the Si terraces and not on the terrace step edges: the first one assumes that one monolayer high islands or dips remained on the Si terraces, with lateral size in the range of the observation limit of the AFM. Continuous coverage with either Ga or P results in a shifted sublattice of the GaP crystal above the islands or dips. During the growth, a/4 shift in the sublattices results in an antiphase boundary as illustrated in Figure 5.17 (a).

Considering the need for the local charge neutrality, there is a further possibility that implies the breaking of the continuous lattice planes of the first GaP monolayers. Figure 5.17 (b) illustrates the interface configuration when the first layer is heterogeneous, consisting of Ga- and P-covered areas. As this sublattice is mixed, APBs develop above the connections of the different parts of the first monolayer. Although this hypothesis of nucleation deals with the breaking of the first monolayer, it does not follow the exact local charge distribution and does not investigate the possible role of the breaking of the uppermost Si monolayer. The simple model introduces the mixed coverage of the Si terraces with Ga and P. This mixed coverage leads to a dense APB network in the first monolayer. Using the TEM techniques, an upper limit can be given for the lateral size of the generated APDs. These APDs have 15 nm maximal lateral extension at the interface. This means, that the Ga or P coverage is continuous up to 75-80 atoms in one lateral direction. The smallest observable APDs had 2-3 nm lateral extension. Since this value is close to the resolution limit of the dark field TEM method, no information from below this size can be retrieved. According to the proposed nucleation model, APDs above the Ga or the P-covered areas are buried by self annihilation of the APDs in the first 15 nm of the grown layer. One phase becomes dominant and determines the main phase of the single phase GaP crystal. The self annihilation phenomenon of these small APDs was found to be independent of growth temperature. These self annihilating Type II APDs were present in samples, grown at low temperature (450°C), in which Type I APDs penetrated through the whole layer lying on the {110} planes (Figure 5.9), and also in samples grown at high temperature (575-675°C), in which Type I APDs kinked from the {110} planes to the {111} planes and self annihilated.

The presence of Type II APDs in Molecular Beam Epitaxially (MBE) grown samples [28] also supports the model. Small self annihilating APDs were present in high density in GaP layers grown on 4° misoriented Si (001) substrates at various temperatures,

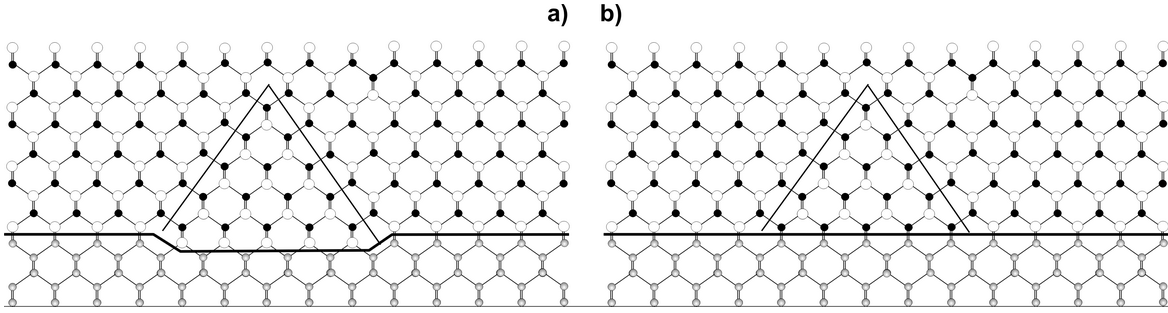


Figure 5.17.: Origin of the small APDs formed on the Si terraces: (a) with continuous first layer of Ga, covering a monolayer deep Si surface dip, (b) with not continuous Ga first monolayer on the atomically smooth Si terrace.

though this misorientation enhanced the double step formation, hence suppresses the probability for APD generation.

The next section shows that the resulting polarity of the main phase is independent from the element deposited first. The extent to which the polarity of the main phase can be influenced by GaP MOVPE growth conditions will also be discussed in the next section.

### 5.5.2. Growth conditions and polarity

The previous section introduced the concept that the polarity of the main phase of the GaP crystal was the result of a “competition” between two phases that are locally present during the GaP nucleation. Investigations of GaAs heteroepitaxy by Fischer et al. [27] showed that the polarity can alter by changing the growth conditions. A continuous first monolayer of either Ga or P was assumed in their study.

The results of the present work indicate, however, that the first monolayer might be discontinuous. The sublattice switch takes place locally. The Si surface is covered both with Ga and P, but segregated into Ga and P monolayer islands covering the entire surface. The lateral extension of these domains was up to 15 nm. Which of the two possible phases will become the main phase of the GaP crystal depends on the GaP growth conditions as will be discussed in the following.

The polarity of the main phase of the GaP layer is found to be different at different nucleation conditions. The polarity studies with the nucleation and growth conditions are summarized in Table 5.1.

From the available data, the following conclusions can be drawn:

- The resulting polarity of the main phase is reproducible. The same growth conditions resulted in the same polarity.
- The dominating element of the first monolayer, thus the resulting polarity did not depend on the first element led into the reactor. (Compare sample I. (Ga

## 5. Heteroepitaxy and defect characterization (GaP on Si)

	Nucleation			Growth		Polarity
	Nucleation sequence [sec]	P/Ga	$T_{nucl}$ [°C]	P/Ga	$T_g$ [°C]	
I	1Ga/1GI/1P/1GI/(1P/1GI/1Ga/1GI)x12	80//80	450	20	675	Ga
II	1P/10GaP/(1P/1GI/1Ga/1GI)x10	100//80	400	20	575	P
III	1P/5GaP/(1P/1GI/1Ga/1GI)x15	120//80	400	20	675	Ga
IV	1P/5GaP/(1P/1GI/1Ga/1GI)x15	120//80	400	50	575	Ga

Table 5.1.: Polarity of the GaP layers for different growth conditions. Nucleation sequence: the time in seconds and the source, which was opened is indicated. The P/Ga ratios separated by the double slash refer to the different parts of the nucleation of the first column. In all cases the nucleation was followed by continuous GaP growth with the indicated P/Ga ratio. The polarity is viewed in the  $[1\bar{1}0]$  observation direction.

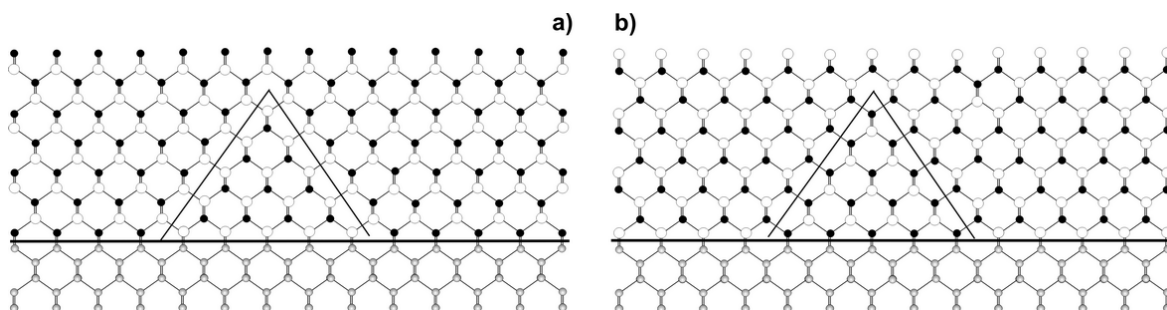


Figure 5.18.: Final polarity of the GaP layer determined by the domination of (a) the P-polar or (b) the Ga-polar domains. The crystal models are simplifications of the mixed interfaces indicating first monolayers with Ga-majority and P-majority as complete monolayers in the domains.

led first in the reactor during FME nucleation) with sample II. (P led first into the reactor during combined nucleation))

A possible explanation for the determination of the final polarity takes the V/III ratio in the nucleation into account: the first monolayer of the GaP covers the Si surface as the local charge neutrality determines it. The bonds at the interface are both Si-Ga and Si-P bonds. Their mixing takes places not only locally, but throughout rather large areas (up to  $15 \times 15 \text{ nm}^2$  are covered with Ga or P). The driving force for the mixing of the coverage is the charge neutrality. The APBs developing above the borders of the adjacent Ga and P covered areas tend to develop as non-stoichiometric Ga - Ga or P - P  $\{111\}$  antiphase boundaries, if one of the elements is prevalent in the nucleation. The crystal models in Figure 5.18 illustrate the two possible  $\{111\}$  APB configurations in the conventional observation direction. If the  $\{111\}$  APB consists of Ga - Ga false bonds (as shown in Figure 5.18 (a)), there is more Ga in the material than in the stoichiometric GaP crystal. Hence the main phase of the material is P-polar. The other possibility, that the  $\{111\}$  APB is built from false P - P bonds, as presented in Figure 5.18 (b). In this case the dominating main phase is Ga-polar.

According to this model, if there is locally more Ga or P incorporated into the material, in the form of the non-stoichiometric  $\{111\}$  APBs, this determines the resulting polarity of the dominating phase. The P/Ga ratio can be taken as measure for this mechanism. The simple model would use a threshold value describing the combined nucleation mode. Below a specific P/Ga ratio more Ga is incorporated and result in a P-polar main phase. Above this value, more P is incorporated in the form of P - P  $\{111\}$  APBs, therefore the dominating phase is Ga-polar. If one studies Table 5.1, the comparison of the rows suggests that, if such a threshold existed, it would be between P/Ga values of 100 and 120 in the first seconds of growth: the main phase was found to be Ga-polar in the case of P/Ga=120 value during continuous nucleation. The main phase was P-polar if the value of P/Ga=100 was used during the continuous nucleation. This would also suggest, that the dominant polarity is determined within the first monolayers deposited in the first 5 seconds of growth. However, preliminary polarity results of FME-nucleated layers suggest that FME nucleation leads to Ga-polar layers, irrespective of the V/III ratio in the first seconds of growth.

In the frame of this work, a complete systematical study was not carried out to exclude or include the influence of other growth parameters (such as temperature, growth sequence). This knowledge, however can serve as a basis for further dedicated quantitative studies on GaP polarity and nucleation conditions.

## 5.6. Detection and evolution of other planar defects

The main types of crystal defects in the low-lattice mismatched heteroepitaxial GaP layers on Si are antiphase boundaries, stacking faults and microtwins. Until now this work has mainly focused on the detection, formation mechanisms and annihilation of antiphase boundaries (APBs) and antiphase domains (APDs). In this paragraph, mechanisms, that may contribute to the formation and evolution of other planar defects will be summarized. The origin and also the way of suppression, of stacking faults and microtwins was introduced in Section 5.1.

As shown, all planar defects are generated at the beginning of the growth. It was shown by HRTEM measurements of the first GaP monolayers (Figure 5.5), that nucleation by flow rate modulated epitaxy (FME) results in 2D nucleation layers that are stacking fault- and microtwin-free.

This section discusses more aspects of stacking fault evolution. In order to learn more about the formation of stacking faults and twins in GaP, experiments were carried out to find the optimal growth conditions and describe their evolution. The following parameters of the deposition were investigated to examine their influence on the formation of stacking faults and twins.

- The element first led into the reactor.

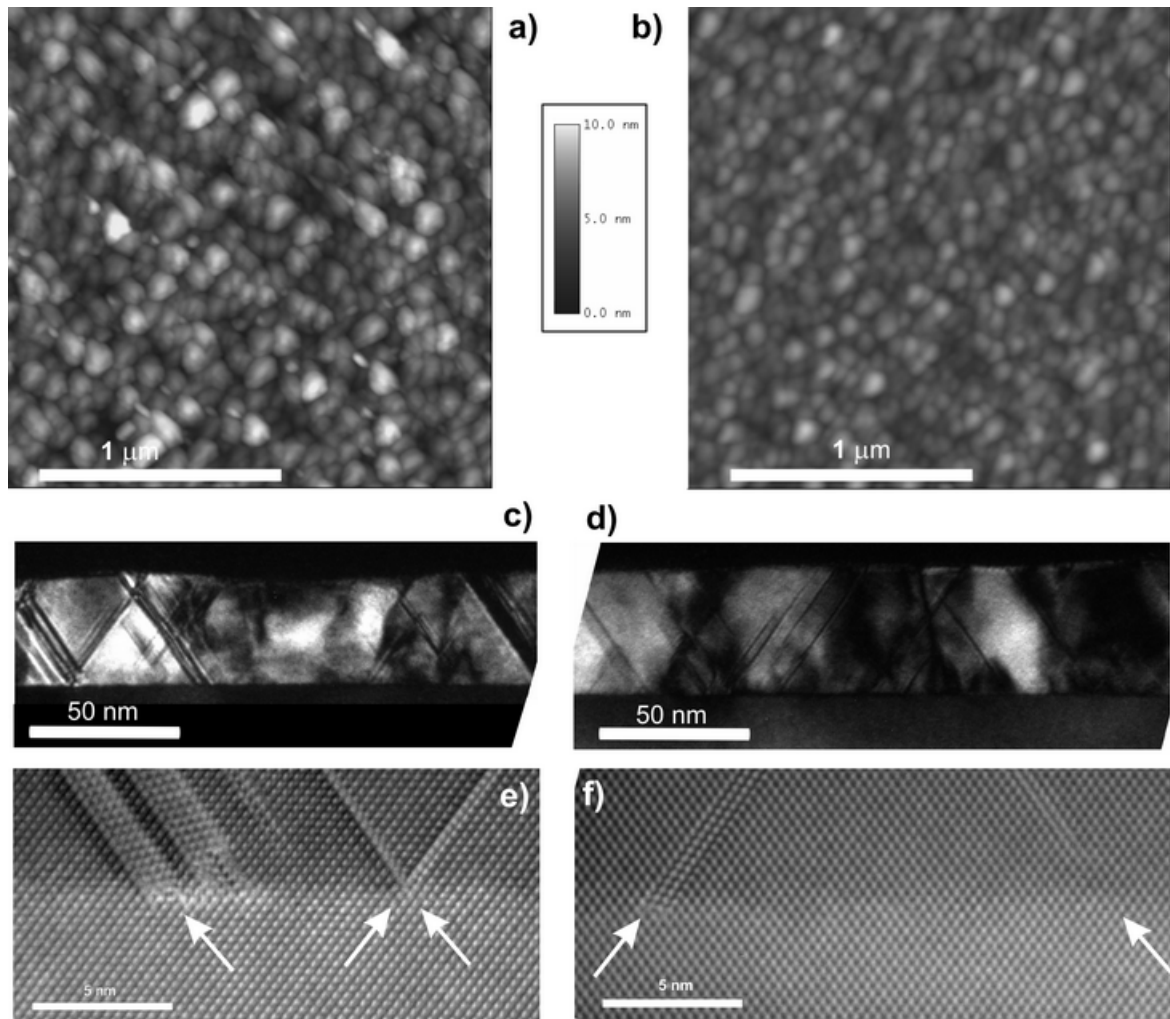


Figure 5.19.: AFM and 002 dark field TEM and HRTEM images of a 36 nm thick GaP layer. The growth was started in (a),(c) and (e) with Ga first monolayer and in (b),(d) (f) with P first monolayer. The HRTEM image (e) shows a band of microtwins and two stacking faults. (f) shows multiple stacking faults.

- The growth sequence. (FME vs. continuous nucleation)
- Nucleation and growth temperature.

To investigate the influence of the first monolayer, the following comparison was made: two layers were grown with same growth conditions ( $T_{growth}=525^{\circ}\text{C}$ ,  $\text{P}/\text{Ga}=5$ , not annealed Si-surface), but having a different first monolayer. The results are shown in Figure 5.19 ((a), (c), (e): Ga first monolayer, (b), (d), (f): P first monolayer).

Figure 5.19 (a) and (b) compares the surface morphology of the samples using AFM. The surface morphology is similar; the samples have the same, grain-like undulation.

The film started with Ga, however, has a larger surface undulation (exceeding the grayscale of the AFM image).

To determine whether the surface undulation is due to the evolution of planar defects, cross sectional TEM samples were prepared and investigated. The results can be summarized as follows: both layers are patterned with antiphase domains, but exact qualitative analysis was difficult due to the presence of other planar defects that were present also in high density. Stacking faults and microtwins on the  $\{111\}$  planes were detected in both samples. Their density was quite large: the average separation distance, as derived from dark field micrographs was  $\sim 10$  nm. There was no large difference in the density of the stacking faults and microtwins between the two samples. However, the extension of the planar defects was different for both samples. The sample started with Ga first contained thicker bands of microtwins and the stacking faults appeared to have accumulated. The stacking faults were multiple in all cases found in this sample. The sample started with P first contained more uniformly distributed stacking faults.

High temperature growth was shown to be necessary for the annihilation of Type I APDs, but as seen from this study, it resulted in rough layers if used also in the nucleation step. Hence, a low temperature nucleation scheme followed by a high temperature overgrowth was chosen.

The effect of the growth sequence at low temperature (at  $400^\circ\text{C}$  and  $450^\circ\text{C}$ ) on the nucleation was discussed in Section 5.1. Dependence of stacking fault and microtwin evolution on nucleation conditions will now be discussed. As shown, stacking faults were present in the GaP layers, which were nucleated by either continuous or combined mode (Fig 5.5). Figure 5.20 presents a 55 nm thick GaP layer nucleated by combined mode: at  $400^\circ\text{C}$  with continuous operation of the sources at P/Ga=80 for 10 seconds, and followed by Flow Rate Modulated epitaxy at  $450^\circ\text{C}$  for the rest of the growth at P/Ga=100. The surface was smooth (within 2 nm surface undulation as shown in Figure 5.20 (a)), but the AFM did not reveal the underlying crystal defects: stacking faults were present in the layer in very high density. They were observable, however, in both cross sections (Figure 5.20 (c) and (d)). This was detected also in plan view TEM images of the layer, as shown in Figure 5.20 (b). The APB structure derived from the 020 dark field image reflected the Si surface. The dark line-like contrast originated from the antiphase boundaries of GaP crystal. In addition to the APBs triangular dark contrast was observed. The features were identified by weak beam dark field imaging: the alternating bright and dark fringe structure identified the stacking faults (as described in Section 3.3.6). The triangles lie on the  $\{111\}$  planes with their tip on the GaP-Si interface. They are depicted with arrows on the  $2\bar{2}0$  weak beam dark field images, shown as insets in Figure 5.20 (b). They were approximately 50 nm wide at the top of the 55 nm thick layer. The underlying Si substrate of this sample was similar to the one of the sample shown in Figure 5.8, in which stacking faults were not present. The difference between the samples is the nucleation scheme used

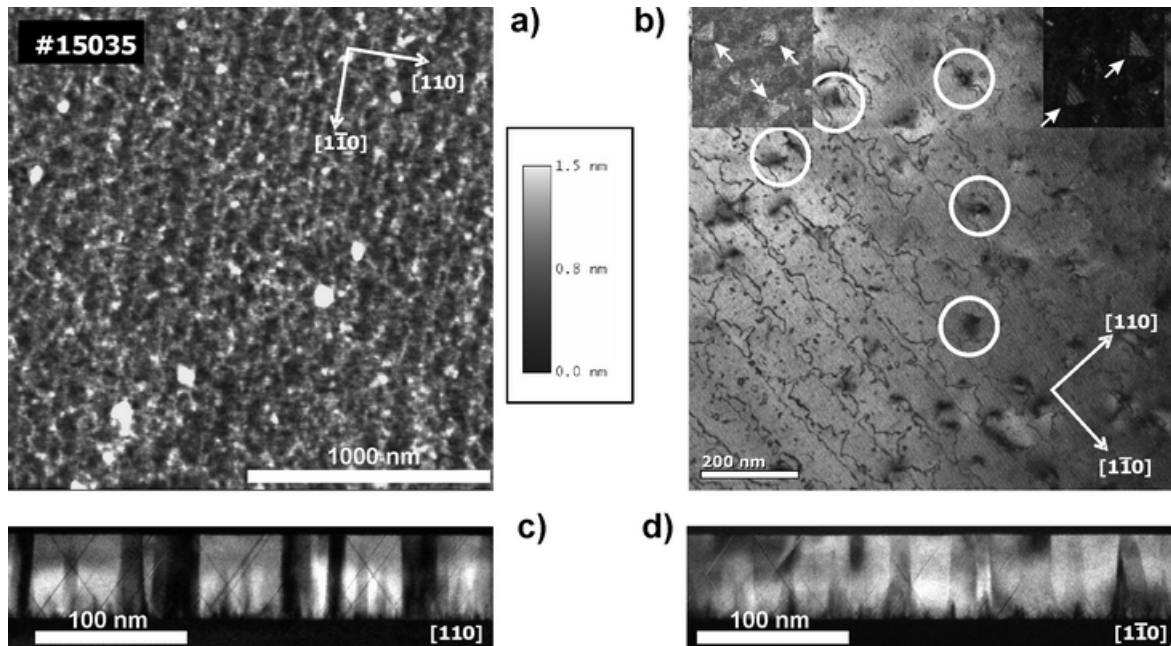


Figure 5.20.: A 55 nm thick GaP layer nucleated by the combined scheme: the nucleation layer growth is continuous (1 sec P, 10 sec GaP with P/Ga=80 at 400°C temperature), followed by Flow Rate Modulated epitaxy (with P/Ga=100 at 450°C temperature). The surface morphology is shown on (a) AFM image. The imprint of the Si-surface can be recognized in the (b) 020 dark field plan view image. The layer is not single-phase: it was grown on optimized Si-surface and at low temperature. The layer has large density of stacking faults: They are observable in both cross-sections: (c) [110] and (d)  $[1\bar{1}0]$ . They can be seen from the plan view as well: the insets in (b) are weak beam dark field images using the  $2\bar{2}0$  reflections, showing the fringe contrast of stacking faults. The stacking faults appear only as a shadow on (b) - marked with circles.

(combined nucleation in Figure 5.20 and FME in Figure 5.8). This again proves that FME nucleation leads to stacking fault-free GaP layers.

The next experiment investigated the evolution of stacking faults in the GaP layers, nucleated by the combined mode. The layer shown in Figure 5.21 was nucleated at 400°C: 10 second continuous operation of the sources at P/Ga=100, followed by alternating operation (FME) at P/Ga=80. The overgrowth took place at 575°C at P/Ga=20 up to 46 nm of layer thickness. The key characteristics of the layer can be seen in the 200 plan view dark field image in Figure 5.21 (a). The sawtooth pattern following the parallel lines corresponds to the antiphase domain structure of the layer, as seen from top, as discussed in Section 5.4. Slightly dark shadows on the bright areas of the dark field image (marked by arrows) were observed in Figure 5.21 (a). Since this layer was nucleated in combined mode, stacking faults may be expected in the film. Weak-beam dark field image (Figure 5.21) (b) revealed shadows corresponding to stacking faults. The difference between this and the former sample was that, in this sample the stacking faults were observed only in one pair of  $\{111\}$  planes. They were

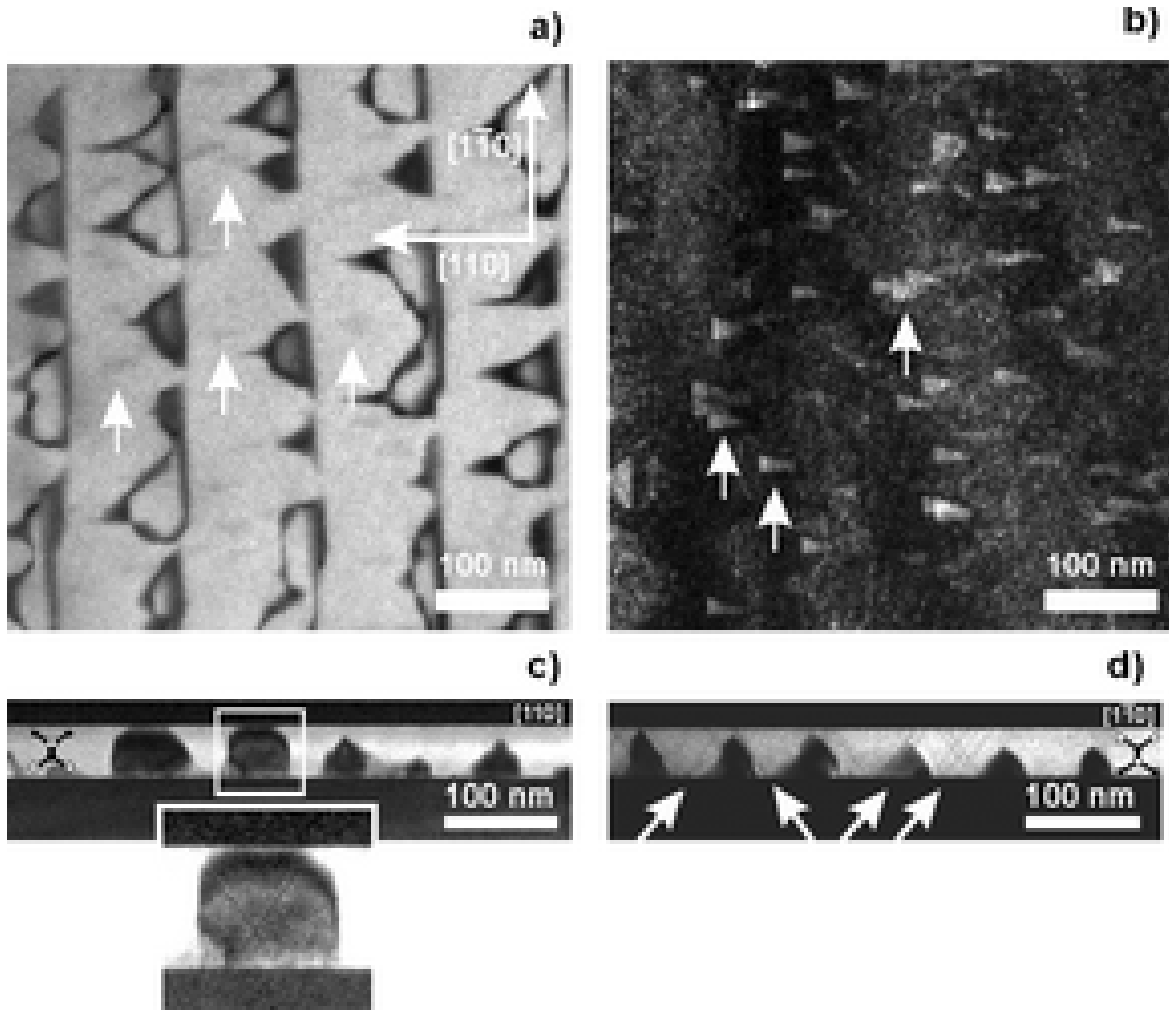


Figure 5.21.: Correlation between stacking faults and polarity I: Plan view micrographs of a 45 nm thick GaP layer, (a) 200 dark field image, (b) Weak-beam 220 dark field image. Cross sectional 002 dark field images in (c)  $[110]$  zone axis, (d) in  $[1\bar{1}0]$  zone axis.

observed only in one cross section direction, as shown by the white arrows in Figure 5.21 (c) and (d). They appeared only on the  $(111)$  and  $(\bar{1}\bar{1}1)$  planes; the normal of these planes is perpendicular to terrace edges of the Si surface. Only two stacking faults were observed in the  $[110]$  cross section in Figure 5.21 (c), and these were present in an antiphase domain only. Hence, it is possible, that the stacking fault orientation is related to the polarity of the GaP material. The fact that stacking faults were found in both cross sections in Figure 5.20 (c) and (d) might be due to the higher density of the antiphase material. A GaP layer with reversed polarity was also affected by the stacking faults, but on the other pair of  $\{111\}$  planes, that are supporting this model. Figure 5.22 illustrates the stacking fault evolution of a GaP layer nucleated by combined mode, starting with continuous mode starting with P only, and after one

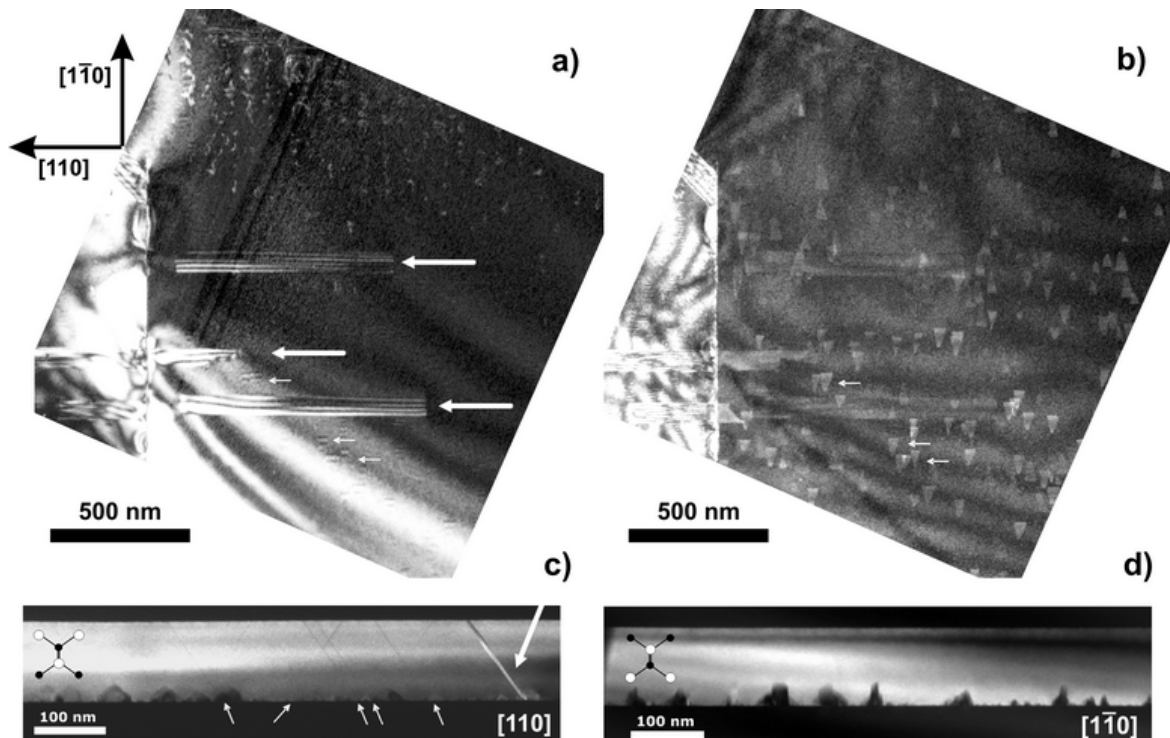


Figure 5.22.: Correlation between stacking faults and polarity II: Plan view and cross sectional micrographs of a 140 nm thick GaP layer. (a) 200 dark field image, (b) 200 weak beam dark field image, (c) cross sectional 002 dark field image with  $[110]$  zone axis and (d) with  $[1\bar{1}0]$  zone axis. The wide white arrows depict microtwins and the smaller ones stacking faults. The vertical line on the plan view images is a crack in the TEM sample.

second, opening the Ga as well, for 5 more seconds at  $P/Ga=120$ . This was followed by the Flow Rate Modulated mode. The nucleation temperature was  $400^{\circ}\text{C}$  and the continuous overgrowth temperature was  $675^{\circ}\text{C}$ , with  $P/Ga=20$ . This layer contained stacking faults, as indicated by small white arrows, in the weak beam dark field image in Figure 5.22 (b). These stacking faults had the same character as in the previously described layer. They originated from a localized area and lay on the  $(\bar{1}11)$  and  $(1\bar{1}1)$  planes. In contrast to the previous sample, the symmetry axes of the triangles were parallel to the terrace edges as shown in the top part of the 200 dark field plan view image (Figure 5.22 (a)). Stacking faults were observable in the  $[110]$  cross section (Figure 5.22 (c)), but are absent in  $[1\bar{1}0]$  (Figure 5.22 (d)). Comparing the orientation of the stacking fault with the polarity analysis, it transpired, that the P-terminated  $(\bar{1}11)$  and  $(1\bar{1}1)$  planes were affected by the stacking faults. These findings support the speculations of Narayanan, who also observed stacking faults in CBE nucleated GaP islands [84]. In addition to stacking faults, broad bands of microtwins developed in this sample, parallel to the stacking faults. The thickness of the microtwins was  $\sim 5$  nm, and the width was up to 1000 nm. The exact formation mechanism of stacking

faults and microtwins in these samples is yet to be determined. Further studies are proposed to unravel this behavior.

### Interaction of APBs and stacking faults

Since APBs and stacking faults/microtwins may lie on the same  $\{111\}$  planes in GaP films, the possibility of a microtwin or stacking fault bordering an APD must be considered. This phenomenon was not observed. There was no correlation between the formation of  $\{111\}$  APBs and stacking faults on the  $\{111\}$  planes. Referring to Section 5.1, that GaP nucleates three dimensionally at higher temperature and the stacking faults form as these islands grow laterally. If one assumes that nucleation occurs usually on step edges or kinks on the surface which is also the origin of the APBs, the stacking faults should be laterally separated from the APBs. Based on this assumption, as the nucleated GaP islands grow or meet each other, the stacking faults form on those areas of the Si surface where there is no Si step, and therefore, no APB. Another possible reason for defect formation is contamination of the Si surface, which results in generation of stacking faults.

The interaction of antiphase boundaries lying on other planes than  $\{111\}$  and stacking faults can be seen in Figure 5.23 (a). This image shows an APB starting from the middle of the image from the Si surface and penetrating through the whole layer. More planar defects are visible: T1 is a few layer thick microtwin, and multiple stacking faults (SFs). All stacking faults originated from a point at the Si surface and open and lie on one specific  $\{111\}$  plane. In the case of this image, the point from where they depart was in front of or behind the plane of the image. The diagram in Figure 5.23 (b) show how a part of a stacking fault may be “lost” during TEM sample preparation. Clearly, the stacking fault SF1 originates from the GaP-interface. The origin of SF2 is not present in the foil, since it was sputtered away during sample preparation. The 5-10 nm thick TEM foil contains only the part of the SF, which is indicated by the darker gray color. This image also shows how the APB is laterally separated from the stacking faults. Hence, the nucleation of APBs and stacking faults are independent from one another.

The HRTEM micrograph and dark field micrographs prove also that stacking faults have no influence on antiphase boundaries. The APB in Figure 5.23 was intersected by SF2, but no other interaction is observed.

The summary of the evolution of stacking faults and microtwins is the following: these defects originate during the nucleation step of the GaP layer and are the result of inappropriate nucleation conditions. If present, they penetrate through the whole layer and reach the surface. The intersection of APBs and stacking faults does not modify their propagation. The stacking faults show no self annihilation behaviour when intersecting with other stacking faults. At high temperature (525°C) or using continuous nucleation mode, both of them are present in very high density (deteriorat-

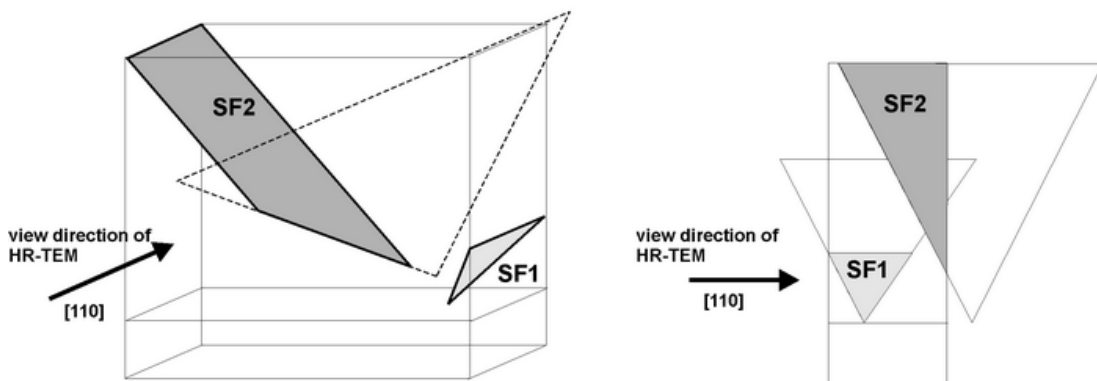
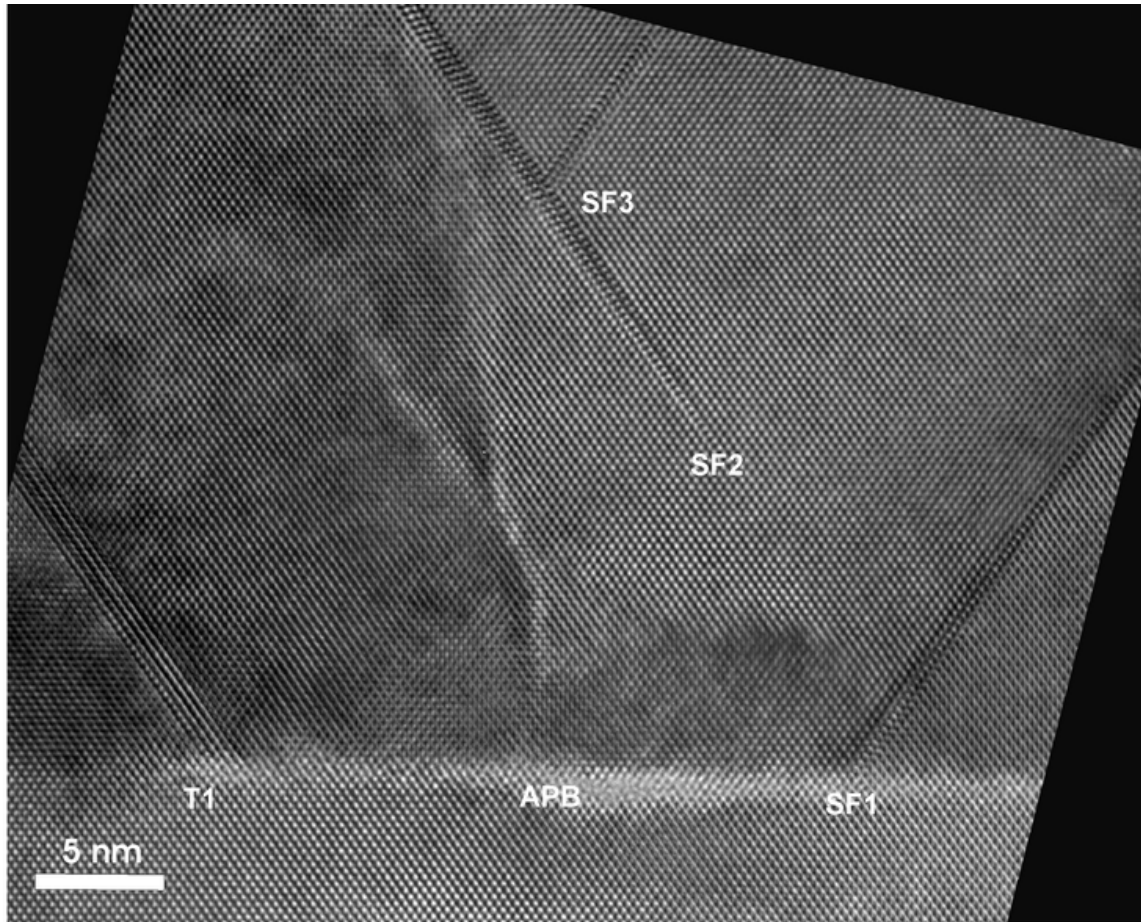


Figure 5.23.: High Resolution image of stacking faults and microtwins (T1) and a kinking 110 APB which is intersected by a stacking fault (SF3). All the SFs are multiple stacking faults. All the planar defects originate from the surface, even SF2 and SF3. They originate from a single point and their lower part is in front of or behind the image plane. That part of the TEM foil was simply cut out from the material during the preparation. (#14805)

ing the crystal structure). In low temperature combined mode nucleation (400-450°C) their density is significantly lower. The stacking faults originate from localized areas on the GaP-Si interface and mostly spread as triangles on the {111} planes. In single phased material they appear only on one pair of the {111} planes, namely on those which are equal by 180° rotation around [001]. The stacking faults on the other pair of {111} appear if the polarity of the layer is reversed. According to the polarity analysis, the P-terminated {111} planes are affected by the stacking fault evolution. The formation of microtwins is somehow less conceivable. This type of planar defect appears as a 1-5 nm thick band of material which is in twin relation with the GaP crystal. The width of this defect can reach 1000 nm. This is hardly explainable by coalescence of the nucleated GaP islands in the continuous or combined nucleation mode.

## 5.7. Summary of optimized nucleation and growth conditions

After presenting the evolution of planar defects in the low lattice mismatched GaP thin layers grown heteroepitaxially on Si (001) substrates, this final list summarizes the optimized growth conditions for defect free heteroepitaxy, which were obtained in the framework of this work:-

1. **Si substrate and pretreatment.** The nominally exact Si (001) substrates should have a slight ( $0.1^{\circ}$ - $0.2^{\circ}$ ) misorientation towards a  $\langle 110 \rangle$  direction in order to promote double step formation. The wafers should undergo the modified Shiraki-pretreatment prior to growth.
2. **Si-buffer growth and annealing.** The silicon wafer should be loaded into the MOVPE reactor and heated up to  $975^{\circ}\text{C}$  for 15 min in order to remove the native oxide. After cooling down to  $850^{\circ}\text{C}$  the Si homoepitaxy should be carried out with Vapour Phase Epitaxy (VPE) using Silane ( $\text{SiH}_4$ ) as Si-source and Pd-purified  $\text{H}_2$  as carrier gas. The reactor pressure should be 200 mbar. After the buffer growth the wafer should be annealed at 950 mbar in  $\text{H}_2$  atmosphere for 10 minutes at  $975^{\circ}\text{C}$  in order to develop the double steps on the Si surface.
3. **GaP nucleation.** The proper nucleation step is responsible for the continuous two dimensional nucleation layer and the avoidance of stacking faults and microtwins. It should take place at low temperature ( $400$  or  $450^{\circ}\text{C}$ ) by Flow-Rate Modulated Epitaxy using tertiarybutyl phosphine (TBP) and triethyl gallium (TEGa) at low reactor pressure (50mbar). The nucleation sequence should be the following: TBP should be opened for one second and closed for another second (growth interruption), TEGa should be opened and closed after one second for a second. This four second unit should be looped for 10-15 times. The used P/Ga ratio was 100-120.
4. **GaP overgrowth.** The overgrowth of the few nm thick nucleation layer should take place at higher temperature ( $575^{\circ}\text{C}$ - $675^{\circ}\text{C}$ ), in order to promote the kinking phenomenon and the self annihilation of the  $\{110\}$  APBs on the  $\{111\}$  planes. The overgrowth should be carried out at 50 mbar reactor pressure and with P/Ga value between 20 and 100.

5.7. Summary of optimized nucleation and growth conditions

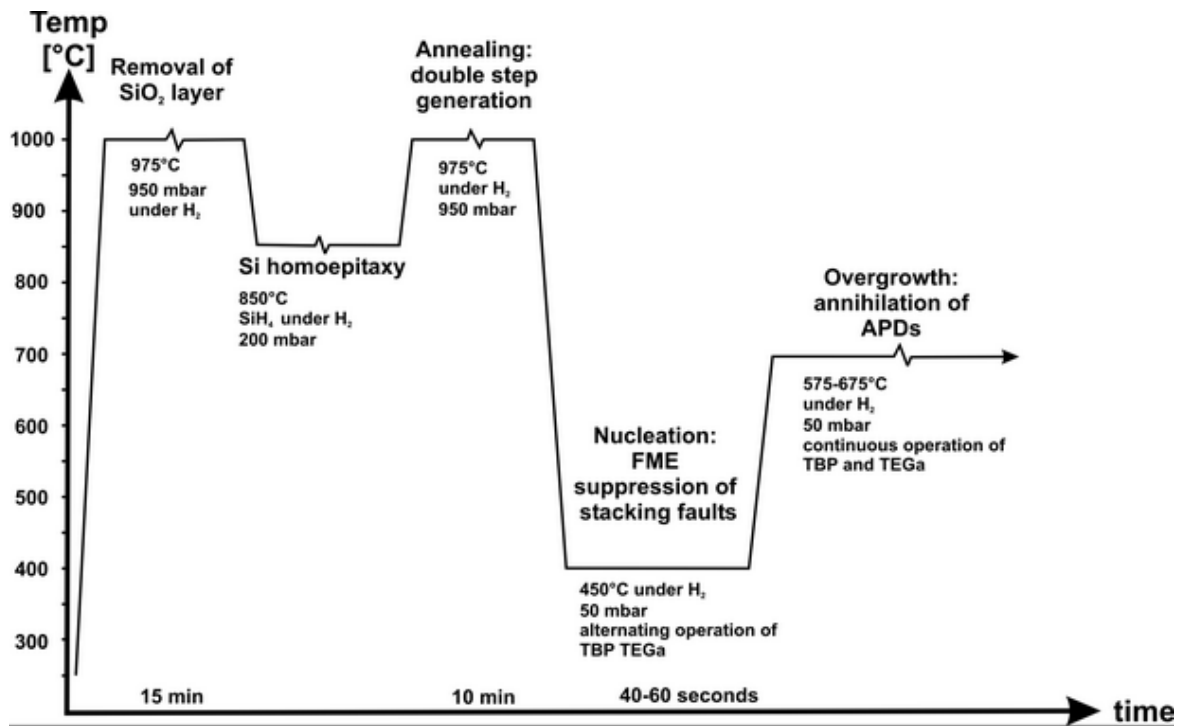


Figure 5.24.: Scheme of the GaP heteroepitaxial MOVPE process of the pretreated Si wafers showing the main steps. The time axis is exaggerated.

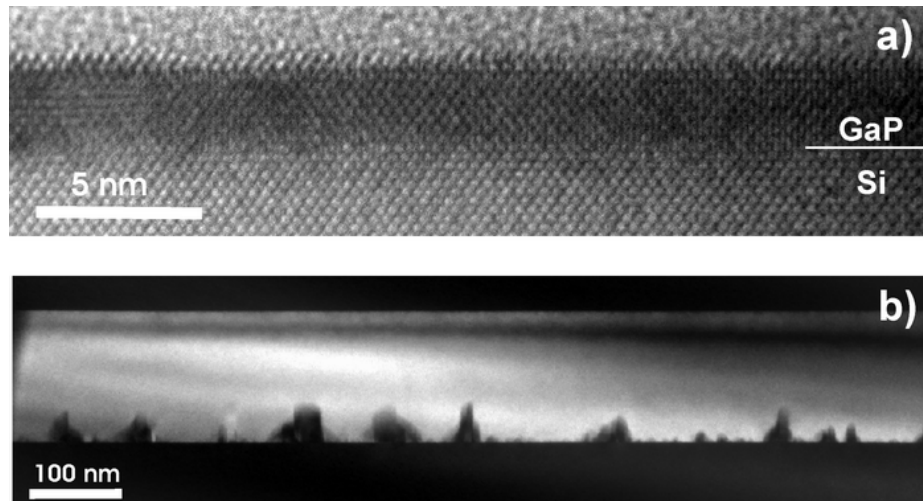


Figure 5.25.: Optimized GaP growth on Si (001) substrate: (a) HRTEM image of FME-nucleated stacking fault- and microtwin-free GaP nucleation layer. (b) 002 dark field image of a 140 nm thick single phased GaP layer grown on Si.

## 6. Summary

The first part of the thesis presented compositional evaluation of ternary quantum well structures grown on GaAs and GaP substrates using the chemical sensitive 002 dark field imaging in Transmission Electron Microscopy (TEM). The composition retrieved by the dark field intensity measurements and the structure factor calculations were compared with compositional values of High Resolution X-Ray Diffraction (HRXRD) measurements and their dynamical simulations. It was found in various ternary material systems, that the compositional evaluation of dilute ternary quantum wells are erroneous, when determining the dark field intensities with the *virtual crystal approximation*. The estimate can be made more precise by taking the *static atomic displacement* (SAD) of the first neighbor atoms of the isovalent impurities into account. The static atomic displacement and the structure factor of the various zincblende materials were calculated with the Valence Force Field (VFF) method. The correctness of the VFF method was proven with ab initio Density Functional Theory (DFT) calculations. In order to avoid the computational demands a simple expression was proposed to calculate the bond distortions due to the dilute impurities. It was found, that impurities in GaAs and GaP like boron or nitrogen introduce the largest values of static atomic displacement. Impurities which have covalent radii similar to the atoms of the host crystal do not distort the host lattice, hence can be described by the virtual crystal approximation. This is also the case when incorporating impurities above the dilute limit.

When calculating the structure factors, the atomic scattering factors are usually taken into account by the isolated atom approximation. Our refined structure factor calculations included the recalculation of the atomic scattering factors by DFT. However, the effect of the slight change in the atomic form factors was found to be a secondary factor in comparison to the SADs in the determination of the dark field intensities.

The second part of the thesis demonstrated the optimization process of the heteroepitaxial thin-layer growth of GaP on Si substrates by Metal Organic Vapour Phase Epitaxy (MOVPE). The low lattice matched GaP nucleated on Si could be the link in the transfer of the direct band gap material Ga(NAsP) onto Si substrates. For future integration with the CMOS process, the material system was optimized using nominally exact Si (001) substrates. As learned from the GaAs/Si and InP/Si heteroepitaxy, the defect density has to be kept low in order to avoid the degradation of the fabricated laser devices. The lattice mismatch of the GaP/Si material system is

---

low (0.36%), defects due to lattice relaxation do not appear in thin layers: the critical thickness is above 70 nm. As dealing with heteroepitaxy, the main defect types that arise are planar defects: antiphase boundaries (APBs), stacking faults (SFs) and microtwins (MTs).

The main objectives of the thesis were the identification, the description of the evolution and the suppression of these defects. Transmission Electron Microscopy was used to image the crystalline layers and gain structural information from the defects.

To image the antiphase related crystal domains (APDs), conventional techniques, such as dark field imaging with the 002 and  $00\bar{2}$  reflections were used. These reflections are most affected by the antiphase disorder, hence are suitable for investigating the APD structure. Our simulations showed that the micrographs obtained with the 002 and  $00\bar{2}$  reflections with the usual tilting conditions are sensitive for antiphasing for TEM foil thickness above 60 nm. Since APDs below this lateral size was found in the material system, we proposed another technique. The usage of the different  $\{111\}$  reflections was found to be suitable also for imaging antiphasing in thinner TEM sample regions (10-20 nm), what was proven by intensity simulations using the Bloch wave method. Imaging with these reflections does require a lower tilt, hence the projection of the plane of the antiphase boundaries in the observation direction does not disturb the images. This improved technique was also employed during the growth optimization process.

The efforts to deposit single phase material were made exploiting two phenomena: the evolution of double steps on the Si (001) surface and the self-annihilation of the formed APDs. In order to understand the evolution of the Si surface, its morphology was investigated by Atomic Force Microscopy (AFM). It was known from literature, that the Si (001) surface tends to form double steps under long high temperature (1000°C) annealing. Studies on post growth annealing of the homoepitaxially grown Si buffer layer in  $H_2$  atmosphere showed, that the disordered surface of the as-grown Si buffer layer undergoes a transformation into a stepped surface. According to similar results in the literature, the dangling bonds of the surface Si atoms form dimers (2x1 or 1x2 surface reconstruction). The experiments of this work supported also the former findings, namely, that the tendency of double step formation is stronger if the nominally exact Si (001) surface has a slight tilt towards one of the equal  $\langle 110 \rangle$  directions. In such a case the dimers of the double stepped terraces are parallel with the step edges and the dimers of the remaining monolayer high platforms are perpendicular to the terrace step edges.

The antiphase structure of the GaP thin layers was correlated to the monostep morphology of the annealed Si-buffer. Cross sectional and plan view TEM investigations with crystal phase sensitive dark field imaging in comparison with the AFM studies proved the monostep edges of the Si surface to be the origin of APBs. These APBs were named being of Type I. Cross sectional TEM revealed, that small APDs formed also on the terraces of the Si surface. Those were referred to as being separated by Type

II APBs. The origin of Type II APBs can be either one monolayer deep dips on the Si surface, which were not resolved by the AFM or nucleation of non-continuous first monolayer of the GaP. The driving force of the possible mixing of the first monolayer was attributed to the charge neutrality of the GaP/Si heterointerface. Irrespective of the origin, we observed the self annihilation of the Type II APBs, when their lateral size were below 15-20 nm at the GaP/Si interface. The APBs of Type I penetrated through the whole GaP layer when the growth temperature was low (450°C). At higher growth temperature (575-675°C) the Type I APBs showed a kinking behavior and were laying mainly on the {111} planes. When the lateral separation of the monosteps was lowered by optimizing the annealing conditions of the Si substrate and choosing its right slight misorientation, the Type I APBs showed self annihilation in the first 30-50 nm of the layer thickness. Above this layer thickness the GaP material was single phase.

Convergent Beam Electron Diffraction (CBED) investigations in cross section revealed the crystal polarity of the non-centrosymmetric GaP material.

The other types of planar defects – stacking faults and microtwins – were identified in cross sectional and plan view weak beam and high resolution TEM imaging. The multiple stacking faults were found to be originating from laterally confined regions of the heterointerface and laying on the P-terminated {111} planes. Thicker bands of microtwins were also found on the P-terminated {111} planes with a width of up to 1000 nm. The formation of stacking faults was attributed to the lateral growth of the nucleated GaP islands when using continuous nucleation scheme at low temperature. The exact origin of the wide microtwins was not revealed, however both stacking fault- and microtwin-free GaP layers were deposited using Flow Rate Modulated Epitaxy (FME).

The thesis presented the essential prerequisite of the transfer of the direct band gap Ga(NAsP) material onto Si substrates: planar defect-free GaP thin film heteroepitaxially grown on nominally exact Si (001) substrates. The next steps towards the integration were already made during the preparation of this thesis. In order to be able to grow thicker layers without relaxation, nitrogen should be incorporated into the GaP layers. Since boron has a similarly low covalent radius - being also a possible candidate for strain compensation - the growth of (BGa)P thin layers on Si will be also investigated. Ga(NAsP) quantum well structures will be deposited on the Si/GaP/GaXP (X=N, B) structure and optimized for the optoelectrical application.

From the aspects of structural characterization the APBs will be investigated by aberration-corrected High Resolution TEM imaging in combination with exit wave reconstruction, since it supplies finer information of the atomic structure of crystal defects, than the available conventional microscopes.

## 7. Zusammenfassung

Das Thema der vorliegenden Arbeit ist die quantitative Strukturbestimmung von III/V- und III/V auf Si- Halbleiterstrukturen.

Der erste Teil der Dissertation beschäftigt sich mit der Evaluierung der Zusammensetzung ternärer Quantenwell-Strukturen (QW). Dies erfolgt mit Hilfe der Transmissionselektronenmikroskopie (TEM) und zwar unter Verwendung der Dunkelfeldabbildung mittels des chemisch sensitiven 002 Strahls. Die Zusammensetzungen, die mit den Dunkelfeldabbildungen und Strukturfaktorberechnungen bestimmt wurden, wurden mit Zusammensetzungswerten, die aus dynamischen Simulationen von hochauflösenden Röntgenbeugungsmessungen (HRXRD) erhalten wurden, verglichen. In verschiedenen ternären Materialsystemen führen die simulierten Dunkelfeldintensitäten, die auf der Näherung virtuell perfekter Kristalle basieren, zu einer fehlerhaften Abschätzung der Zusammensetzungen. Die Genauigkeit kann mit der Einführung der statischen Verschiebungen (SAD) der ersten Nachbaratome verbessert werden. Die statischen Verschiebungen und die Strukturfaktoren verschiedener Zinkblende-Materialien wurden mit der Valence Force Field (VFF) Methode berechnet. Die Genauigkeit der VFF-Methode wurde mit ab initio Dichtefunktionaltheorie-Berechnungen (DFT) bestätigt. Um den immensen computergestützten Rechenaufwand zu vermeiden, wurde zur Berechnung der Bindungsverzerrungen des Kristalls eine einfache Formel vorgeschlagen. Fremdatome mit kleinen kovalenten Radien in GaAs und GaP, wie Bor oder Stickstoff, verursachen die größten Verschiebungen der Nachbaratome. Fremdatome, die ähnliche kovalente Radien haben wie der Wirtskristall, verzerren die Bindungsstruktur nicht. Dadurch kann der Strukturfaktor in diesem Fall mit Hilfe des virtuellen Kristalls berechnet werden. Das ist auch bei höherer Fremdatomkonzentration der Fall. Bei der Berechnung der Strukturfaktoren werden die atomaren Streufaktoren üblicherweise mit der isolierten Atom-Näherung berechnet. Die verfeinerten Strukturfaktorberechnungen dieser Arbeit berücksichtigen atomare Streufaktoren, die mittels der DFT-Methode berechnet werden. Es gibt allerdings eine unerhebliche Veränderung der korrigierten Streufaktorwerte.

Der zweite Teil der Dissertation stellt den Optimierungsprozess des heteroepitaktischen Dünnschichtwachstums von GaP mittels Metallorganischer Gasphasenepitaxie (MOVPE) auf Si-Substraten dar. Das GaP/Si Materialsystem ist aufgrund seiner niedrigen Gitterfehlpassung ein mögliches Glied im Transfer des Direkt-Halbleiters Ga(NAsP) auf Si Substrate. Für die zukünftige Integration in den CMOS-Prozess wurde das Wachstum des Materialsystems auf nominell exakten Si (001) Sub-

straten untersucht. Wie von Materialsystemen wie GaAs/Si und InP/Si bekannt ist, muss die Defektdichte unterdrückt werden, um die Degradation der gefertigten Laserstrukturen zu vermeiden. Da die Gitterfehlpassung des GaP/Si Materialsystems niedrig ist (0.36%), erscheinen Defekte aufgrund der Relaxation des Gitters nicht in dünnen Schichten. Die Defekte, die demzufolge in diesem Materialsystem auftreten, sind Antiphasengrenzen (APB), Stapelfehler (SF) und Mikrozwillinge (MT).

Eine Zielsetzung der Dissertation war die Identifizierung, die Beschreibung des Verhaltens und die Unterdrückung dieser Defekte. Um die kristallinen Schichten abzubilden und strukturelle Information zu erhalten, wurden verschiedene Techniken der TEM benutzt. Die Antiphasendomänen (APD) wurden mit konventionellen Techniken wie Dunkelfeldabbildungen mittels der 002 und  $00\bar{2}$  Strahlen untersucht. Diese Strahlen werden am meisten von der Antiphasenunordnung beeinflusst und sind deswegen für die Strukturuntersuchung der Antiphasendomänen besonders gut geeignet. Die Simulationen der Intensitäten der 002- und  $00\bar{2}$ -Strahlen zeigen, dass bei der verwendeten Probenkippung diese Strahlen sensitiv für die Antiphasenunordnung sind, wenn die Probendicke 60 nm beträgt. Da Antiphasendomänen auch unterhalb dieser Grössenskala in dem untersuchten Materialsystem bestehen, wurde eine weitere Technik vorgestellt. Die Simulationen der Strahlintensitäten haben gezeigt, dass die 111-Strahlen für die Abbildung der Antiphasendomänen in dünneren TEM-Probenbereichen (10-20 nm) geeignet sind. Eine Abbildung mit diesen Strahlen benötigt eine geringere Kippung der TEM-Probe, deshalb ist die störende Projektion der APBs in der Beobachtungsrichtung auch geringer. Diese verbesserte Technik wurde auch während der Wachstumsoptimierung verwendet.

Um eindomäniges Material herzustellen, wurden folgende Phänomene ausgenutzt: einerseits die Bildung von Doppelstufen an der Si (001) Oberfläche, andererseits anderen die Selbstannihilation der entstandenen Antiphasendomänen.

Die Morphologie der Si (001) Oberfläche wurde mittels Rasterkraftmikroskopie (AFM) untersucht. Wie aus der Literatur bekannt ist, neigt die Si (001) Oberfläche zu Doppelstufenbildung während lange Ausheizschritte bei hoher Temperatur (1000°C). Untersuchungen ausgeheizter homoepitaktischer Si-Bufferschichten haben gezeigt, dass die ungeordnete Oberfläche der gewachsenen Si-Bufferschichten sich in eine gestufte Oberflächenstruktur umwandelt. Die unabgesättigte Bindungen der Si-Oberfläche ordnen sich in einer Dimerstruktur (2x1 und 1x2 Oberflächenrekonstruktion) an. Die Untersuchungen dieser Arbeit zeigen, dass die Tendenz zur Doppelstufenbildung stärker ist, wenn die nominell exakte Si (001) Oberfläche eine geringe Fehlorientierung in einer der  $\langle 110 \rangle$  Richtungen aufweist. In diesem Fall sind die Dimere der Doppelstufen mit den Stufenkanten parallel, und die Dimere der monostufigen Plateaus sind senkrecht zu den Stufenkanten.

Die Antiphasenstruktur der GaP Dünnschichten wurde mit der Monostufenstruktur der ausgeheizten Si-Bufferschicht korreliert. TEM Querschnitts- und Aufsichtuntersuchungen mit kristallphasensensitiven Dunkelfeldabbildungen im Vergleich mit den

---

AFM-Studien haben bestätigt, dass die Monostufen der Si-Oberfläche der Ursprung der APBs sind. Diese APBs wurden als Typ I bezeichnet. TEM Querschnittsuntersuchungen haben gezeigt, dass kleine Antiphasendomänen sich auch an der Terrassen der Si-Oberfläche entwickelt haben. Diese Domänen sind von Typ II-APBs begrenzt. Als Ursprung der Typ II-APBs können monostufen-tiefe Vertiefungen fungieren, die mit dem AFM nicht aufgelöst werden können. Eine andere Möglichkeit könnte darin bestehen, dass die erste Monolage des GaP-Kristalls nicht ausschliesslich aus einer Atomsorte besteht. Die Triebkraft der möglichen Mischung der ersten Monolage kann auf die Ladungsneutralität der GaP/Si Grenzfläche zurückgeführt werden. Die Typ II-APBs annihilieren stets, wenn ihr lateraler Abstand niedriger war als 15-20 nm. Die Typ I-Antiphasengrenzen durchdringen bei niedriger Wachstumstemperatur (450°C) die ganze Schichtdicke. Bei höherer Wachstumstemperatur (575-675°C) sind die Typ I-APBs auf die {111} Kristallebene abgeknickt. Wenn der laterale Abstand der Si-Monostufen mittels optimierter Ausheizbedingungen und optimaler Fehlorientierung der Si-Substrate reduziert wurde, kam es in den unteren 30-50 nm der Schicht zu einer Annihilation der Typ I-APBs. Das Material war im darüberliegenden Bereich der Schicht dann eindomänig. Durch Untersuchungen mittels konvergenter Elektronenbeugung (CBED) wurde die Kristallpolarität des nicht zentrosymmetrischen GaP-Kristalls in Querschnittsgeometrie bestimmt. Andere Typen von Planardefekten, wie Stapelfehler und Mikrozwillinge, wurden mit Hilfe von Schwachstrahl- und Hochauflösungsabbildungen des TEMs in der Querschnitts- und Aufsichtsgometrie identifiziert. Die Mehrfachstapelfehler entstehen aus lokal begrenzten Bereichen der GaP/Si-Grenzfläche. Es wurden Stapelfehler und Mikrozwillinge an der P-terminierten {111} Ebene gefunden. Die Mikrozwillinge weisen eine Breite von bis zu 1000 nm auf. Die Bildung der Stapelfehler kann mit dem lateralen Wachstum der 3D-nukleierten GaP-Inseln korreliert werden, wenn die Nukleation bei niedriger Temperatur in kontinuierlichem Wachstumsmodus stattfindet. Der genaue Ursprung der breiten Mikrozwillinge konnte nicht eindeutig erklärt werden, jedoch wurden planardefektfreie GaP-Dünnschichten mittels flussratenmodulierter Epitaxie (FME) hergestellt.

Diese Dissertation hat die essentiellen Voraussetzungen für den Transfer des direkten Halbleitermaterials Ga(NAsP) auf Si (001) Substrate vorgestellt. Es wurde die Möglichkeit aufgezeigt, wie planardefektfreie GaP Dünnschichten auf nominell exakten Si (001) Substraten hergestellt werden können. Um dickere GaP Schichten auf Si ohne Gitterrelaxation wachsen zu können, muss Bor oder Stickstoff in den GaP-Kristall eingebaut werden. Auf verspannungskompensiertes Si/GaP/(BGa)P oder Si/GaP/Ga(NP) können dann Ga(NAsP) Quantenwellstrukturen abgeschieden und deren optoelektronische Eigenschaften optimiert werden.

Eingehendere strukturelle Untersuchungen der Antiphasengrenzen mittels aberrationskorrigierter hochauflösender TEM sind geplant, in Kombination mit Elektronen-Austrittswellenrekonstruktion, um feinere Informationen auf atomarer Skala über die Kristalldefekte aufdecken zu können.

# A. Appendix

## A.1. Abbreviations

AFM Atomic Force Microscope  
APB Antiphase Boundary  
APD Antiphase Domain  
CBE Chemical Beam Epitaxy CBED Convergent Beam Electron Diffraction  
CMOS Complementary Metal Oxide Semiconductor  
COLC Center of Laue Circle  
CTF Contrast Transfer Function  
DFT Density Functional Theory  
DFTEM Dark Field Electron Microscopy  
FME Flow rate Modulated Epitaxy  
FOLZ First Order Laue Zone  
FFT Fast Fourier Transformation  
FME Flow Rate Modulated Epitaxy  
HOLZ Higher Order Laue Zone  
HRTEM High Resolution Transmission Electron Microscopy  
HRXRD High Resolution X-ray Diffraction  
LDA Local Density Approximation  
MBE Molecular Beam Epitaxy  
MEE Migration Enhanced Epitaxy  
MOVPE Metalorganic Vapour Phase Epitaxy  
MQW Multi Quantum Well  
MT Microtwin  
QW Quantum Well  
RCA Radio Corporation of America  
SAD Selected Area Diffraction  
SF Stacking Fault  
TEM Transmission Electron Microscope  
TBP tertiarybutyl phosphine  
TEGa triethyl gallium  
TMGa trimethylgallium  
UDMHy unsymmetric dimethyl hydrazine  
VFF Valence Force Field  
ZOLZ Zeroth Order Laue Zone

## A.2. TEM sample preparation

### A.2.1. Cross section sandwich samples

Different sample preparation methods exist for preparing thin TEM foils. The TEM community itself is quite divided concerning the best recipes of the perfect TEM sample. Samples for high resolution investigation should contain extremely thin (up to 15 nm thick) regions, without re-sputtered material on the electron-transparent region. For this case the best method is similar to the one used in these investigations, but differing in the followings steps: the cut wafer pieces are not glued together, but clamped into the Ti-holder. The other difference is in the Ar-ion milling; the samples are sputtered first from one side while the guns operated oscillating around a perpendicular direction to the glue line, and then from the other side. This results in a hole with not symmetrical shape and since it is sputtered from one side, one sample side is lost, while some of the sputtered material can reach the sample on the opposite side of the sample interface, and can be deposited on it, increasing the unwanted amorphous part on the sample. This method of preparation results also in a wedge-shaped sample geometry, but only a small electron transparent area at the very thin area is perfect. These areas are satisfactory for high resolution imaging, since it requires sample areas up to a few 100 nm lateral size. The parts of the wedge-shaped sample with 30-150 nm thickness suffer from thickness undulations. If dark field images are required, this thickness domain is needed, with smooth surfaces, and possibly constant thickness. This is better achievable with the rotating Ar-ion milling. The following part describes the standard methods for TEM sample preparation used in this work. It was optimized for the N-containing heterostructures by T. Torunski, and is explained in details in [62].

1. Cleave 5mm x 6mm rectangles from the wafer. (A.1 1.).
2. Glue them together face to face with GATAN G1 epoxy resin. The thinning ratios: 1 volume part hardener and 10 volume part thinner. Place the parts between the jaws of a small teflon-coated vice and press them together. The pressure determines the distance between the sample pieces. The optimal distance between the two sample pieces is a few 100 nm. Bake it for 10 minutes in pre-heated oven at 140°C.
3. Cut 0.9mm x 1.8 mm large dices with a diamond wire saw (WELL) in the desired crystallographic direction. (The glued waferpieces should be mounted on ceramic sawing plate with hot wax) (A.1 2.).
4. Mount a dice into a 3 mm diameter Ti holder. The glue line has to face up. The Ti-holders we use are available from Balzers, and have various slit width: 0.6, 0.8, 1.0 mm. The one should be used, in which the sample has mechanical

## A. Appendix

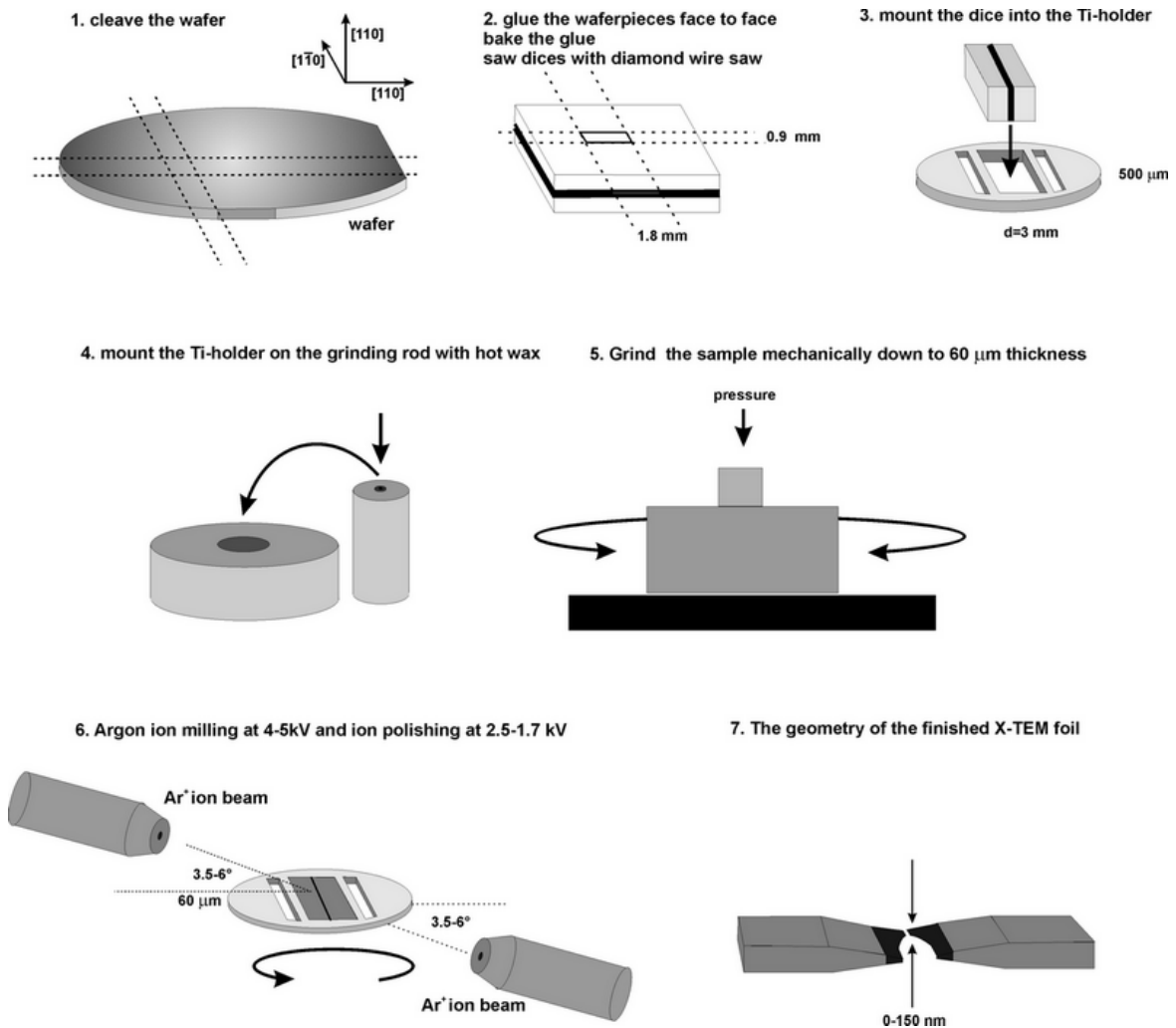


Figure A.1.: Cross sectional TEM sample preparation with Ti-holder

contact to the holder. The GaP wafers are  $325\ \mu\text{m}$  thick, therefore we use the  $0.6\ \text{mm}$ ; the Si wafers are  $275\ \mu\text{m}$  and  $550\ \mu\text{m}$  thick, for them we use Ti-holders with  $0.6$  or  $1.0\ \text{mm}$  slits. Glue the dice with the same G1 epoxy and bake it again for 10 minutes at  $140^\circ\text{C}$ . In this step the sample can be kept on a piece of teflon (A.1 3.).

5. Mount the hardened Ti holder onto a grinding rod with molten wax (A.1 4.).
6. Grind the sample down to  $400\ \mu\text{m}$ . Use diamond paste, alcohol-water solution and lapping discs. Grind first with  $15\ \mu\text{m}$  grain size paste, then 3 minutes with  $3\ \mu\text{m}$  and 3 minutes with  $1\ \mu\text{m}$  grain size paste. Clean the sample with water and propanol when changing to finer grain size, in order to avoid mixing the pastes and promote the smooth mirror-like sample surface, which is the essential

prerequisite for proper ion-milling. Reaching 400  $\mu\text{m}$  thickness, flip the sample on the grinding rod and grind the sample down to 60  $\mu\text{m}$  from the other side. Always when removing the wax from the sample, use acetone bath to remove the wax and isopropanol to remove the acetone rests. (A.1 5.).

7. Mount the 60  $\mu\text{m}$  thick Ti-holder into the specimen stage of the ion milling machine. Operate it at 4.5-5 kV for the rough ion polishing step, which results in maximal 10-15  $\mu\text{m}/\text{h}$  milling speed in the case of Si. Use both ion guns: one from the top, one from the bottom. The sample is rotated continuously during sputtering. The optimal sputtering angle of the guns is around  $5^\circ$  inclined from the horizontal direction. After a small hole appeared, decrease the angle of the beam to  $3.5\text{-}5^\circ$  and the milling energy to 2.5, then 2.0 and 1.7 kV and polish for 20 minutes with each energy (A.1 5.).

The ion-milling system, used at the Philipps University is a GATAN Precision Ion Polishing System (PIPS). It uses  $\text{Ar}^+$  ion plasma source with high tension between 1 - 5kV. It has two ion guns, that can be operated alternating for time saving. The sample is rotated through the whole sputtering and polishing process.

The second method, which results samples with better contact to the sample holder of the microscope does not use any Ti-holder. The grinding and the ion-milling step can be the same, but the sample is self-supported: the recipe is the following as illustrated on A.1:

1. Cleave two 5mm x 6mm rectangles from the wafer (A.1 1). Cut also a few pieces of the same size from a wafer of the same substrate material.
2. Glue them together face to face with GATAN G1 epoxy resin. (Use the resin mixing ratios and baking times like above). Glue a few more wafer chips (dummies) on both two back sides of the sandwich pair to get a 5 mm thick wafer stack. Harden the glue.
3. Cut 0.9 mm plates of the stack in the desired crystallographical direction ( $[110]$ ,  $[\bar{1}\bar{1}0]$ ,  $[010]$ ) with a diamond wire saw (A.1 2).
4. Cut 3 mm diameter disks out of the plates with the help of an ultrasonic disc cutter. Use the sawing slurry of water and SiC fine powder (A.13).

At this point one has a 0.9 mm thick, 3 mm diameter disc containing only the semiconductor material and the glue. From this stage, the end processing is the same, as in the above mentioned method. The disc can be treated as a sample in a Ti-holder. Although this method is said to be having better contact with the sample holder of the TEM, we observed no difference in the drift what is known to be the result of the bad

A. Appendix

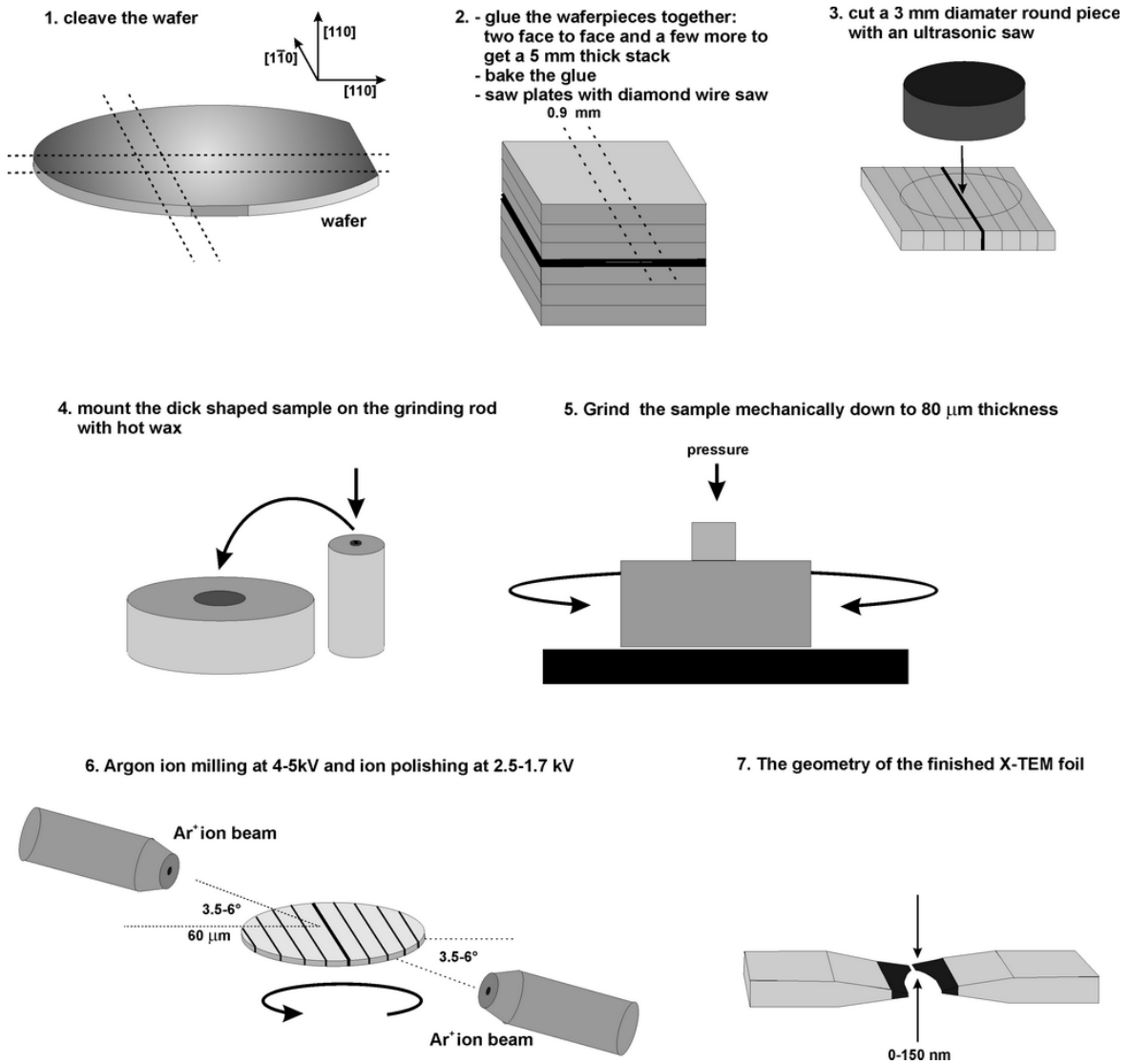
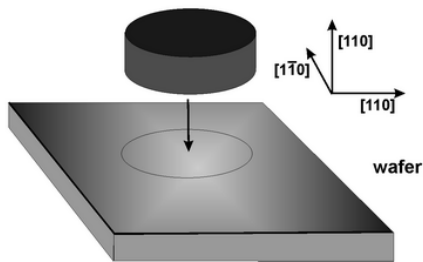


Figure A.2.: Cross sectional TEM sample preparation with self-sustaining samples

1. cut 3 mm diameter disc of the wafer piece



6. Argon ion milling at 4-5kV and ion polishing at 2.5-1.7 kV

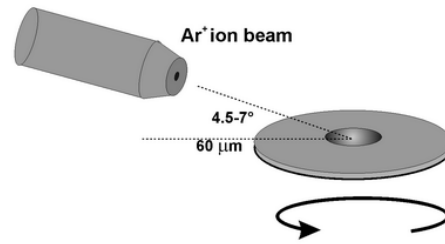


Figure A.3.: Plan view TEM sample preparation

sample - TEM sample holder electric contact. The electric contact of the first method can also be improved by mounting a 3 mm diameter copper or gold hole aperture (a 3 mm diameter thin metal film with a 1 mm hole in it) between the TEM sample and the holding jaws of the TEM sample holder.

### A.2.2. Plan View samples

For the defect characterization and to be able to investigate large lateral areas, the material can be investigated “from the topview”, namely in the  $[001]$  zone axis: this is the **plan view**. The preparation of the plan view samples is easier and faster. How it differs from the cross sectional preparation is shown on A.3. One cuts a 3 mm diameter disc from a piece of the wafer using the ultrasonic disc cutter (A.1 1). This is followed by the same mechanical grinding and polishing steps like in the cross sectional preparation. The only difference is, that the sample is only touched and treated from the back side of the wafer. So as ion-milled: the  $60\ \mu\text{m}$  thick back-side polished sample is mounted onto the post-holder of the PIPS and ion sputtered from the back side, using only one ion gun in continuous mode. The beam energies are the same (4.5-5 kV in the rough sputtering phase and 2.5, 1.0, 1.7 kV at the fine polishing stage).

# Bibliography

- [1] D. A. MILLER, *Proc. IEEE* **88**, 728 (2000).
- [2] L. PAVESI, L. D. NEGRO, C. MAZZOLENI, G. FRANZO, and F. PRIOLO, *Nature* **408**, 440 (2000).
- [3] G. FRANZO, F. PRIOLO, S. COFFA, A. POLMAN, and A. CARNERA, *Appl. Phys. Lett.* **64**, 2235 (1994).
- [4] G. DEHLINGER, L. DIEHL, U. GENNSER, H. SIGG, J. FAIST, K. ENSSLIN, and D. GRÜTZMACHER, *Science* **290**, 2277 (2000).
- [5] H. RONG, A. LIU, R. JONES, O. COHEN, D. HAK, R. NICOLAESCU, A. FANG, and M. PANICCIA, *Nature* **433**, 291 (2005).
- [6] S. FANG, K. ADOMI, S. IYER, H. MORKOC, and H. ZABEL, *Journal of Applied Physics* **68** (7), R31 (1990).
- [7] T. EGAWA, T. JIMBO, Y. HASEGAWA, and M. UMENO, *Appl. Phys. Lett.* **64**, 1404 (1994).
- [8] B. KUNERT, K. VOLZ, J. KOCH, and W. STOLZ, *Journal of Crystal Growth* **298**, 121125 (2007).
- [9] B. KUNERT, K. VOLZ, J. KOCH, and W. STOLZ, *Appl. Phys. Lett.* **88**, 182108 (2006).
- [10] B. KUNERT, S. REINHARD, J. KOCH, M. LAMPALZER, K. VOLZ, and W. STOLZ, *phys. stat. sol. (c)* **3**, 614 (2006).
- [11] B. KUNERT, A. KLEHR, S. REINHARD, K. VOLZ, and W. STOLZ, *Electronic Letters* **42**, 10 (2006).
- [12] K. MOMOSE, H. YONEZU, Y. FUJIMOTO, K. OJIMA, Y. FURUKAWA, A. UT-SUMI, and K. AIKI, *Jpn. J. Appl. Phys.* **41**, 7301 (2002).
- [13] T. KUAN and C.A.CHANG, *J. Appl Phys* **54**, 4408 (1983).
- [14] F. GLAS, *Philos. Mag.* **84**, 2055 (2004).

- 
- [15] P. N. KEATING, *Phys. Rev.* **145**, 637 (1966).
- [16] K. VOLZ, O. RUBEL, T. TORUNSKI, S. D. BARANOVSKII, and W. STOLZ, *Appl. Phys. Lett.* **88**, 081910 (2006).
- [17] P. A. DOYLE and P. S. TURNER, *Acta Cryst.* **A24**, 390 (1968).
- [18] A. ROSENAUER, M. SCHOWALTER, F. GLAS, and D. LAMOEN, *Phys. Rev. B* **72**, 085326 (2005).
- [19] W. A. HARRISON, E. A. KRAUT, J. R. WALDROP, and R. W. GRANT, *Phys. Rev. B* **18**, 4402 (1978).
- [20] H. KROEMER, *Journal of Crystal Growth* **81**, 193 (1987).
- [21] G. AMINOFF and B. BROOME, *Zeitschrift für Kristallographie* **80**, 355 (1931).
- [22] D. HOLT, *J. Chem. Phys. Solids* **30**, 12971308 (1969).
- [23] L. C. BOBB, H. HOLLOWAY, K. MAXWELL, and E. ZIMMERMAN, *J. Appl. Phys.* **37**, 3909 (1966).
- [24] D. VANDERBILT and C. LEE, *Phys. Rev. B* **45**, 19 (1992).
- [25] M. HENZLER and J. CLABES, *Proc. 2nd Intern Conf. on Solid Surfaces. [Japan. J. Appl. Phys. Suppl. 2, Part 2]*, 389 (1974).
- [26] R. KAPLAN, *Surface Science* **93**, 145 (1980).
- [27] R. J. FISCHER, N. C. CHAND, W. F. KOPP, H. MORKOC, L. P. ERICKSON, and R. YOUNGMAN, *Appl. Phys. Lett.* **47**, 397 (1985).
- [28] Y. TAKAGI, H. YONEZU, K. SAMONJI, T. TSUJI, and N. OHSHIMA, *J. Cryst. Growth* **187**, 42 (1998).
- [29] T. SAKAMOTO and G. HASHIGUCHI, *Japan. J. Appl. Phys.* **25**, L57 (1986).
- [30] J. W. MATTHEWS and A. E. BLAKESLEE, *J. Cryst. Growth* **27**, 118 (1974).
- [31] R. PEOPLE and J. C. BEAN, *Appl. Phys. Lett.* **47**, 322 (1985).
- [32] Y. OKADA and Y. TOKUMARU, *J. Appl. Phys.* **56**, 314 (1984).
- [33] I. KUDMAN and R. J. PAFF, *J. Appl. Phys.* **43**, 3760 (1972).
- [34] N. HAYAFUJI, H. KIZUKI, M. MIYASHITA, K. KADOIWA, T. NISHIMURA, N. OGASAWARA, H. KUMABE, T. MUROTANI, and A. TADA, *Jpn. J. Appl. Phys.* **30**, 459 (1991).

- [35] A. ROSENAUER, *Transmission Electron Microscopy of Semiconductor Nanostructures - An analysis of Composition and Strain State*, Heidelberg, Springer, Springer Tracts in Modern Physics 182, 2003.
- [36] J. C. H. SPENCE and J. M. ZUO, *Electron Microdiffraction*, Plenum Press, New York, 1992.
- [37] W. O. SAXTON, M. A. O'KEEFE, D. J. H. COCKAYNE, and M. WILKENS, *Ultramicroscopy* **12**, 75 (1983).
- [38] D. B. WILLIAMS and C. CARTER, *Transmission Electron Microscopy: A Textbook for Materials Science*, Plenum Press New York and London, 1996.
- [39] P. B. HIRSCH, A. HOWIE, R. B. NICHOLSON, D. W. PASHLEY, and M. J. WHELAN, *Electron microscopy of thin crystals*, Butterworths, London, 1965.
- [40] J. S. REID, *Acta Cryst.* **A39**, 1 (1983).
- [41] L. REIMER, *Transmission Electron Microscopy*, Heidelberg Springer, Springer Series in Optical science, 1993.
- [42] H. BETHE, *Annalen der Physik* **87**, 55 (1928).
- [43] B. FULTZ and J. HOWE, *Transmission Electron Microscopy and Diffractometry of Materials*, Springer, 2002.
- [44] A. THUST, W. M. J. COENE, M. O. DE BECK, and D. V. DYCK, *Ultramicroscopy* **64**, 211 (1996).
- [45] K. URBAN, C. M. SCHNEIDER, T. BRÜCKEL, S. BLÜGEL, K. TILLMANN, and M. LENTZEN, *Probing the Nanoworld*, Research Centre Jülich, Institute of Solid State Research, 2007.
- [46] G. C. GLAS, F. and P. HÉNOC, *Philos. Mag. B* **62**, 373 (1990).
- [47] J. L. MARTINS and A. ZUNGER, *Phys. Rev. B* **30**, 6217 (1984).
- [48] F. GROSSE and J. NEUGEBAUER, *Phys. Rev. B* **63**, 085207 (2001).
- [49] I. VURGAFTMAN, J. R. MEYER, and L. R. RAM-MOHAN, *J. Appl. Phys.* **89**, 5815 (2001).
- [50] LANDOLT-BÖRNSTEIN, *Numerical Data and Functional Relationships in Science and Technology Crystal and Solid State Physics, vol. III*, Springer, Berlin, 1972.
- [51] V. FOCK, *Zeitschrift der Physik* **62**, 795 (1930).

- 
- [52] W. KOHN and L. J. SHAM, *Phys. Rev* **137 (6A)**, 1697 (1965).
- [53] W. KOHN and L. J. SHAM, *Phys. Rev.* **140**, A1133 (1965).
- [54] P. BLAHA, K. SCHWARZ, G. K. H. MADSEN, D. KVASNICKA, and J. LUITZ, Wien2k: An Augmented Plane Wave + Local Orbitals Program for Calculating Crystal Properties, Technical report, Karlheinz Schwarz, Techn. Universität Wien, Austria,, 2001.
- [55] N. F. MOTT, *Proc. Roy. Soc.* **A127**, 658 (1930).
- [56] T. MARSCHNER, *Strukturelle Eigenschaften verspannter und verspannungrelaxierter Heteroepitaxieschichten*, PhD thesis, Fachbereich Physik der Philipps-Universität Marburg, 1995.
- [57] A. ISHIZAKA and Y. SHIRAKI, *J. Electrochem. Soc.* **33**, 666 (1986).
- [58] D. ASPNES and J. IHM, *Phys Rev Letters* **57**, 3054 (1986).
- [59] *Multi Mode Scanning Probe Microscope Instruction Manual*, Digital Instruments Inc., Santa Barbara, USA (Veeco), 1996.
- [60] L. VEGARD, *Zeitschrift für Physik* **5**, 17 (1921).
- [61] D. NEUMANN, H. ZABEL, R. FISCHER, and H. MORKOC, *J. Appl. Phys.* **61**, 1023 (1987).
- [62] T. TORUNSKI, *Elektronmikroskopische Untersuchungen zur quantitativen Analyse N-haltiger III/V-Halbleiterheterostrukturen*, PhD thesis, Philipps Universität Marburg, 2005.
- [63] L. T. ROMANO, I. ROBERTSON, J. E. GREENE, and J. SUNDGREN, *Physical Review B* **36**, 7523 (1987).
- [64] J. E. E. BAGLIN, editor, *R.C. Pond, J. P. Gowers, D. B. Holt, B. A. Joyce, J. M. Neave, and P. K. Larsen*, Materials Research Society Symposium Proceedings, 1984.
- [65] P. A. STADELMANN, *Ultramicroscopy* **21**, 131 (1987).
- [66] E. SPIECKER, *Inst. Phys. Conf.* **180**, 233 (2003).
- [67] M. TANAKA, M. TERAUCHI, and K. TSUDA, *Convergent Beam Electron Diffraction*, JEOL Ltd., 1994.
- [68] J. TAFTO and J. SPENCE, *Journal of Applied Crystallography* **15**, 60 (1982).

- [69] E. SPIECKER, *Development of Quantitative TEM Techniques and Their Use In Microstructure Studies of Thin Film Materials*, Habilitationsschrift, 2007.
- [70] E. SPIECKER, *Ultramicroscopy* **92**, 111 (2002).
- [71] K. MARTHINSEN, T. LINDHEIM, and R. HOIER, *Acta Cryst* **53**, 366 (1997).
- [72] K. TSUDA and M. TANAKA, *Acta Cryst.* **A55**, 939 (1999).
- [73] T. G. and M. J. GORINGE, *Transmission Electron Microscopy of Materials*, Wiley-Interscience, New York, 1979.
- [74] K. KAMBE, *Ultramicroscopy* **10**, 223 (1982).
- [75] J. COWLEY and A. MOODIE, *Acta Cryst.* **10**, 609 (1957).
- [76] K. TILLMANN, A. THUST, and K. URBAN, *Microsc. Microanal.* **10**, 185 (2004).
- [77] P. R. C. KENT and A. ZUNGER, *Phys. Rev. B* **64**, 115208 (2001).
- [78] G. HART and A. ZUNGER, *Phys. Rev. B.* **62**, 13522 (2000).
- [79] L. BELLAICHE, S. H. WEI, and A. ZUNGER, *Phys. Rev. B.* **54**, 17568 (1996).
- [80] O. RUBEL, I. NÉMETH, W. STOLZ, and K. VOLZ, *Phys. Rev. B.* - submitted (2007).
- [81] I. NÉMETH, T. TORUNSKI, B. KUNERT, W. STOLZ, and K. VOLZ, *J. Appl. Phys.* **101**, 123524 (2007).
- [82] S. OBERHOFF, *Morphologie innerer Grenzflächen in verdünnt stickstoffhaltigen III/V-Materialsystemen*, PhD thesis, Philipps University Marburg, 2007.
- [83] D. COHEN and C. CARTER, *Journal of Microscopy* **208**, 84 (2002).
- [84] V. NARAYANAN, N. SUKIDI, K. J. BACHMANN, and S. MAHAJAN, *Thin Solid Films* **357**, 53 (1999).

# Academic Biography

**1979.10.12** Born in Wolfen/Germany

**1994-1998** ELTE Apáczai Csere János High School, Budapest, Hungary

**1998-2004** Budapest University of Technology and Economics, Hungary  
Faculty of Natural Sciences  
M.Sc. in Engineering Physics

**2001-2004** Eötvös Lóránd University, Budapest, Hungary  
Certified Teacher of Physics

**2005-2008** Philipps University Marburg, Germany  
PhD. Candidate at the Central Technology Laboratory, Physics Department,  
Philipps University, Marburg  
PhD. Scholarship of the European Graduate College  
“Electron-Electron Interactions in Solids” (Marburg–Budapest)  
International Research Training Group 790

**2006-2007** Student representative of the International Research Training Group 790  
*Electron–Electron Interactions in Solids* (Marburg-Budapest)

# Acknowledgements

At this point I thank everyone who made the completion of this thesis possible and helped me and taught me on the way.

First of all, I would like to thank my supervisor Dr. Kerstin Volz for all the time, knowledge and patience she invested in me. It has been a privilege to work with her and I am proud to be her first “official” Phd. Student.

Köszönöm Kerstin!

I thank Dr. Wolfgang Stolz for creating a thriving scientific and working environment where I could work on this topic.

I would like to thank Professor Florian Gebhard and Professor Peter Thomas for giving the opportunity to join the European Graduate College “*Electron-electron interaction in solids*” IRTG 790 and the EGC for the financial support through the years.

I thank Dr. Bernardette Kunert for the growth of the samples which were presented in the thesis, for the dynamic discussions and for her cheering working spirit.

I am very grateful to Dr. Oleg Rubel who did the DFT and VFF calculations for the refined structure factor calculations for this thesis. I could turn to him with him any question at any time. Spasibo Oleg!

I thank Dr. Torsten Torunski for introducing me to the TEM measurements.

I thank the technical crew of the CTL, Thomas Ochs, Stefan Reinhard and Celina Becker for the support in technical problems.

I would like to thank Dr. Tim Adams for the critical reading and the grammar-correction of the thesis.

I thank Michael Pokoj for helping fixing computer problems.

I thank for the whole CTL Team for the helping hand, the memorable “Sommer- and Weihnachtsfests” and the friendly atmosphere: Dr. Tim Adams, Celina Becker, Dr. Bernardette Kunert, David Lackner, Dr. Michael Lampalzer, Heidi Metzdorf, Dr. Stefan Oberhoff, Thomas Ochs, Michael Pokoj, Stefan Reinhardt, Dr. Oleg Rubel, Elke Vaupel, Dr. Wolfgang Stolz, Dr. Kerstin Volz, Vivien Voßebürger.

I am indebted to Erdmann Spiecker at the Christian Albrechts University, Kiel for the showing the hints of the CBED-experiments and the fruitful discussions about crystal polarity.

I thank Kenji Tsuda for providing the CBED simulation software MBFIT.

I would like to thank Michael Hellwig for helping by the “Ididnttouchanythingits-justsuddenlyswitchedoff”-like problems in the TEM Lab at the Philipps University.

I would like to acknowledge Dr. Béla Pécz and Dr. Lajos Tóth at the Research Institute for Technical Physics and Materials Science (MFA) in Budapest for providing me the possibility to use the energy-filtered microscope.

I also thank Árpád Barna, István Kovács and Andrea Jakab for showing some new hints of TEM-sample preparation at the MFA.

There are also a couple of people, who made my Marburg-stay unforgettable: Camilla, Daniel, Giuseppe, Miriam, Thomas and the Marburger Kletterers.

---

Ezúton szeretnék köszönetet mondani mindazoknak, akik mellettem álltak nemcsak a disszertáció írásakor, hanem azon a bizonyos rögös úton...

A marburgi “Hängerienkomjuniti”-nek a sok Unterstüccungért, hogy ennyire gut vorangekommen bin: Ági, Gyulus, Jócó, Kornél, Mester, Noémi, Péter

A “Mikorjösszhaza?” otthoniaknak: Gyuri, Máté, Miki, Misi, Péter, Viki

A családomat illeti a legnagyobb köszönet. Köszönöm édesanyámnak, Larisza Mes-cserjakovának és édesapámnak, Németh Józsefnek, hogy elindítottak ezen az úton és sok áldozatot hozva végigsegítettek rajta. Köszönöm Nektek, és Neked, Ági, hogy mindvégig bíztatok bennem.